Irradiation Effects on the Deformation of Oxide Dispersion Strengthened Steels

A thesis submitted for the degree of Doctor of Philosophy
at the University of Oxford
Trinity Term 2015

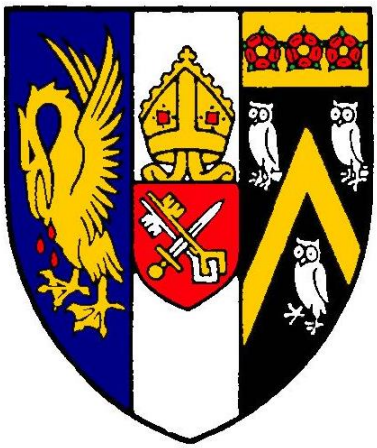

Eleanor M. Grieveson

Department of Materials and Corpus Christi College

Supervisor: Professor Steve G. Roberts

"With magic, you can turn a frog into a prince.
With science, you can turn a frog into a PhD
and you still have the frog you started with."

— Sir Terry Pratchett, The Science of Discworld [1]

(No frogs were harmed in the creation of this thesis.)

Abstract

This study concerns four high performance structural alloys designed to withstand the extreme temperature and irradiation environment inside fusion and fission fast breeder reactors: two Reduced Activation Ferritic Martensitic (RAFM) steels (Fe-14wt%Cr and a European standard alloy EUROFER97) and two equivalent Oxide Dispersion Strengthened (ODS) steels (Fe-14wt%Cr ODS (CEA ODS) and EUROFER ODS).

Neutron irradiation of the samples was impractical due to timescale and specific handling requirements for radioactive samples. Instead, ion implantation was used to simulate the helium and damage of neutron irradiation. Samples of each alloy were subjected to a range of ion implantations: 75appm He, 2000appm He, 2000appm He + 4.5dpa Fe and 2000appm Ne. The matrix of four materials and five implantation conditions was analysed using the following experimental techniques: nanohardness indentation, Vickers hardness testing, micropillar compression, microcantilever bending, transmission electron microscopy (TEM) and energy-dispersive X-ray spectroscopy (EDX).

These techniques were used to compare the properties of the unimplanted materials and their response to implantation. Yield stress (σ_y) was comparable across hardness testing and microcantilever bending, and consistently showed σ_y Fe-14wt%Cr < EUROFER < EUROFER ODS < CEA ODS. When subject to helium implantation, 75appm He caused insignificant changes in σ_y while 2000appm He increased σ_y in all materials. This increase was most significant in Fe-14wt%Cr due to its low grain boundary density and lack of oxide/carbide particles. The particle dispersions in the other materials act as helium traps, preventing the formation of TEM visible bubbles and reducing the hardening effects of the helium.

Across all results it becomes clear that, although not to the degree of the ODS materials, EUROFER is more radiation resistant than Fe-14wt%Cr. It therefore appears that it is the presence of a complex microstructure including small grains and a distribution of oxide or carbide particles, rather than the specific inclusion of oxide nanoparticles, that provides RAFM steels with superior irradiation resistance properties.

Preface

The work presented in this doctoral thesis has been carried out at the Department of Materials, University of Oxford from Michaelmas Term 2010 to Trinity Term 2015 under the supervision of Professor Steve G. Roberts. All of the research carried out for this thesis is original and where the work of others has been included, it has been clearly referenced and acknowledged. No part of this thesis has been submitted for a degree at this, or any other university. Some of the work has been published in peer-reviewed journals and presented at conferences and seminars as detailed below:

Posters:

Hardening Effects of Helium in Fe-based ODS Alloys; E.M. Grieveson, S.G. Roberts
> *Materials for Fission and Fusion Power - ODS Workshop, Oxford, September 2012*
> *Rolls-Royce Materials, Chemistry and Corrosion PhD Conference, Derby, November 2012*

Micromechanical Testing of Irradiation Effects in ODS-Alloys; E.M. Grieveson, S.G. Roberts
> *Symposium of Fusion Engineering (SOFE), San Francisco, USA, June 2013*
> *Rolls-Royce Materials, Chemistry and Corrosion PhD Conference, Derby, November 2013*

Fusion. Powering our Future; E. M. Grieveson
> *Armourers and Brasiers Alumni Event, January 2014*

External Presentations:

Symposium of Fusion Engineering (SOFE), San Francisco, USA, June 2013
(Prize for Best Student Presentation)

EUROMAT, Seville, Spain, September 2013

ODISSEUS, Dresden, Germany, December 2013

Armourers and Brasiers Alumni Event, January 2014
(Elevator Pitch Second Place Prize)

Paper:

Investigation into irradiation effects in ODS steels using ion implantation and micromechanical testing; E. M. Grieveson, S. G. Roberts, July 2013
SOFE 2013 Conference Proceedings

Acknowledgements

My thanks for help with this project go to:

Steve Roberts for supervision, ideas, questions and Pratchett quotes.

Dave Armstrong and Ben Britton for being the go-to Postdocs for any questions.

My parents for always asking what I was up to, for managing to remember all the different acronyms I use and for proof reading to check my spelling and grammar!

Tom for forgiving me for subjecting him to science overload and proof reading.

The Oxford Materials TSG and RSG for keeping the microscopes up and running for as much time as possible, particularly Greg for teasing me every time he saw me, asking: "What have you broken now?"

Adrian and Nianhua at the Surrey Ion Beam Centre and Yves, Sylvain and Eric at JANNUS, CEA Saclay for running my ion beam implantations.

Julia Greer at CalTech for letting me visit and use the SEMentor and Seok-Woo Lee for helping me perform all my experiments out in California.

Mr George and Mr Danvers for providing the best local, edible, cold, creamy stress relief!

The various MFFP students who have swapped microscope sessions, collected samples, helped to understand my results and suggested we go for coffee when everything was going wrong. Especially Stella (for being in it with me for 8 years) and Mike (for EBSD scans).

And anyone else who's ever listened to me complaining that the FIB is broken... again!

Thanks for financial support go to:

Engineering and Physical Science Research Council
Rolls-Royce Plc.
The Worshipful Company of Founders
The Worshipful Company of Armourers and Brasiers
Corpus Christi College, Oxford

Acronyms and Abbreviations

AFM	Atomic Force Microscopy
APT	Atom Probe Tomography
CalTech	California Institute of Technology
CEA	Commissariat à l'Energie Atomique et aux Energies Alternatives
CCFE	Culham Centre for Fusion Energy
CNRS	Centre National de la Recherche Scientifique
CRSS	Critical Resolved Shear Stress
D	Deuterium
DBTT	Ductile-Brittle Transition Temperature
DEMO	Demonstration Power Plant
dpa	Displacements Per Atom
dpa*	$\frac{\text{Implanted He}}{\text{Displacement Per Atom}}$
EBSD	Electron Backscatter Diffraction
EDX	Energy-Dispersive X-ray spectroscopy
EELS	Energy Electron Loss Spectroscopy
EFDA	European Fusion Development Agreement
EMP	Electron Microprobe
F/M	Ferritic/Martensitic
FIB	Focused Ion Beam
GenIV	Generation IV (Fission Reactors)
GFR	Gas-cooled Fast Reactor
GIF	Generation IV International Forum
GND	Geometrically Necessary Dislocations
HFIR	High Flux Isotope Reactor
HIP	Hot Isostatic Pressing
HRTEM	High Resolution Transmission Electron Microscopy
IFMIF	International Fusion Materials Irradiation Facility
ITER	International Thermonuclear Experimental Reactor
JET	Joint European Torus
KIT	Karlsruhe Institute of Technology

KMC	Kinetic Monte Carlo
LFR	Lead-cooled Fast Reactor
LIPAC	Linear IFMIF Prototype Accelerator
MA	Mechanical Alloying
MD	Molecular Dynamics
MFFP	Materials for Fusion and Fission Power
MSR	Molten Salt Reactor
NFA	Nanocluster-strengthened Ferritic Alloy
NRT	Norgett, Robinson and Torrens
ODS	Oxide Dispersion Strengthened
pka	Primary Knock-on Atom
RAFM	Reduced Activation Ferritic Martensitic
RPV	Reactor Pressure Vessel
SANS	Small Angle Neutron Scattering
SCWR	Super Critical Water-cooled Reactor
SEM	Scanning Electron Microscopy
SFR	Sodium-cooled Fast Reactor
SRIM	Stopping Range of Ions in Matter
T	Tritium
TEM	Transmission Electron Microscopy
UTS	Ultimate Tensile Strength
VHTR	Very High Temperature Reactor

Contents

Chapter 1
Background and Literature

1 Introduction

"We say that we will put the sun into a box. The idea is pretty. The problem is, we don't know how to make the box."
Sébastien Balibar, Director of Research, CNRS [2]

If nuclear energy is to become a contributor to future power production, we must recognise that current fission methods are limited, and invest in fusion and fission fast-breeder reactors. These will require new high performance structural alloys. The first wall in a nuclear fusion reactor needs to withstand working temperatures of 550-800°C, bombardment by high energy neutrons with a flux of $10MWm^{-2}$ causing at least 100dpa (displacements per atom) and implantation and transmutation of helium up to 1200appm for a working cycle of five years [3]. A Generation IV (GenIV) fission reactor will have similar operating conditions to a fusion reactor: working temperature 300-1000°C, up to 200dpa and ~20appm of implanted helium [4] over a working lifetime of up to 60 years [5].

There are some important differences between fusion and fission systems. Fusion systems have much higher energy neutrons (fusion: 14MeV/neutron; fission: 1.67MeV/neutron [6]) which lead to hydrogen and helium production by transmutation (also present in fission, but in lower concentrations due to the lower neutron energy [7]). GenIV reactors will use lithium, lead or molten salt coolants as opposed to water, helium or liquid Li-Pb for fusion [4]. However, there are sufficient similarities in

working environments that much of the materials research is applicable to both systems.

1.1 Nuclear Fusion Power

Nuclear fusion power will harness the energy from the reaction of deuterium and tritium to produce helium and high energy neutrons [8]. A nuclear fusion reactor confines a toroidal plasma in a magnetic field. Since the neutrons produced have no electrical charge, they are unaffected by the magnetic fields and carry away ~80% of the produced energy (14MeV/neutron) on emission. Collision with the reactor walls releases energy as heat which can be harnessed to create steam to drive turbines for power. Incident neutrons also cause tritium breeding within the walls, which can be captured and recycled into the reactor.

1.1.1 JET/ITER/DEMO

Ignition is the critical point at which a fusion reactor starts to produce more energy from the plasma than was required to initiate the reaction. Currently the most efficient fusion reactors are based on a tokamak torus design. JET (Joint-European-Torus) at CCFE Culham, Oxfordshire, has produced up to 30MW and run reactions for up to 60s at a time [9]. It is, however, unable to reach the critical ignition point, due to its relatively small size (see Figure 1). The fusion product is a combination of the conditions within the reactor (temperature*reactant density*confinement time). The reactor temperature is almost at the maximum structural limit, and increasing the reactant density would require stronger magnets (>15T is not feasible) and a greater power input. Confinement time is the only easily adjustable parameter – by increasing the volume of the plasma. The larger the plasma volume, the smaller its surface-area to volume ratio. This provides the particles in the middle of the plasma with a longer lateral mean-free-path so energy is retained better than in a smaller volume. The

confinement time – a measure of the rate of energy loss to its environment – increases with volume [10].

Following JET, the next step is to build ITER (International Thermonuclear Experimental Reactor) [11] at Caderache, France. Construction of the tokamak complex is underway and assembly of the reactor started in 2015. The first plasma run in ITER is expected by 2020, with deuterium-tritium operations starting in 2027 [12][13]. It will be a test bed for the large-scale plasma physics required for a reactor and for the reactor materials.

Following ITER it is hoped that the even larger DEMO (demonstration power plant) will be built. With an in-situ system to convert lithium to tritium and a heat extraction system for power generation it will be the test of whether fusion power can become a reality. With increases of 15% in linear dimensions and 30% in plasma density over ITER, it should produce up to 500MW of electricity [14]. Construction is due to start in early 2030s. The ultimate aim is to feed fusion electricity to the grid by 2050 [15].

A major challenge for a fusion reactor is the extreme conditions to which the structural materials will be subjected whilst sustaining minimal property loss during prolonged operation. The first wall plasma facing materials will be exposed to $2MWm^{-2}$ and a $10^{18}m^{-2}s^{-1}$, 14MeV neutron flux; they must show minimal sputtering, deposition, damage and tritium retention. The divertor is the exhaust component, which will convert the kinetic energy of charged particles into heat for power production. Its materials must cope with power densities of $20MWm^{-2}$ [16]. Plasma pulses of up to 500s will possibly occur in ITER (cf. 10s in JET); electron, ion and power fluxes in ITER will be 2-3 times higher, causing accumulated damage four orders of magnitude higher [16]. The conditions in ITER will differ from a fully functioning reactor, but they will allow us to gain a better idea of what is needed.

The adverse conditions require the development of special materials. Neutron irradiation causes the formation of dislocation loops and internal production of helium and hydrogen by transmutation will cause embrittlement and changes in creep properties. We need to investigate these changes to understand how best to build a reactor that will last an economic working lifetime (~60 years).

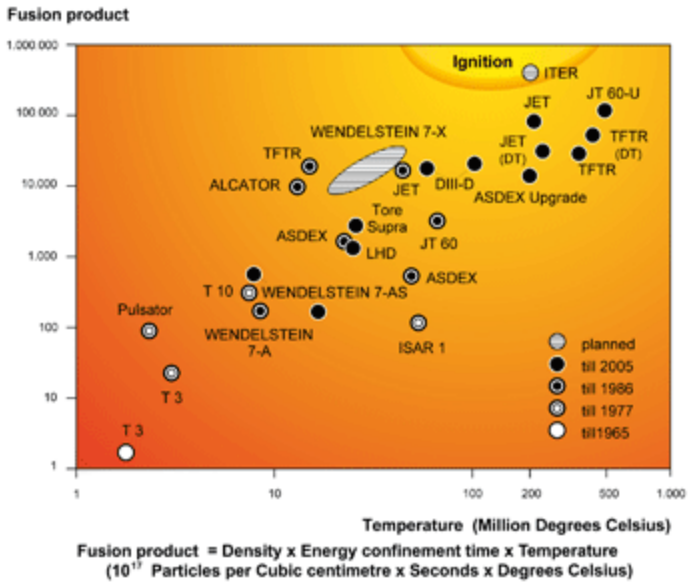

Figure 1 - Progress of fusion product vs. temperature for a series of fusion reactors [17].

Table 1 - Probable operating conditions of ITER, DEMO and a Fusion Reactor [16]

	ITER	DEMO	Reactor
Power (GW)	0.5	2.5-5	2.5-5
First wall heat flux (MWm^{-2})	0.1-0.3	0.5	0.5
Divertor heat flux (MWm^{-2})	10	15-20	20
First wall neutron flux (MWm^{-2})	0.78	2	2
Displacements per annum (dpa)	3	50-80	100-150
First wall He transmutation rate (appm/dpa)	10		
First wall H transmutation rate (appm/dpa)	45		

1.2 Nuclear Fission Power

Fission power utilizes the energy released when unstable uranium or plutonium isotopes are split and produce neutrons. Currently in use are Generation II and III reactors (GenI being early prototypes). Near term deployment will be in the form of GenIII+ reactors with improved designs, efficiency and economics. The next major step in design will be GenIV, expected to be in commercial use around 2030 [18].

1.2.1 Generation IV Reactors

GenIV reactors are currently being developed to provide a sustainable, more efficient way of producing nuclear fission power. The goals set by the Generation IV International Forum (GIF) are as follows [19]:

- Sustainability – providing energy generation to meet clean air objectives, long-term availability of systems, effective fuel utilisation, minimisation of nuclear waste and reduction in the stewardship burden.
- Economics – clear life-cycle cost advantages over other energy sources and a level of financial risk comparable to other energy projects.
- Safety and Reliability – to excel in safety and reliability, a low likelihood of reactor core damage and eliminating the need for offsite emergency response.
- Proliferation Resistance and Physical Protection – increase the assurance that GenIV systems are the least desirable route for theft of weapons-usable materials and provide increased physical protection against acts of terrorism.

Six systems have been selected by GIF for further study [20], details in Table 1:

- Very High Temperature Reactor (VHTR)
- Sodium-cooled Fast Reactor (SFR)
- Super Critical Water-cooled Reactor (SCWR) – high-temperature, high-pressure, operates above the thermodynamic critical point of water.
- Gas -cooled Fast Reactor (GFR)
- Lead-cooled Fast Reactor (LFR)
- Molten Salt Reactor (MSR) – circulating molten salt fuel mixture, epithermal-spectrum reactor, full actinide recycle fuel cycle.

These ensure all possible aspects of the power generation cycle are addressed while providing overlapping coverage of the capabilities.

These systems will use materials subjected to adverse conditions and, although not the same as in the fusion environment, they will be sufficiently similar that research into the high temperature, neutron flux and helium implantation conditions will be relevant.

Table 2 – Overview of GenIV reactor systems [21]

System	Neutron spectrum	Coolant	Outlet Temperature (°C)	Fuel cycle	Size (MW_e)
VHTR	Thermal	Helium	900-1000	Open	250-300
SFR	Fast	Sodium	500-550	Closed	50-150 300-1500 600-1500
SCWR	Thermal/Fast	Water	510-625	Open/Closed	300-700 1000-1500
GFR	Fast	Helium	850	Closed	1200
LFR	Fast	Lead or Lead/Bismuth	480-570	Closed	20-180 300-1200 600-1000
MSR	Thermal/Fast	Fluoride salts	700-800	Closed	1000

2 Irradiation Effects

It is important to understand the response of a material to the effects of irradiation before it goes into service. The reactor components must withstand the conditions with minimal property degradation for an economic working lifetime. For the first wall of a fusion reactor this is at least five years, for structural components it will be longer – GenIV reactors have a proposed lifetime of 40-60 years.

There are three main irradiation effects from fast neutrons:

a) cascade damage from the incident neutrons.

b) introduction of helium (and hydrogen) into the lattice via implantation from the plasma and transmutation of elements in the wall material.

c) transmutation of basic alloy elements causing a change in alloy composition.

2.1 Cascade Damage

The formation of a damage cascade will occur within 10^{-11} seconds and proceeds in the following order [22] (see Figure 2):

- An energetic incident neutron collides with a lattice atom.
- The neutron transfers kinetic energy to that atom.
- This causes displacement of the atom from the lattice (it becomes the primary knock-on atom (pka)).
- Passage of the pka through the lattice causes further knock on atoms.
- This forms a displacement cascade.
- Finally the pka (and other knock-on atoms) stop as interstitials when they run out of energy.

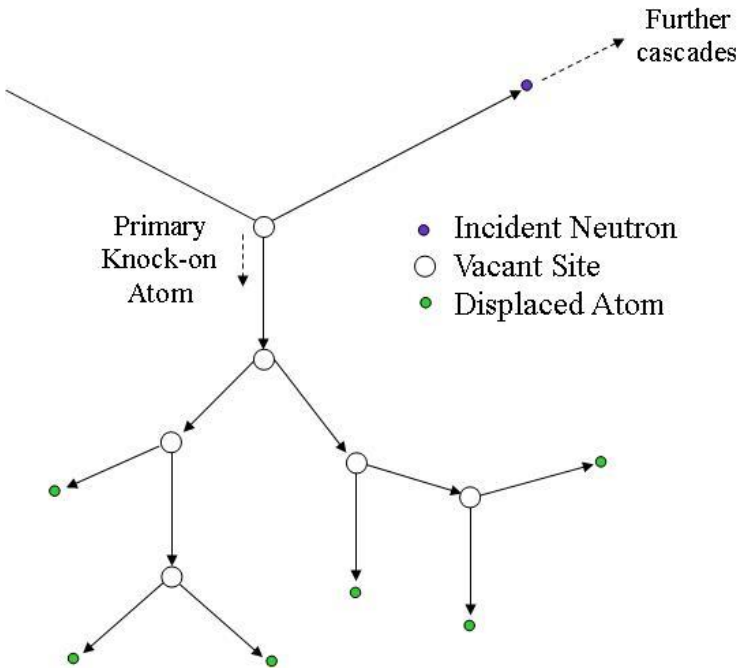

Figure 2 - Neutron damage cascade

These damage cascades cause the formation of point defects (interstitial atoms and vacancies) which cluster into dislocation loops and voids in the material [23]. Interstitials are more mobile in nature, therefore clusters tend to be predominantly interstitial. However, if impurities are present in the material, impurity-defect clusters and bubbles are also likely to form [24]. Large numbers of defects in the lattice will restrict the possible dislocation motion when the material is put under stress; this is irradiation-induced hardening.

Although all materials will exhibit effects of irradiation hardening, some have greater resistance. OPTIFER steels with reduced boron content show less hardening after neutron irradiation than those containing significant amounts (boron increases the Ductile-Brittle Transition Temperature (DBTT) of the alloy and irradiation causes it to transmute to helium) [25]. In iron-chromium alloys the largest increase in hardness is seen at 2.5%Cr with the smallest at 9%. This has led to further work on Fe-Cr alloys concentrating around 9%Cr [26].

Oxide dispersion strengthened (ODS) materials (and similar structures, e.g. precipitate rich materials) show better irradiation damage resistant properties than many other materials. The precipitates in the material act as sinks for vacancies and point defects [27]. ODS material can be resistant to coarsening and dissolution under irradiation damage to at least 0.7dpa at 300°C. The Y-Ti-O precipitates themselves are stable over 500-700°C up to 150dpa [28]. These results apply to ODS containing Ti and may not be applicable to Ti-free steel irradiated with neutrons; more experimentation is needed – see Section 4.3.

The decrease in embrittlement at higher irradiation temperatures is due to the annealing effect from the heat of irradiation. One way of reducing the embrittlement effects in a reactor would be to re-anneal the materials in-situ, e.g. the pressure vessel steel would recover after 70-150 hours at 450°C [22]. This would be relatively easy; the issue would be the effect on any other components in the reactor.

2.2 Helium

High helium concentrations at grain boundaries can cause embrittlement and a reduction in the mechanical strength of the material [29]. As helium is implanted or transmuted, the matrix reaches saturation between 30-50% depending on the microstructure – grain boundaries will be able to hold a higher He density. At greater doses, the helium fills voids in the lattice, is re-emitted or forms surface blisters. If the material is simultaneously being neutron irradiated or heavy-ion implanted then the microstructure will be modified such that induced vacancies will form cavities [30][31].

In non-precipitate-rich materials the cavities form with a bimodal size distribution. Cavities in the lattice grow as they accumulate gas atoms, forming vacancy-gas atom complexes. The standard nomenclature is that small high pressure gas-filled cavities are referred to as bubbles, while larger ones with a low gas pressure are called voids. Once they reach a critical radius (~0.5nm [31]), bubbles can grow through accumulation of

vacancies without additional gas atoms and at this point form voids [31]. A void is a cavity that grows with a bias-driven mechanism – absorption of vacancies without the aid of gas atoms. The critical radius when the change of growth method occurs depends on material parameters (e.g. grain size, dislocation density), irradiation conditions and the microstructure [31].

Under irradiation small vacancy clusters will dissolve and grow as helium-filled cavities. There is a critical bubble radius (typically ~0.5nm in ferritic steels), which determines whether vacancy clusters will shrink or grow [24][31][32][33]:

$r_c = r_b$ (small stable bubble radius)

$r_c = r_v^*$ (larger unstable critical void radius)

$r_c > r_v^*$ (cavities grow unstably into voids)

There is also a critical bubble helium content (m*): m is the number of helium atoms in a bubble, and m* is the critical number at which the bubble transforms to a growing void at critical radius r_c. The value of m* is controlled by interface energies, stress fields and precipitates. Helium bubbles with $m<<m^*$ are excellent defect sinks and therefore reduce or prevent void swelling [24].

Bubbles strongly associate with dislocations, boundaries and precipitates. Those on dislocations are usually larger and fewer than at grain boundaries and precipitates [34]. In steels with no or few precipitates, helium is mostly attracted to grain boundaries. This can cause problems with embrittlement and higher concentrations of helium can cause large shifts in ductile-brittle transition temperature [35] (see Figure 3) and yield stress [36]. In materials with matrix/precipitate or matrix/defect interfaces (other than grain boundaries), the precipitates and defects form low energy traps for the helium atoms and therefore a fine, dense precipitate structure leads to a fine, dense concentration of bubbles. The mechanical property effects of helium/defect

combinations are discussed further (with specifics regarding ODS steels) in Section 4.3.4.

Higher irradiation temperatures increase the diffusion coefficient of helium in the matrix causing the formation of fewer bigger bubbles, decreasing the helium content in the lattice, decreasing the dpa* (implanted He/dpa) and therefore decreasing embrittlement by reducing helium at grain boundaries [25].

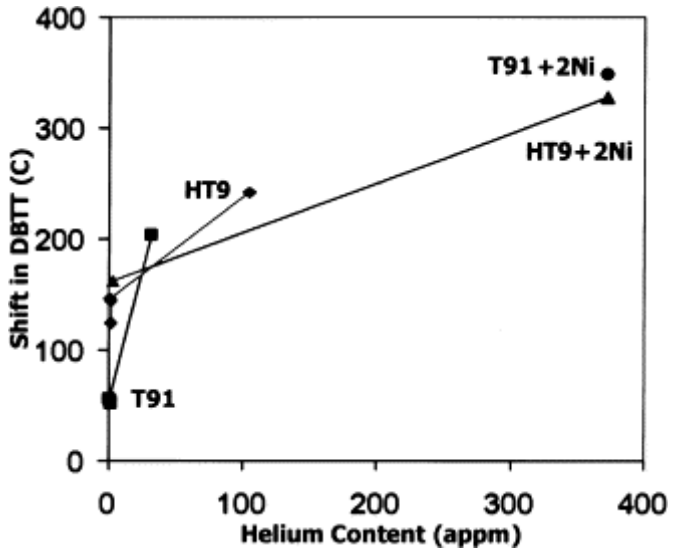

Figure 3 - Shift in DBTT as a function of helium content in a selection of steels [35].

3 Simulation of Irradiation Damage

The problem with investigating the effects on structural materials of a nuclear reactor is that we cannot have a fusion or GenIV reactor from which to take test materials. There are three possibilities for researching the damage that would be caused: neutron irradiation, ion implantation and computer simulation.

3.1 Neutron Irradiation

It is possible to generate direct neutron irradiation by exposing the materials in a fast neutron fission reactor (e.g. BOR60) or a facility such as the High Flux Isotope Reactor (HFIR) at Oak Ridge National Laboratory, USA [37].

The main problems with using neutron irradiated samples are radioactivity, limited specimen volumes and slow damage accumulation rate. Any experimental work requires use of dedicated 'hot cell' equipment and minimum sample sizes. Some groups do work with neutron irradiated material, but they have to design their experiments on a several year time scale (e.g. materials irradiated in 2003 had to be stored until 2006 in order to allow sample radioactivity to decay before handling [38]). Once samples are at a level of radioactivity low enough to be handled, a small sample size is important to reduce contamination of equipment and for the safety of researchers [39].

Experiments performed on neutron irradiated ferritic/martensitic steels have shown that below ~400°C, radiation at low radiation dose, <10dpa causes an increase in yield stress and a decrease in elongation. These effects increase as the irradiation temperature drops. Above ~400°C, thermal effects dominate any mechanical property changes, such as yield stress steadily dropping as temperature increases [40].

A significant advantage of neutron irradiation as a simulation over ion implantation (Section 3.2), is its depth of implantation. Whereas ion implantation can only create damage in the top few microns of a sample, neutron irradiation will pass through a much thicker sample, making macro-sample testing possible.

The International Fusion Materials Irradiation Facility (IFMIF) is a proposed accelerator-based neutron source that will simulate the 14MeV neutrons produced by a fusion reactor using deuterium-lithium stripping reactions. Current plans are for IFMIF to be built in Japan in collaboration with the EU, US and Russia [41]. The Linear IFMIF Prototype Accelerator (LIPAC) is currently being installed. LIPAC Data "will support the start of construction of IFMIF whenever the fusion community demands a fusion-relevant neutron source" [42]. Once constructed, LIPAC and IFMIF will provide fusion reactor-like conditions for materials testing.

3.2 Ion Implantation

The most commonly used form of physical simulation of neutron damage is implantation of heavy ions. Frequently self-ion irradiation is used – the incident ion is effectively the pka. Co-implantation of gases, e.g. He and H, can also be used to simulate the gas ions that come from fusion plasma or that are transmuted in the material during fission or fusion. The main differences between ion implantation and neutron irradiation are:

1) The energy of the incident particles (ions: 2keV to 60MeV depending on implanter and experimental design; neutrons: up to 14MeV for fusion and ~2MeV for fission depending on the reactor and location within it), the dose rate (heavy ions: ~1-5 dpa/hour, neutrons: 1-5 dpa/year).

2) The damage profile: implanted ions lose energy quickly (by electronic interactions at high energy or by collisions at low energy) and therefore have shallow penetration. The depths are scattered and produce a non-uniform energy profile because of varying electronic and nuclear energy losses. Neutrons, however, produce a much deeper and flatter damage profile [22] (Figure 4).

Ion implantation is limited. It fails to match dose rates (the same dose a reactor might cause over several years may be ion implanted over a few hours or days), isotope

transmutation and gas production [28]. It does, however, provide a radiation-free method of producing damage in materials for experimental testing.

The important consideration when using ion implantation is how it compares as a simulation of neutron irradiation damage. If ion implantation is to be used as a true representation of neutron irradiation it should yield the same measure of radiation effect. The path is unimportant if the final product (measured in terms of damage type and concentration) is the same.

The comparison should be in terms of dose rates, temperatures and energies. Experiments changing these parameters will produce visible effects that can be measured [43]. Specifically these look at the nature, size, density and distribution of dislocation loops and defects, and help determine whether elements are enriching or depleting in a region [22].

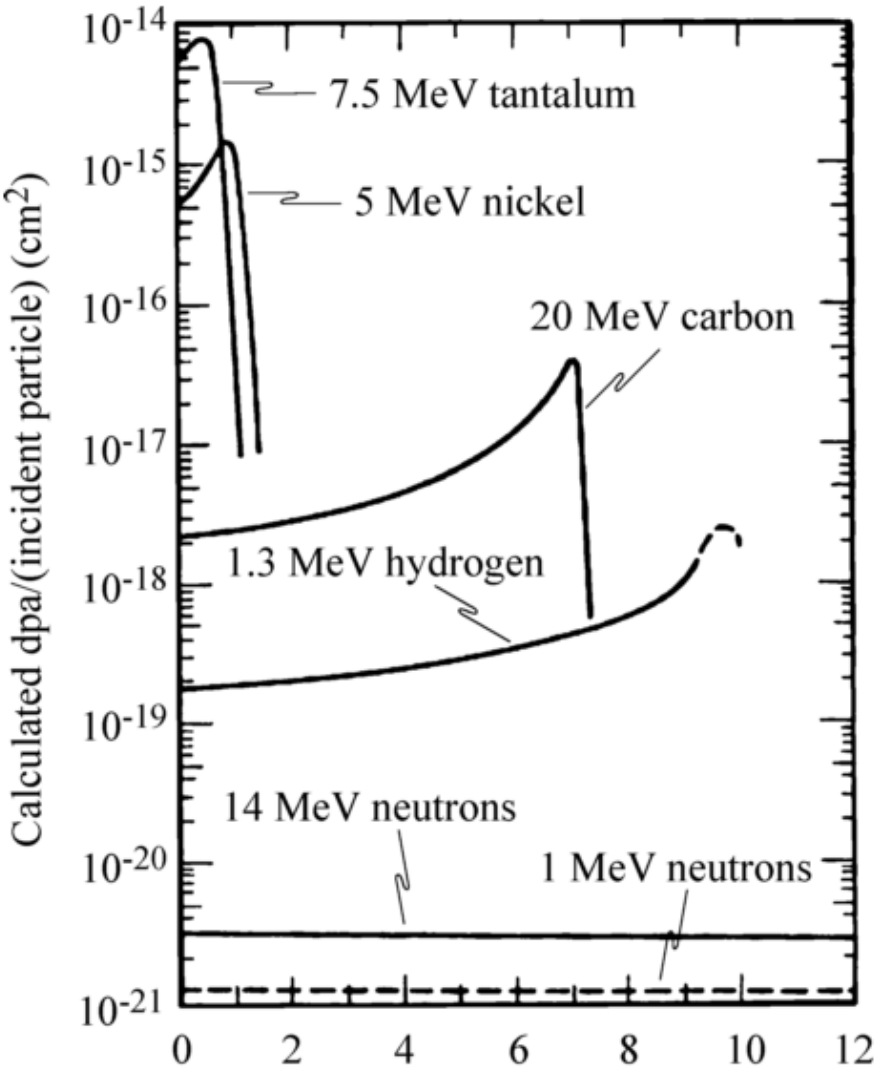

Figure 4 - Relative displacement damage depths for various energetic particles [22]

3.2.1 Ion Implantation of Steels

When doing experimental work on the effects of helium the important issue is the combined effect of helium and irradiation. There is a significant difference in the damage between single implantation (He) and dual implantations (He+Fe) [44]; simultaneous implantation causes greater hardening than sequential implantation. Also the result depends on the order of implantations (Fe before He, vice versa or simultaneous) [45]. Single beam He implantation into EUROFER 97 at 500°C shows some dislocation loops and causes a slight increase in hardness [44]. The equivalent (i.e. same He concentration) dual-beam (He+Fe) at 300°C causes fine, high pressure cavities (nm/sub-nm) with a uniform distribution parallel to the surface and highest density in the top 1500nm [44]. The same irradiations in non-ODS steel showed a change in microstructure, forming much larger cavities with faceted shapes rather than fine spherical bubbles [44]. In a nuclear reactor the helium production will occur at the same time as the neutron irradiation, therefore the most suitable method for simulation is simultaneous helium + heavy ion implantation [46].

A range of experiments [44][47][48] showed that ion implantation provides a reasonable simulation of neutron irradiation, but damage is produced differently and this needs to be taken into consideration when designing irradiation programs.

3.3 Computer Simulation

The final option using computer modelling [22][49] is the only way of understanding the spatial and temporal development of a cascade. Three types of model most commonly used:

- Binary Collision Approximation – this gives a good approximation of the collision stage, e.g. modelling crystalline targets without restrictions on chemistry [22]
- Molecular Dynamics (MD) – this gives the most realistic description of atomic interactions in the cascades, e.g. dislocation cluster formation [50]
- Kinetic Monte Carlo (KMC) – this produces dynamic predictions at the mesoscale, e.g. studying the interactions of defect sinks [51]

In combination MD and KMC cover the entire radiation time scale. Computer simulation can be effectively used to predict the type of damage that neutron irradiation will cause, but is less effective in predicting changes in material responses with changes in composition/microstructure – this still requires experimental data.

SRIM (Stopping Range of Ions in Matter) software is a Monte Carlo simulation code that was written for the calculation of ion beam damage and was used in this project to predict damage depths in order to plan ion implantation experiments (see Section 11). In 1975, Norgett, Robinson, and Torrens (NRT) developed a secondary displacement model for computing the dpa with a given energy [52]. The NRT model was adopted by the international radiation community as the standard method for computing atomic displacement rates [53].

4 Materials

The materials used in a nuclear reactor must be chosen to withstand the extreme environment inside the reactor, whilst also having the correct properties for structural use and being an economic choice.

For both GenIV fission and fusion reactors there are many details to be considered for the material choice [54][55]. Fission requirements for components such as the reactor pressure vessels (RPV) include temperatures up to 660°C, radiation doses up to 200dpa and highly corrosive environments [54]. In fusion, the reactor temperatures and damage are similar (or higher) and the materials considered must be not easily sputtered nor emitted into the plasma. Compositions are required that do not substantially affect the plasma chemistry and radiation level. Tritium retention also has to be considered. It must not be absorbed into the walls because it is radioactive (unlike H and D) but the tritium breeding ratio also needs to be taken into account. Most tritium retention is due to co-deposition with eroded carbon forming T-saturated carbon co-deposits, therefore minimising the carbon content of the wall materials will reduce retention [55] (hence the reason that SiC and C composites are not suitable).

Various options are being investigated including beryllium alloys for the first wall, tungsten for the divertor of fusion reactors, ODS and zirconium alloys for fuel cladding, nickel-based superalloys and ferritic, martensitic and austenitic steels RPV for fission reactors. This report, however, concentrates on iron-based alloys for structural use in both fusion and fission applications.

4.1 Low Activation

Low activation elements are those with high levels of radioactivity immediately after use, but which quickly decay to a 'mostly harmless' level. There are only a few elements that have sufficiently low activation isotopes: C, Cr, Fe, Mn, O, P, Si, Ta, Ti, V and W [56][57].

Of this list, iron-based alloys become the obvious structural material because steels are some of the best researched and longest used materials. High temperature, corrosion resistant variants (usually using chromium and carbon) are already in operation in many power-production, chemical and industrial uses. So the aim is to replace any high activation elements in the steel (such as Ni, Cu, Mo, Nb) with low activation ones (Cr, V, Ti) and characterise any property changes.

Ideally the first wall of a fusion reactor will be in service for at least five years to minimise reactor time offline and reduce the number of replacement procedures. Once removed, the material will be allowed to cool until the radioactivity has sufficiently decayed for parts to be handled.

Figure 5 shows the calculated levels of residual radioactivity with time in a selection of elements as if they had been in the first wall of a fusion reactor for five years. After 100 years, only iron, chromium and vanadium are below the hands-on level of ~10^{-5}Svh^{-1}.

Current low activation materials, for example EUROFER 97 (Table 3), would reach a low activity waste level after 100 years (~10^{-3}Svh^{-1}) [58]. To be hands-on safe however, the radioactivity needs to be two orders of magnitude lower [59]. Most of the activation comes from impurities in the material (such as Nb, Cu, Ni, Mo, and N [60] (Ni, Nb and Mo highlighted in red in Figure 5)). It is technically feasible to reach the required low levels, but it would require careful feedstock control and production lines reserved for reduced activation materials. Once reactors are in commercial production, this may be feasible but currently it is not economical.

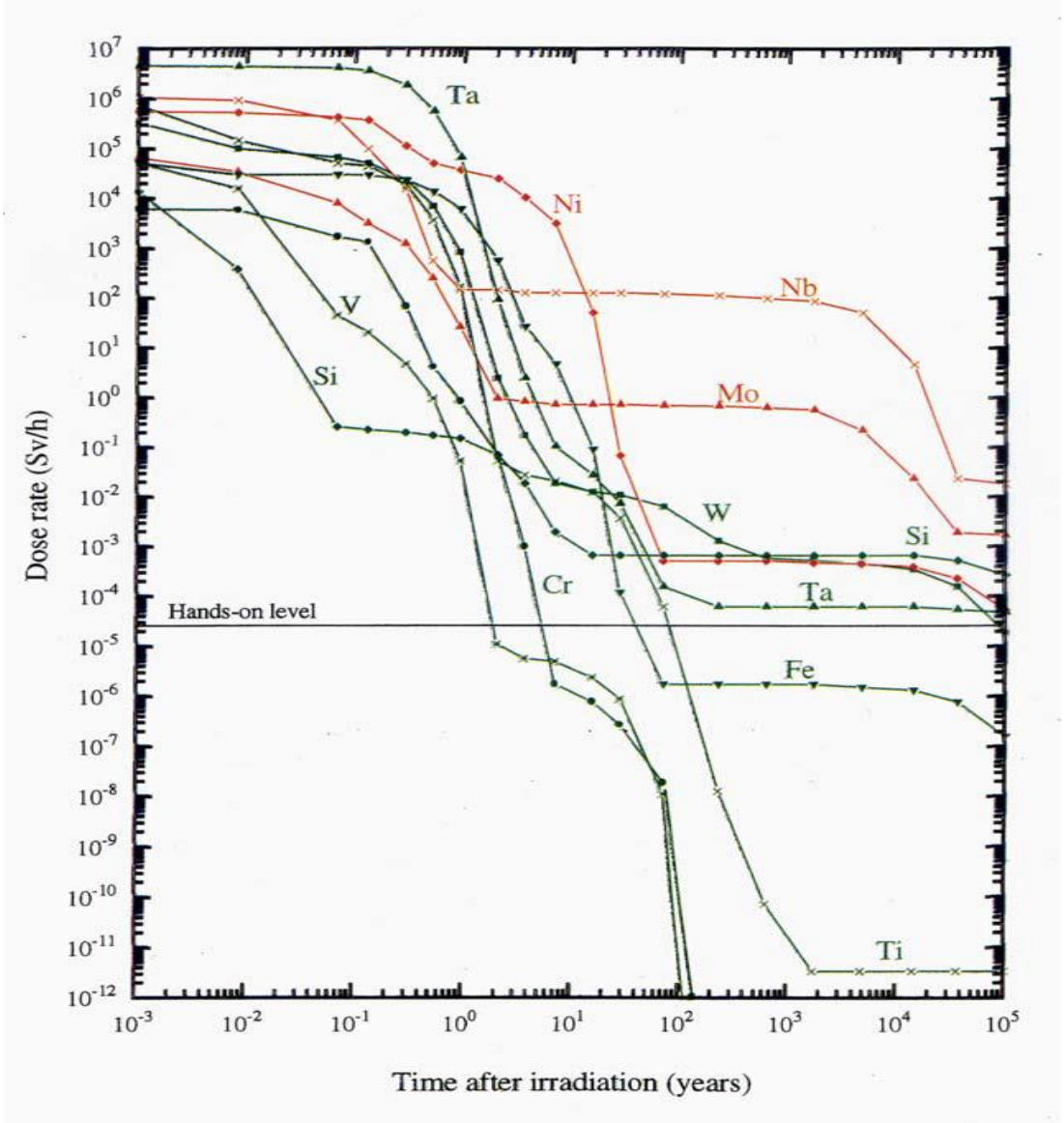

Figure 5 - Calculated radioactivity versus time of selected elements after exposure to a typical fusion neutron spectrum (five years exposure to 20MWy/m² at the first wall) [57]

4.2 Ferritic/Martensitic Alloys

Steels are some of the most highly developed materials available and ferritic/martensitic (F/M) steels are already in use for many high temperature applications (furnace parts, heat exchangers, valves, pumps etc.). Stainless steel would be an obvious starting point as it is has corrosion resistant properties. Most stainless steels contain nickel which is a high activation element; so nickel free iron-chromium alloys are an area that is being currently researched (see below). In reduced activation F/M (RAFM) steels, Nb, Ti and Mn are being replaced by Ta, V and Cr respectively [61] (Nb, Ti, Ta and V – carbide formers and grain refiners; Mn and Cr – increase hardenability).

Once the properties of iron-chromium alloys and their response to irradiation are established within the 0-12wt%Cr range, they can act as a model for future research with the addition of other elements as strengtheners and carbide formers. These simple binary alloys can be used to verify and fit data to material models [62].

The main areas of research for F/M alloys are their upper usage temperature limit, the effects of irradiation damage and the effects of helium on the materials' fracture properties. All current alloys show hardening and increase in yield stress when irradiated at low temperatures. In F/M alloys this occurs below 400°C, but as irradiation temperature increases, the rise in yield strength due to irradiation decreases and becomes negligible above 400°C [63]. The ideal operating temperature of both GenIV and fusion reactors will be between 500 and 1000°C [3][21], so it is the upper temperature limit that is of greater interest. If the limit could be increased to 600-650°C, it would significantly reduce design problems and allow liquid metal cooling systems to be used.

Some alloy compositions have been established, e.g. EUROFER steels designed as reduced activation alloys [59]. The most commonly used is EUROFER 97 (full

composition in Table 3 below). Comparing mechanical properties with other RAFM steels such as OPTIFER and F82H, 0.2% yield stress, ultimate tensile strength and creep strength all show similar trends to the other materials (Table 3).

EUROFER 97 is due to be formed into test blanket modules for ITER to investigate its response to true reactor conditions. Precipitation and dispersion strengthened RAFM alloys are also being investigated both to increase working temperatures and deal with helium implantation. ODS alloys are one class of materials under consideration.

Table 3 - Specified chemical compositions of RAFM steels [59][61][64][65]

	EUROFER 97		***F82H***	***OPTIFER***
Elements	**Weight %**	**Target values**	**Weight %**	**Weight %**
Cr	8.5–9.5	9.0	7.7	9.3
C	0.09–0.12	0.11	0.09	0.11
Mn	0.20–0.60	0.40	0.16	0.50
P	<0.005	-	0.002	46 ppm
S	<0.005	-	0.002	50 ppm
V	0.15–0.25	-	0.16	0.26
B	<0.001	-	0.0002	61 ppm
N_2	0.015–0.045	0.030	0.006	0.016
O_2	<0.01	-	0.01	47 ppm
W	1.0–1.2	1.1	1.94	0.96
Ta	0.06–0.09	-	0.02	0.066
Ti	<0.01 (100 ppm)	-	100 ppm	-
Si	<500 ppm	-	1100 ppm	0.06
Nb	-	<10 ppm	1 ppm	-
Mo	-	<50 ppm	30 ppm	-
Ni	-	<50 ppm	200 ppm	-
Cu	-	<50 ppm	100 ppm	-
Al	-	<100 ppm	30 ppm	80 ppm
Co	-	<50 ppm	50 ppm	-
As +Sn+Sb+Zr	-	<100 ppm	<50 ppm	-
Yield Strength at 400°C (MPa)	340		340	350
Creep Strength at 400°C (MPa)	360		345	370

4.3 Oxide Dispersion Strengthened Materials

ODS materials are metallic alloys containing a fine dispersion of (usually) nanosized oxide particles. Currently, uses include nickel-based ODS superalloys for high temperature applications such as turbine blades [66] and heat exchanger tubing [67]. Commercially available alloys include PM2000 and MA956.

ODS ferritic alloys are in development specifically for use in the nuclear industry [68] as high creep strength radiation damage resistant materials. Their main difference from commercial ODS alloys is the lack of aluminium. Al is not a reduced-activation element, PM2000 and MA956 contain ~5%Al, nuclear ODS alloys contain <100ppm. The dispersed oxide particles form a high density of fine scale features to act as dislocation obstacles and nucleation sites for He bubbles and to promote vacancy-interstitial recombination [69]. Nucleation of He bubbles is considered useful because it reduces the concentration of helium segregating to grain boundaries with consequent embrittlement.

Ferritic steels have low creep strength at high temperatures, thereby limiting their operational temperatures to 550°C [70]. ODS ferritic steels have an increased operating temperature (up to ~800°C) for higher efficiency and high chromium ODS is expected to have high strength at high temperature, corrosion resistance and dimensional stability in irradiation environments [46].

4.3.1 Processing

The most common ferritic ODS alloys under investigation use yttrium as the oxide forming element, often combined with titanium. The high density of coherent, nanometre-scale Y-Ti-O nanoclusters is produced by mechanical alloying of Fe-Cr-Ti and Y_2O_3 powders followed by consolidation through hot isostatic pressing (HIP) or hot extrusion [71][72].

The mechanical alloying process allows the fabrication of materials containing low solubility or immiscible phases [73]. The yttrium oxides are insoluble in the ferritic matrix at all feasible melting temperatures. Mechanical alloying works by repeated cold welding, fracturing, and re-welding of powder particles in a high-energy mill [74]. The Y_2O_3 powder dissolves into the Fe-Cr-Ti during the mechanical alloying process [75] and then during heat treatment/consolidation (e.g. HIP) it forms Y-Ti-O enriched nanoclusters [76]. Clusters formed in annealed mechanically alloyed powders are almost identical to those in the final compressed alloy [77]. The Y-Ti-O particles after HIP/extrusion are much smaller (depending on original powder size) than the original yttria powder and are far from the stoichiometric Y-O composition. Combined with atom probe and X-ray diffraction evidence, this indicates they are not crushed remains of the initial powder but rather have been formed during processing [76][77].

The microstructure of the alloy can be altered by changing the mechanical alloying conditions; for instance, increasing the mechanical alloying temperature leads to increased nanocluster size and a smaller number density and volume fraction of particles [78]. Although is it possible to produce the alloys without any titanium content, both Y and Ti are needed for nanocluster formation at high densities at higher HIP temperatures. In one study, after annealing at 1100°C, the material without Ti contained ~12nm precipitates, whereas in material containing Ti the precipitates were ~2nm diameter – the Ti acts as precipitate refinement [79]. Dislocation pinning increases tenfold with Ti-containing nanoparticles relative to ODS without Ti [80]. A comparison of 12YWT and 12YW alloys revealed a higher number density ($1.4x10^{24}$ and $3.9x10^{23}m^{-3}$ respectively) of particles in the YWT with the average size of particles similar but slightly larger in the YW alloy (radius: 2.0 and 2.4nm respectively; the Ti content aids nucleation of the particles [76]. A high oxygen level was observed and may be a result of trapping of oxygen by W, Cr and Ti atoms in the matrix [76]. These

particles were tested for their high temperature properties and were stable for at least 4000 hours at 850°C and 14,500 hours at 800°C.

To create the oxide particles a high oxygen solubility is needed, which requires the creation of lattice vacancies by non-equilibrium processes (e.g. mechanical alloying (MA)). MA ODS alloys contain significantly higher oxygen concentrations (~1000ppm) than conventionally cast ferritic alloys (few ppm)[75]. This oxygen comes from Y_2O_3 during milling and from oxides on the powder surfaces and inclusions. Vacancies play an indispensable part in enhancing the oxygen/titanium binding energy in the presence of Ti [81]. They bring the binding energy of O closer to the formation energy of TiO_2, thereby stabilizing coherent nanoclusters in the lattice. Adding Y further increases presence of vacancies, but if too much Y is present, $Y_2Ti_2O_7$ forms [81]. For the formation of stable nanoclusters, the atomic % of Ti needs to be higher than that of Y [81]. High levels of Ti and O (controllable through high purity powders and purification of mechanical alloying atmosphere [82]) are not ideal, however, as they tend to form TiO_2 rather than yttrium based oxides [81].

It is not just the distribution of particles in the material that affects the irradiation properties. Tests on ODS RAFM steel of varying tungsten content showed that the material with W seemed to be unaffected by irradiation while the material without W shows a stronger radiation induced hardness increase. ODS without W contained fewer particles and had reduced yield strength. It was concluded that a particle density of $10^{23}m^{-3}$ was needed to remove radiation damage efficiently [83].

4.3.2 Processing Issues

A range of outstanding issues with ODS F/M alloys must be addressed before they can be put into commercial use [24]. These include the use of MA [74] and powder processing as opposed to the standard alloy manufacturing route of melt processing followed by rolling or forging. Not only is it more expensive to use MA, it is currently only available on a small scale. If large quantities of these alloys are to be produced work must be done to scale up the ball milling process (low energy drum mills can currently produce up to 100kg powder at a time [84]). Hot isostatic pressing (HIP) and extrusion are the only widely used methods of compressing the powders into a bulk material. Extrusion is only useful for components of a uniform cross-section and produces an anisotropic grain structure [24], while HIP constrains the possible dimensions; the largest available HIP (Bodycote plc.) currently has a work zone of ~5m^3.

The high temperature strength of the materials makes these processes difficult to use. Observations suggest that inclusion-carbide-free ODS alloys with fine equiaxed grains have the potential for very high strength and toughness if they can be made reproducibly [24].

There is also an issue with joining the materials. Standard welding methods are impossible due to the nanostructured microstructure. Adhesives and mechanical joining are also unsuitable. Any method of joining must minimise changes to the microstructure (and properties). Both friction welding [85] and inertial welding [86] have been successfully used to join parts, but both caused significant distortion of the microstructure (Y_2O_3 particles agglomerate and float out of the weld pool [85]). Diffusion bonding and friction stir welding have also been tried with ODS materials and the properties were only moderately degraded by severe deformation. However, more testing is required [87].

Finally the homogeneity within each batch of alloy and the batch-to-batch variability must be investigated. Once a specific composition and processing route has been determined, for optimal properties it is important that it be easily reproduced and each batch be consistent.

4.3.3 Oxide Particles

The nanocluster stoichiometry is significantly different from stable TiO_2 and $Y_2Ti_2O_7$ oxides, therefore the description "oxide dispersion strengthened" is in fact inaccurate [81]. The strengthening obstacles are not the original oxides but rather nanoclusters formed during processing, and so could technically be called a nanocluster-strengthened ferritic alloy (NFA). (This thesis however, will continue to use the ODS terminology.)

There is debate as to the nature of the ODS particles in ferritic alloys. It is suggested that the precipitates have a core/shell structure (where there is a variation in composition through the precipitate) [33][88][89] but some observations indicate otherwise [90] (see Figure 6). The structure of precipitates in ferritic ODS has been characterised using atom probe tomography (APT) [88][91][92] and high resolution transmission electron microscopy (HRTEM) [33][89][93].

The current view on precipitate formation is that during mechanical alloying, the Y_2O_3 powder dissociates and the yttrium and oxygen dissolve into solution. It then reprecipitates into Y_2O_3 (or more complicated Ti/Al containing) nanofeatures on heating of the alloy during HIP or extrusion [94][95].

High magnification Transmission Electron Microscopy (TEM) images show sharp and irregular particle/matrix interfaces [33], presumably from ablation and/or cleavage fracture during MA. Amorphous regions suggest, however, that solid state amorphisation does occur during MA through disordering and solute mixing.

A suggested mechanism of the formation of the oxide nanofeatures is [33]:

1. fragmentation of the Y_2O_3 powder (during MA)
2. dissolution of yttrium and oxygen into the matrix
3. agglomeration and amorphisation of the oxide fragments with the matrix material (during MA)
4. crystallization of the amorphous agglomerates above a critical size forming precipitates during hot consolidation (potentially with a complex oxide core and solute enriched amorphous shell)

The nucleation of the crystalline complex-oxide core occurs within a large amorphous particle and depletes the shell which remains amorphous. The shell thickness depends on the size of the precipitate – in bigger precipitates the core will cause more depletion and therefore form a thicker shell.

APT of MA957, ODS Fe-13Cr and ODS EUROFER 97 [88][96] revealed precipitates with an yttrium and oxygen rich core and a vanadium and chromium enriched shell (Figure 6c). Y_2O_3 is the most stable oxide and has the highest free energy of formation of the Cr, V, Ti and Y oxides. This presents a high nucleation barrier to forming crystalline Y_2O_3 precipitates and an amorphous shell would decrease the interfacial energy, therefore the nucleation of oxides is favoured. A solute rich shell reduces interfacial energy and can increase thermal stability, therefore adding Ti to the material allows an increased number density of oxide particles to form [88][96].

Core-shell structures have been observed to disappear after annealing at 900°C for 168 hours, suggesting that they form during crystallisation when the amorphous oxide agglomerates are far from chemical equilibrium [89].

Other characterisation experiments with both atom probe and TEM have shown no core/shell structure to the precipitates [90]. It has been suggested that the formation of a core/shell structure depends on the matrix composition, precipitate composition and size, and processing parameters.

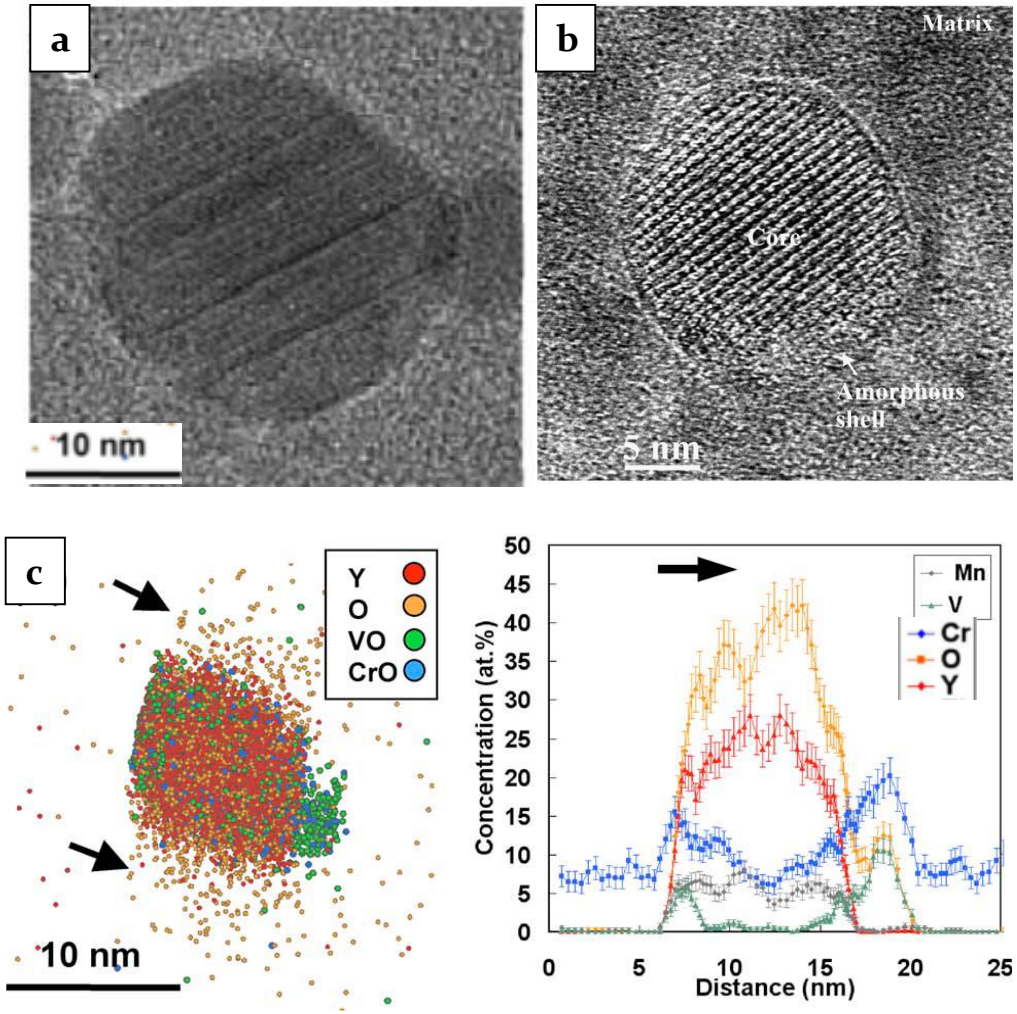

Figure 6 - Core/shell structure evidence: against – no visible structure - a) TEM of MA957 [90] and for – visible core/shell - b) TEM of K3-ODS [89] and c) APT of ODS EUROFER 97 [88]

Annealing YWT alloys has no significant effect on the grain or precipitate size (even after 14,500 hours at 1000°C only negligible coarsening has been seen) [75]. The nanofeatures coarsen above 1150°C (they have a very high activation energy and slow time dependence) but are remarkably stable between 800-1000°C [87]. This means that once a suitable morphology has been obtained, there is little issue with it changing during service.

Mechanical forming of an ODS material is complicated due to its high strength properties. The powder must be compressed or extruded into a shape close to the design of the final component, as it is not easy to reform afterwards (the alloy cannot be melted and moulded, for instance). It is possible with repeated heat treatments and cold rolling for ODS to be rolled out, but it must be performed at a specific cooling rate for ferrite and not martensite to be formed [97].

Comparing ODS EUROFER with a standard EUROFER, the ODS variant shows higher yield strength, tensile strength (35% higher – see Figure 7) and higher ductility (particularly for extruded material) [59][98]. Comparison of Fe-14wt%Cr and an ODS variant showed similar enhancement of tensile and strength properties combined with promotion of grain refinement and improved densification [99]. It was concluded that it is the Y-O rich dispersion that is responsible for the stability of the induced structure, even up to 850°C [99].

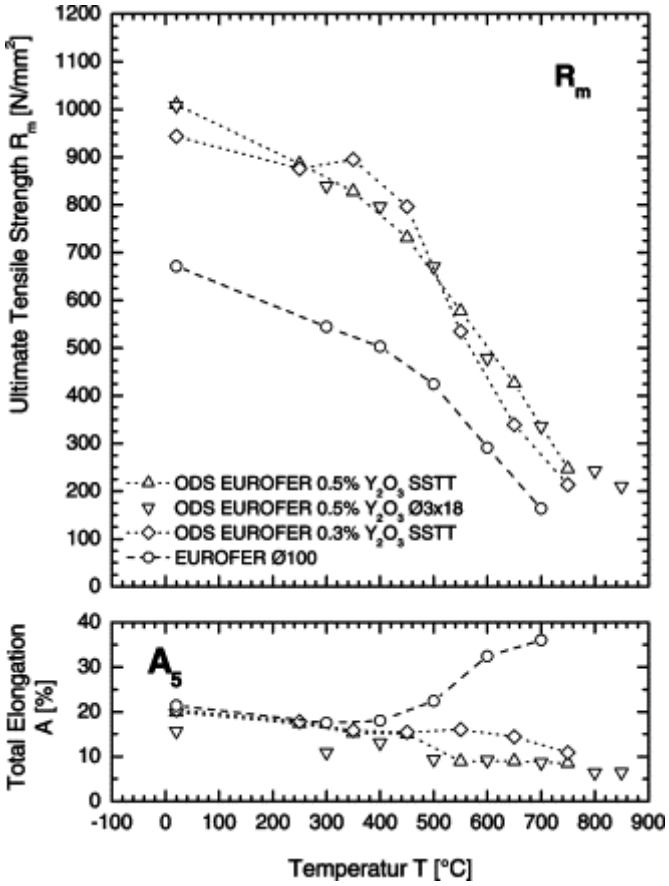

Figure 7 - Comparing Ultimate Tensile Stress (UTS) and elongation at a range of temperatures EUROFER and varieties of ODS EUROFER [98]

4.3.4 Helium Bubbles in ODS Alloys

One consequence of irradiation in steels is the implantation and transmutation of helium bubbles within the metal matrix. Helium bubbles will always form at a particle/matrix interface if available as these are lower energy sites. This means that the nanofeatures in ODS steels are ideally suited for helium capture [75]. If a sufficiently high number density of small sized particles is present, then the majority of the helium will be captured. Very little will be present at the grain boundaries, so grain boundary embrittlement should not occur [100].

If the helium is only trapped weakly by nanofeatures (such as oxides, or carbides), it will move around between several precipitates before reaching a grain boundary so delaying embrittlement [26]. Helium bubbles in the matrix are useful as helium sinks, but too many may degrade the material properties. The ideal would be a high number density of small size particles to provide maximum surface area for helium trapping.

The morphology of precipitates affects the cavity and bubble growth; voids attached to precipitates can show large growth rates because they are low energy interfaces in the matrix and collect point defects [101]. If they act as a preferential sink for interstitials they can retard void growth, but this depends on whether the precipitates are coherent or incoherent; coherent precipitates will have no net accumulation of point defects [22].

A matrix/precipitate interface forms a low energy trap for the helium atoms and, therefore a fine, dense precipitate structure leads to a fine, dense concentration of bubbles. The most refined bubble distribution is found in materials with the finest oxide dispersion. If helium in the system is diluted over many bubbles acting as recombination sites then few voids will form.

Experiments have shown that the number density of ODS particles in materials can be equal to down to ten times lower than the number density of He bubbles [102][103]. There may be other sites attracting vacancies and helium. They are possibly very fine

nanosized oxide particles (below TEM resolution) or possibly there are α' phase particles forming in high chromium ferritic steels under irradiation (α' is a 90-95 at%Cr content Fe-Cr phase [104]). Small angle neutron scattering (SANS) suggests the first possibility and the second is indicated by high Cr content steels (≥9wt%) having reduced swelling compared with other compositions [103].

In ODS materials the bubble nucleation rate under irradiation is significantly higher and <5nm cavities exist in much higher density than in non-ODS material [103]. Overall swelling due to helium is significantly lower in ODS than non-ODS; also in ODS, the swelling remains constant with displacement damage (in non-ODS steel it increases) [45][103]. This is due to the high density of small cavities able to trap the helium. Even in low dose (few dpa) regions of the ODS material the cavity number density is still high, indicating that the ODS has specific trapping sites for He. This allows enhanced cavity nucleation at an early stage during irradiation and limits subsequent cavity growth [103].

In a study of various iron alloys, bimodal cavity evolution occurred earliest in austenitic steels followed by ferritic steels and lastly in some of the ODS steel being tested. One ODS steel did not develop a bimodal bubble distribution, only a high density of tiny bubbles [31]. Fine bubble distribution is favourable as it contains a high helium volume while minimising the retardation of dislocation movement through the lattice.

The nanosized bubbles contain pressures of 100-1000 bar [100]. To be imaged by analytical TEM requires the bubbles to be stably contained within the foil (and filled with gas). If the ODS particles touch the top or bottom of the foil, the gas will have escaped.

It has been observed that most bubbles press out into the matrix from the precipitate (Figure 8). This suggests formation during irradiation by diffusion to a low energy boundary. Some have also been observed to press inwards (Figure 9) and has been suggested were therefore formed during the HIP stage when the ODS particles could be plastically deformed [100].

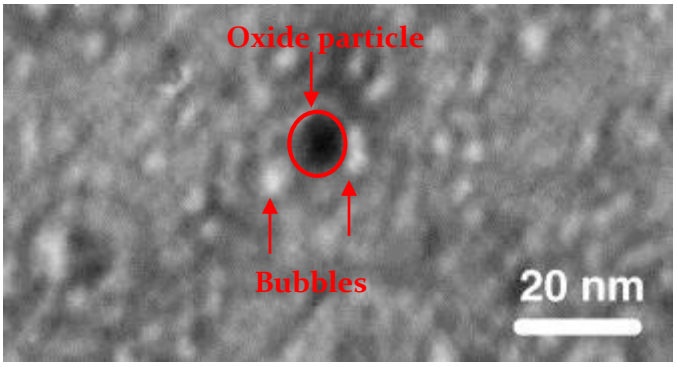

Figure 8 - Cavities adjacent to oxide particles in dual-ion irradiated K3-ODS steel suggest the interface between oxide particle and matrix is suitable for trapping gas atoms [103].

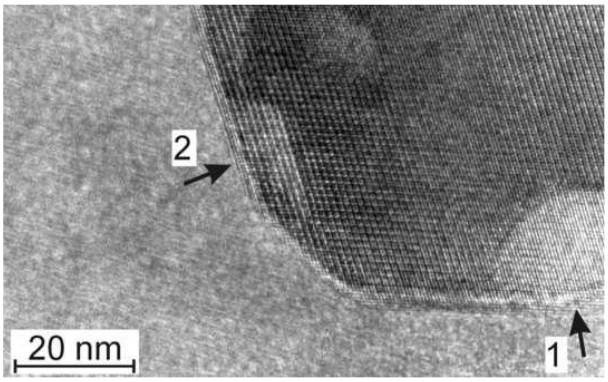

Figure 9 – Bubbles pressing into an ODS particle [100]

The effect of helium implantation has been investigated on other ODS materials. In Cr-2W-4Al ODS steel (grain size 850nm by 0.5-3μm (extruded)), a range of precipitates of alumina (10-1000nm), titanium-rich (10–100nm) and yttrium-aluminium complex oxides were finer still. Significant irradiation-hardening was observed at 300°C but only slight hardening at 500°C for both single He and dual (He+Fe) beam [69].

High concentrations of helium implantation (1000appm) at 550°C showed no effect on the DBTT of 9 and 14wt%Cr ODS steels and no intergranular fracture was observed upon Charpy testing the implanted materials. Non-ODS material showed an increase in DBTT and intergranular fracture. Fine oxides and fine grain boundaries in the ODS materials acted as helium traps and suppressed hardening and grain boundary degradation [105].

4.3.5 Future Development

The future use of ODS steels in nuclear applications is distinctly possible, but further research is required. Development of ODS alloys requires detailed investigation and characterisation of all mechanical and microstructural properties and their changes with composition, processing route, helium implantation, irradiation damage, irradiation temperature, dpa and dose rate. This will require both experimental and modelling work.

ODS steels offer higher operating temperatures but are complicated and expensive to mechanically alloy and make. Ideally, elevated temperature steels produced through conventional processing are needed (or a cheaper way of processing ODS). Precipitate strengthening with MX (metal halide) particles is one possibility. A thermo-mechanical treatment process developed at Oak Ridge National Laboratory (USA) has produced a high strength martensitic nitrogen-containing steel [106] but more work is still needed.

Development of the compositions and microstructures to provide the best irradiation tolerance in these materials has already had decades of research and it is

now possible to customise microstructures and hence adjust mechanical properties. Initial work on the processing route and pressing conditions and their effect on microstructure has been performed by Gorley (Oxford Nuclear Materials) [107]. He produced a set of materials, all of the same composition, each processed with different milling conditions. Using a low milling energy (i.e. speed of the mill) and minimising the milling time (until the Y_2O_3 powder has just been fully combined) can cause up to a 20% increase in ultimate tensile strength. This is thought to be due to the milling conditions minimising oxygen pick up and chip off from the milling balls into the powder, thereby reducing the contamination.

If we are to use ODS steels in the near future, the research and development schedule must be accelerated to address high neutron irradiation fluxes and transmutant helium combined with high operating temperatures. Creating finely dispersed nanometre-scale precipitates and understanding their irradiation responses are the keys to success [108]. Only through detailed microscopy and mechanical testing can we advance our knowledge and with it, the GenIV and fusion nuclear programs.

This thesis concentrates on the effects of helium on the deformation of ODS steels. Ion implantation was used as a simulation of transmuted helium, therefore the samples produced only contained a thin damaged surface layer. This means macro-scale mechanical tests were not suitable, and therefore micromechanical testing methods were required. These are discussed in the next section.

5 Micromechanics

Experiments using ion implantation to simulate reactor damage are limited to the thin surface layer that can be penetrated by the ions. Micromechanical testing is an established method of investigating the mechanical properties of materials when only small sampling volumes are available – nanoindentation and Focused Ion Beam (FIB) milling of cantilevers and pillars can be used to obtain useful and accurate mechanical data.

5.1 Nanoindentation

The most basic small scale mechanical testing is hardness testing through surface indentation. Traditional hardness indentation testing is performed by pressing a sharp tip into the surface of the material under a known load [109]. The tips are made of diamond or other very hard substances such as carbides. A range of tip geometries can be used according to the mechanical data required or the sample shape/orientation available. Once the tip is unloaded, the dimensions of the remaining indentation can be measured and then depending on the tip shape used, the relevant equations are applied to determine the material hardness [109]. As the results rely on measurement of the indent in the sample, the lower size limit of testing is dependent on the resolution of the microscope.

The capability of measuring the material properties during nanoindentation was realised in 1981 by Pethica et al. [110]. The first nanoindenter consisted of a diamond indenter tip attached to a capacitive displacement transducer sensitive to movements of 0.2nm. A coil and magnet system applied a variable load with a resolution of 2μN. Continuous measurements of load and displacement were recorded during indentation, thereby providing the change in hardness with depth. For thin surface film applications this can provide detailed information about the separate materials and the change in properties at interfaces.

Modern nanoindenter systems use coil-magnet assemblies or piezo-electric transducers to move the indenter tip and capacitance gauges to measure displacement [111]. Systems can be fitted with piezo-electric stages for fine scale X-Y movements. Combined with an optical microscope they can be used to within a positioning accuracy of ±0.5μm. For greater positional accuracy, the sharp diamond tip can also be scanned across a surface to provide a topological map similar to an atomic force micrograph [111].

Basic in-situ indentation has been in existence since 1968 [112] but dedicated systems have only recently been built to include electron microscopes for more detailed imaging and filming the indentation process [113]. Correlating visual information with the hardness data provides interesting links between load jumps and slip bands [114]. Nanoindentation systems have been co-installed with both scanning [115][116] and transmission electron microscopes [117][118].

Nanoindenters record the load and displacement incrementally up to a maximum load which is held in order to stabilise the specimen before unloading. This hold period can also be used to measure creep in a specimen or the thermal drift of the system. They can perform tests either under load-controlled or displacement-controlled conditions using a feedback loop from a force or displacement sensor to ensure a smooth test [119]. Load-displacement data can be analysed to determine hardness and elastic modulus [120]. A load-displacement nanoindentation graph can be coupled with high resolution electron microscopy of the indentation to provide detailed information on the deformation mechanisms.

While nanoindentation is versatile and can be applied to most materials systems, it has its weaknesses. It is well designed for testing hardness, but the plastic zone shape and size and the complex stress state around the indenter tip make the calculation of

yield stress inaccurate; therefore nanoindentation is usually reserved for surface hardness testing.

The issue of size effects will be discussed in Section 5.3.1.

5.2 Micromechanics

The investigation of properties such as yield stress, small scale bend, compression and tensile testing is also possible using a nanoindentation system when combined with FIB milling.

A simple and widely used test geometry is the microcantilever – essentially a small scale beam bending experiment. Micromechanical testing using a nanoindenter was first tried by Weihs for the deflection of silicon microcantilevers [121]. The load displacement response can be recorded during testing and so yield stresses and elastic moduli can be accurately measured if a good model of the cantilever is used.

Micropillar compression uses the same nanoindentation system to record the load-displacement data during testing. A flat ended tip/punch is used to press micron sized pillars down their axis. The load-displacement data combined with imaging can provide insights into the dislocation properties at small scale. Tensile testing is also possible, although it requires more complicated sample and indenter tip geometries. Capped pillars can be gripped and deformed to necking or fracture to investigate deformation and the ultimate tensile strength of materials on the small scale [122].

These various test geometries can be combined to give a full overview of the mechanical properties of materials when only a small sample size or thin film material is available.

5.2.1 Microcantilevers

Microcantilever testing was developed in 1998 for investigation into the mechanical properties of deposited thin films [123]. Since then the use of microcantilevers has spread to fracture testing [124], investigating grain boundary properties [125] and small scale bulk property testing [126].

The most commonly used method of micro-cantilever production is focused ion beam (FIB) milling. This allows the manufacture of cantilever beams to the exact dimensions, cross-section and location required, e.g. across a grain boundary (Figure 10). The most commonly used shapes are triangular and pentagonal cross-sections, as these can be made simply by tilting the sample and undercutting with the ion beam. The cantilever manufacturing will be discussed in Chapter 5.

Microcantilevers are easily tested using a standard unmodified nanoindenter. The indenter tip is either optically aligned or scanned to provide a topographical map. It is placed in the centre of the end of the cantilever and vertically displaced to the required depth or load. The tip may cause a small amount of plastic deformation and leave a small indent in the surface. If significant, this can be accounted for and can actually be useful for analysis when the measured distance between the applied force and the bent/fractured area of the beam is required to calculate the stress and strain applied.

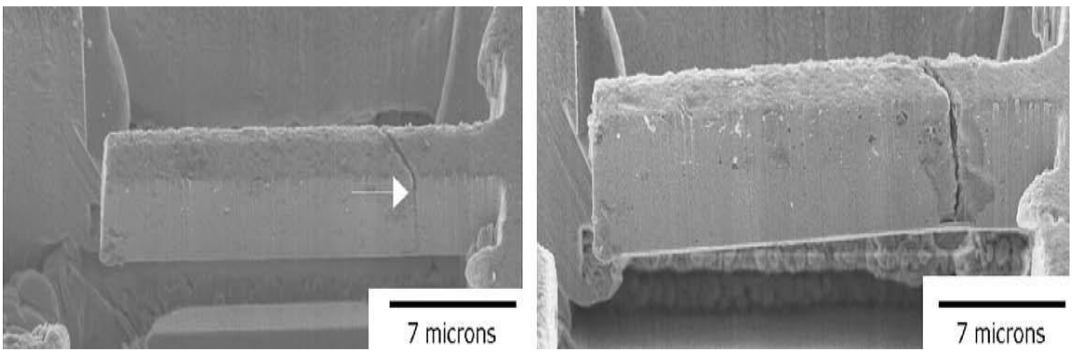

Figure 10 - Cantilever used to test stress corrosion cracking at grain boundaries [125]

5.2.2 Micropillars

Micropillar testing provides a simpler stress state than cantilevers and nanoindentation, although the production method is more complicated. To be accurate, compression tests rely on the sample having a constant cross-section, therefore a parallel sided pillar is needed if the compression model of a perfect cylinder is to be used [127]. Pillars can be made in a variety of ways, electro-deposition and FIB cutting being the most common bottom-up and top-down methods respectively [116]. When the properties of an implanted layer are being tested, top-down production is the only option.

The problem with using FIB milling is that the ion-beam has a Gaussian profile so a vertical mill will not produce perfect vertically sided pillars. During milling some redeposition occurs, so the dimensions depend on the geometry and re-deposition rate/range [128]. The Gaussian beam profile has more effect at high currents where the beam tails extend further (Figure 11). To avoid the tail effects a series of concentric mills are used to first remove bulk material at high current (~3000pA) and then successively lower currents to refine the shape of the pillar (Figure 12a).

Other methods of pillar production include lathe milling – a series of vertical cuts moving the sample around in a circle to produce a smooth sided pillar (Figure 12b) [129] and annular milling at an angle so the beam profile is vertical [129]. Both of these systems have been successfully automated but require sophisticated high-resolution SEM and image recognition software. Further details on the milling process used in this study are discussed in Chapter 4.

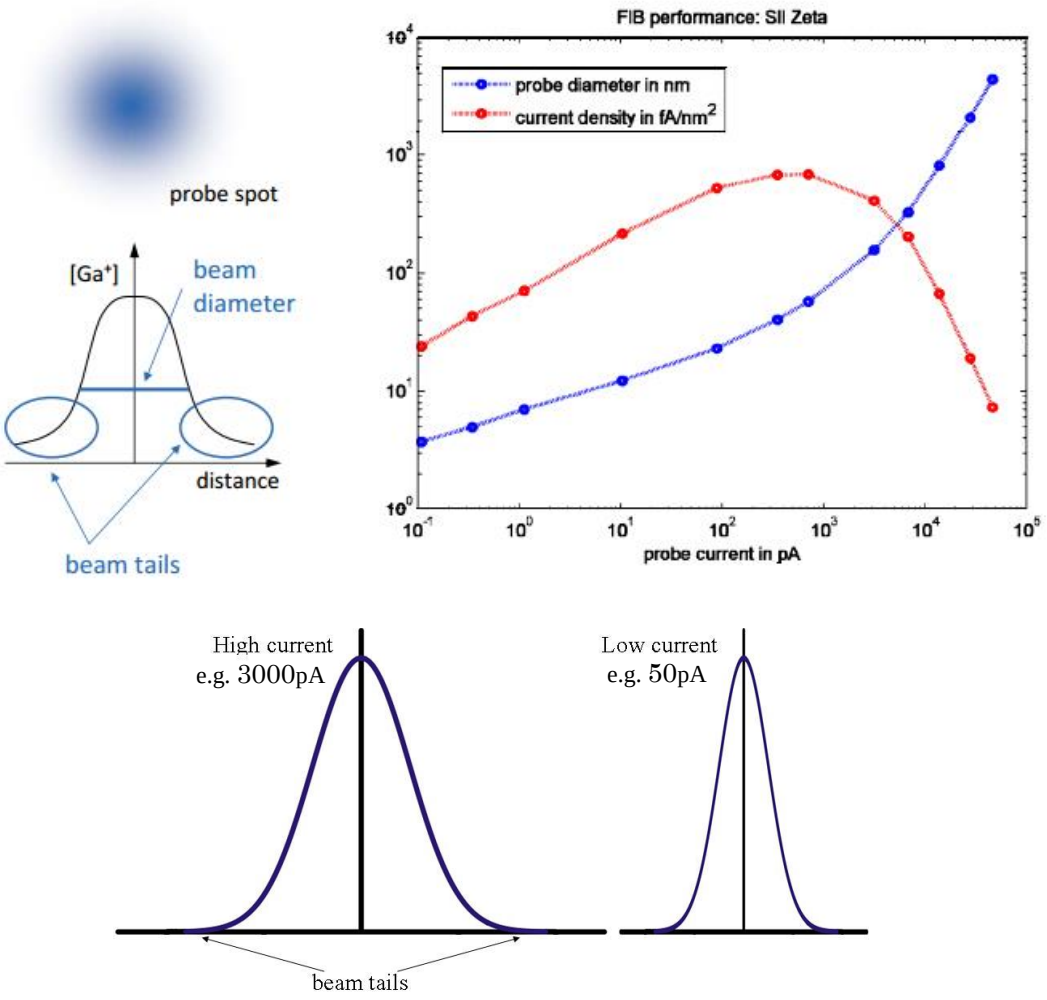

Figure 11 - Gaussian ion beam profiles [130]

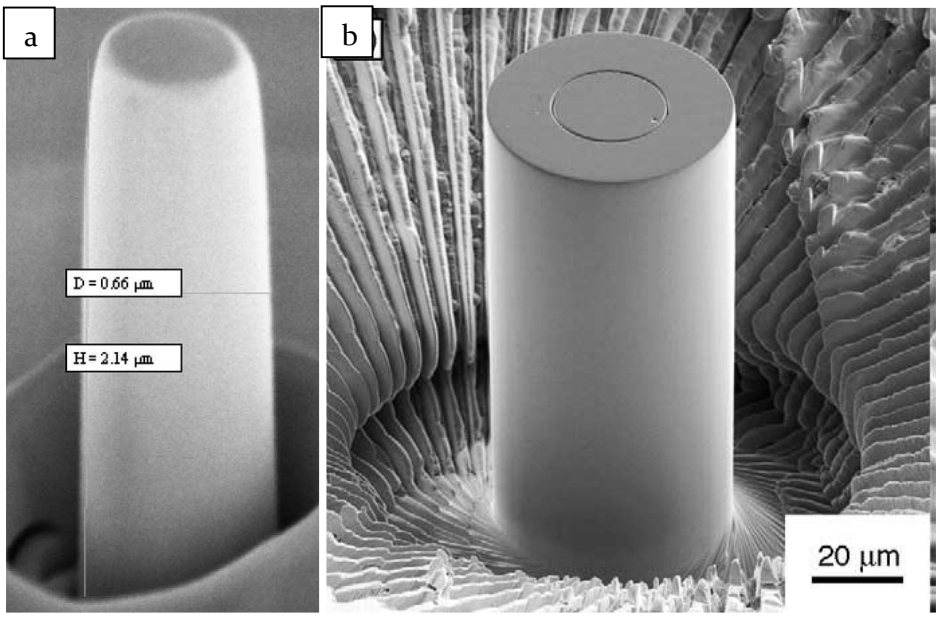

Figure 12 - (a-left) Gold nanopillar produced by Greer using annular milling [131]. **(b-right) $Ni_3(Al,Hf)$ parallel sided lathe milled micropillar produced by Uchic** [129].

5.3 Size Effects

A significant issue with micron sized mechanical property testing is that measurements are not independent of the scale on which they are tested. Hardness is inversely proportional to indent size at depths less than ~1.5μm. Deeper than 1.5μm, hardness plateaus out at a value of $H \approx 3\sigma_y$ (σ_y is yield stress) [112]. Yield stresses have also been shown to increase when tested micromechanically [132].

5.3.1 Indentation Size Effects

Many groups have observed the hardness increasing as indent depth decreases (Figure 13) [133]. Indentations less than 1μm deep may give hardness values up to five times the macroscopic value. This difference may be due to strain gradient effects - large strain gradients are inherent in small indentations and can cause a higher density of dislocations, leading to local hardening [134].

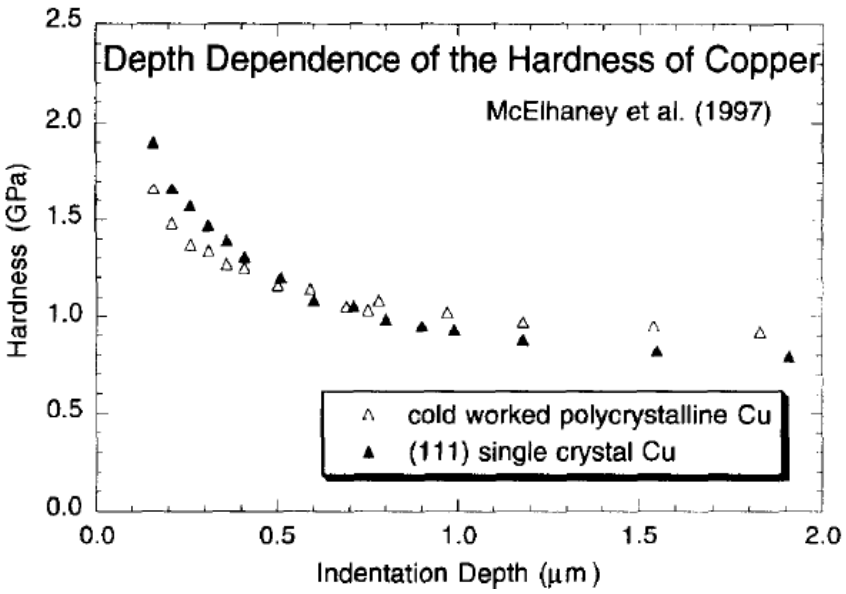

Figure 13 - Indentation size effects in copper [133]

5.3.2 Cantilever Size Effects

Size effects in microcantilever testing have been investigated both experimentally [135] and analytically [136]. A strong size dependence is observed with the cantilever cross-sectional area – the critically resolved shear stress (CRSS) increases rapidly as the width drops below 2μm (Figure 14). A proposed mechanism to account for the size effect [137] suggests that surface dislocations in cantilevers move towards the neutral axis when the cantilever is tested and pile-up along slip planes; this causes a back stress on the dislocation sources. The smaller the cantilever, the shorter pile up distance, so the greater is the strain gradient.

Other possible mechanisms include strain gradient plasticity theory – stress is a function of both strain and strain gradient, where the greater the imposed strain gradient, the greater the degree of hardening. At a micron scale, therefore, where a greater strain gradient is observed per unit stress, microcantilevers will be stronger than millimetre scale equivalents [138].

Finally, dislocation starvation and dislocation truncation have also been suggested as causes for changes in strength of micromechanical specimens. These are more applicable to micropillars and will therefore be explored in the next section.

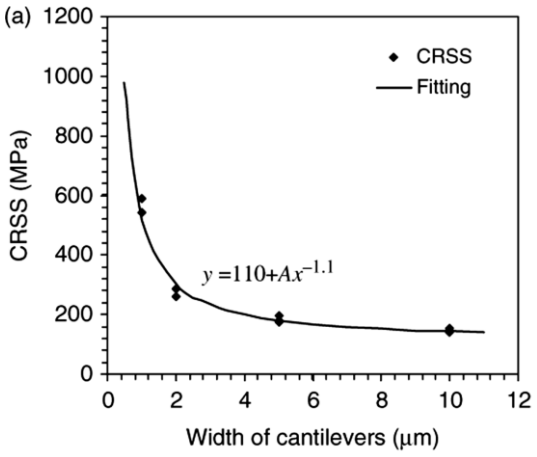

Figure 14 - Size effect in Microcantilevers [135]

5.3.3 Pillar Size Effects

Micropillar compression shows a size effect [132]. Large diameter pillars (10-40μm dia.) show easy glide deformation, but below 10μm dia. deformation becomes dominated by displacement bursts. The model of dislocation starvation has been used to explain this, using the availability of dislocations and their source lengths to rationalise the relationship between pillar diameter and yield strength [139]. Plastic deformation of bulk samples leads to dislocation motion causing cross-slip, strain jumps and dislocation multiplication leading to strain softening [132]. At the micron scale, dislocations will run out and annihilate at a free surface before they interact. The overall reduction in dislocation density means higher stresses are required to nucleate new dislocation sources causing yield stress increases.

In experiments on pure nickel pillars of a range of sizes (1-40μm – Figure 15), the strength increases up to 15 times the bulk crystal value. Basic processes for plastic deformation are affected as the sample size decreases; the dislocation source distribution changes and dislocation multiplication is restricted as dislocations escape the crystal [140].

The aspect ratio of the pillars also affects the extent to which dislocation starvation occurs. At high ratio (>3:1, height:diameter) deformation occurs in the top section and so dislocations run out and annihilation will happen. In low ratio (<3:1) pillars, if the dislocation slip plane is at a sufficiently high angle, dislocations may run to and from the bulk of the specimen so the reduction in dislocation density is less and thus starvation theory is not appropriate.

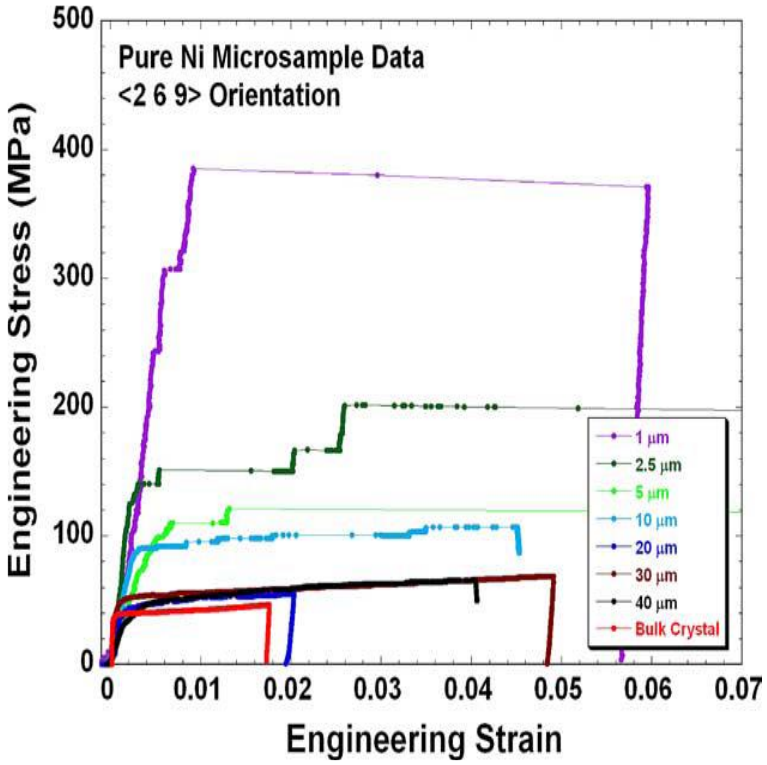

Figure 15 - stress vs. strain for single pillar samples at various diameters; results typical of the average stresses at each diameter. Work by Dimiduk et al. [140].

6 Literature Review Summary

Nuclear fission and fusion could both feature in the future of energy generation, but although detailed engineering plans have been made, there are significant issues with currently available materials. Significant investigation is needed into how material properties change when subjected to extremes of temperature and irradiation. The major issues caused by irradiation are cascade damage and helium introduction to the material lattice. Previous work has revealed the need to investigate the propagation, location and mechanical effect of helium bubbles formed during irradiation.

A wide range of potential nuclear structural materials is being investigated. Steels have a long history for power plants. RAFM steels, with the advantage of low activation properties, have therefore become a major focus of fusion and GenIV fission material research. The addition of ODS particles reduces the concentration of helium segregating to grain boundaries therefore improves high temperature mechanical properties and reduces the effects of embrittlement caused by helium implantation and transmutation, providing stability in a high neutron flux environment. The positive effects of the addition of ODS particles has, however, mostly been investigated in isolation. For ODS materials to become a viable contender in future nuclear power plants, the effects of ODS particles needs to be equal or superior to other already available and characterised microstructural refinements (such as grain size, alloying and carbide addition). The effects of the ODS particles must therefore be investigated in combination with other refinements to determine their capability and potential.

Ideally investigations would use materials implanted under reactor conditions, however, this is impractical. Therefore, ion implantation has been developed as a valid approximation for experimental purposes. This has the drawback of only forming thin layers of damaged material, however, nanohardness and micromechanical testing methods can be accurately applied to the small material volumes available.

7 Project Aims

This DPhil project set out to investigate the mechanical property changes caused by implantation of helium (as an analogue for reactor conditions). The initial aim was to determine whether helium segregating to grain boundaries increased grain boundary fracture. The microcantilever experiments performed to test this were inconclusive as none of the samples could be made to fracture (ODS, non-ODS, helium or no helium).

The project therefore moved on to assessing how various implantations (He, He+Fe and Ne) changed the mechanical properties of four ODS and non-ODS materials, and to probe how the materials responses were affected by their differing microstructural features.

Chapter 2 details the four materials investigated, followed by a description of the various ion implantations that were chosen to simulate the effects of transmutation that would be seen under reactor conditions.

Chapter 3 outlines the use of both nano- and micro-scale hardness testing to investigate the hardening effects of implantation and the correlation of hardening depth with the predicted ion penetration.

Chapter 4 uses micropillar compression testing to investigate deformation mechanisms and their variations with material and implantation.

Chapter 5 demonstrates the use of microcantilever bend testing to look at the effects of microstructure on the materials' stress/strain and deformation responses.

Chapter 6 applies TEM to the analysis of dislocation/microstructure interactions and the formation of bubble-like features caused by ion implantation.

The final two chapters draw together the results from the various experimental methods to analyse the overall effects seen in the materials and compare and contrast the use of the different methods; before finally suggesting further work that could be pursued to provide further explanation and extend the work presented here.

Chapter 2
Materials and Preparation

8 Reduced Activation Ferritic Martensitic Steels

RAFM steels for nuclear reactor applications were discussed in Chapter 1 because they retain only minimal residual radiation at the end of a working lifetime. Previous research has shown that steels with 9wt%Cr have the maximum neutron radiation resistance (minimum swelling and low transmutation to radioactive isotopes). A minimum of 12.7wt%Cr is required to ensure a ferritic matrix at all operating temperatures, and so allowing for changes due to other added elements, most research agrees on 14wt%Cr as a suitable content for nuclear-use steels. For this project, two pairs of steels were investigated:

1. ~9wt%Cr – maximum irradiation resistance
2. ~14wt%Cr for a fully ferritic matrix at all operating temperatures (i.e. room temperature up to 1000°C).

8.1 Oxide Dispersion Strengthened Steels

ODS steels were developed for nuclear purposes giving high temperature and radiation resistant properties with the ability to reduce the adverse effects of implanted and transmuted helium.

Although a variety of oxide formers (e.g. hafnium and aluminium) can be used, the most commonly investigated is yttrium forming yttria (Y_2O_3). The ODS materials used here contain yttria.

9 Materials Used

Four iron-chromium alloys were used to investigate how changes in materials composition and structure affect the effects of ion implantation:

- Fe-14wt%Cr – a model alloy to give an experimental baseline.
- Fe-14wt%Cr ODS – this variant is the model alloy with added oxide dispersion and other alloying elements, named in this thesis as CEA ODS.
- EUROFER 97
- EUROFER 97 ODS

EUROFER 97 was selected by the European fusion program as a reference structural material and will be used as test blanket modules for ITER. Its ODS variant was developed to provide superior tensile and creep properties [141].

All known information on these materials has been included in this chapter; any missing details were neither provided by the material source nor available elsewhere. 'Measured composition' refers to the specifications given by the source of each material.

9.1 Fe-14wt%Cr

Produced for EFDA (European Fusion Development Agreement). All details came from the EFDA Contract 06-1901 Final Report on Model Alloy Preparation (2007).

Nominal composition (wt%): Fe-14Cr

Measured composition (wt%): Fe-14.25Cr-0.0005C-0.0007S-0.0004O -0.0005N-0.001P

Fabrication route:

- Melt processing of Fe and Fe-Cr starting materials
- Hot forging (1150°C)
- Cold forming (reduction ratio 70%)
- Recrystallisation (1 hour, 850°C, argon atmosphere)
- Air cooling

Electron Back-Scattered Diffraction (EBSD) was performed by M. Gorley (Oxford Nuclear Materials) on all materials using a JEOL JSM-6500F Scanning Electron Microscope (SEM). Fe-14wt%Cr has very large (~200μm) equiaxed grains (Figure 17). To avoid grain orientation effects, all tests were performed on multiple grains to obtain average values. The large grain size of this material however, allowed experiments to be performed within single grains to look at the material properties while avoiding grain boundary effects.

Figure 16 - Bulk Fe-14wt%Cr
Sample slices were cut perpendicular to the length of the cylinder.

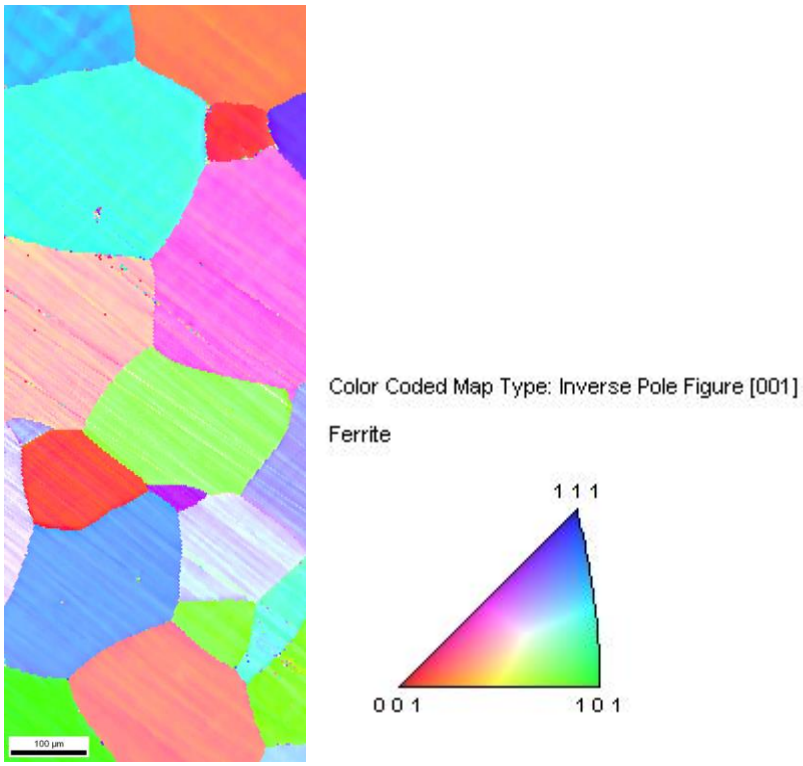

Figure 17 - EBSD map of Fe-14wt%Cr

9.2 Fe-14wt%Cr ODS (CEA ODS)

This was provided by CEA Saclay (le Commissariat à l'énergie atomique et aux énergies alternatives), Paris, France. Produced for the GETMAT Project (Nuance 12), compositional information and fabrication route were provided with the material, but confidentiality agreements prevent any further disclosure of processing details.

Nominal composition (wt%): Fe-14Cr-1W-0.3Ti-0.3Y_2O_3

Measured composition (wt%): Fe-13.65Cr-1.17W-0.30Ti-0.26Y-0.27Si-0.16Ni -0.33Mn-0.0014Mo and C, N, O traces

Fabrication route:

- Powder attrition
- Canning
- Degassing (48 hours)
- High temperature extrusion (1100°C)
- Air quench
- Annealing (1050°C, 1h)

CEA ODS has an elongated grain structure down the direction of extrusion (left to right in Figure 19). A bimodal grain structure is present, large grains (~10-50μm) separated by bands of smaller grains (~1-10μm). The larger grains are not of continuous orientation, but consist of sub-grains (~1-4μm) of similar orientations (N.B. the red/pink grain across the centre of Figure 19 is made of sub-grains with orientations around [001]).

Figure 18 - Bulk CEA ODS
Note the canning material from extrusion around the circumference of the bulk. Sections were cut perpendicular to the extrusion direction and then sample slices cut in cross-section to this – therefore the final sample surface is parallel with extrusion.

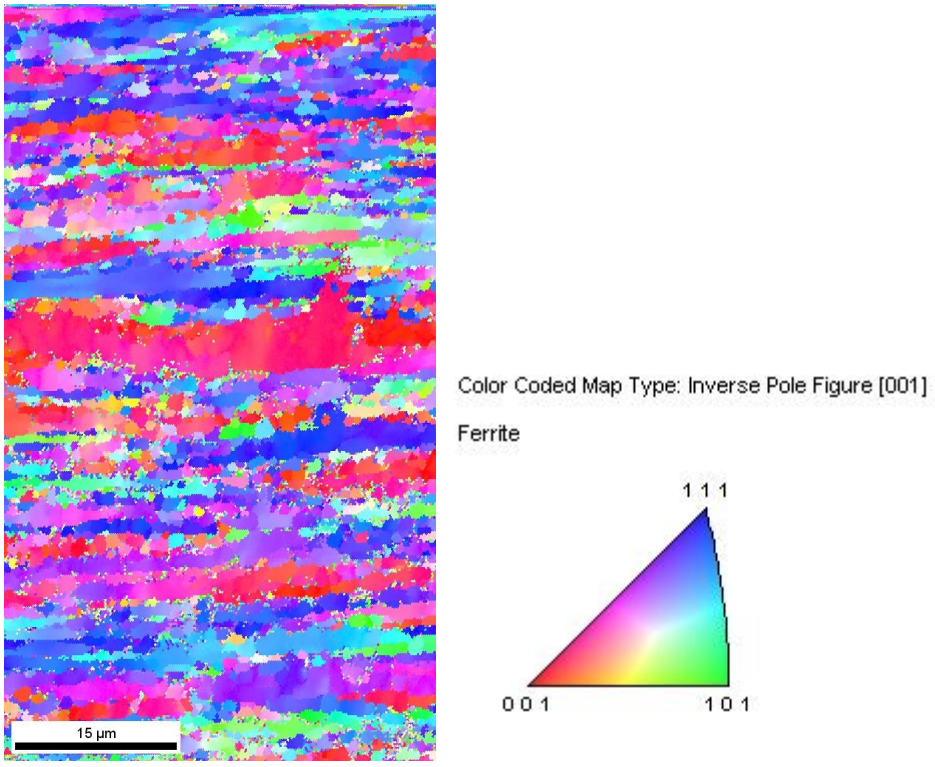

Figure 19 - EBSD map of CEA ODS
Note the image scale is different to the Fe-14wt%Cr.

9.3 EUROFER 97

This material was fabricated by Saarschmiede for EFDA and provided by KIT (Karlsruhe Institute of Technology), Germany, batch EUROFER 97/2, heat 993393.

Nominal composition (wt%): Fe-9Cr-1.1W-0.4Mn-0.2V-0.12Ta

Measured composition (wt%): Fe-8.81Cr-1.07W-0.53Mn-0.20V-0.12Ta

Fabrication route:

- Vacuum induction melting
- Vacuum arc remelting
- Billet forging
- Rolling into plates/bars
- Normalisation at 960°C for 1.5 hours in oil
- Annealing at 750°C for 4 hours in air

EUROFER has an equiaxed structure with grains ~2-5μm diameter. These small grains form clusters (~10-15μm) with low angle grain boundaries within the clusters' and high angle grain boundaries between clusters. The grain clusters orientations have a wide spread (see Figure 21).

Figure 20 - Bulk EUROFER
Sample slices were cut perpendicular to the flat top surface.

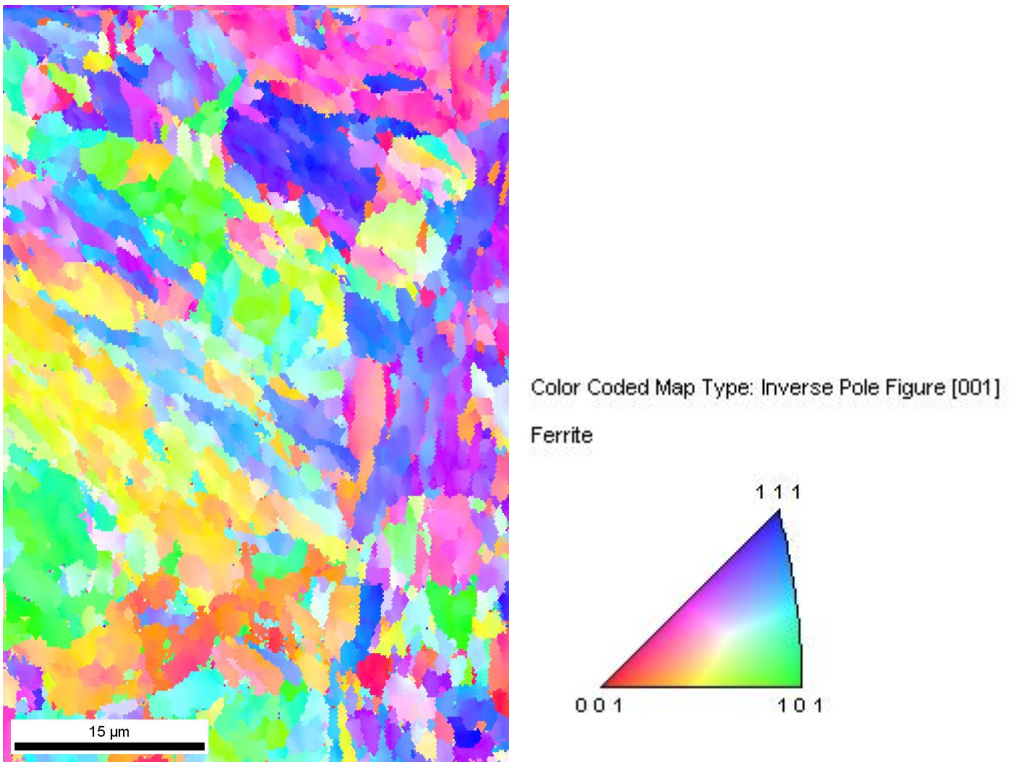

Figure 21 - EBSD map of EUROFER
note the image scale is different to the Fe-14wt%Cr.

9.4 EUROFER 97 ODS

This material was fabricated and analysed by Plansee Ltd, and provided by KIT (Karlsruhe Institute of Technology), Germany.

Nominal composition (wt%): Fe-8Cr-1.0W-0.4Mn-0.2V-0.13Ta-0.1C-0.06Si

Measured composition (wt%): Fe-8.25Cr-0.9W-0.35Mn-0.24V-0.13Ta-0.05C -0.33Si-0.1O-0.02Co-0.02N-0.01P

Fabrication route:

- Gas atomisation of EUROFER steel
- Attrition of EUROFER with 0.3wt% Y_2O_3 powders
- Canning
- Degassing
- Hot isostatic pressing
- A series of cross-rolling and annealing stages (details unavailable) to produce a plate of 6mm thickness

EUROFER ODS has an equiaxed structure with grains of ~1-3μm diameter (see Figure 23).

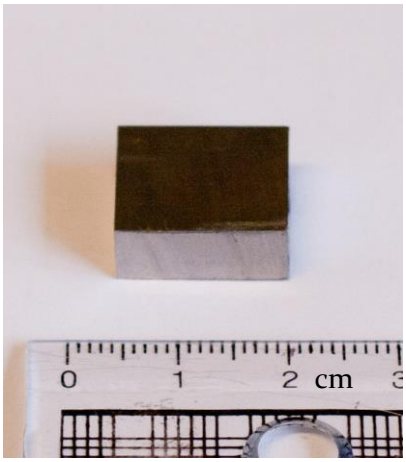

Figure 22- Bulk EUROFER ODS
Sample slices were cut perpendicular to the flat top surface.

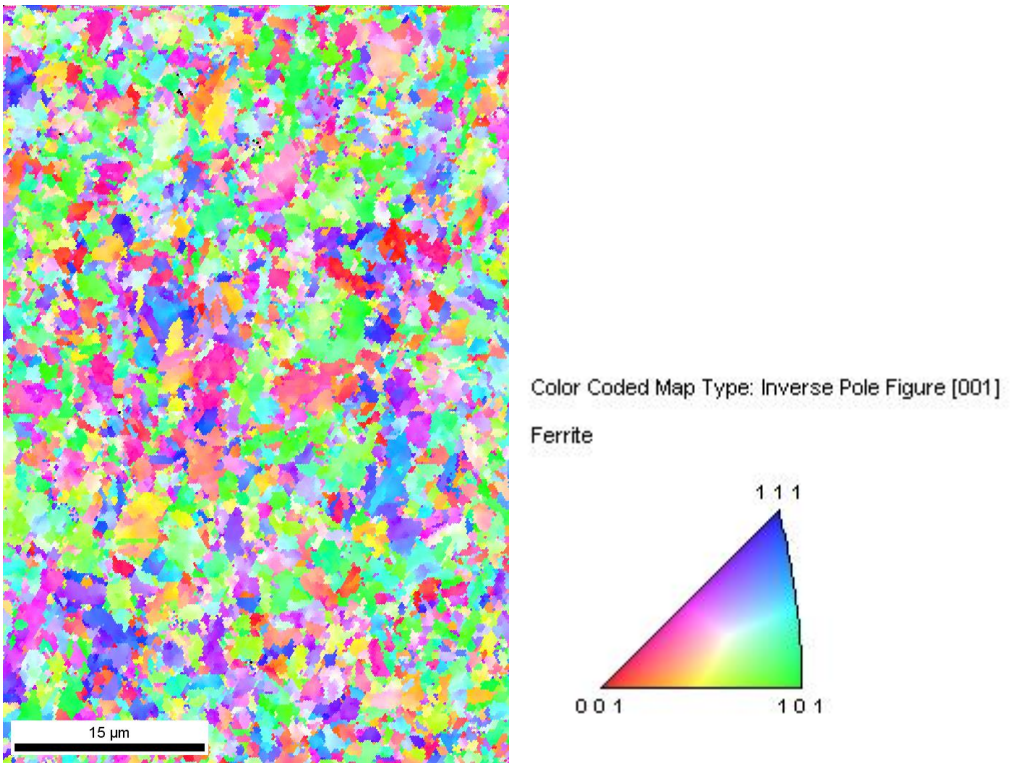

Figure 23 - EBSD map of EUROFER ODS
note the image scale is different to the Fe-14wt%Cr.

10 Sample Preparation

Microscope samples were mounted onto JEOL aluminium Ø12.5 x 5mm stubs. Exact shape depended on the shape and dimensions of the bulk material: ~1 mm thick slices were cut with a Buehler IsoMet Low Speed Saw, then slices were divided into ~8x8mm sections.

Cut samples were hot wax mounted onto a polishing disc, ground on 400 and 600 grit silicon carbide papers to form one flat surface, flipped and re-mounted, then ground on 400, 600, 800, 1200, 2500 and 4000 grit to a smooth finish. Each was polished using 40nm colloidal silica + 10% hydrogen peroxide solution on a chemo-mechanical polishing cloth for ~30 minutes until all grinding scratches were removed. Polished samples were thoroughly cleaned with acetone and ethanol.

One set of the materials was immediately mounted onto 12.5mm stubs using silver conductive paint. The remaining polished pieces were subjected to various ion implantations of helium, dual (helium and iron) or neon before mounting in the same way as the unimplanted specimens.

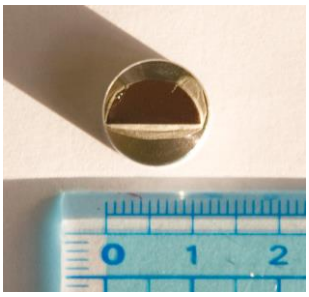

Figure 24 - Fe-14wt%Cr

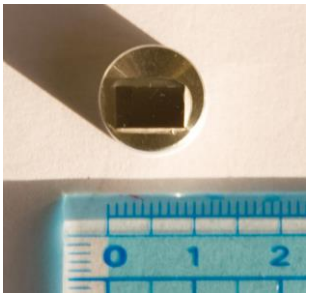

Figure 25 - CEA ODS

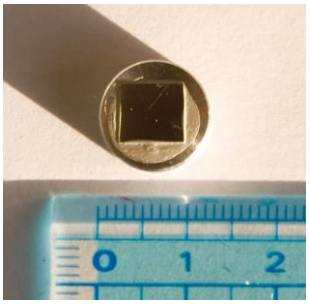

Figure 26 - EUROFER

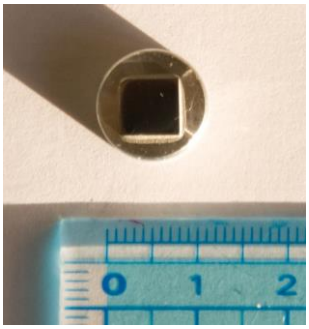

Figure 27 -EUROFER ODS

11 Ion Implantation

11.1 Surrey Ion Beam Centre

Implantations were performed at the Surrey Ion Beam Centre, University of Surrey [142]. The implantation area is designed for 4-inch silicon wafers, therefore a custom sample plate was made to hold a large number of small samples. Thermocouples are attached to the front and back of sample plates to ensure a constant implantation temperature and temperature distribution.

All implantations involved successive implantations of different energies to create a flat profile to a specific depth. As can be seen from Figure 34, Figure 36 and Figure 39 the calculated profile has sharp peaks higher than the required appm; these peaks are calculated based on a single implantation and immediate return to room temperature after implantation. It was shown, that with multiple implantations and the sample being held at high temperatures during and slow cool down after implantation, the implanted impurities would begin to diffuse, broadening the implantation profile, softening the sharp peaks and producing an approximately even concentration over the implanted layer [143][144].

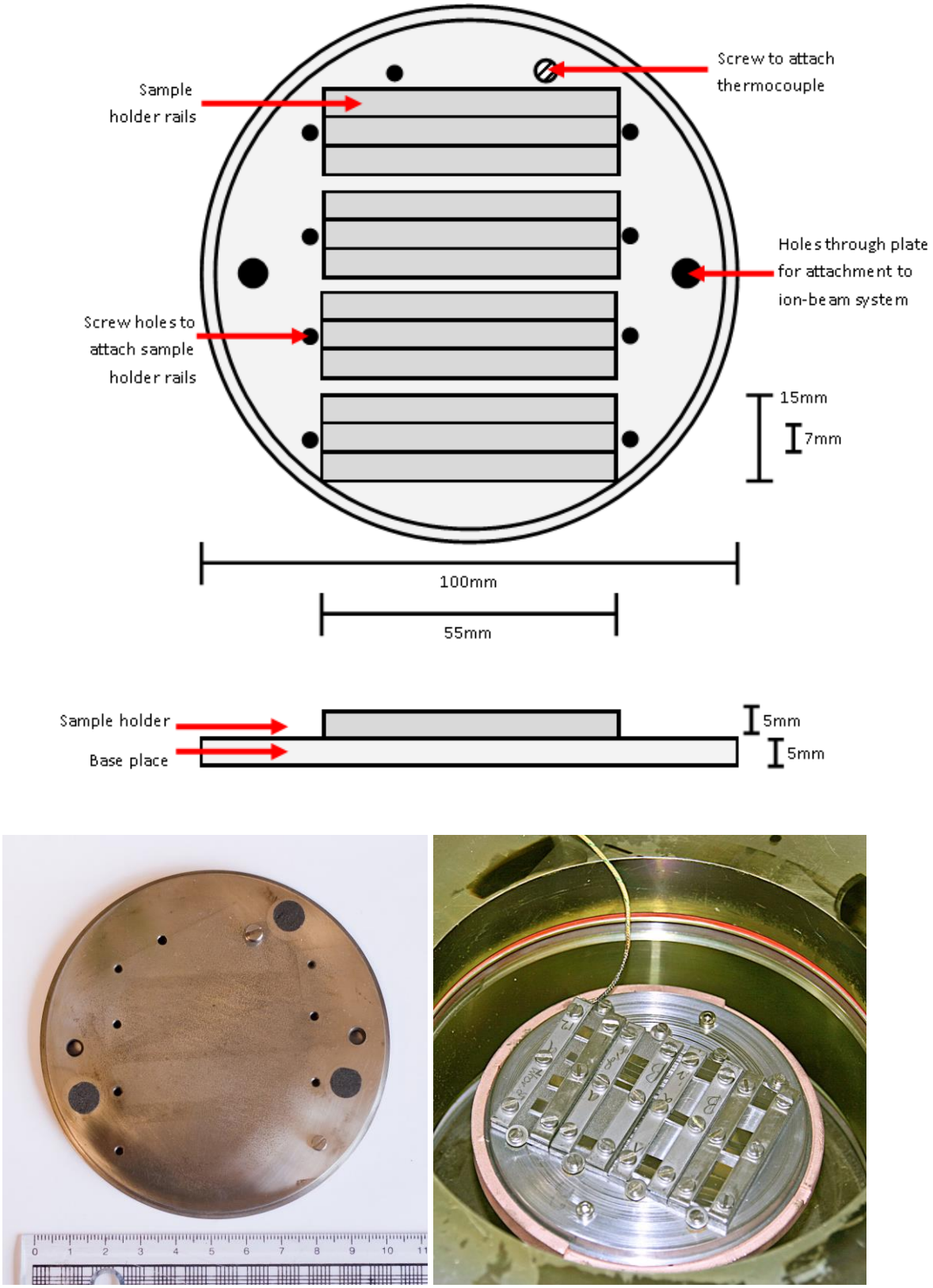

Figure 28 - Surrey sample plate – schematic, baseplate without sample holding rails and mounted in target chamber with attached thermocouple.

Figure 29 - Surrey Ion Beam target chamber

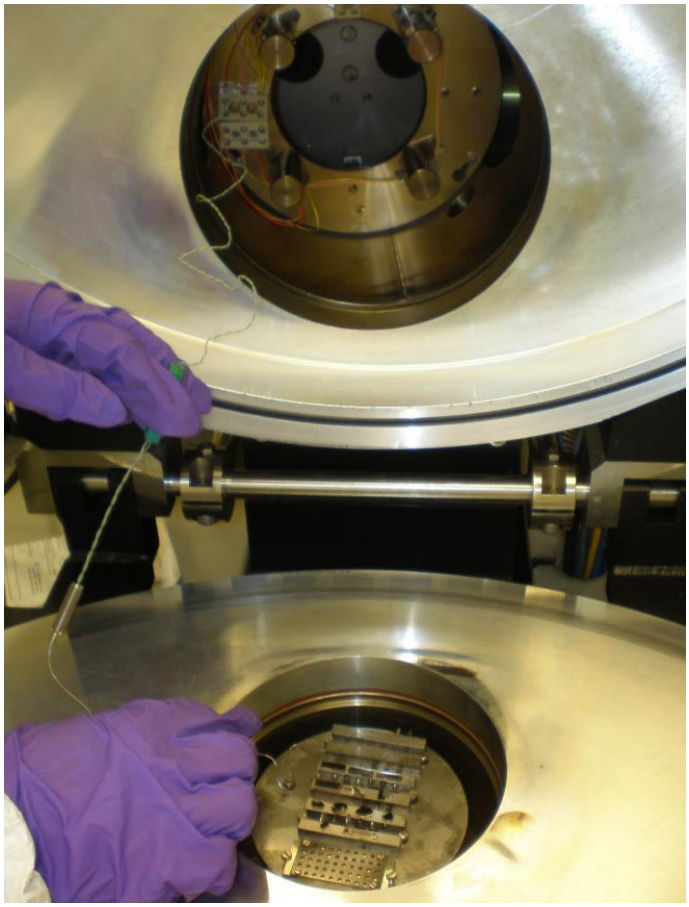

Figure 30 - Attaching the thermocouple to the mounted sample plate.

11.1.1 75appm He

The first experiment was a low dose implantation of helium ions to produce a He density of 75appm to a depth of 1μm from the surface of the material. The conditions were chosen to investigate the effect of a low dose of helium on the surface hardness (below the limit where helium effects become significant, ~100appm He [145]).

Using the 2MV High Energy Implanter at its lowest energy setting of 1.0MeV, helium is implanted below the material surface. Due to their small size there are fewer He atomic collisions and their few electrons cause low interaction with the lattice. The deceleration of the implanted helium ions is quite uniform, therefore the concentration profile after implantation forms a sharp peak, i.e. a very thin (~0.2μm) layer a few microns (>1.5μm) below the surface (Figure 31).

Implantations can be simulated with SRIM software. This models the implantation depth and dpa of ions being injected into a substrate. The program gives typical trajectory patterns of displaced atoms and damage profiles of dpa vs. depth. The calculations of dpa/appm are contained within the SRIM software.

An ion trajectory plots the path and resting point of the implanted ions. In Figure 31a each black line shows the simulated path of one ion (He injected into Fe at 1MeV) and Figure 31b shows the number of implanted ions coming to rest with depth into the materials.

For micromechanical testing, implantation into the surface layer of the samples i.e. from 0μm depth is required, and therefore when using a 1MeV ion beam, an aluminium degrader foil must be used in front of the sample surface to ensure some ions come to rest directly below the surface.

Multiple SRIM calculations were performed to determine the required thickness of foil. In order to implant helium to the surface with a 1MeV beam, a 3μm thick aluminium sheet was required. Figure 32 shows the ion trajectories coming to rest just

as they enter layer 2 (the iron sample). Figure 33 shows the 3μm thick aluminium foil mounted in the degrader set up in the Surrey ion beam. The degrader is a 10cm diameter circle positioned directly in front of the sample plate while the beam is in operation.

Implanting He through an aluminium degrader at 1MeV produces a thin surface layer of implanted material (~300μm deep). For mechanical testing, this layer needs to be thicker and therefore higher energy ions need to be implanted to greater depths. Simulations must be run for multiple energies. Once the collision event and ion trajectory data are collected, the different energies can be combined and the dose level of each energy varied to achieve the desired implantation profile.

To implant 75appm He in an approximately flat profile to ~1μm depth, three successive implantations through the degrader at energies of 1.0, 1.15 and 1.3MeV were required. Each was used to give a dose of 2×10^{14} ions/cm^2, giving a total dose of 6×10^{14} ions/cm^2. The implantation was performed at 300°C. See Figure 34 – cumulative ion ranges of the three implantation energies and Figure 35 – the (minimal) damage caused by the incident helium ions in dpa.

No Fe-14wt%Cr sample was implanted with 75appm He, as the material was not available at the time of the experiment.

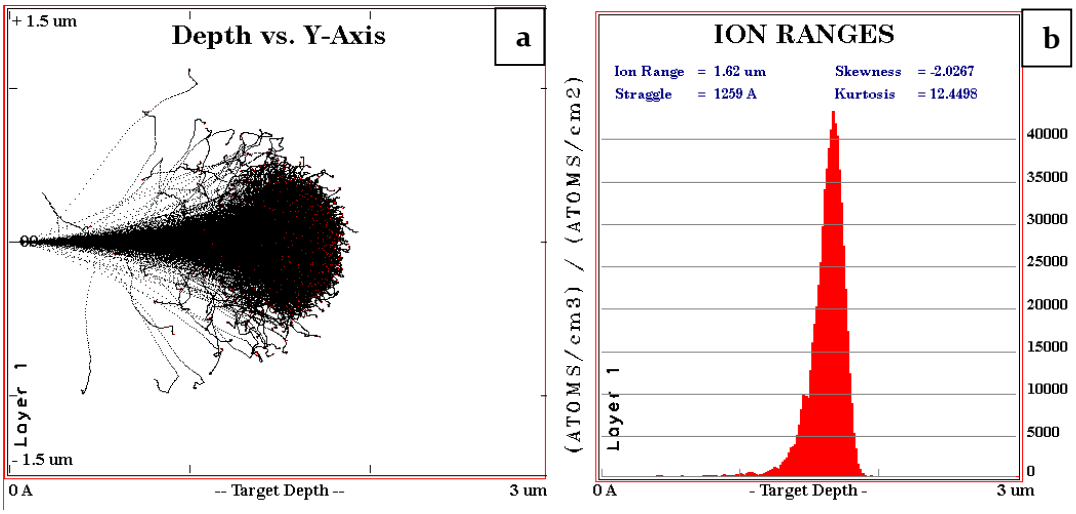

Figure 31 -SRIM calculated incident ion trajectories and range
5000 He ions implanted at 1MeV into an Fe substrate

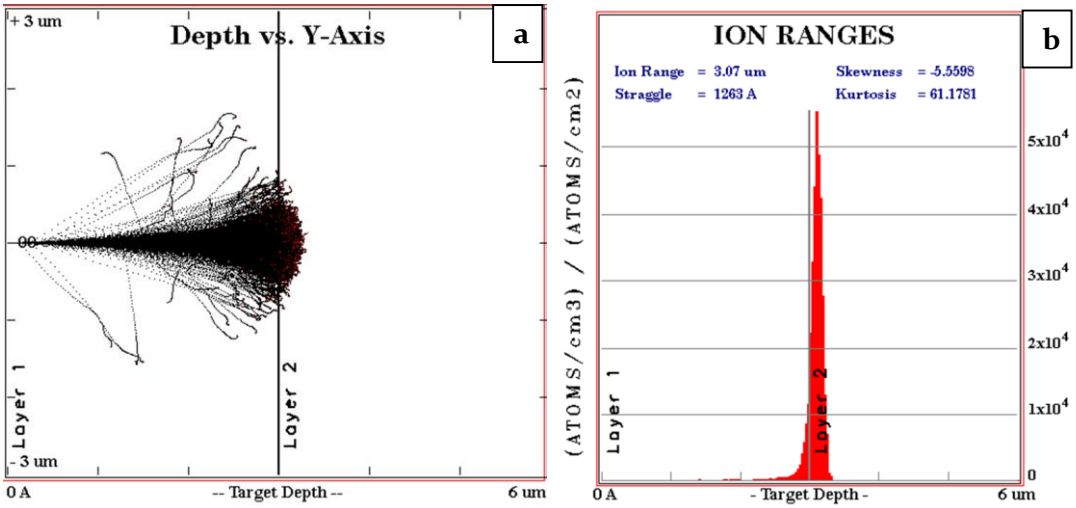

Figure 32 - SRIM calculated incident ion trajectories and range
5000 He ions implanted at 1MeV through 3µm Al (layer 1) into an Fe substrate (layer 2)

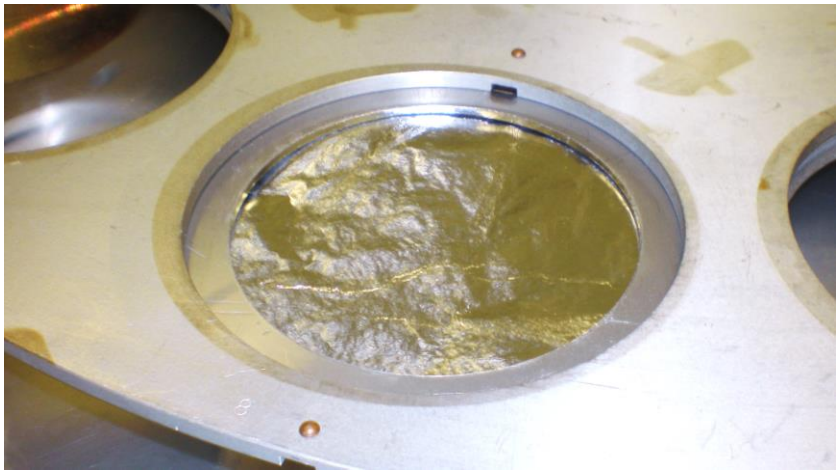

Figure 33 - 10cm diameter, 3µm thick Al degrader foil in position in the Surrey Ion Beam

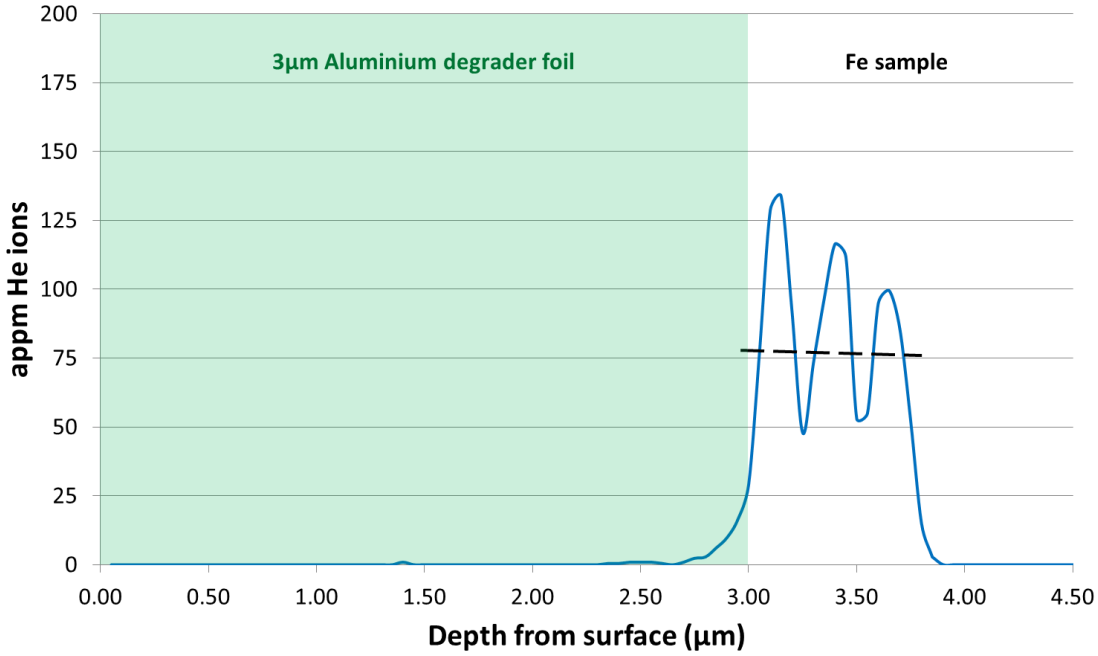

Figure 34 - SRIM Implantation profile, 75appm He to 1µm depth.
The green area represents the aluminium degrader foil the ions pass through before coming to rest in the iron sample (the white area).
The dashed line is a calculated mean concentration.

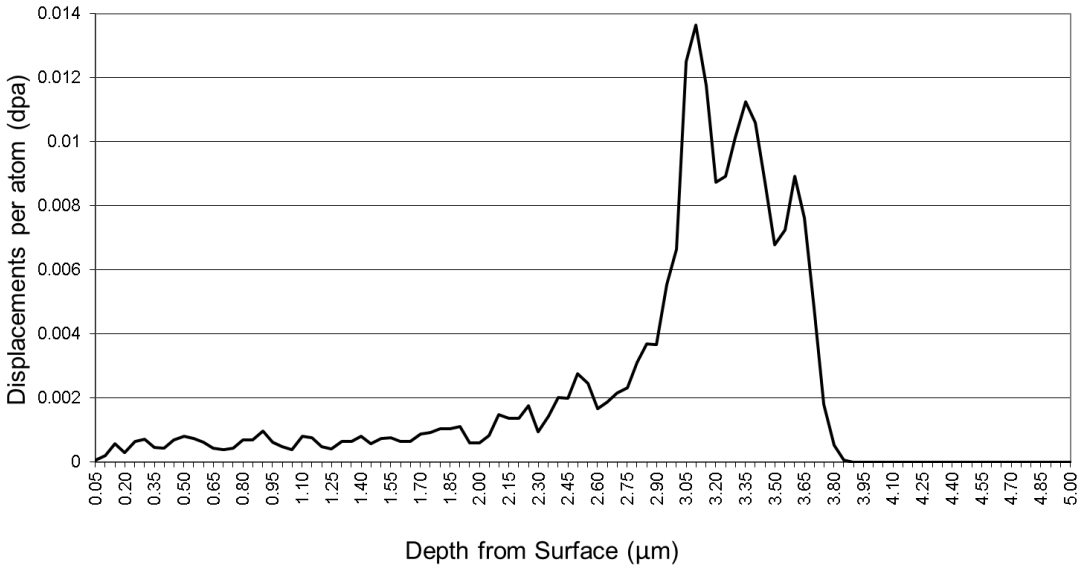

Figure 35 - SRIM calculated damage in the sample caused by the helium implantation using conditions as in Figure 34.

11.1.2 2000appm He

The second implantation experiment used a higher dose of helium to investigate material property changes when the saturation is well above the limit of the lattice absorbing helium into interstitials (~100appm [146]).

Samples were helium ion implanted at the Surrey Ion Beam Centre at 300°C ± 10°C to ~2000appm He in a flat profile to ~3μm depth. The depth of 3μm was chosen to enable microcantilever testing in the damaged material (Chapter 5). Bulk samples were mounted on the same stainless steel plate used in the 75appm implantation and the thermocouple temperature was recorded. For this implantation, a new lower energy ion beam was available, therefore rather than using degrader foils to ensure the implanted ions started at the surface, a wider range of energies was used (0.2MeV-1.8MeV).

1) The first set of implantations was performed in the 2MV High Energy Implanter using 1.2, 1.4, 1.6 and 1.8MeV for doses of $5x10^{15}$ ions/cm^2 for all but the 1.8MeV which was at $6x10^{15}$ ions/cm^2.
2) The plate was transferred to the 2kV High Current Implanter for Implantations at 0.2, 0.3, 0.4, 0.6, 0.8 and 1MeV with doses of $5x10^{15}$ ions/cm^2 for all but the 0.3MeV which was at $1x10^{15}$ ions/cm^2. All implantations were performed at 300°C ± 10°C.

The total dose of all implantations was $4.75x10^{16}$ ions/cm^2. These conditions produced an approximately flat profile of 2000appm helium to a depth of 3μm.

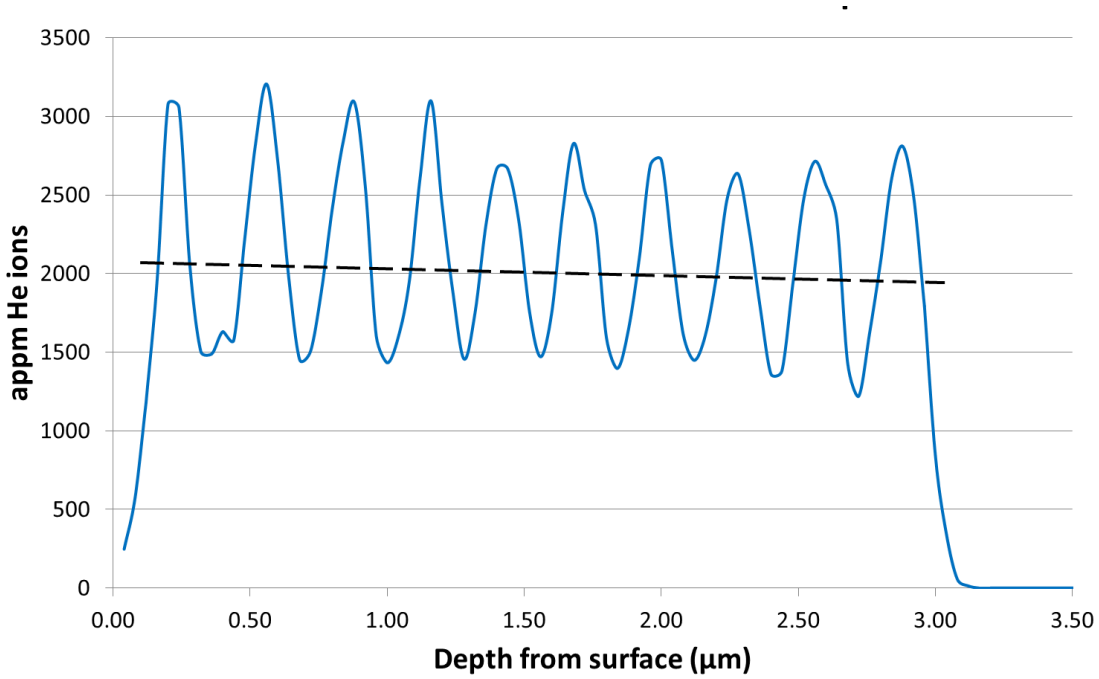

Figure 36 - SRIM Implantation profile, 2000appm He to 3µm depth

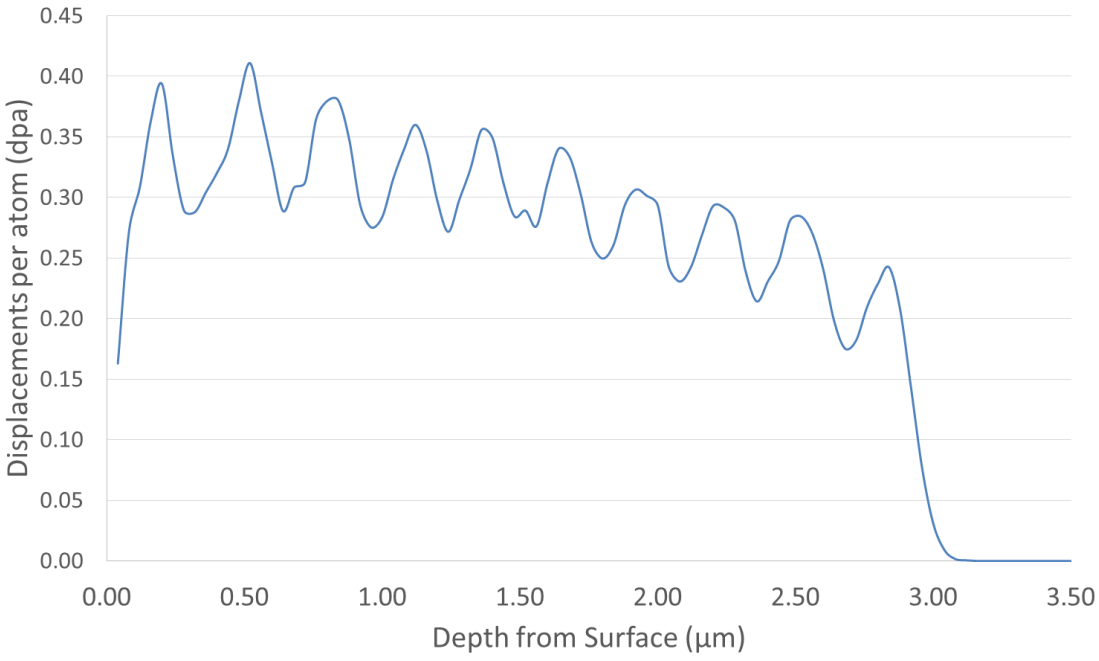

Figure 37 - SRIM calculated damage in the sample caused by the helium implantation

11.1.3 2000appm Ne

Helium has too low an atomic mass to be detectable using Energy-Dispersive X-Ray spectroscopy (EDX) scans. Neon is similar to helium – it does not chemically interact with the Fe-Cr alloys, but has a bigger atomic number, so should appear in EDX scans. Neon can be used as an analogue for helium provided the implantation doses are adjusted so the gas concentration is equivalent [147]. A high dose of neon was used (2000appm), chosen to match the helium implantation. Neon has a larger atomic mass than helium and consequently greater energy transfer during collisions which leads to a higher damage rate and shorter range. 1.2μm was the maximum depth possible using the 2MeV implanter.

Energies of 0.2, 0.5, 1.0, 1.5 and 2MeV were used to implant doses of 3.8, 4.5, 5.0, 3.0 and 7.0×10^{15} ions/cm^2 respectively. The total dose was 2.33×10^{16} ions/cm^2. This produced an approximately flat profile of 2000appm neon to a depth of 1.2μm.

Figure 39 and Figure 41 show the neon concentration and damage profile. It should be noted that there are five implantation energies but only four distinct peaks on these graphs because the 1.5MeV implantation was added to fill the deep trough at ~0.9μm that can be seen in Figure 38. A lower dose was used at 1.5MeV as a peak was not required, simply a gapfill to ensure the average implantation (seen as a black dashed line on the graphs) was constant around 2000appm.

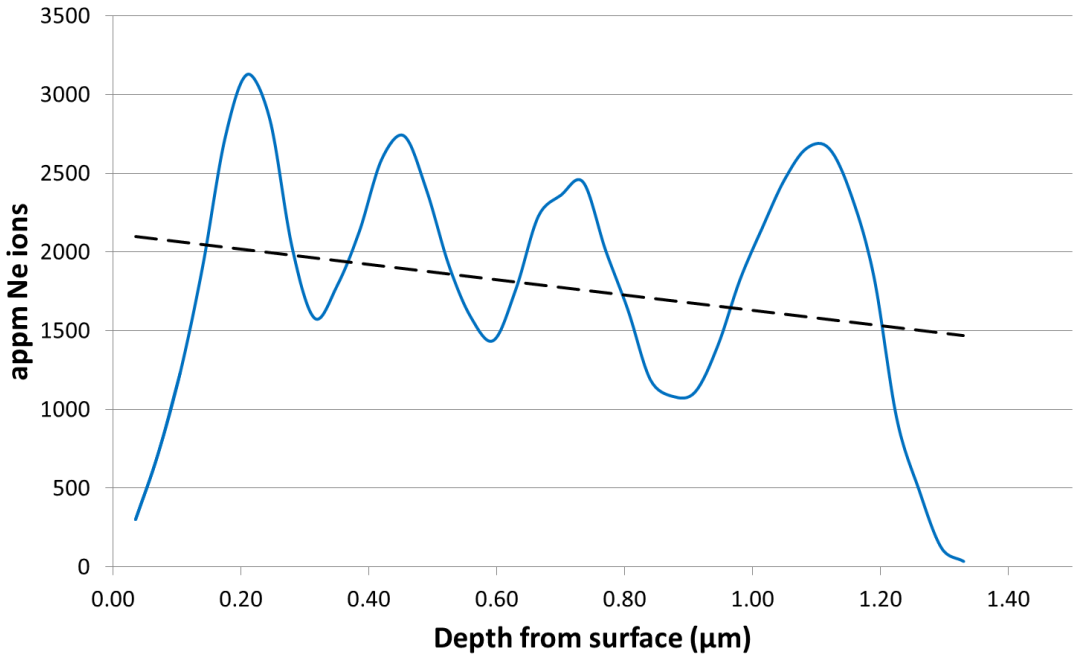

Figure 38 - SRIM implantation profile with 4 implantations (0.2, 0.5, 1.0, 2.0 MeV)

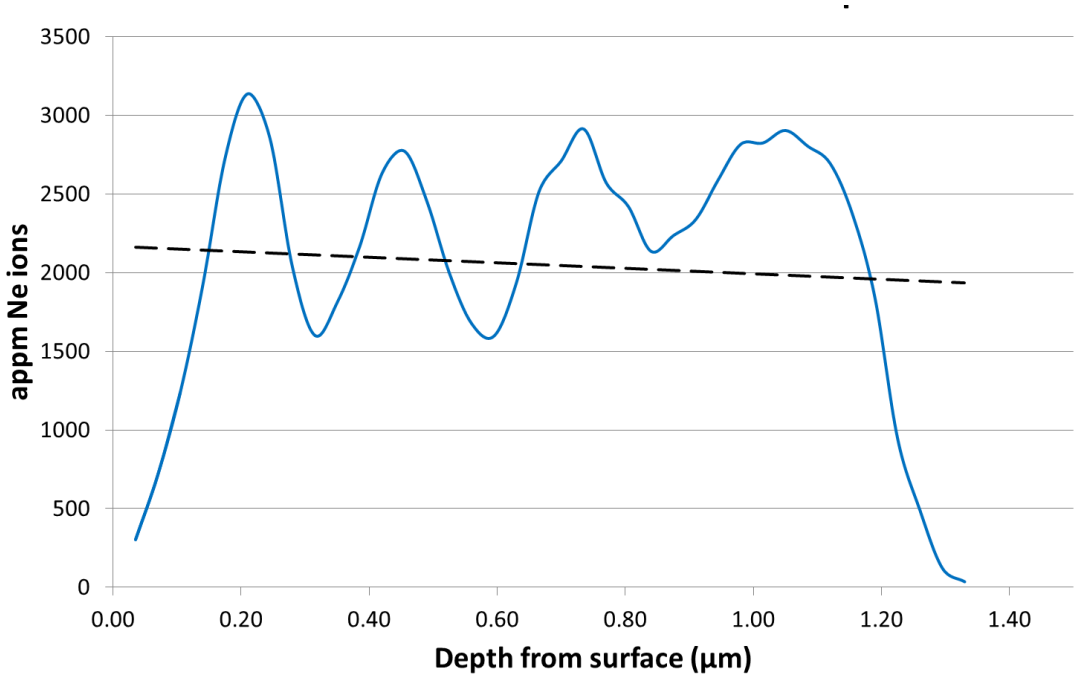

Figure 39 - SRIM implantation profile, 2000appm Ne to 1.2µm depth
Profile is made of 5 implantations (0.2, 0.5, 1.0, 1.5, 2.0 MeV);
this is the profile used in the final samples.

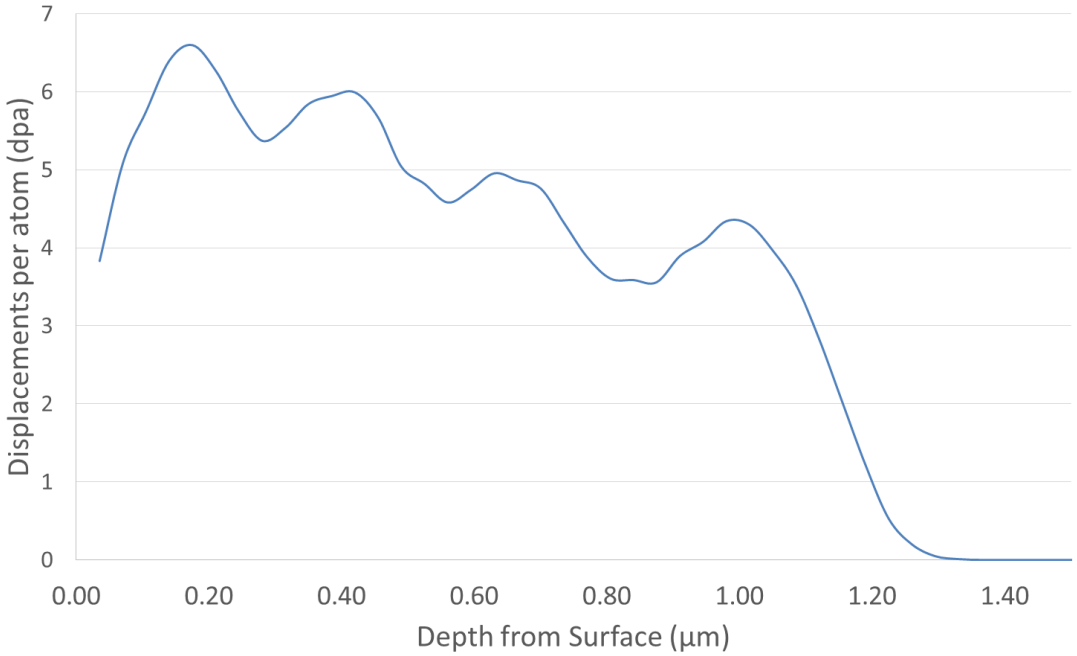

Figure 40 - SRIM damage profile with 4 implantations (0.2, 0.5, 1.0, 2.0 MeV)

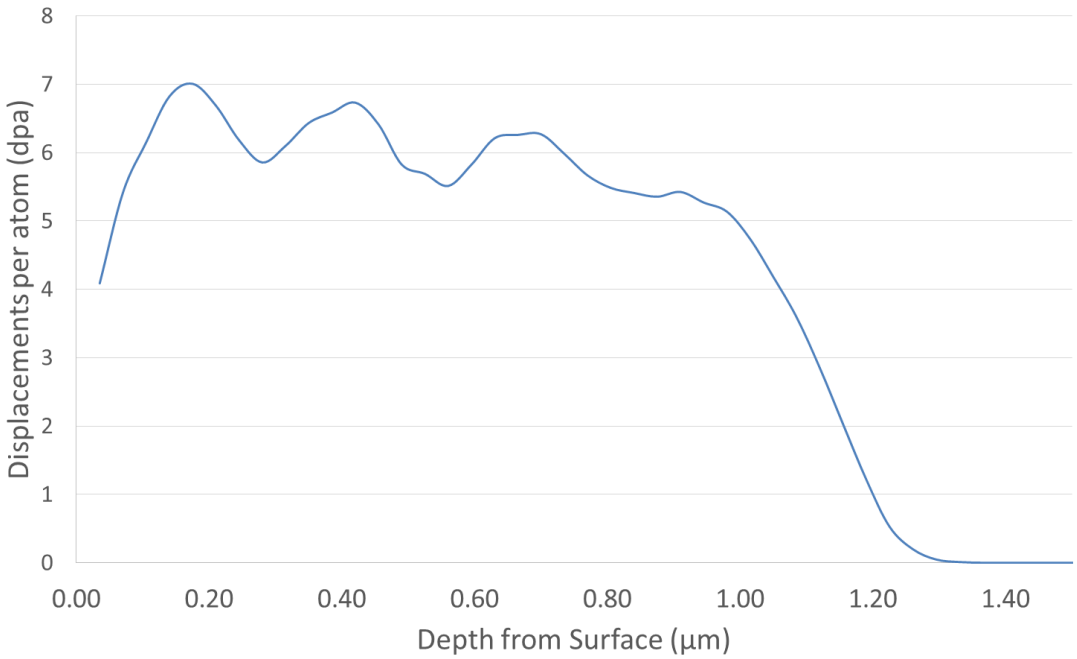

Figure 41 - SRIM damage profile, 2000appm Ne to 1.2µm depth
Profile is made of 5 implantations (0.2, 0.5, 1.0, 1.5, 2.0 MeV);
this is the profile used in the final samples.

11.2 JANNUS Facility, CEA Saclay

To investigate the material property changes in more reactor relevant conditions, self-ion implantation was used to simulate the neutron damage that would occur. This was combined with the helium implantation simulating transmutation.

The Surrey Ion Beam Centre can only perform single beam implantations. The facility at CEA Saclay, Paris, France [148] was used to investigate the mechanical property changes induced by combined helium and iron implantation.

The JANNUS facility has three beam lines which can be used individually or in combination. The beams all run at fixed single energies, and therefore to create a range of implantation depths within the material, degrader foils of varying thickness are mounted in a holder which is rotated in front of the beam line (Figure 44) as in the 75appm He implantation – Section 11.1.1. The overall implantation profile can be calculated by combining the profiles created by implantation of the same dose through each of the five degrader foils (and one profile without a degrader – the empty slot in the holder).

The implantation area is significantly smaller; JANNUS: 2.5cm diameter cf. Surrey: 10cm diameter. A special sample plate had to be designed to accommodate as many samples in the smaller available area (Figure 42).

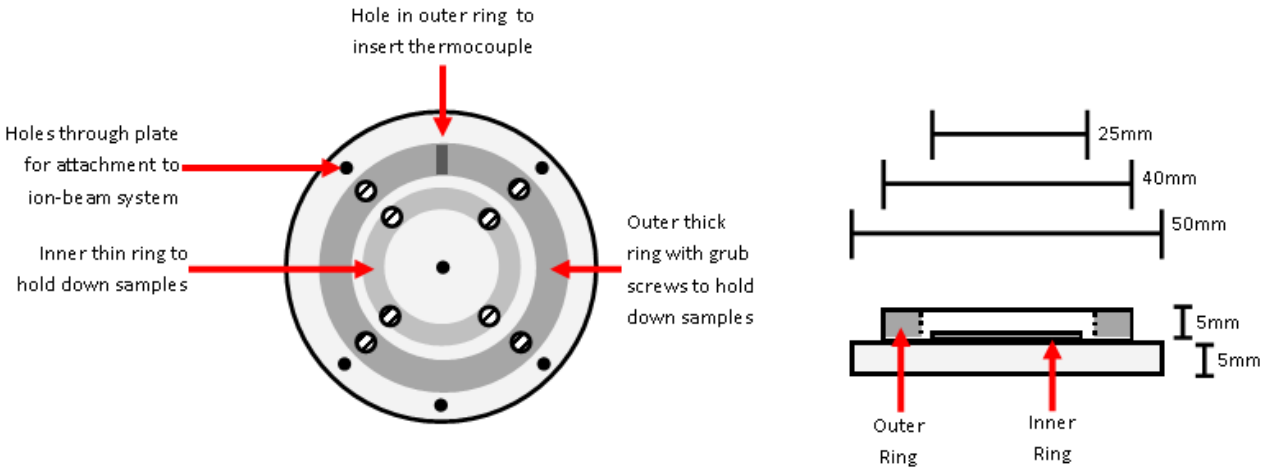

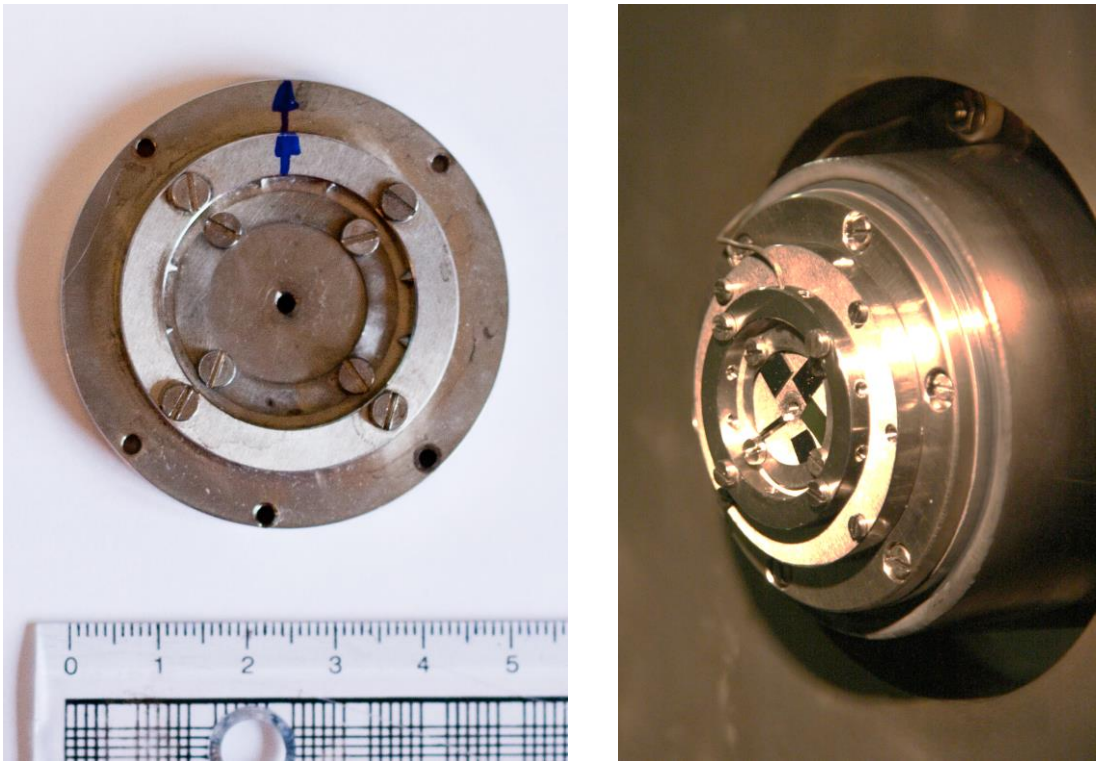

Figure 42 - JANNUS sample plate
Schematic, baseplate and mounted in target chamber with attached thermocouple.

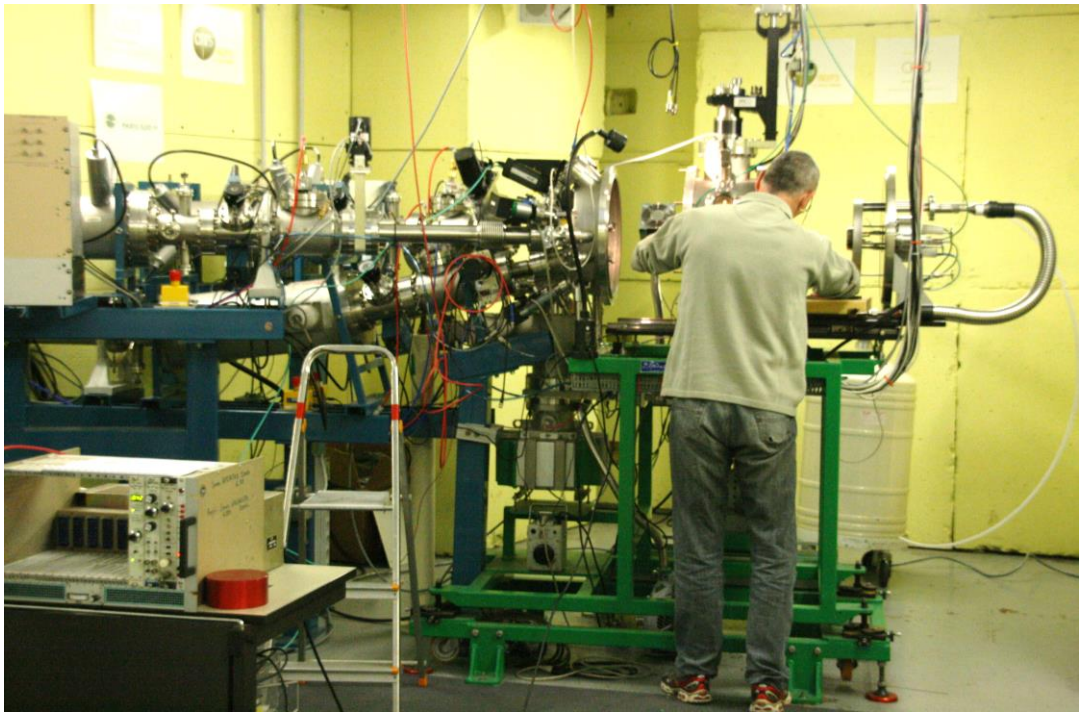

Figure 43 - JANNUS Beam Line

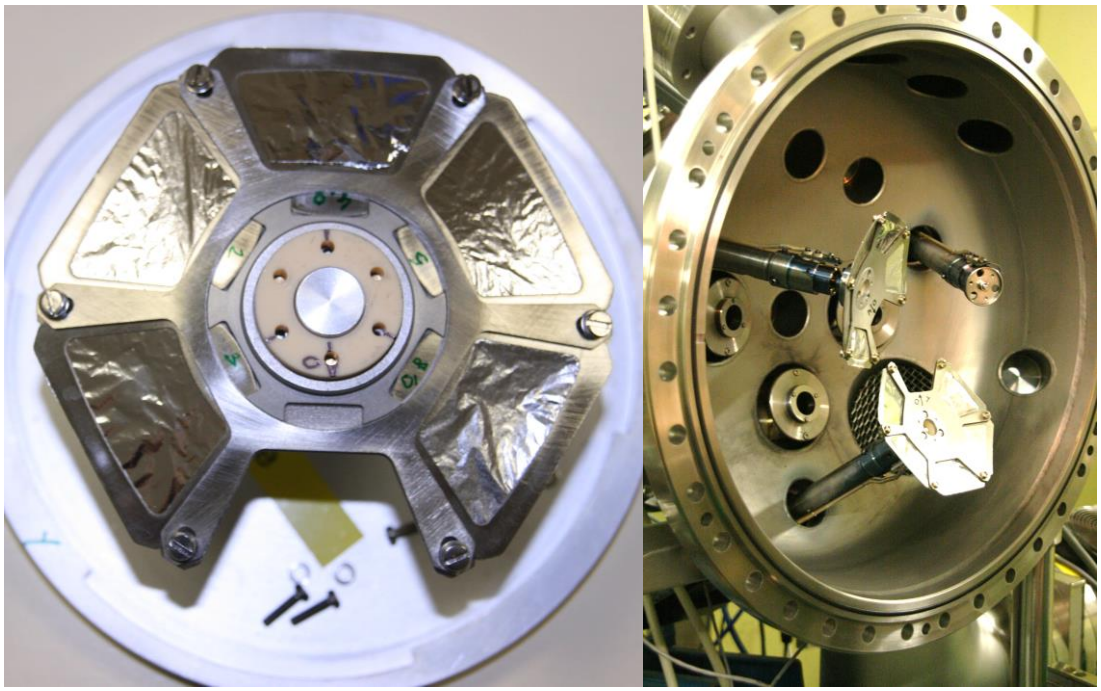

Figure 44 – Mounted degrader foils in holder and holders in position over the beam lines.

11.2.1 2000appm He + 4.5dpa Fe

A set of samples was dual-beam implanted at JANNUS, with ~2000appm He and Fe to cause 4.5dpa damage, both to a depth of 3.5μm (implantation temperature 300°C.) These implantation conditions were obtained using Fe^{8+} ions at 24MeV, with aluminium degrader foils of 5, 3.8, 2.8, 1.6 and 0.8μm and an empty slot. The second beam line used He^{+} at 2MeV with degraders of 5, 4, 3, 2 and 0.8μm and an empty slot (Figure 44).

2000appm of helium was used for direct comparison with the Surrey 2000appm samples (Figure 45). Ideally the samples should then have been implanted to 200 dpa of iron ion damage as reactor conditions will give 10appm He per dpa damage [16]. However ~60 days of beam time would be required for 200dpa of damage to be created with an ion beam (at the energy used). Increasing the beam current leads to melting of the degrader foils. 4.5dpa of damage was the maximum that could be introduced during the beam time available (Figure 46).

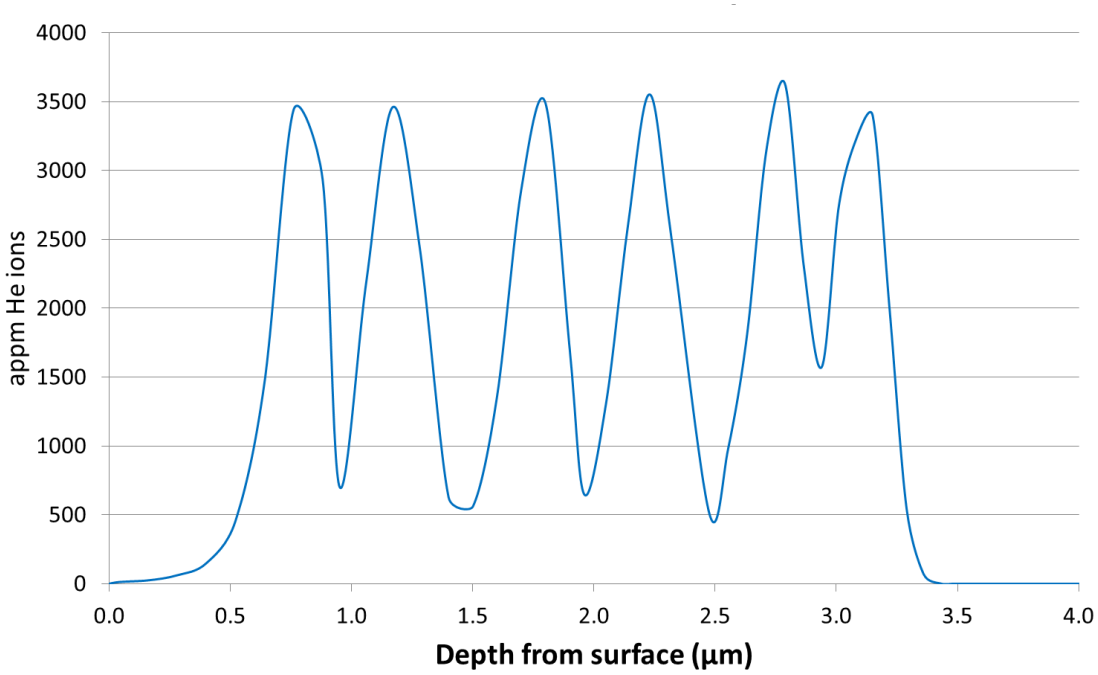

Figure 45 - SRIM damage profile of implantation of He to produce 2000appm to 3.5µm depth

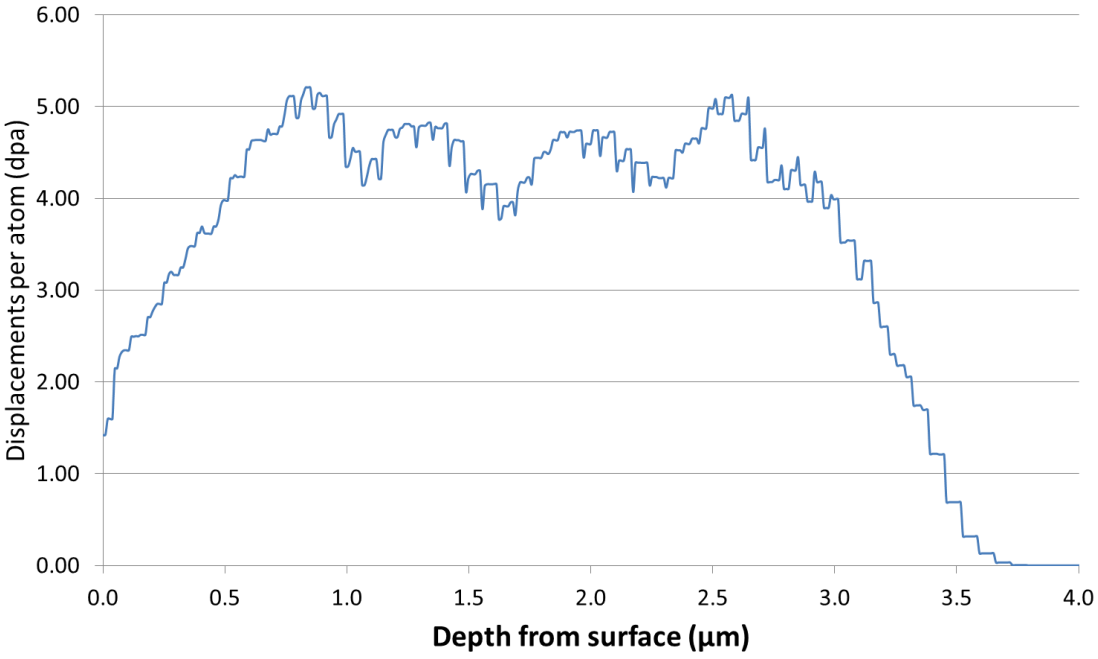

Figure 46 - SRIM damage profile of implantation of Fe to produce 4.5dpa damage to 3.5µm depth

12 Summary of Samples

Samples for this project were made in the following material and implantation conditions:

	Unimplanted	75appm He	2000appm He	2000appm He + 4.5dpa Fe	2000appm Ne
Fe-14wt%Cr	✓	×	✓	✓	✓
CEA ODS	✓	✓	✓	✓	✓
EUROFER	✓	✓	✓	✓	✓
EUROFER ODS	✓	✓	✓	✓	✓

Figure 47 and Figure 48 compare the gas concentrations (appm) and damage levels (dpa) respectively, for all of the implantations.

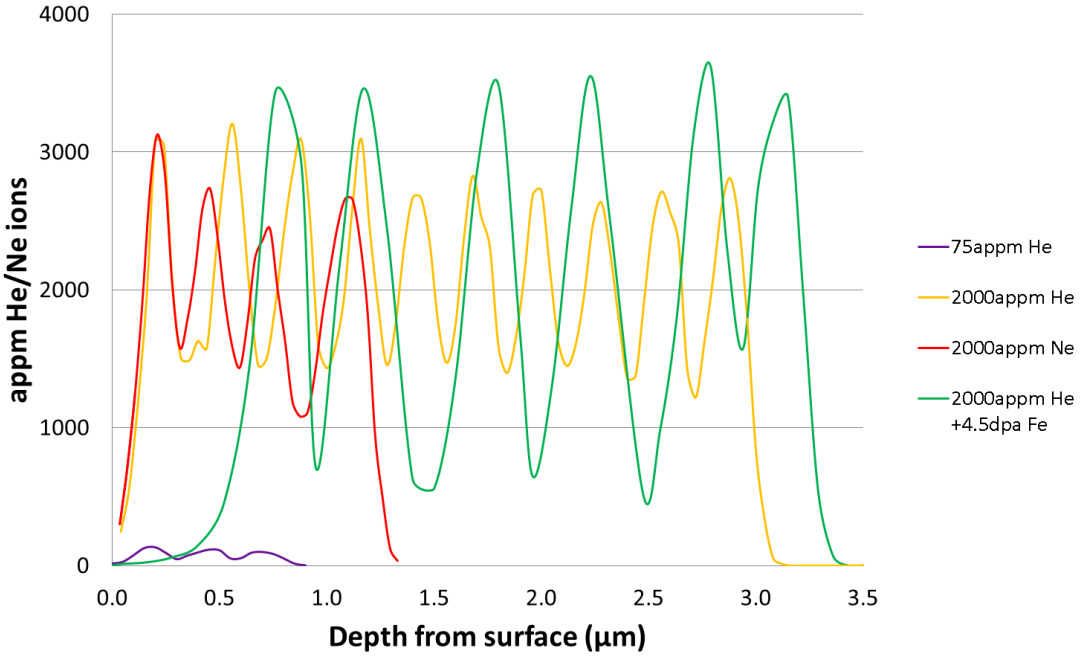

Figure 47 - Comparison of appm levels for all implantation

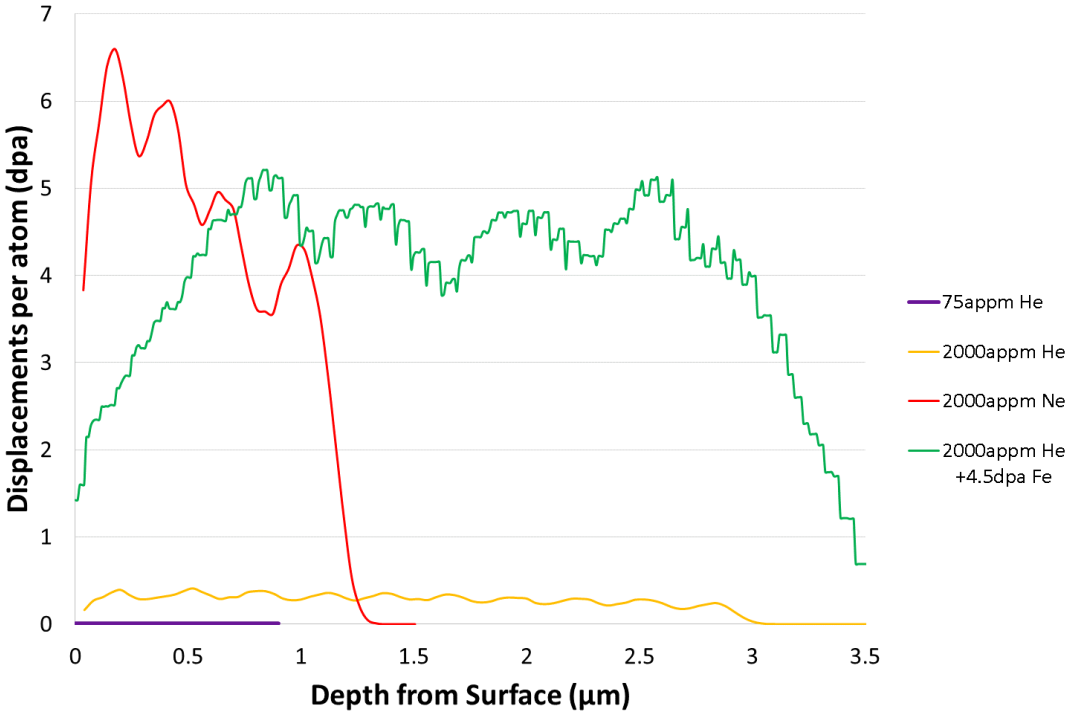

Figure 48 - Comparison of dpa levels for all implantation

Chapter 3
Indentation Hardness Testing

13 Nanoindentation Methodology

An MTS Nanoindenter XP was used with a Berkovich tip and continuous stiffness measurement [149] to measure hardness as a function of depth. Nanoindentation uses a coil-magnet assembly or piezo-electric transducers to press a sharp diamond indenter tip into the test material and measures the displacements with a capacitance gauge [149]. Indentation into irradiated materials measures how irradiation affects the hardness and also the depth variation of hardness changes.

Each sample was tested using 3000nm deep indentations in arrays of four by five indentations with spacing of 50μm (Figure 49 shows part of an array in Fe-14wt%Cr). 50μm spacing is large enough to ensure the plastic zones of each indentation do not interact (assuming plastic zone extends equally to approximately seven times indentation depth ≈20μm [150]). For each test on the Fe-Cr alloys, a set of identical indentations were also performed on a fused silica sample. The hardness properties of fused silica are well documented and so the silica indentations can be used to calibrate the hardness data for the Fe-Cr alloys [149]. Multiple tests across a range of grains were performed on each alloy and implantation condition to ensure the results were repeatable.

Agilent's Nanosuite software was used to output the hardness data in the form of depth vs. hardness graphs for each individual indentation; the data could then be exported to Microsoft Excel. Using Agilent's Analyst software the hardness could be averaged over multiple indentations. Each line on the following graphs is an averaged hardness/depth curve over 20 indentations. The error bars show one standard deviation.

Table 4 - Nanoindenter settings

Depth	3000nm
Loading Rate	5nm/s
Harmonic Displacement	2nm
Frequency Target	45Hz
Drift	0.05nm/s
Surface Approach	1000nm
Surface Approach Velocity	10nm/s
Surface Stiffness	200N/m

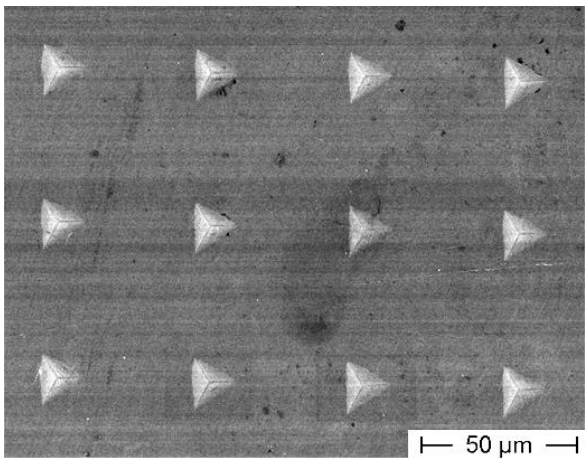

Figure 49 - Indentation array on Fe-14wt%Cr

14 Nanoindentation Results

14.1 Unimplanted Materials

All materials were tested in their unimplanted state. This provides a comparison baseline. Figure 50 shows that the ODS variants are harder than their non-ODS equivalents.

All data lines curve upwards at low displacement; an increase in hardness from a baseline large indent value. This is a widely documented phenomenon called the Indentation Size Effect and was discussed in Section 5.3 [134][151][152][153]. The plateau value of each material is accepted as the bulk hardness value, and in metals, hardness is approximately three times the yield stress [154][155]. Due to this size effect at low depths, the bulk hardness values have been taken as those at 1500nm depth, in the plateau region. The hardness at 400nm depth was also recorded. In the implanted materials, the hardening effect is limited by the depth of implantation. In order to quantify the hardening effects the results must all be recorded at the same depth: 400nm – the greatest depth where the plastic zone is contained within the implanted layer (assuming the plastic zone is ~7 times indentation depth [150], 400nm x~7=~2800nm which is less than the 3000nm implantation depth). Numerical data from all unimplanted samples is compared in Table 6.

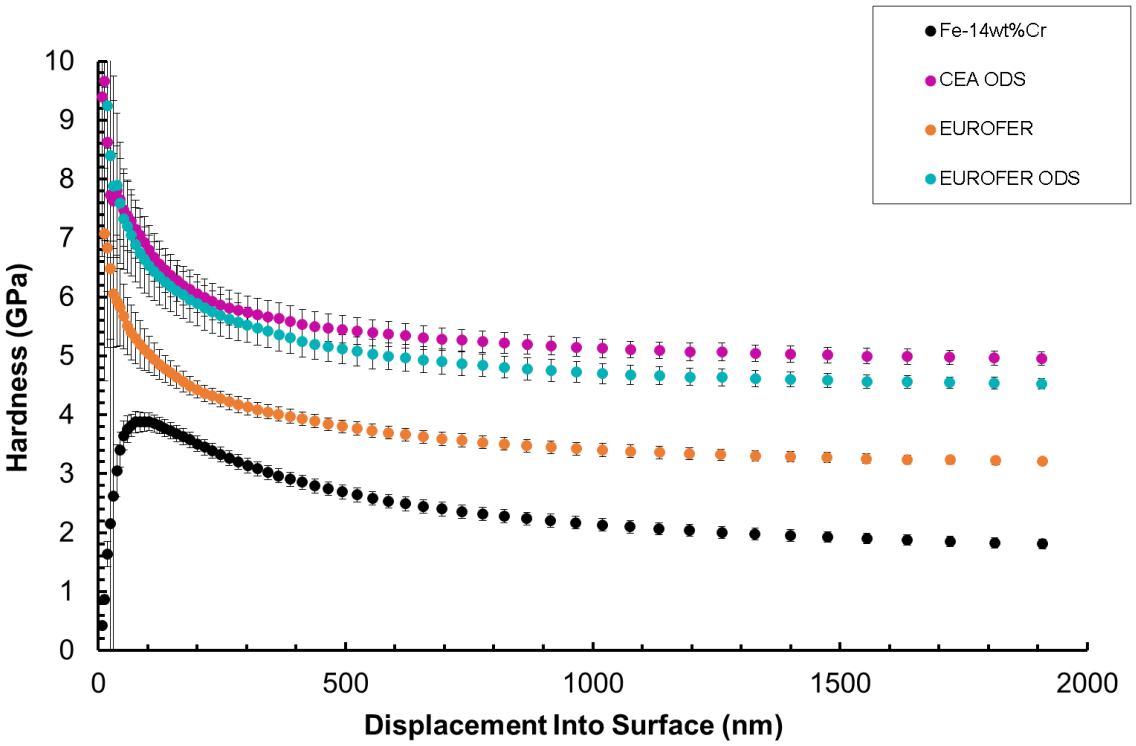

Figure 50 – All materials tested in the unimplanted condition. The three smallest grain size materials (Table 5 - CEA ODS, EUROFER and EUROFER ODS) have the highest hardness, and of those the two ODS variants are the greatest. At shallow displacement there is a significant size effect seen in all materials, but the hardness starts to plateau after around 1000nm displacement.

Table 5 - Grain sizes

Material	***Grain Size***
Fe-14wt%Cr	200µm
CEA ODS	Bimodal: ~10-50µm and ~1-5µm
EUROFER	~2-5µm
EUROFER ODS	~1-3µm

Table 6 - Unimplanted hardness at 400nm and 1500nm depth

(GPa)	***Fe-14wt%Cr***	***CEA ODS***	***EUROFER***	***EUROFER ODS***
Hardness at 400nm depth	2.85 ±0.14	5.53 ±0.23	3.93 ±0.11	5.24 ±0.25
Hardness at 1500nm depth	1.92 ±0.06	5.01 ±0.13	3.27 ±0.09	4.58 ±0.12

14.2 Helium Implanted Materials

The first two implantations were designed to examine the effects of low and high dose helium – 75appm He to a depth of ~1µm and 2000appm He to a depth of ~3µm (as discussed in Section 11) (see Figure 51). There are no data for the 75appm He in Fe-14wt%Cr as the material was unavailable at the time of the implantation.

Figure 52 to Figure 55 show that the low dose of 75appm He has an almost zero effect on the hardness (in both EUROFER materials the 75appm He line appears below the unimplanted line but the points are within the one standard deviation error). Implantation with 2000appm He causes a significant hardness increase – this is more pronounced in the non-ODS material. Also visible on the graphs and most noticeable in the Fe-14wt%Cr is a shoulder in the hardness around the 450nm depth mark on the 2000appm He line.

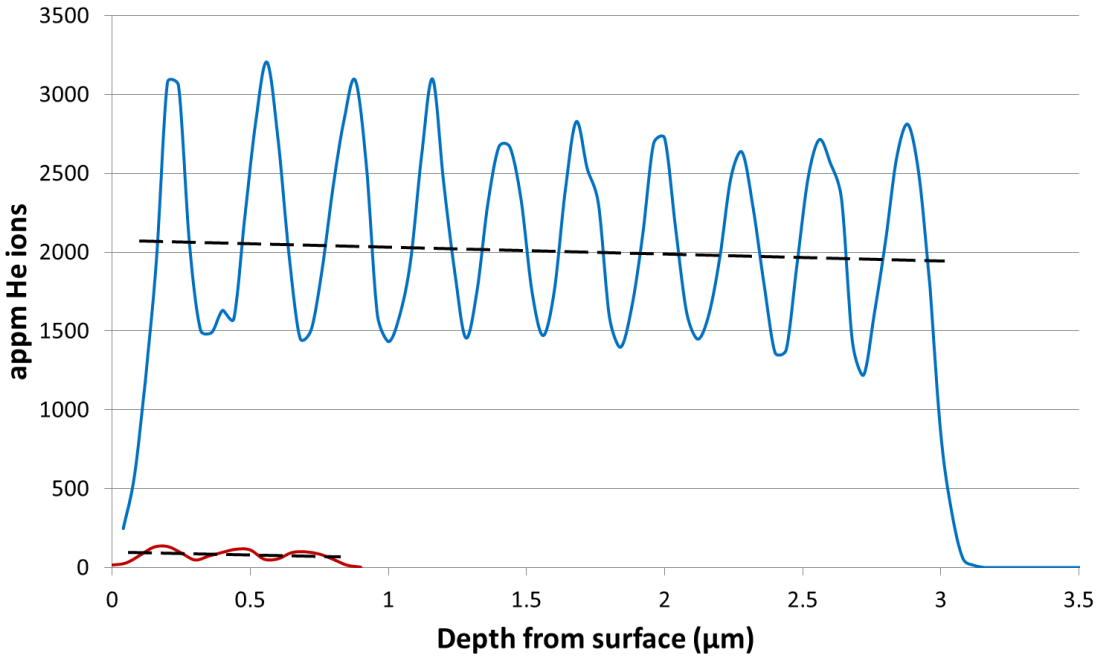

Figure 51 - SRIM calculated He concentration with depth for 75appm He (red) and 2000appm He (blue) implantations.

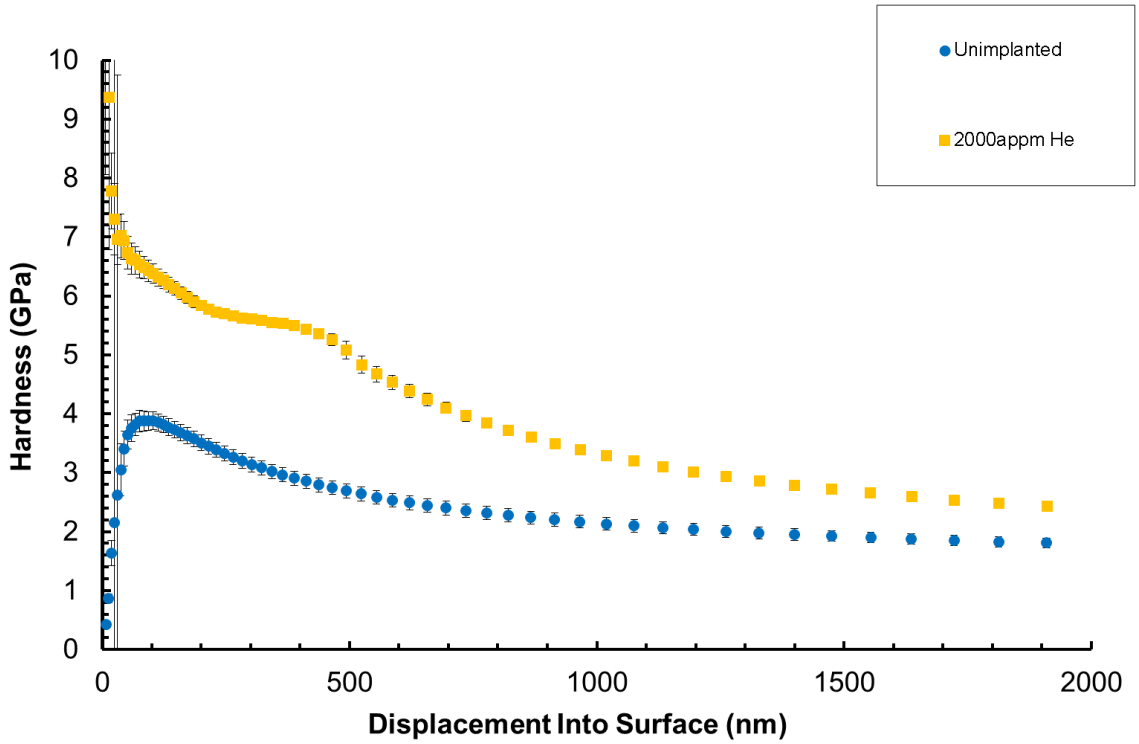

Figure 52 - Fe-14wt%Cr – note the shoulder in results at ~450nm depth in the 2000appm He.

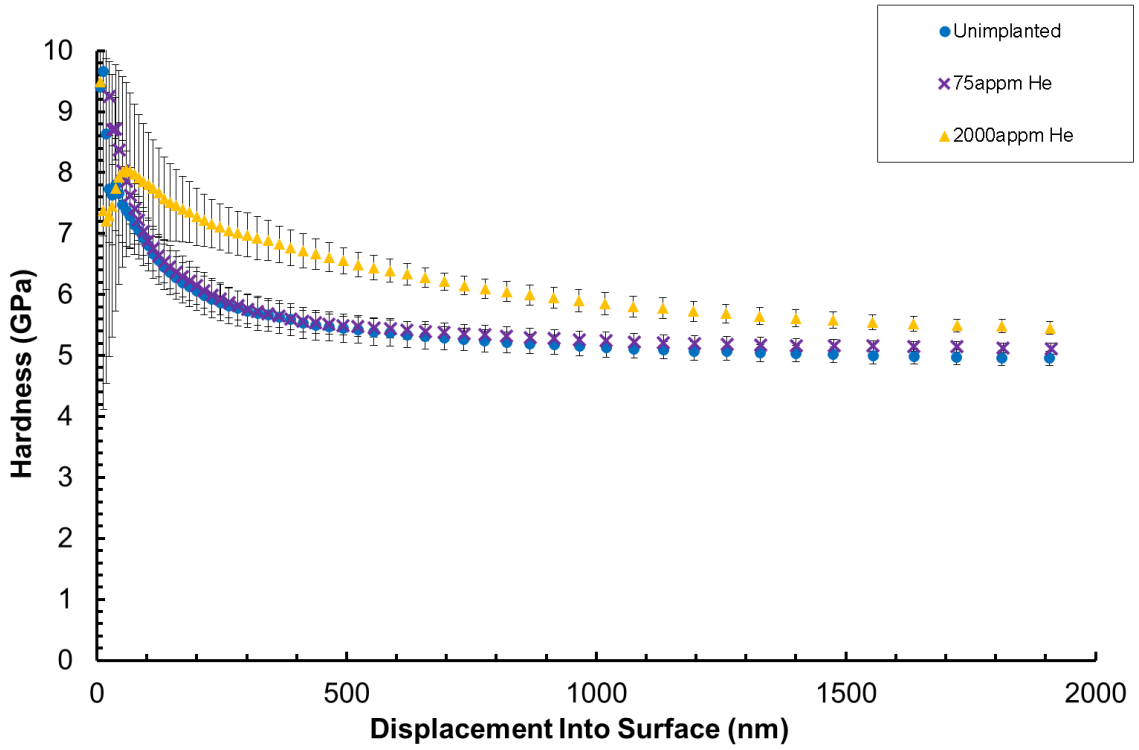

Figure 53 - CEA ODS – The 75appm He implantation causes no significant hardening. Most of the 75appm He data points are within the error bars of the unimplanted data.

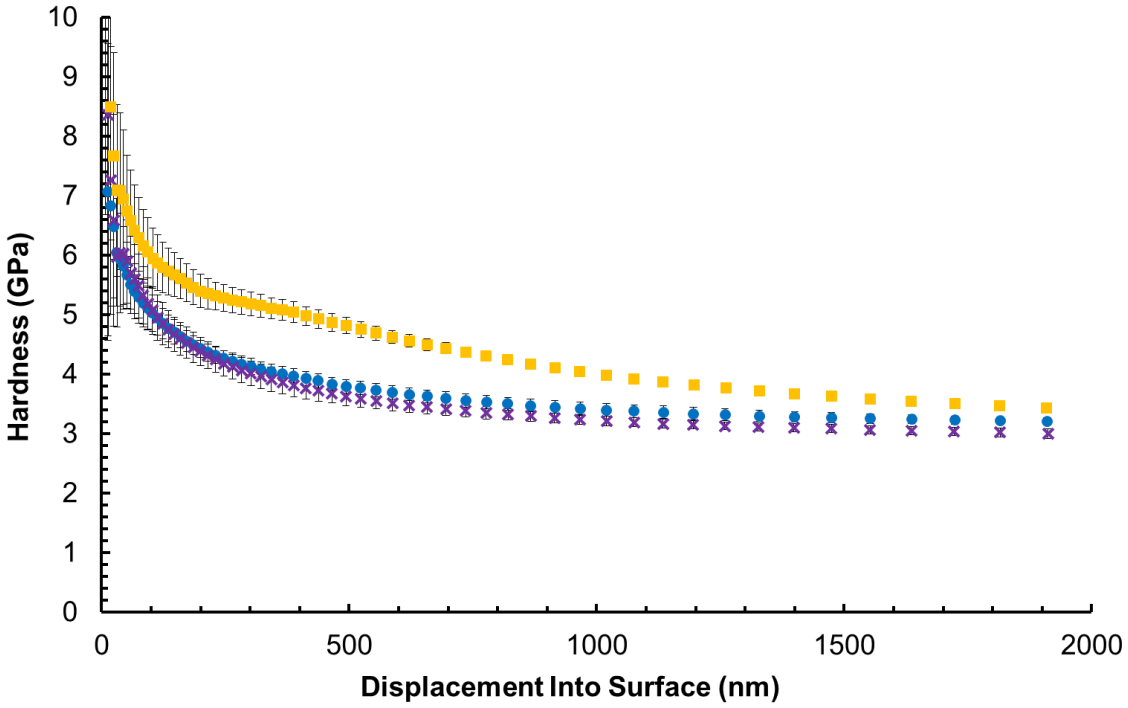

Figure 54 – EUROFER – Note the shoulder in results at ~450nm depth in the 2000appm He.

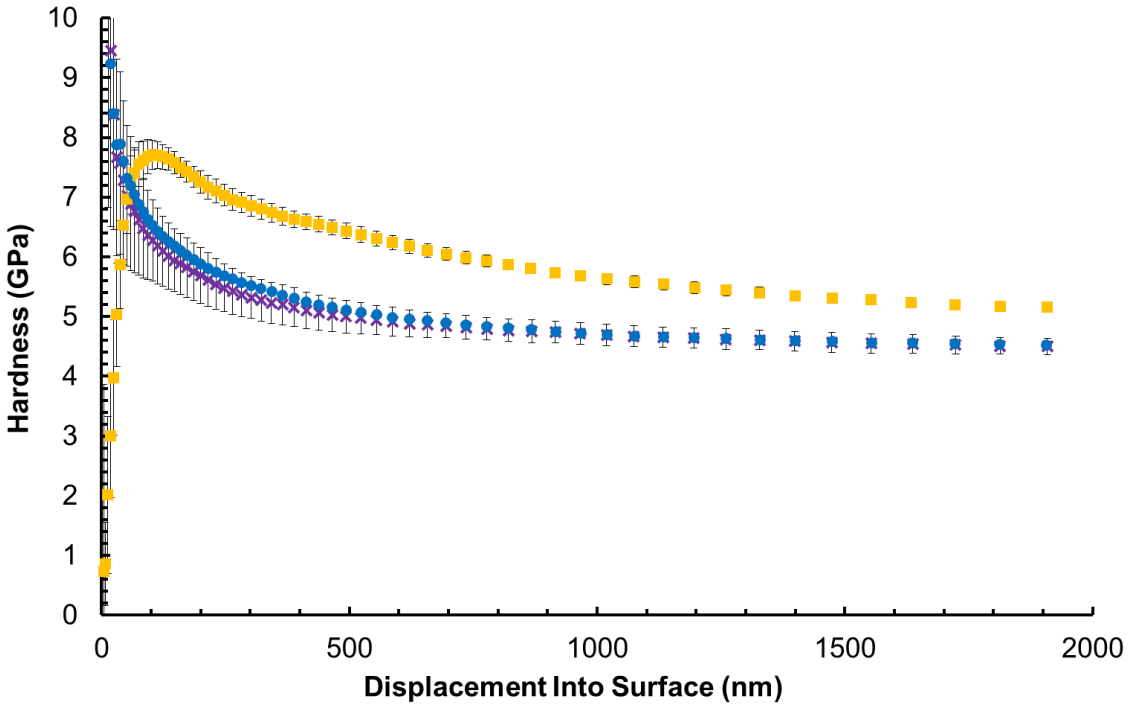

Figure 55 -EUROFER ODS – The ghost of a shoulder can just be seen.

Comparison of the materials in the 2000appm He condition (Figure 56) shows the spread of hardness at 400nm depth has decreased relative to the unimplanted material (Figure 50): unimplanted range (CEA ODS minus Fe-14wt%Cr) =2.68GPa; range at 2000appm He (CEA ODS minus EUROFER) =1.74GPa. Figure 57 shows that although the implantation of helium has a hardening effect on all the materials, the effect is greatest in the Fe-14wt%Cr which started with much lower hardness values in the unimplanted state.

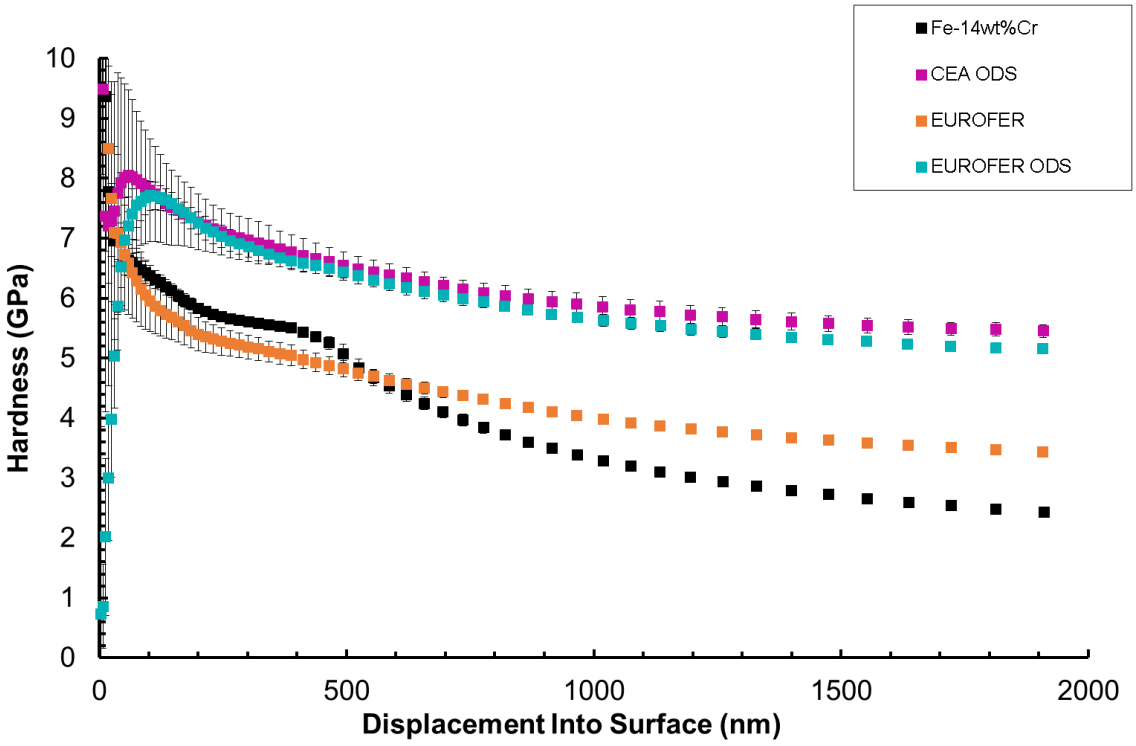

Figure 56 – Implantation of 2000appm helium increases the hardness of all the materials. The ODS materials are almost equivalent in hardness after implantation, and the non-ODS materials are almost equivalent in the region where the indentation plastic zone is within the implanted layer (~400nm).

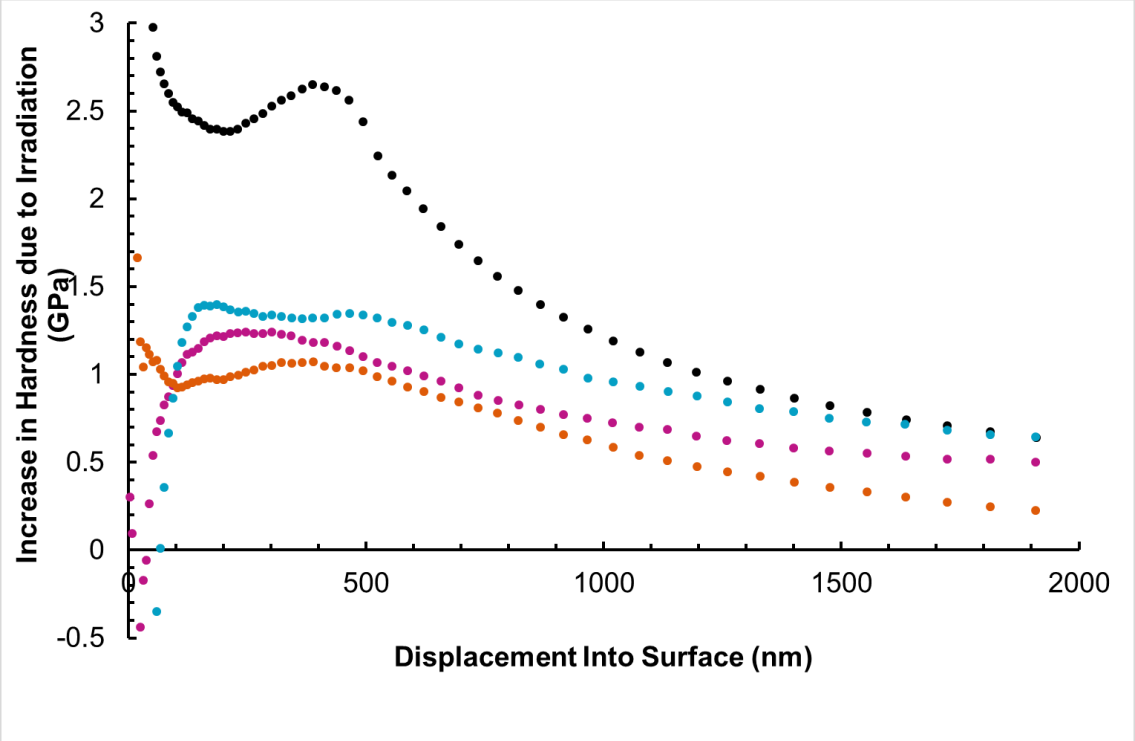

Figure 57 - Showing the increase in hardness due to implantation of 2000appm helium (2000appm He hardness with depth minus unimplanted hardness with depth for each material). Fe-14wt%Cr shows significantly higher hardening compared to CEA ODS, EURFOER ODS and EUROFER, which all show very similar hardening profiles with depth.

14.3 Helium + Iron Implanted Materials

The simultaneous dual-beam helium and iron implantation created 4.5dpa of damage and 2000appm of helium to a depth of 3.5μm (Figure 58) (Section 11.2.1).

Figure 59 to Figure 62 show that in the dual-beam implanted samples, the hardening effect of He is less than in the He-only implantation (numerical comparison in Table 7).

Table 7 - Increase in average hardness at 400nm depth (implanted minus unimplanted)

(GPa)	*Fe-14wt%Cr*	*CEA ODS*	*EUROFER*	*EUROFER ODS*
2000appm He	2.58	1.19	1.05	1.35
2000appm He + 4.5dpa Fe	0.45	0.24	0.40	0.69

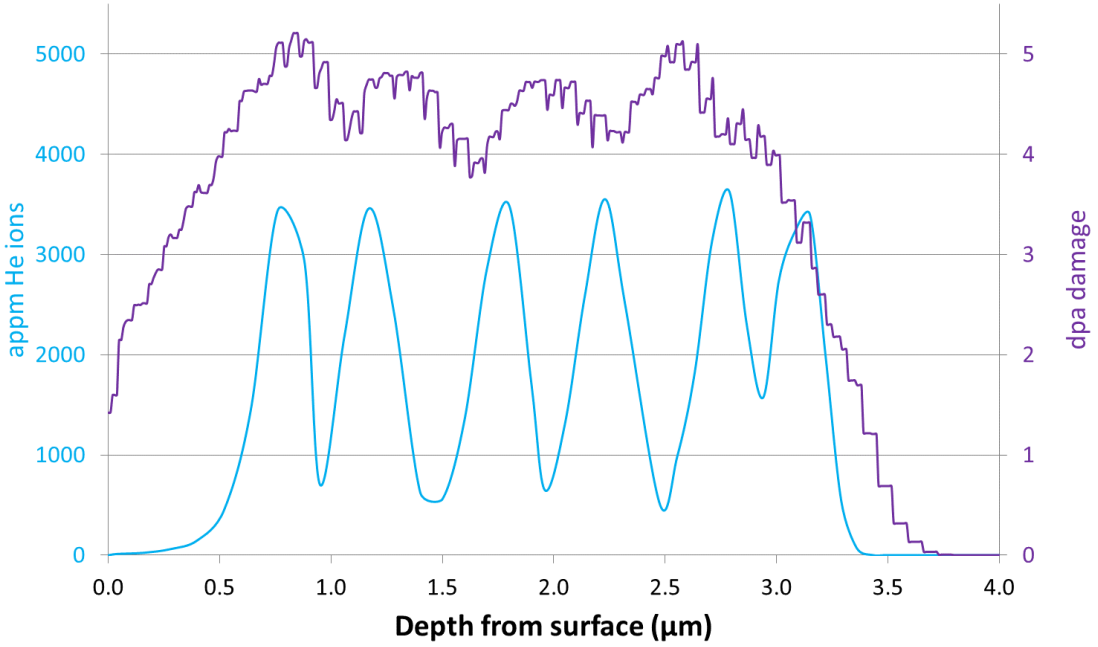

Figure 58 - SRIM calculated profiles of implanting ~2000appm He (blue) and ~4.5dpa Fe (purple) to ~3.5µm depth.

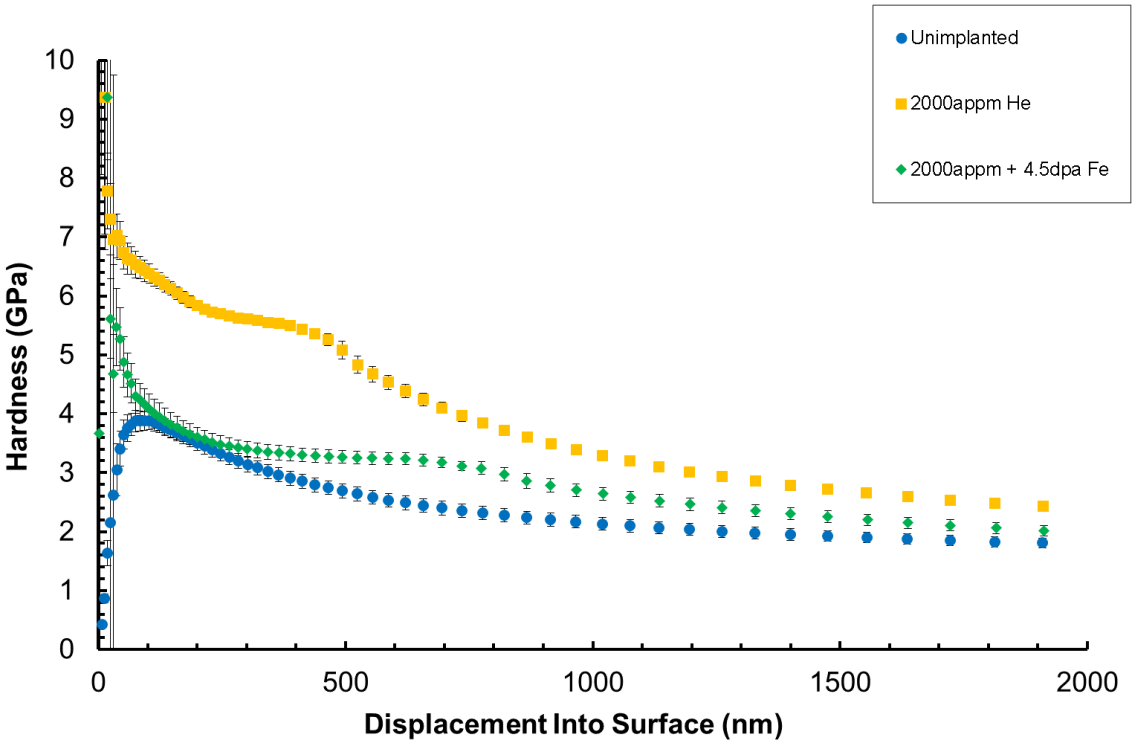

Figure 59 - Fe-14wt%Cr – The shoulder in the He+Fe results is deeper than in the He only implantation but shows less hardening effect.
Where the unimplanted and He+Fe data meet at 100-250nm depth is most likely due to size and surface effects in the unimplanted sample causing an error in measured hardness.

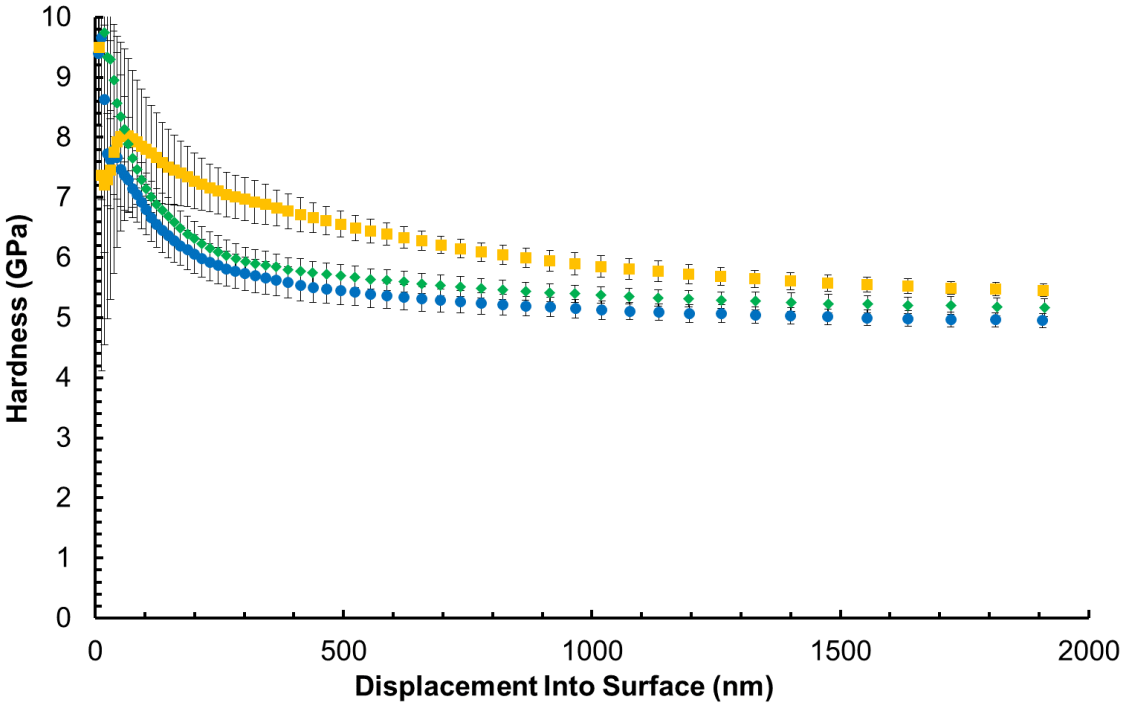

Figure 60 - CEA ODS – No visible shoulder in results. The He+Fe is consistently ~0.4GPa higher than the unimplanted hardness (and lower than the He only implantation).

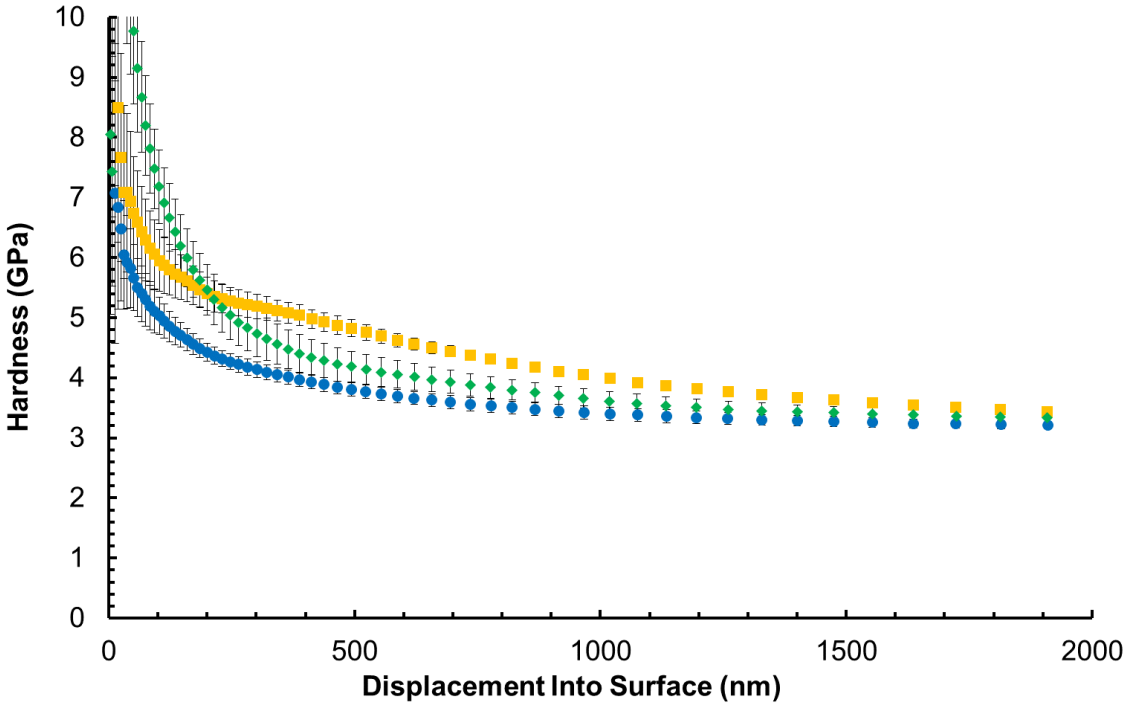

Figure 61 – EUROFER – A similar increase in hardness to the CEA ODS results, but with a more significant surface/size effect present in the He+Fe causing the rapid increase below 200nm.

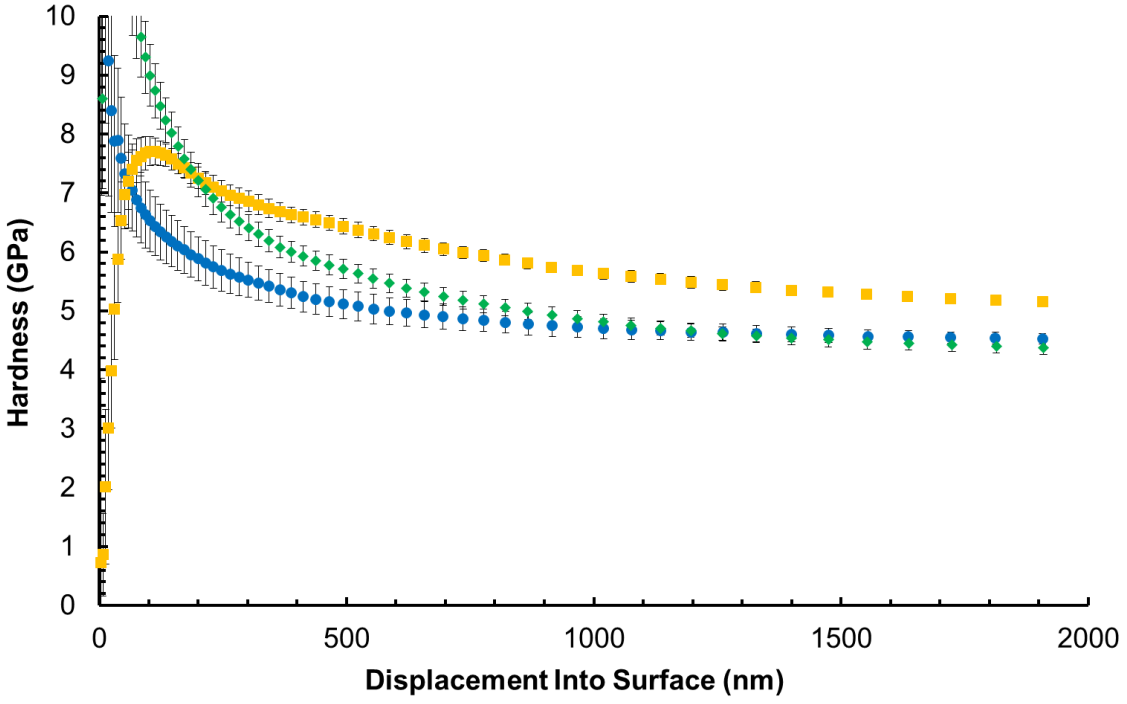

Figure 62 - EUROFER ODS – Very similar hardness trends to the EUROFER above.

14.4 Neon Implanted Materials

Neon was implanted so the samples could be chemically mapped to verify the implantation range (helium has too low an atomic mass to be detected and implanted iron is indistinguishable from the matrix material). Hardness tests confirmed that the effects on the material properties were analogous for helium and neon. Neon ions have a greater atomic mass than helium ions and therefore penetrate a shorter distance into the material lattice before coming to rest. These samples were implanted with 2000appm neon to 1.2μm depth (Figure 63).

The neon and helium implantations give very similar hardness increases (Figure 64 to Figure 67). The neon implantation is slightly harder near the surface. The neon hardness drops off earlier than the helium due to the shallower implantation depth. This is analysed further in Section 16.4.

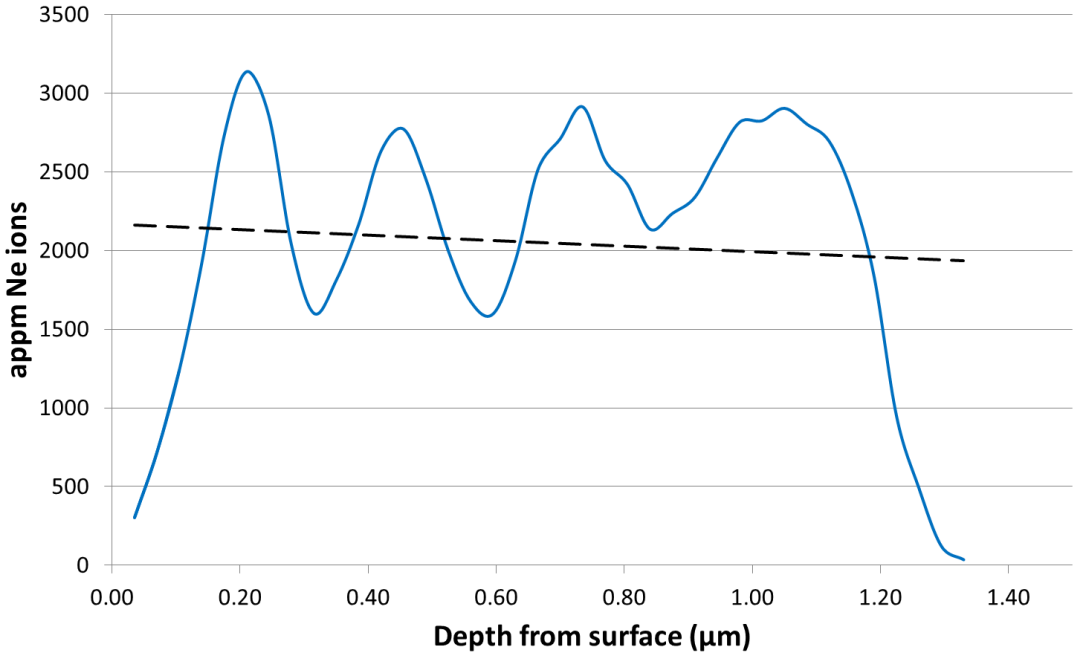

Figure 63 - SRIM calculated Ne concentration with depth

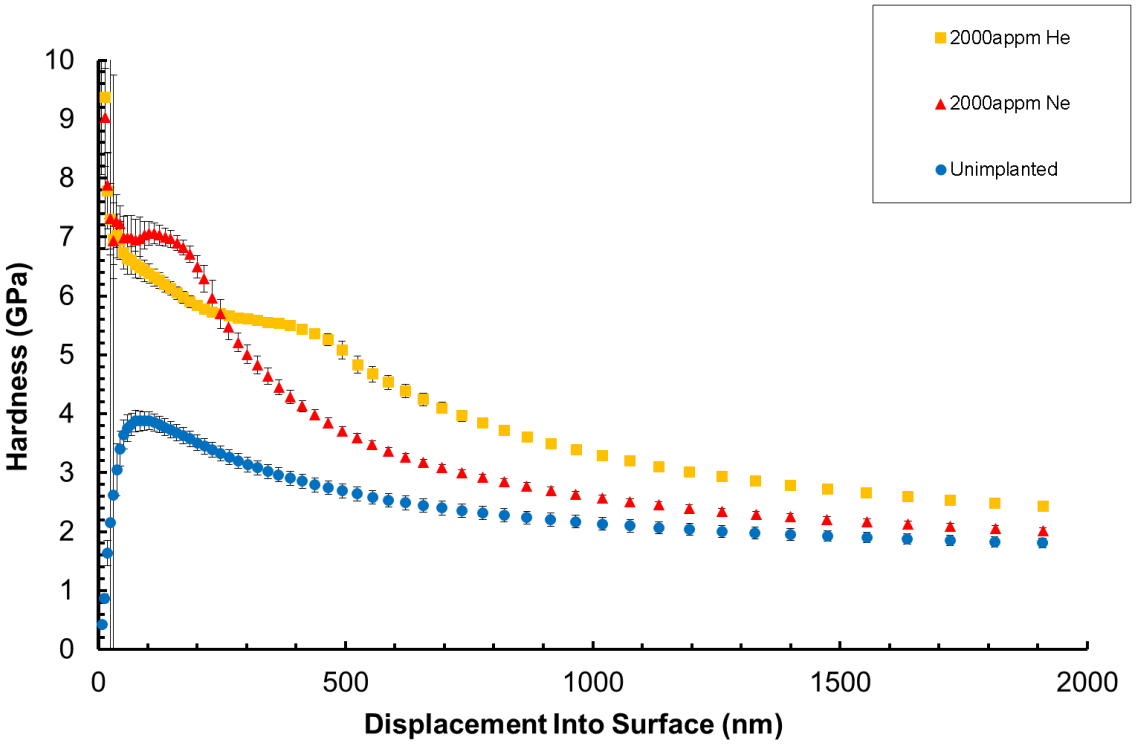

Figure 64 - Fe-14wt%Cr – The Ne implantation shows a similar shoulder to the He implantation, but at a lower depth (because the implantation depth was shallower) and at a higher hardness (neon implantation causes a greater dpa/appm) .
The steeper drop off of the neon hardness is discussed in Section 16.4.

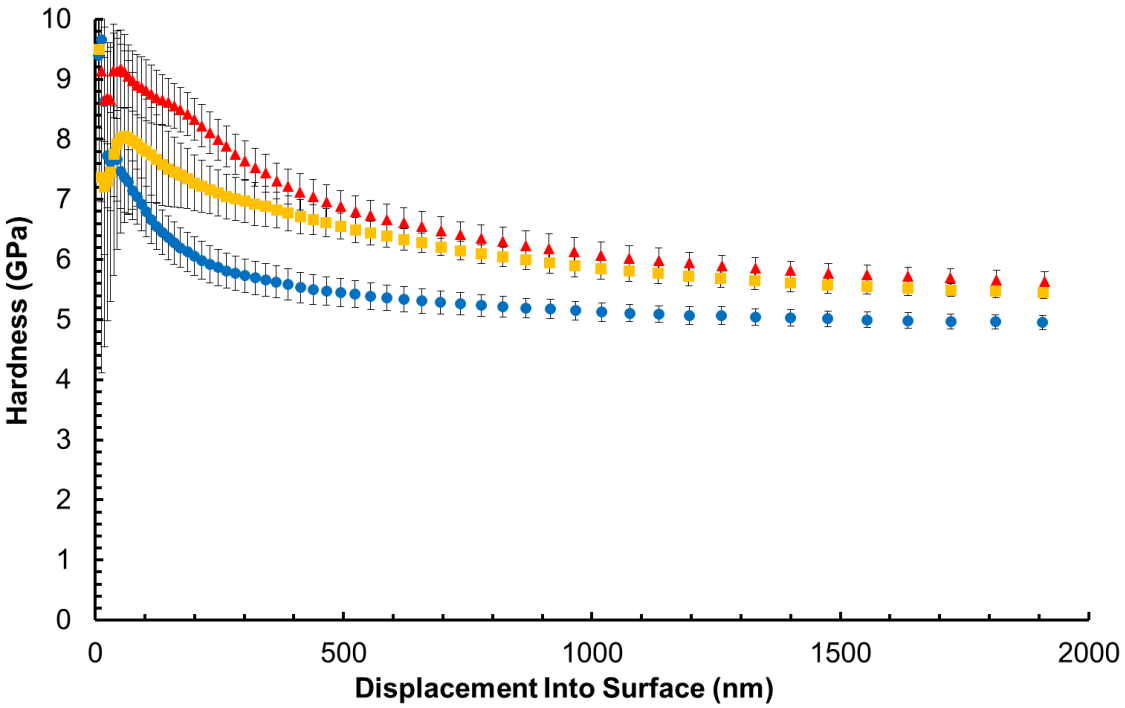

Figure 65 - CEA ODS – The higher hardness and steeper drop off are similar to the Fe-14wt%Cr.

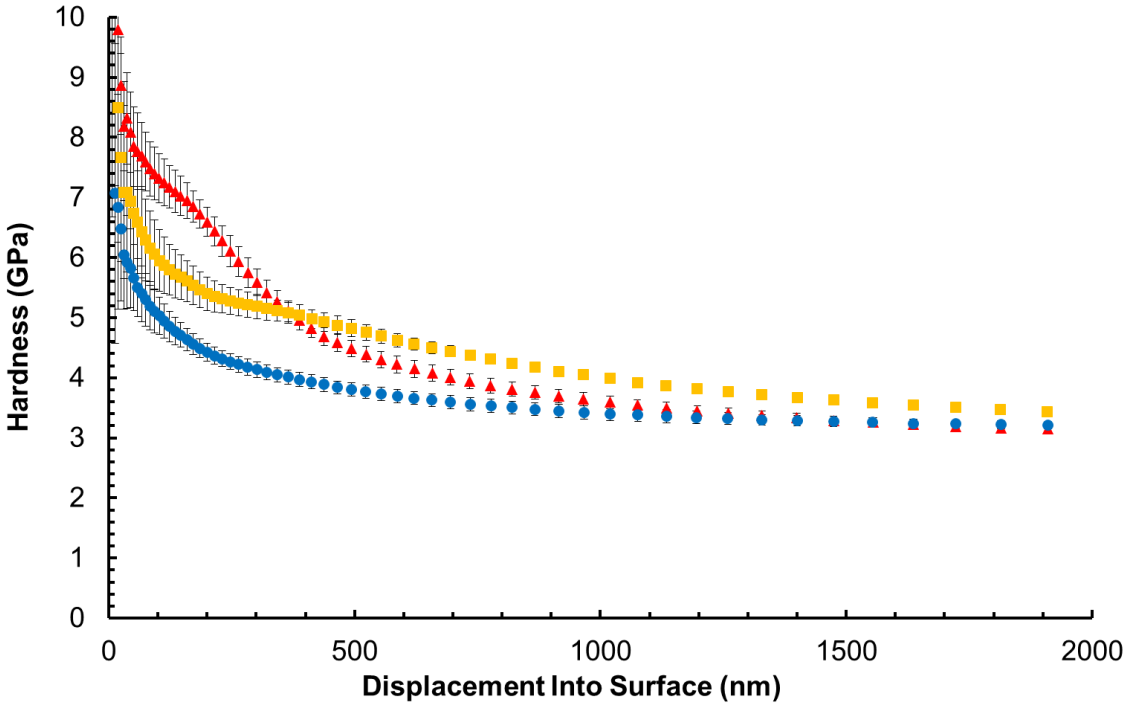

Figure 66 – EUROFER

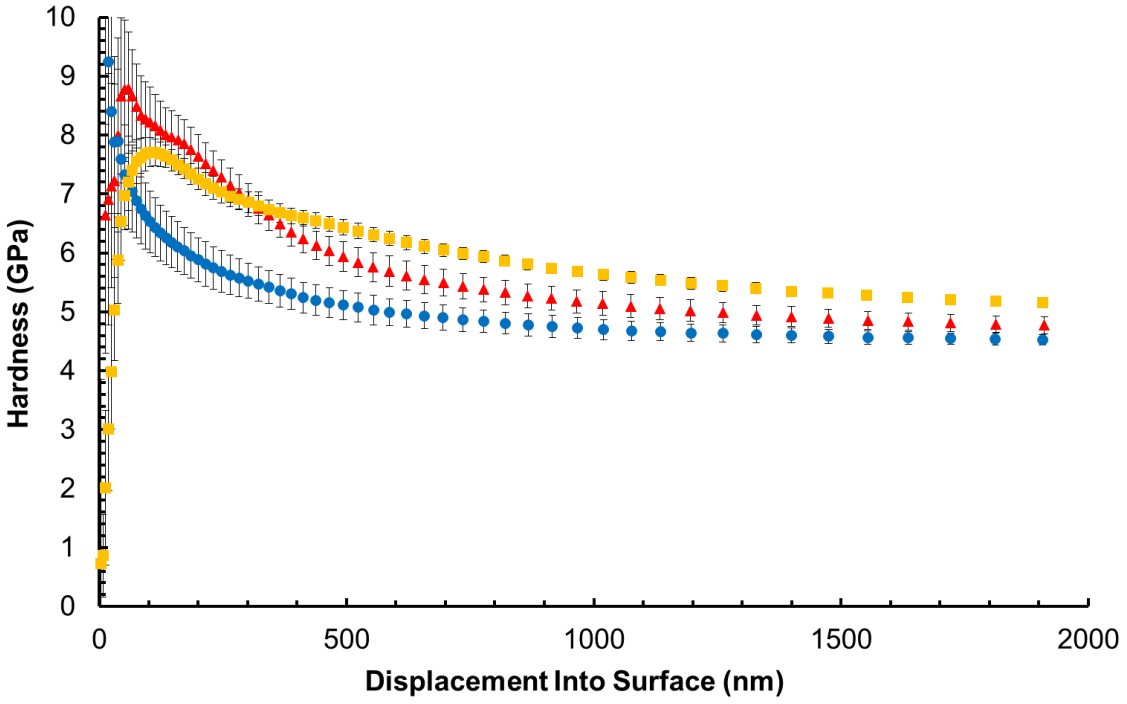

Figure 67 - EUROFER ODS

15 Microindentation

To extend the load/depth range of the nanoindentation results, microscale Vickers Hardness testing was performed on unimplanted samples of each material using a Matsuzawa Seiki Micro Hardness Tester (MTH-1) with loads of 25, 50, 100, 200, 300 and 500g and a load hold time of 10 seconds. Six indentations were made at each load in each sample and the diagonal lengths of all indentations were measured by optical microscopy (Figure 68).

Vickers Hardness is calculated using the following Equation 1 [156]:

Equation 1

$$H_v = \frac{Applied\ load\ (kgf)}{Contact\ area\ of\ indenter\ (mm^2)}$$

$$= \frac{P\ 2sin\,\theta/_2}{d^2}$$

$$= 1.8544\ \frac{P}{d^2}$$

Where:

H_v = Vickers Hardness (kgf/mm^2)

P = applied load in kilograms-force (kgf)

θ = indenter tip angle (136°)

d = measured length of indentation diagonal (mm)

This gives a value of Vickers Hardness in kg/mm^2. For comparison with nanohardness results it can be converted to megapascals by multiplying by gravitational acceleration (9.80665 ms^{-2}) and becomes Equation 2:

Equation 2

$$H_{v\,(MPa)} = 18.1855\ \frac{P}{d^2}$$

Both diagonals were measured on each of the six indentations of each load in all materials, and the twelve results for each were averaged. Using Equation 1 and 2, they were converted to Vickers Hardness in both kgf/mm^2 and MPa (example data of the hardnesses measured using a 200g load – Table 8).

The circular points in Figure 69 indicate hardness measured by nanoindentation – the square points joined by lines indicate the microhardness testing data. Error bars show the range (max. to min.) of measured hardness. The error bars on the microhardness data have a wide variation because the optical measurement relies on a subjective assessment of the position of the corners of each indentation.

The microhardness data points lie at different depths in each material because the same load will produce different depth indentations in each material (depending on the material hardness). The depth was calculated as $^1/_7{}^{th}$ the average diagonal length of the indentations.

Figure 69 shows good correlation between nano- and microhardness indentation test results, although the microhardness data for CEA ODS, EUROFER and EUROFER ODS would not follow a hardness projection from the nanoindentation data.

Table 8 - Vickers Hardness of all unimplanted materials at 200g (average of six indentations)

Vickers Hardness	***Fe-14wt%Cr***	***CEA ODS***	***EUROFER***	***EUROFER ODS***
kgf/mm²	127	404	247	373
GPa	1.25	3.96	2.42	3.66

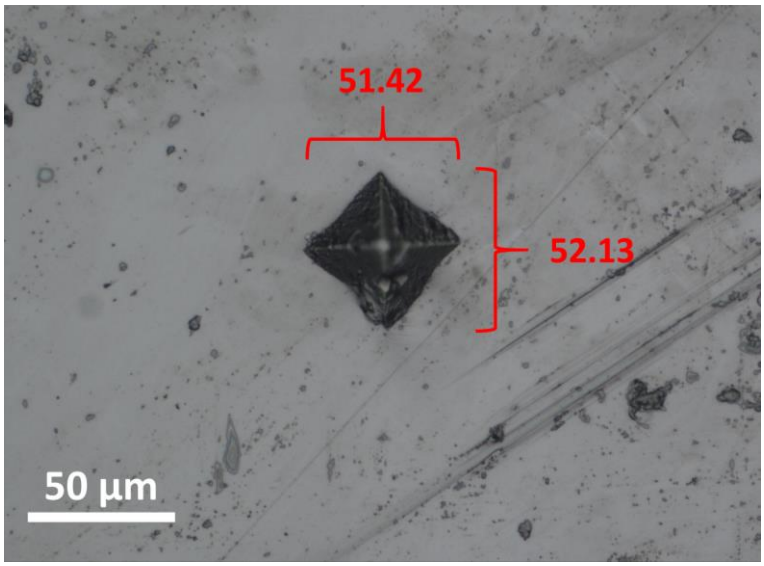

Figure 68 - Vickers Hardness indentation in unimplanted Fe-14wt%Cr showing measurements used to determine hardness of the specific indentation.

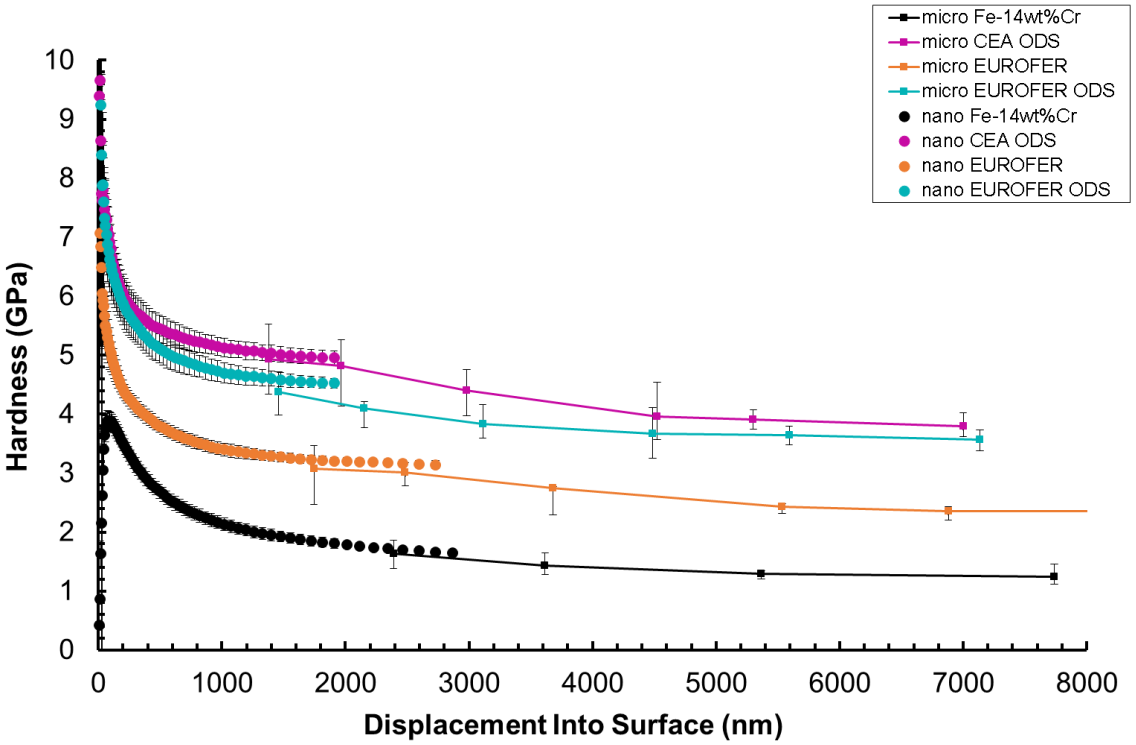

Figure 69 - Hardness data with depth for all unimplanted materials showing nano- and microindentation data. Note that the CEA ODS, EUROFER and EUROFER ODS microhardness data would deviate from a projection of the nanohardness curve, although there is a good correlation in the hardnesses measured in the region where micro- and nanohardness data overlap.

16 Discussion

For deep indentations in any one material, all hardness values for irradiated and unirradiated samples converge as the plastic zone of indentation usually extends to approximately seven times indentation depth [150]. Thus, if the indentation depth is <14% of damage depth the hardness recorded will be representative of the implanted material. If >14% of the damaged depth it will also include contributions from the substrate/bulk hardness [26].

In all the 2000appm He and 2000appm Ne graphs (most noticeable in the Fe-14wt%Cr samples - Figure 64) the implanted lines have a shoulder in the curve (at ~450nm depth in the helium implantations and ~200nm in the neon implantation). The drop in hardness at this point is likely to correspond to the depth at which the plastic zone is expanding out of the implanted layer into the unimplanted bulk material below. Above this depth the hardness values are representative of the implanted layer.

Figure 70 collates the hardness data for all materials in all implantation conditions. The He and He+Fe implantations were ~3μm in depth, therefore the hardness of each sample was recorded at 400nm depth to ensure that any effects of the implantation were accounted for. For the neon implanted samples, hardness was measured at 120nm depth as the implanted layer was shallower (N.B. this difference in depth means a size effect will be present). Figure 71 displays the change in hardness due to each implantation compared with the unimplanted hardness of each material, (the 75appm He samples have been excluded as they all showed insignificant hardening).

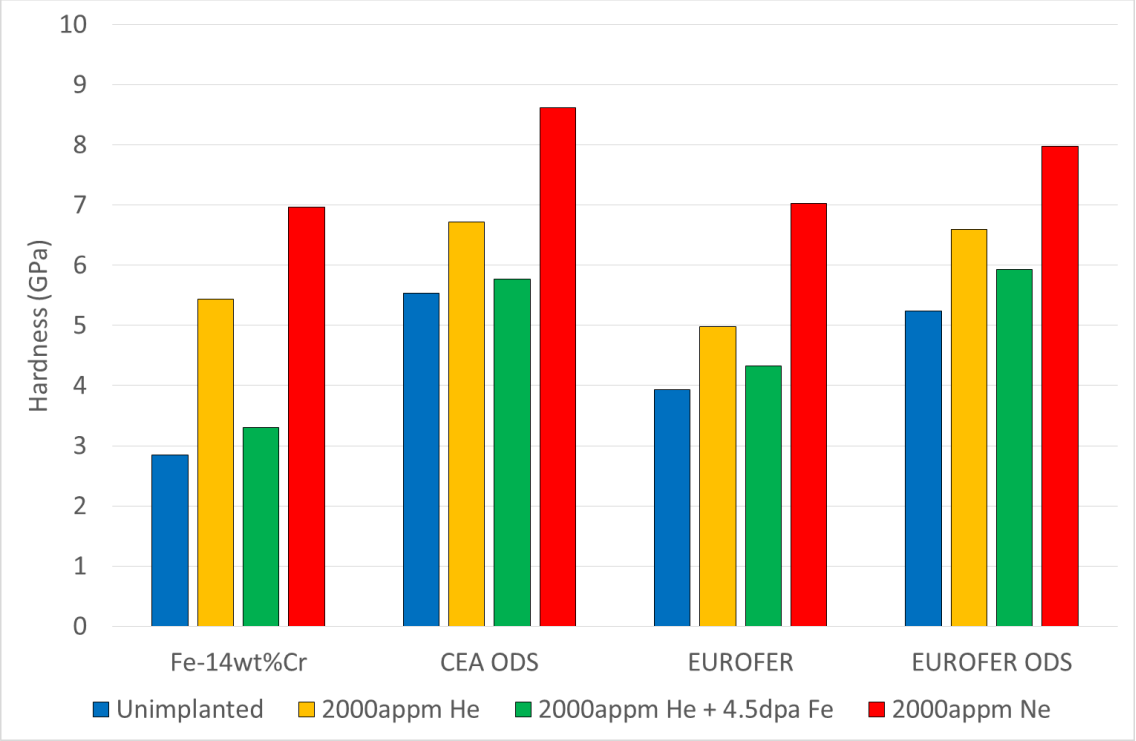

Figure 70 - Hardness for all materials in all implantation conditions (Unimplanted, He and He+Fe measured at 400nm depth, Ne measured at 120nm depth).

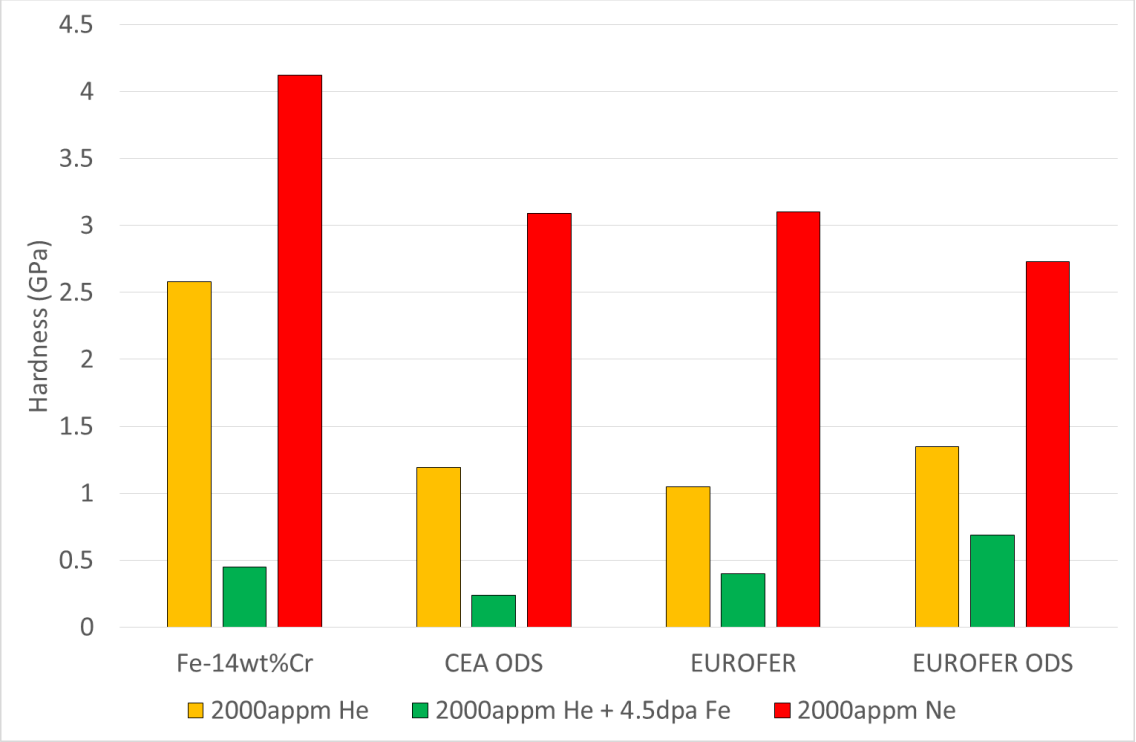

Figure 71 – Hardening effect of each implantation. Increase from the unimplanted value.

16.1 Unimplanted Materials

There are distinct differences between the baseline hardness of the four materials. Fe-14wt%Cr alloy is a high purity, large grain size material; there are very few disruptions to dislocation motion within the lattice. Each indentation will be within one grain or near a single grain boundary, so very little grain boundary effect is seen in the hardness. The other three materials have much smaller grain sizes (~2-5μm); there is an immediate effect on the hardness from grain boundary interaction with dislocations. The effect of grain size on the hardness and yield strength can be characterised using the Hall-Petch Relationship [157][158]. In addition to grain size effects, the other materials contain various precipitates which act as additional restrictions to dislocation motion. Dislocations must either bow round or cut through the particles to move through the matrix. The contributions to hardening (including grain size and precipitate content) will be analysed in the final discussion (Chapter 7).

Although the nanoindentation hardness data appear to reach a plateau by 2000nm depth, testing with deeper indentations using microhardness shows that it is only beyond 6000nm depth that the hardness has reached a flat limit (Figure 69). There is still a slight angle on the CEA ODS and EUROFER ODS lines beyond ~5000nm, but this is within the measured hardness range and more closely spaced data points would be needed to establish whether there is still a size effect. The hardness tester used does not allow for loading increments smaller than those used in this test. The Vickers Hardnesses below (Table 9) were recorded at 7000nm depth, so are representative of the bulk material hardness.

Table 9 - Unimplanted material hardness tested by microhardness indentation at 7000nm depth.

(MPa)	*Fe-14wt%Cr*	*CEA ODS*	*EUROFER*	*EUROFER ODS*
Vickers Hardness at 7000nm depth	1270	3790	2350	3560

16.2 Helium Implanted Materials

All the materials show a significant increase in hardness when implanted with 2000appm He (Figure 71). Fe-14wt%Cr shows the biggest increase (approximately twice that in the other three materials - Table 10).

The hardness increases are due to the helium creating and filling defects in the lattice, so restricting dislocation motion. As helium is implanted, it is most likely to initially fill irradiation-induced vacancies and create point defects in the ferritic matrix. As the concentration increases, the point defects will grow into defect clusters as they collect helium. Above a critical concentration, these helium clusters will grow into bubbles which can cause significant hardening. In iron alloys, hardness results indicate that this concentration is >100appm helium [145]. In previous experiments on similar materials [102], at 2000appm helium, where significant hardening occurs, a bubble population can be seen with TEM.

In ODS materials, the oxide nanoparticles provide low energy locations for the helium to collect and form fine, well dispersed bubbles [159]. This reduces the density of large dislocation motion retarding bubbles and therefore reduces the hardening effect in the material. The hardening effect of a nanoparticle with associated bubbles is almost equivalent to that of a nanoparticle without bubbles, so the extra helium would not be expected to add hardening. The particles also reduce the amount of helium migrating to the grain boundaries, thereby reducing any grain boundary embrittlement.

Table 10 - Increase in hardness at 400nm depth from unimplanted to 2000appm He

(GPa)	*Fe-14wt%Cr*	*CEA ODS*	*EUROFER*	*EUROFER ODS*
2000appm He	2.58	1.19	1.05	1.35

16.2.1 Modelling of Hardness Variation with Depth

Coating and chemically or mechanically altering surface layers to change surface properties is widely used in many applications. These generally increase surface hardness while the core remains relatively soft, enabling components to withstand high fatigue and stress. It is important to know the hardness of the surface layers and how that changes with depth into the bulk material. Bull investigated the hardness response of materials during indentation [160][161][162] and produced the following model for predicting hardness with depth.

The volume of material being plastically deformed by an indenter tip is known as the plastic zone and is assumed to be roughly hemispherical spreading from the surface point of indentation. While the plastic zone is contained within the surface layer, the hardness measured is that of the surface layer. When the plastic zone depth exceeds the layer thickness, both surface layer and substrate contribute to the measured hardness.

Bull provides this equation for calculating the total hardness measured when the radius of the plastic zone is greater than the thickness of the surface layer [161].

$$H = \left(\frac{3t}{2R} - \frac{t^3}{2R^3}\right) H_0^B + \left(1 - \frac{3t}{2R} + \frac{t^3}{2R^3}\right) H_0^S + \frac{3\gamma_s}{2R} + \left(\frac{3}{2R} - \frac{3t^2}{2R^3}\right) \gamma_i$$

H = total hardness
t = thickness of surface layer
R = radius of plastic zone
H_0^B = hardness of bulk material
H_0^S = hardness of surface layer
γ_s = surface energy
γ_i = surface layer/bulk interface energy

This surface coatings model can be applied to chemically or mechanically altered surface layers, including ion implantation, if we approximate that the implanted layer has uniform hardness with depth. The main difference with an implanted layer will be that there is no physical surface/bulk interface, therefore the γ_i component of the equation $\left[\left(\frac{3}{2R}-\frac{3t^2}{2R^3}\right)\gamma_i\right]$ can be disregarded.

With the implanted layer, while we have no way of directly measuring the surface energy component of the hardness, the measured hardness already includes its effects. Therefore, the γ_s component of the equation $\left[\frac{3\gamma_s}{2R}\right]$ is already accounted for in the measured H_0^S. Thus the equation becomes:

$$H=\left(\frac{3t}{2R}-\frac{t^3}{2R^3}\right)H_0^B+\left(1-\frac{3t}{2R}+\frac{t^3}{2R^3}\right)H_0^S$$

The value of t is fixed as the depth of the implanted layer, in the 2000appm He implantation this is ~3μm. The bulk hardness (H_0^B) can be taken as the unimplanted hardness at a depth well out of range of significant size effects (e.g. ~7000nm). The surface layer hardness (H_0^S) can be taken from the data where the plastic zone is entirely within the implanted layer. It is generally assumed that the plastic zone of indentation in metals extends to approximately seven times the depth of indentation [150]. In the helium implanted materials, for the plastic zone to be within the implanted layer of 3000nm, the indentation needs to be <430nm deep. The H_0^S value needs to be an accurate representation of the average hardness of the implanted layer, and therefore needs to avoid significant size effect complications (so should be taken as deep as possible), whilst avoiding issues of the surface layer fading into the bulk material (more common in chemical and mechanical surfacing than with coatings). To allow for uncertainty in the depth of the implanted layer, H_0^S for the 2000appm He materials was taken as the hardness at ~300nm depth.

Figure 72 shows experimental and predicted hardness values for Fe-14wt%Cr, CEA ODS, EUROFER and EUROFER ODS implanted to 3μm depth with 2000appm He. All the curves converge to their respective baseline hardness near 2000nm depth.

The predicted lines for each material follow the shape of the measured implanted hardness curve, but at consistently higher values (Fe-14wt%Cr ~+0.8GPa; CEA ODS, EUROFER and EUROFER ODS ~+0.4GPa); i.e. the model used predicts a greater effect of surface layer on the hardening once the plastic zone moves into the bulk. The adapted model used for these predictions includes the surface energy term in the hardness of the surface layer.

To find a better fit, the model was adapted: a surface energy term was added (nominal value 2) and the surface layer reduced from 7 to 6GPa. Then for CEA ODS, the slope of the predicted curve more closely fit the measured hardness curve (Figure 73). The over-prediction can be attributed partly to indentation size effects. Figure 72 shows the unimplanted in all cases predicted as a flat horizontal line, but the experimental results show significant size effect (hardness increasing at low indentation depth). To accurately predict the implanted layer hardness the model should be adapted to take this into account with H_0^S changing with depth.

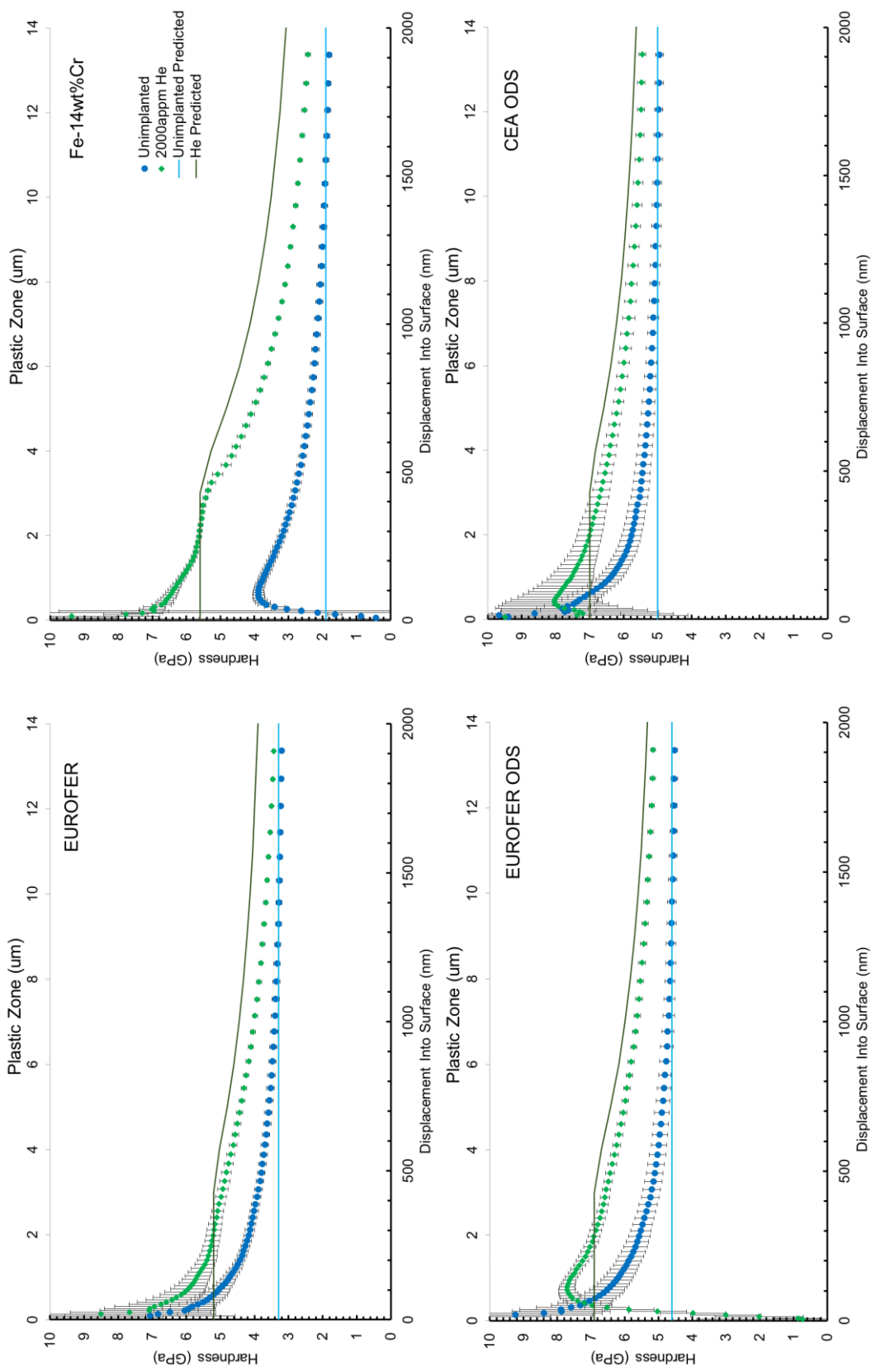

Figure 72 - Fe-14wt%Cr, CEA ODS, EUROFER and EUROFER ODS implanted with 2000appm He, experimental microhardness and predicted results using Bull's model to determine the effects of a hard surface layer and plastic zone size.

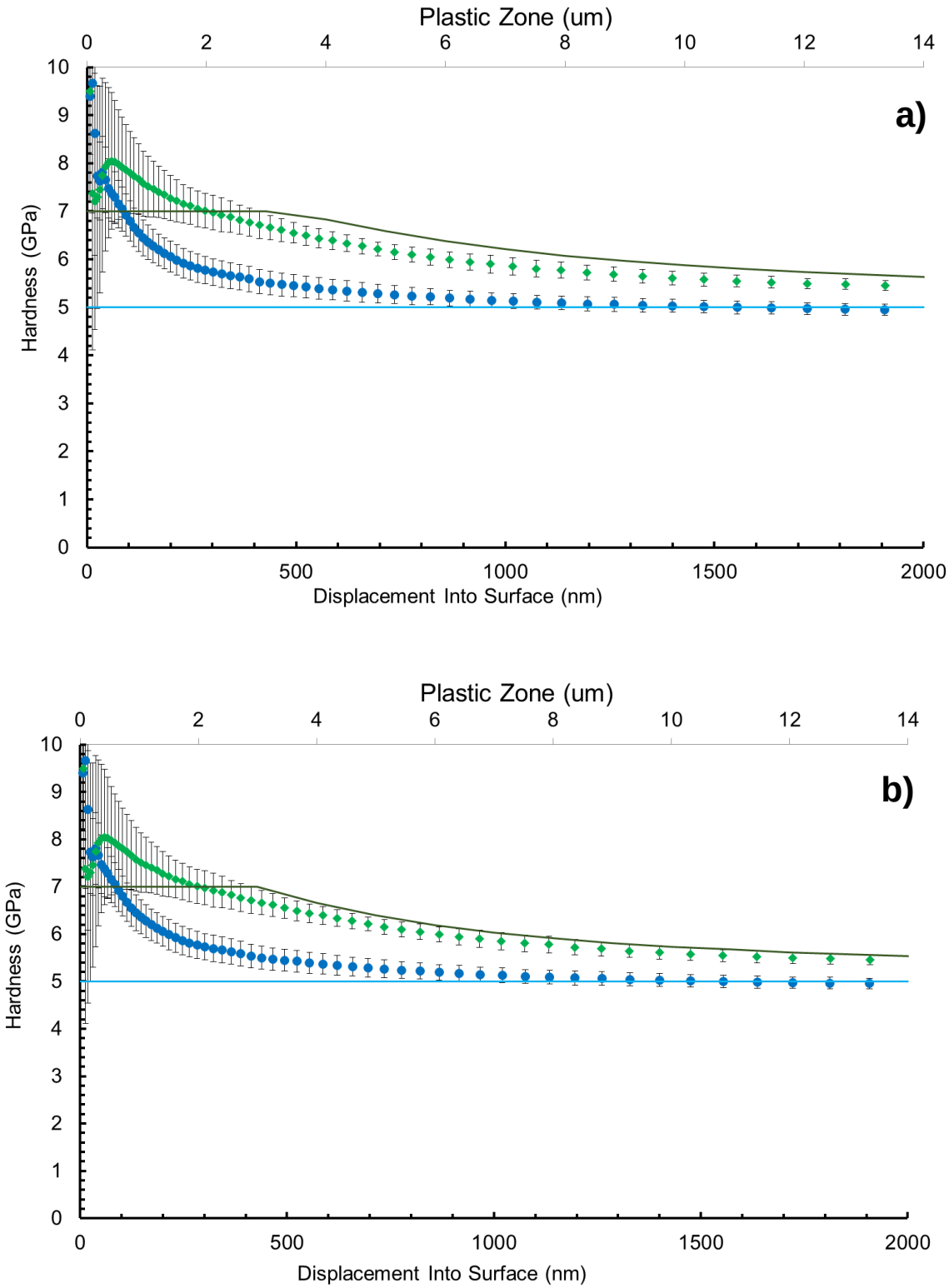

Figure 73 - CEA ODS experimental and predicted hardness values for 2000appm He implantation.
a) original model values
b) using adapted surface layer hardness and surface energy to find a better implanted curve fit

16.2.2 Pop-ins and Strain Bursts

The phenomenon of Pop-ins is attributed to dislocation nucleation and propagation relieving strain beneath the indenter tip during the loading phase of nanoindentation [163]. A characteristic pop-in appears as a small displacement jump (<50nm) at low indentation depth (<100nm) and low load (<1mN). Plastic deformation prior to a pop-in is associated with individual movement of a few newly nucleated or previously existing dislocations [162][163]. The indentation increases the local number of dislocations, causing them to entangle and pin. At a threshold stress, a burst of dislocation movement will occur – this is seen as a pop-in [163].

No true pop-in events appeared in the tested materials. However, small strain bursts can be seen in the load-displacement curves of the implanted specimens. These look very similar in load and displacement size to pop-ins. Figure 74 shows a selection of the load-displacement curves from the Fe-14wt%Cr 2000appm He hardness indentations. At a depth of ~500nm a kink can be seen in each curve. Figure 75 magnifies the kinked section: each line has a ~25nm strain burst at around 480-500nm displacement.

Pop-ins are usually associated with the initiation of dislocations at very shallow indentation depths. At 500nm depth, the plastic zone of the nanoindentations begins to penetrate the bulk material. The bulk material has fewer dislocations (no irradiation-induced lattice damage), so this observed strain burst is likely to be nucleation or rapid expansion of dislocations in the unimplanted material on the edge of the plastic zone. Dislocation loop expansion is held back by the implanted layer, but can balloon out once the dislocations reach the bulk.

This phenomenon was observed in the 2000appm He and 2000appm He + 3.5dpa Fe materials at ~500nm depth and in the 2000appm Ne at ~200nm corresponding with the plastic zone extending into the unimplanted bulk.

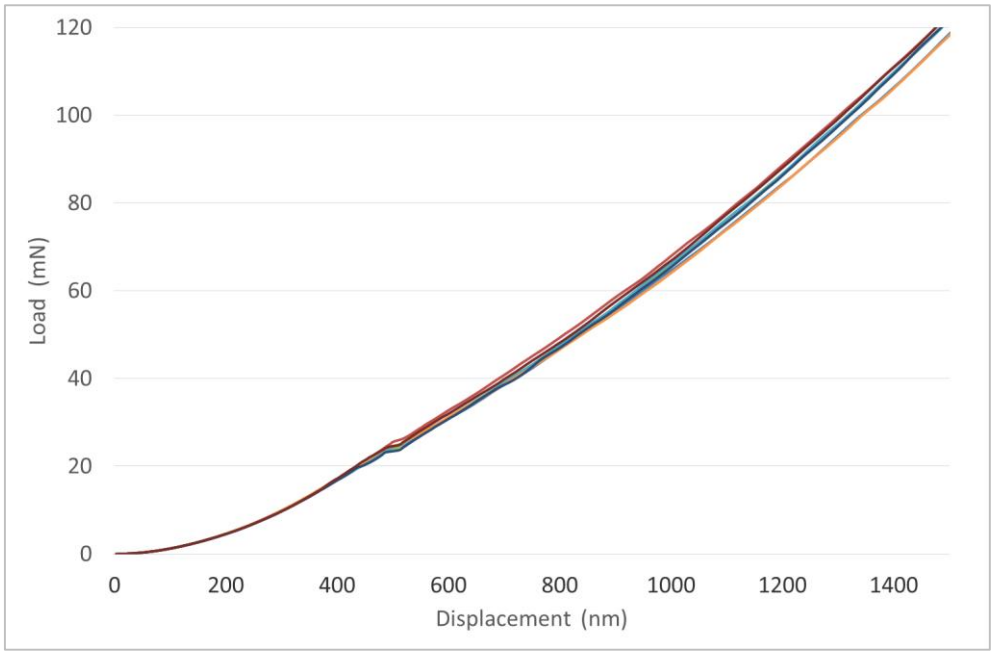

Figure 74 - Load-displacement curves for individual indentations in Fe-14wt%Cr 2000appm He.

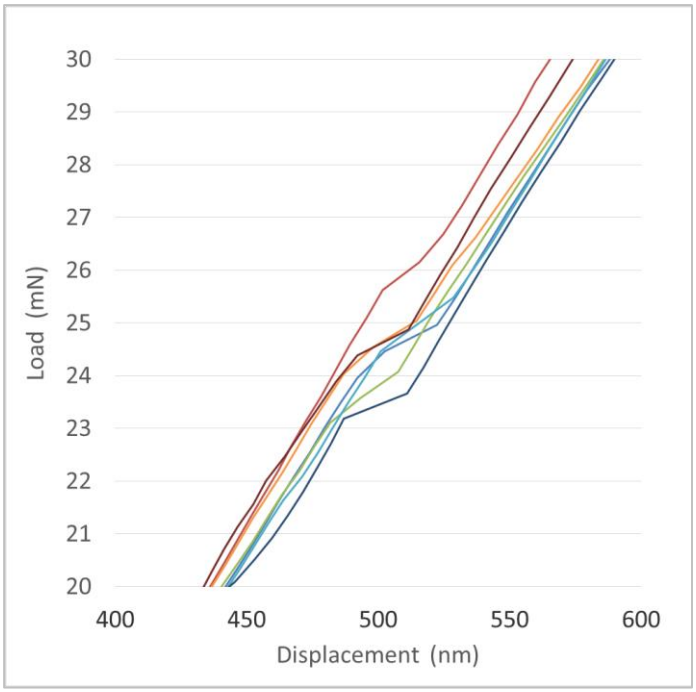

Figure 75 - A magnified section of Figure 74 showing strain burst events in Fe-14wt%Cr 2000appm He.

16.3 Helium + Iron Implanted Materials

The simultaneous implantation of helium and iron into the samples causes an increase in hardness, which is less than that of the single beam helium to the same concentration (Table 11).

Implantation of Fe ions causes residual point defects and prismatic dislocation loops [23]. A possible explanation for the decreased hardening in the dual-beam experiment (compared with the helium alone) is that the implanted helium is attracted to these extra defects, so there is less spread throughout the lattice to form bubbles and to cause hardening.

To confirm this hypothesis, a closer look with TEM is required. This will be discussed in Chapter 6.

Table 11 - Increase in hardness from unimplanted to 2000appm He + 4.5dpa Fe

(GPa)	*Fe-14wt%Cr*	*CEA ODS*	*EUROFER*	*EUROFER ODS*
2000appm He	2.58	1.19	1.05	1.35
2000appm He + 4.5dpa Fe	0.45	0.24	0.40	0.69

16.4 Neon Implanted Materials

In all materials, the increase in hardness due to neon implantation starts higher than that induced by helium implantation, then rapidly drops to approximately the same level as the 2000appm He implantation at ~300nm depth. To compare numerically the hardness increase of the helium and neon implantations, the hardness at a depth of 120nm was recorded for all materials (Figure 77). This depth was chosen (rather than the 400nm used in Figure 71), because the neon implantation was only ~1.2μm deep. Accounting for a plastic zone of seven times indentation depth, the hardness at 120nm depth is only testing implanted material. At this shallow depth, however, significant size effects apply, and therefore the helium result must be recorded at the same depth where it will be subject to the same size effect.

As shown, the neon implantation caused a larger increase in hardening than the helium, despite using the same appm for both implantations. One potential explanation for this is that neon ions have a larger atomic mass than helium and therefore greater energy transfer occurs during collisions in the lattice. This leads to a greater damage per appm implanted (helium: ~$1x10^{-4}$ dpa/appm; neon: ~$1x10^{-3}$ dpa/appm). The higher displacement damage leading to an increase in instantly formed bubbles may explain the increased hardness of the neon implanted sample compared with the helium implanted sample. The hardness model in Section 16.2.1, was also applied to the neon results. As with the helium, it gave an accurate prediction of the location and angle of the hardness shoulder.

Aside from the increased hardening effect, the hardness with depth profile shape and response to implantation is sufficiently similar between the helium and neon implantations that it is a reasonable indication that that neon is distributed within the matrix in a similar way to helium. Therefore neon implanted samples should be suitable

for chemical mapping of the implanted ion distribution. Further work on this distribution in the neon implanted materials can be found in Chapter 6, Section 29.

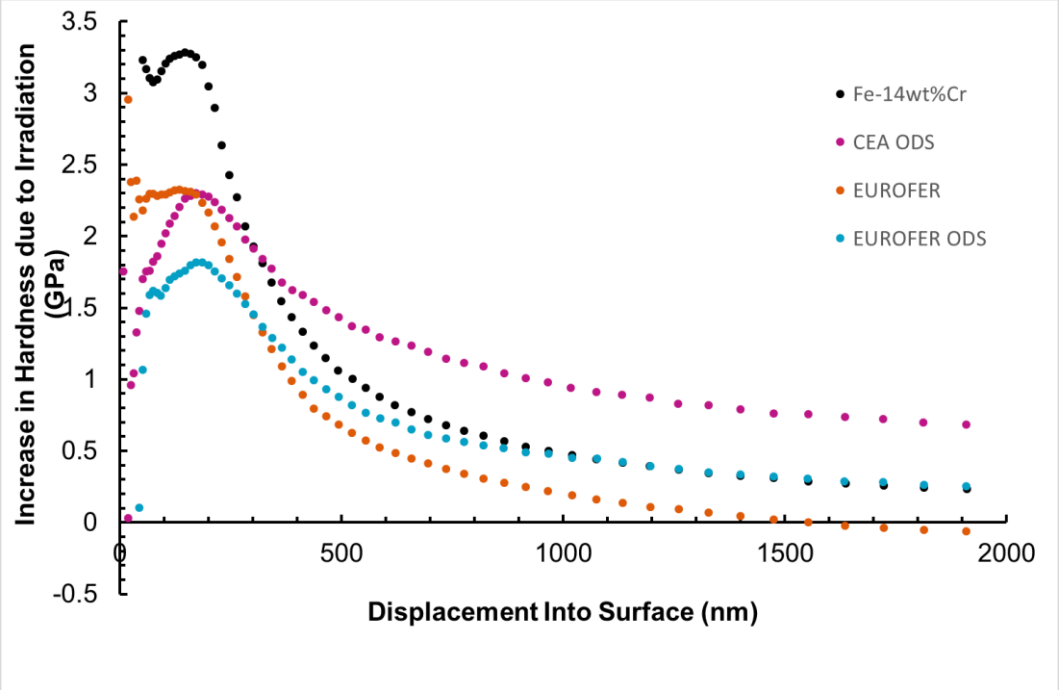

Figure 76 - Showing the increase in hardness due to implantation of 2000appm neon. 2000appm Ne hardness with depth minus unimplanted hardness with depth for each material. Note the similarity with the equivalent helium graph - Figure 57.

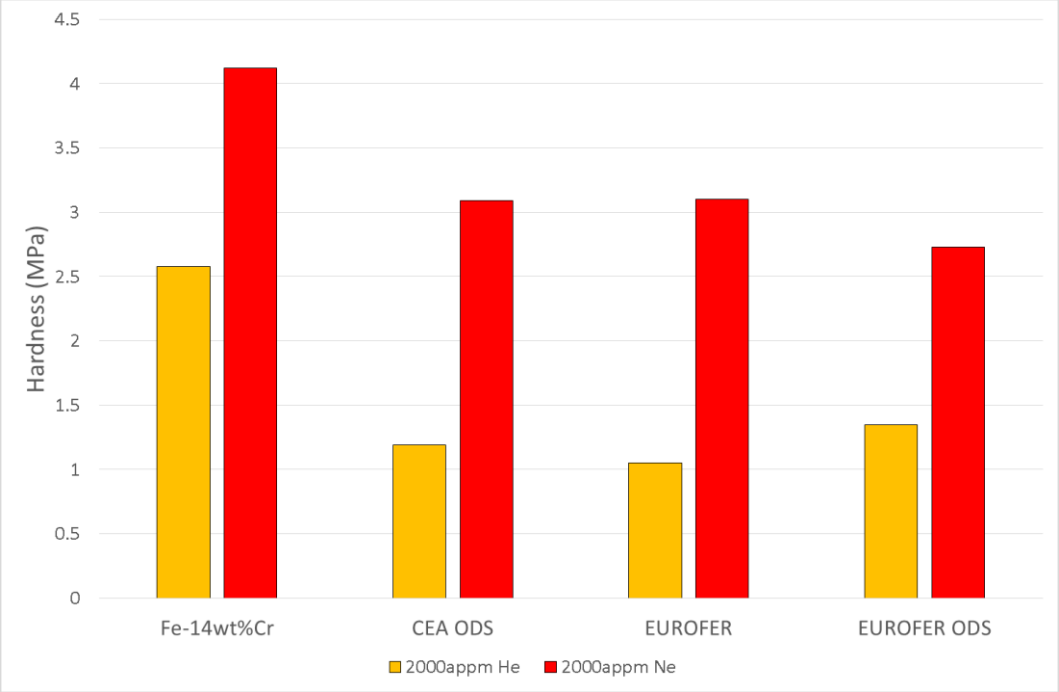

Figure 77 - Increase in hardness at 120nm depth from unimplanted due to helium and neon implantations.

17 Summary

Implantation of ions into a material surface causes damage to the lattice structure. It introduces defects such as vacancies, interstitials, and dislocation loops. These affect dislocation motion through the lattice, which manifests itself as a hardening effect. The measured hardness and change in hardness with implantation are recorded for all materials and implantations in Table 12 and Table 13.

At low dose (below the bubble forming concentration, 75appm He – Section 14.2), there is little hardening, but at high dose (2000appm), implantation of a single species of ion (helium or neon, Section 14.2 and 14.4 respectively) causes significant hardening. Simultaneous implantation of helium and iron also has a hardening effect, but this is less than the single ion implantations. The implanted iron causes greater lattice damage than the lower mass He and Ne. One possibility is that the simultaneously implanted helium fills these defects instead of forming bubbles, therefore removing one of the hardening mechanisms.

In order to investigate these hardening effects further, the microstructure of each material in each implantation needs to be closely examined. FIB-cut cross-section lift-outs have been made for TEM analysis. Full details can be found in Chapter 6.

Table 12 – Measured hardness (GPa) with changing depth and implantation

		Unimplanted	*75appm He*	*2000appm He*	*2000appm He + 4.5dpa Fe*	*2000appm Ne*
Fe-14wt%Cr	***120nm***	1.55	n/a	6.26	3.92	6.97
	400nm	2.85	n/a	5.43	3.32	4.13
	1500nm	1.92	n/a	2.72	2.50	2.21
CEA ODS	***120nm***	6.63	6.64	7.58	6.89	8.62
	400nm	5.53	5.55	6.72	5.77	7.12
	1500nm	5.01	5.16	5.58	5.23	5.77
EUROFER	***120nm***	4.85	4.86	5.79	7.72	7.03
	400nm	3.93	3.77	4.98	4.33	4.82
	1500nm	3.27	3.08	3.63	4.47	3.29
EUROFER ODS	***120nm***	6.34	6.30	7.67	8.48	7.97
	400nm	5.24	5.11	6.59	5.93	6.24
	1500nm	4.58	4.59	5.31	4.51	4.89

Table 13 – Change in hardness (GPa) from unimplanted at with changing depth and implantation

		75appm He	*2000appm He*	*2000appm He + 4.5dpa Fe*	*2000appm Ne*
Fe-14wt%Cr	***120nm***	n/a	4.71	2.37	5.42
	400nm	n/a	2.58	0.47	1.28
	1500nm	n/a	0.80	0.58	0.29
CEA ODS	***120nm***	0.01	0.95	0.26	1.99
	400nm	0.02	1.19	0.24	1.59
	1500nm	0.15	0.57	0.22	0.76
EUROFER	***120nm***	0.01	0.94	2.87	2.18
	400nm	-0.16	1.05	0.40	0.89
	1500nm	-0.19	0.36	1.20	0.02
EUROFER ODS	***120nm***	-0.04	1.33	2.14	1.63
	400nm	-0.13	1.35	0.69	1.00
	1500nm	0.01	0.73	-0.07	0.31

Chapter 4
Micropillar Compression Testing

18 Methodology

Micropillar compression testing is a useful method for investigating how implantation affects deformation mechanisms. Using ion implantation only provides a few microns depth of damage (as discussed in Chapter 2). In order to provide useful information, the entire pillar and the bulk material directly below need to be within the implanted region.

Implanted helium affects hardness and yield stress (Chapter 3 and Chapter 5) but makes little difference to visible deformation mechanisms (discussed in Chapter 5, Section 24.2). Previous work on iron ion implantation of Fe-Cr pillars [164] shows that deformation mechanisms can be significantly affected by the damage caused by incident self-ions (as an analogue for incident neutrons). The 2000appm helium implantation alone causes <0.3dpa damage; in a fusion reactor helium transmutes at a rate of 10appm/dpa, therefore the 0.3dpa is well below the required ratio. As discussed in Chapter 2, Section 11, the highest damage possible implanting Fe ion with available equipment and beam time was 4.5dpa. Therefore a set of samples was produced under dual-beam conditions to 2000appm He + 4.5dpa Fe damage. It was decided that micropillar compression tests should be performed in this dual-beam iron and helium implanted material to determine whether the added lattice damage effects ODS and non-ODS alloys differently.

All samples referred to in this chapter as 'implanted' were simultaneously implanted with 2000appm He and sufficient Fe to cause 4.5dpa of damage to a depth of 3.5μm. All four materials were implanted: Fe-14wt%Cr, CEA ODS, EUROFER and EUROFER ODS.

Previous work [164][165] has concluded that, while useful for investigating the differences in deformation mechanisms between materials and implantations, micropillar compression testing is subject to a size effect reflecting the movement of dislocations on a local scale, rather than flow stresses translatable to larger specimens. To ensure all results are affected only by the pillar and not the bulk below, pillars need to have an aspect ratio greater than 3:1 (height : diameter) [166]. Below 1μm diameter it becomes harder to accurately FIB pillars with parallel sides, and if the diameter is more than a couple of microns the FIB milling time becomes impractical. For these reasons, the pillar dimensions for this project were chosen as ~1μm diameter, ~8μm height.

The implantations were made to a depth of 3μm; this means that 1x8μm pillars cannot be milled vertically into the implanted layer (as they would be cut straight through the damaged region into the unimplanted bulk). What is therefore required is a method of holding the sample perpendicular so that the implanted layer is vertical.

18.1 Sample Preparation

The sample preparation route used was developed for my Masters project [165]. Cut and polished samples (Chapter 2, Section 10) were nickel plated, which helps them to retain their edge during polishing and allows accurate placement of the pillars in the implanted layer (i.e. exactly along the edge of the plate). Electroless nickel plating is an established method for fracture surface microscopy. It uses an autocatalytic reaction to deposit a coating of nickel on a substrate [167]. Each sample was Ni-plated in the solution for 10 minutes to give a ~2μm coating.

Electroless plating requires a solution of: 18g Nickel chloride, 4.4g sodium hypophosphite, 40g sodium citrate, 20g ammonium chloride, and 400ml distilled water.

Heat to 90-100°C and immerse samples in the solution. Nickel is plated at a rate of ~0.015mm/hr.

The polished faces of two nickel plated samples were then glued with Araldite Precision epoxy resin and pressed together to ensure glue coated the entire surfaces and filled the gap. These glued 'sandwiches' were clamped and left to cure under a heat lamp overnight. Once the epoxy resin had cured, the sandwiches were hot-wax mounted onto an aluminium polishing plate with the glued faces perpendicular to the plate surface. The reverse side of the resin mount was ground to 4000 grit to provide a flat back surface. The top surface was ground and polished with grades of silicon carbide paper and colloidal silica (as previously described Chapter 2, Section 10) to create a cross-section of the glued layers. The polished, mounted sandwiches were then glued onto aluminium stubs with cyanoacrylate adhesive and a conductive pathway of silver dag was added.

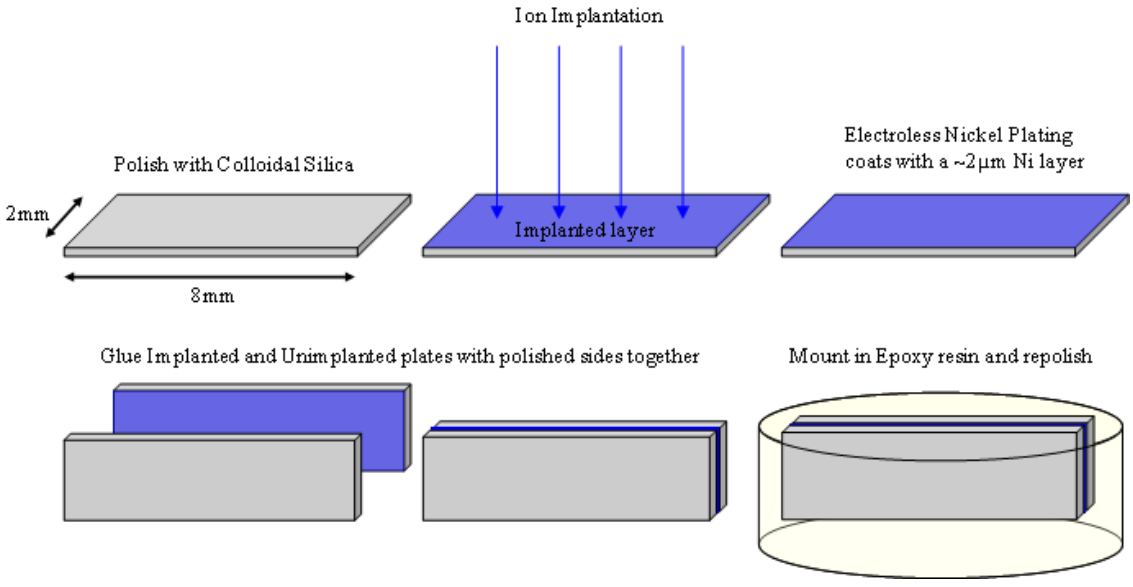

Figure 78 - Sample preparation route

18.2 Focused Ion Beam Milling of Micropillars

To produce perfectly parallel sided pillars requires a set up with automated rotating FIB stage and image/shape recognition software. These were not available for this project and consequently all the pillars have tapered sides. This reduces the viability of the calculated stresses/strains. Therefore, the quantitative data obtained from these experiments should be treated with caution.

In order to produce pillars with almost parallel sides they were annular-milled with Ga+ ions using a FIB. The Fe-14wt%Cr and CEA ODS pillars were milled at CalTech using an FEI FIB Nova-200 Nanolab; the EUROFER and EUROFER ODS pillars were milled in Oxford using an FEI FIB TEM 200. On both machines, a three-stage annular milling process with decreasing currents was used to create the pillars.

First, a rough circular trench was cut using ~1000pA, with dimensions R_o 5µm, R_i 3µm, depth 6µm. The second mill refined using ~500pA, R_o 4µm, R_i 1.5µm. The final polishing cut used ~100pA, R_o 2.5µm, R_i 0.6µm. The finished pillars had diameters ~1µm ±0.1µm, and a height of ~8µm. Figure 79 shows the stages of FIB milling as diagrams of pillar dimensions after each mill and an SEM image displaying FIB cut pillars after each stage.

Stage 1

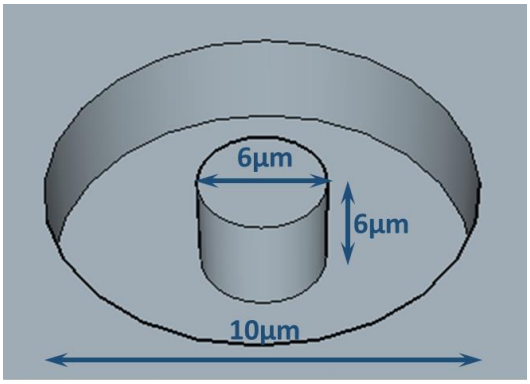

Stage 2

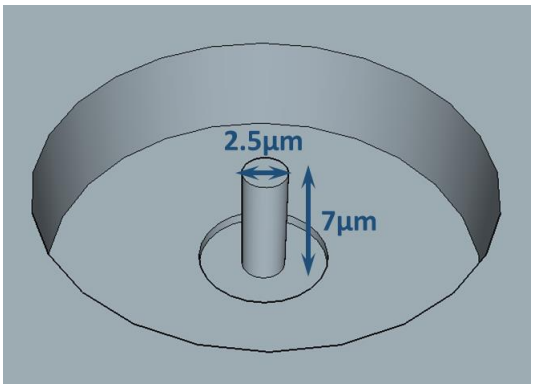

Stage 3

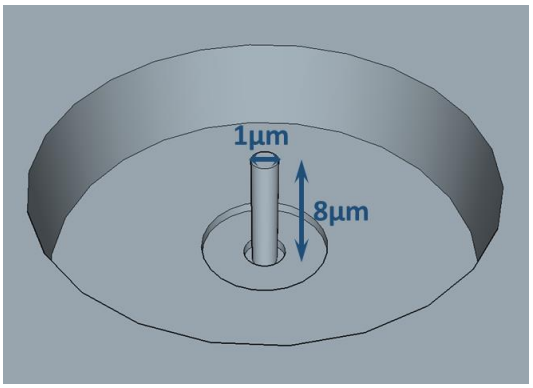

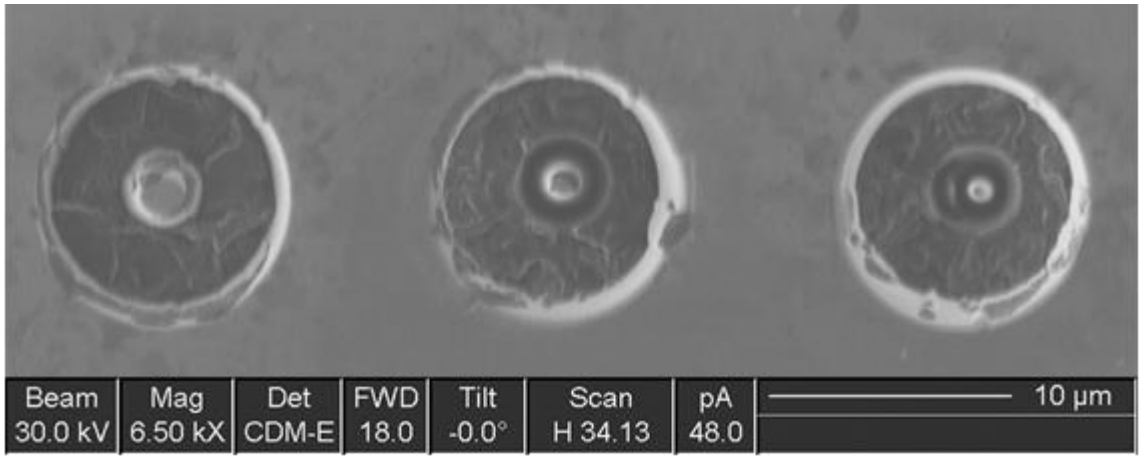

Figure 79 - Stages of FIB pillar milling – SEM image: stage 1, 2, 3 from left to right

18.3 Micropillar Compression Using a Nanoindenter

18.3.1 SEMentor, California Institute of Technology

Pillars in Fe-14wt%Cr and CEA ODS were tested in the SEMentor at the California Institute of Technology. The SEMentor is a custom built microscope in Professor Julia Greer's group at CalTech. It consists of a nanomechanical module similar to a commercial Agilent nanoindenter, inside an SEM using Agilent's Nanosuite software.

Samples are mounted in the nanoindenter on a mechanical stage and the SEM video feature is used to align the flat tip with each micropillar. The micropillars were compression tested using a flat punch with a diameter of 5μm to a displacement of 500nm at a loading rate of $5nms^{-1}$. Load/displacement data and SEM video footage were recorded simultaneously.

All work at CalTech was performed under the supervision of post-doctoral student Seok-Woo Lee. All the tests can be seen in Appendix A – CalTech SEMentor Videos, on the enclosed CD.

18.3.2 MTS Nanoindenter XP, University of Oxford

Due to time constraints at CalTech, EUROFER and EUROFER ODS were not tested in the SEMentor. Sets of EUROFER and EUROFER ODS pillars were tested using an MTS Nanoindenter XP. This provides the same load/displacement data of the pillar compression, but SEM imaging has to be performed before and after testing.

An Fe-14wt%Cr unimplanted pillar was also tested in the Oxford nanoindenter to confirm that the data from the two nanoindenters is comparable (see Section 19.5). The same compression parameters were used in Oxford as in the CalTech tests. The micropillars were compression tested using a flat punch with a diameter of 5μm to a displacement of 500nm at a loading rate of $5nms^{-1}$.

Flat ended nanoindenter tips are commercially available, but to ensure the punch was of suitable dimensions for these specimens it was custom made from an old tip with a broken point. Using the FIB, a flat end was cut on the diamond and then a series of concentric mills used to form a diamond pillar ~5μm diameter and ~4μm tall (Figure 80). Atomic Force Microscopy (AFM) mapping was used to verify the flat end of the cut pillar was perpendicular to the indentation direction.

As there is no in-situ SEM for alignment, in order to compress the pillars, an accurate calibration of the distance between the optical microscope and tip placement was required. A rough calibration was performed away from the testing area (to ensure no pillars were damaged) then a second calibration was made close to the pillar to be tested – in Figure 82 the circular calibration indent from the punch can be seen bottom left of the pillar. The stage movements all rely on mechanical screws, therefore the second calibration needs to be made as close to the test site as possible to reduce movement error while the pillar is aligned under the tip.

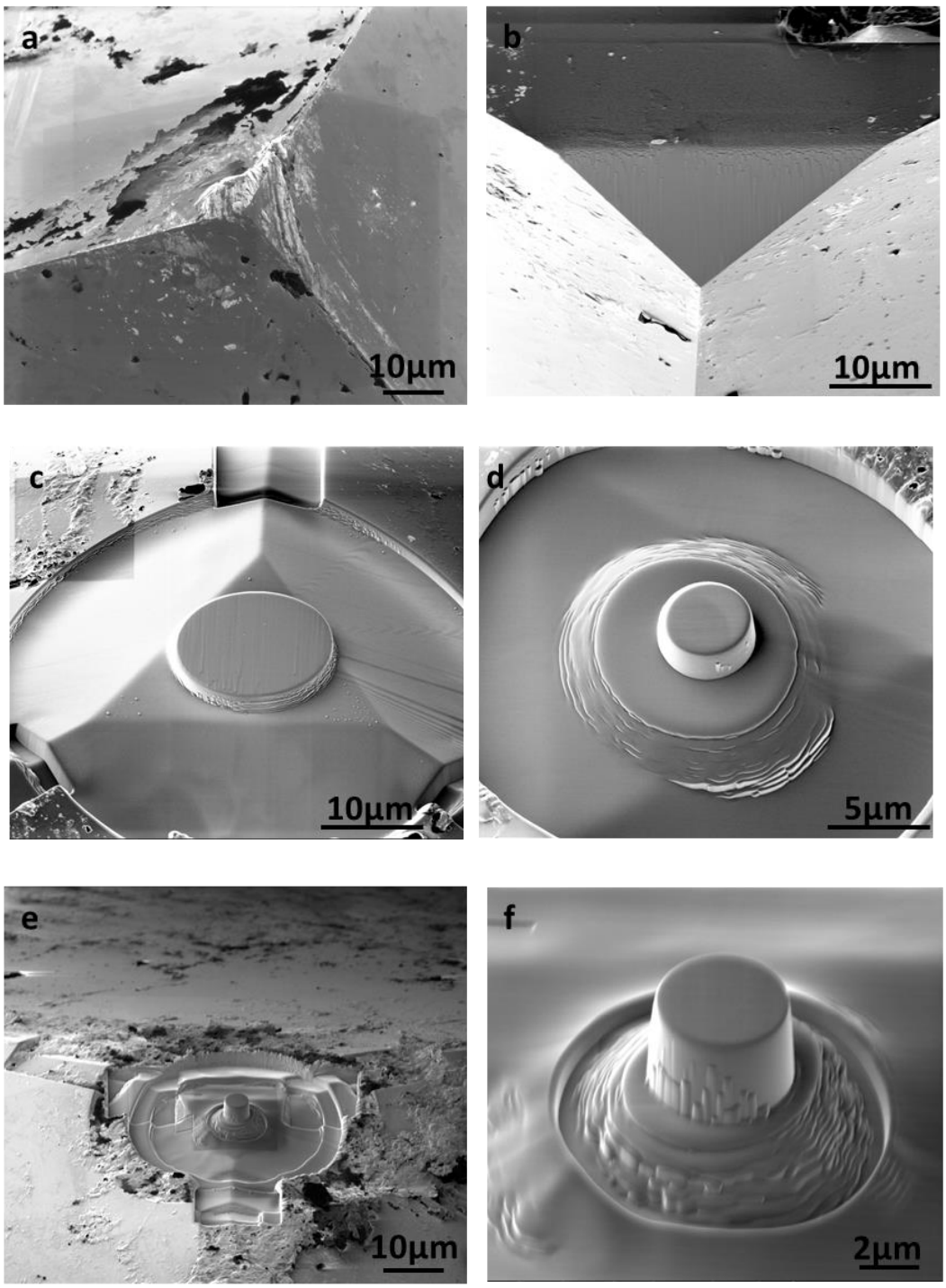

Figure 80 – Milling steps to create diamond punch
a – old indenter tip
b – cut off point to make a flat surface
c – wide annular mill
d – narrow annular mill
e/f – final mill for flat punch

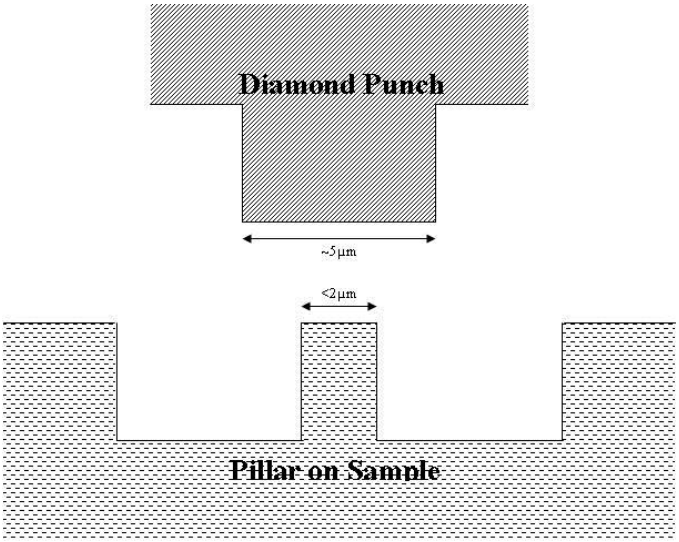

Figure 81 – Diamond punch positioning over sample

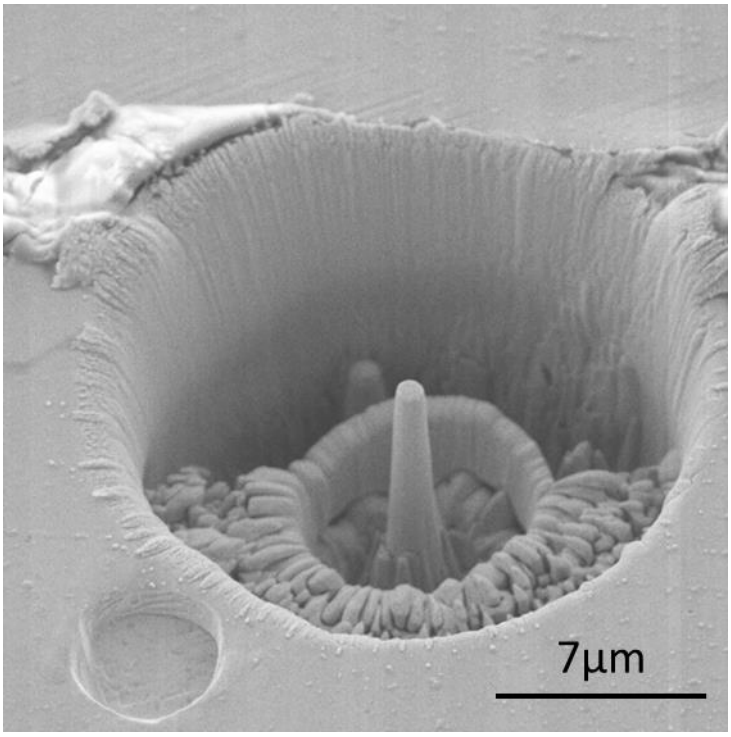

Figure 82 – Pillar with calibration indent bottom left

19 Results

Loading and unloading data were recorded and analysed using MTS Nanosuite software. Multiple pillars were tested in each material in both unimplanted and implanted conditions. Displayed below are images of one representative pillar for each set and graphs of all the pillars in each set (Figure 83 to Figure 105).

All the pillars were milled under the same conditions. Their dimensions are not all identical due to a combination of beam current fluctuations and microstructural effects; therefore the height and diameter of each pillar was measured individually from SEM micrographs. Using these measurements the nanoindenter output of load/displacement was converted to stress/strain.

All the pillars are ~8μm tall and nominally compressed by 500nm which is the equivalent of ~6% strain. Some of the graphs below go significantly past 6% strain; this appears when a large strain jump past the defined test conditions occurs. In the two cases where there has been slip past 15% there are two graphs for the sample; one showing the full extent of the strain burst and one cutting the data off at 15% in order to provide a set of comparable graphs.

19.1 Fe-14wt%Cr – Tested at CalTech

The graphs of deformation in unimplanted Fe-14wt%Cr (Figure 84) show large flat jumps in strain as the stress on the sample increases. All samples show an elastic deformation in the first 1% strain with yield between 0.5 and 0.7GPa (yield stress taken as the first significant change in angle of the curve). The top curve shows a number of small strain jumps before falling into the pattern followed by the other two curves of large strain bursts at small increases of stress. The final large strain burst in the top line of Figure 84 is due to a complete collapse of the pillar, where the graph goes past the expected 10-15% strain.

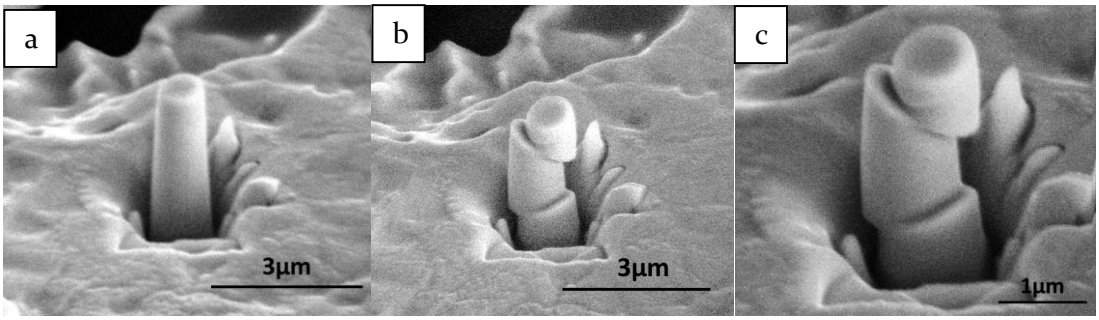

Figure 83 - Unimplanted Fe-14wt%Cr pillar pre-test (a) and post-test (low (b) and high (c) mag) multiple slip lines across the pillar, with a significant distance slipped on each.

Figure 84 - Fe-14wt%Cr Unimplanted – three pillars (full extent of slip (a) and up to 15% strain (b)). Examples of strain bursts are indicated on the top line of (a).

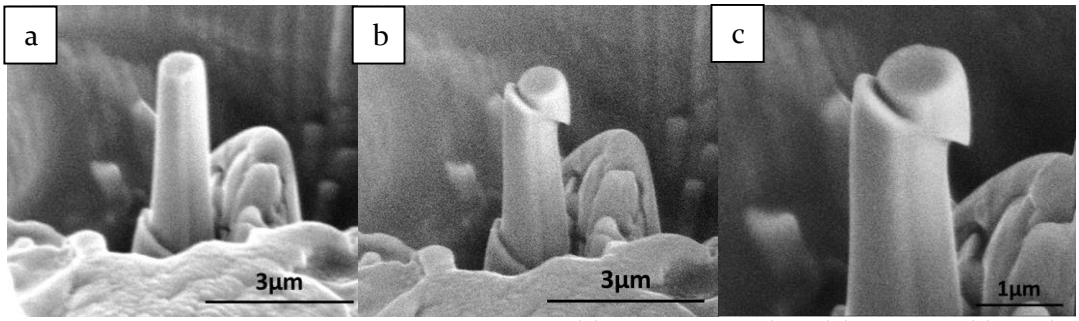

Figure 85 - Implanted Fe-14wt%Cr pillar pre-test (a) and post-test (low (b) and high (c) mag) all the slip contained within one band across the pillar.

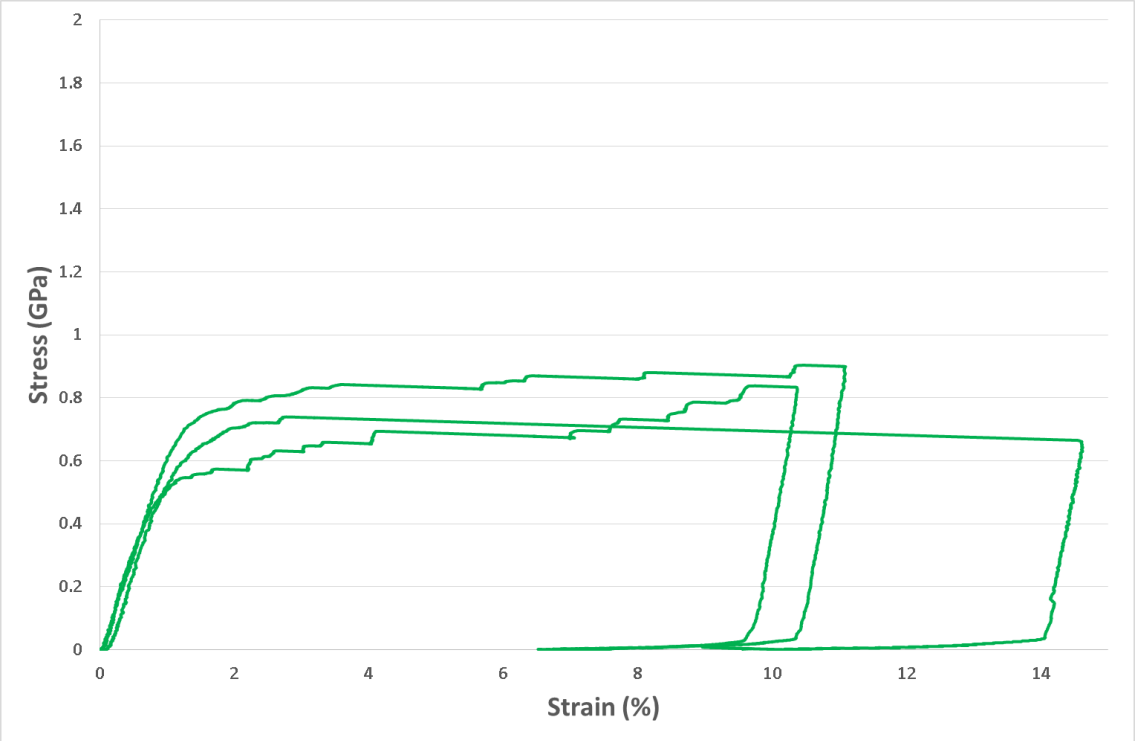

Figure 86 - Fe-14wt%Cr Implanted – three pillars

The graph of deformation in implanted Fe-14wt%Cr (Figure 86) shows an elastic deformation in the first 1% strain with yield between 0.5 and 0.6GPa and multiple short strain bursts as the stress on the sample increases. The increase in stress between each burst is very small: ~0.04GPa/burst. The middle line shows a massive strain burst from ~2.5% that indicates a large slip on the pillar taking the displacement past the 500nm depth.

The post-test pictures of unimplanted and implanted pillars do not appear significantly different; the video footage of deformation however, shows significant differences. This will be discussed further in Section 20.1.

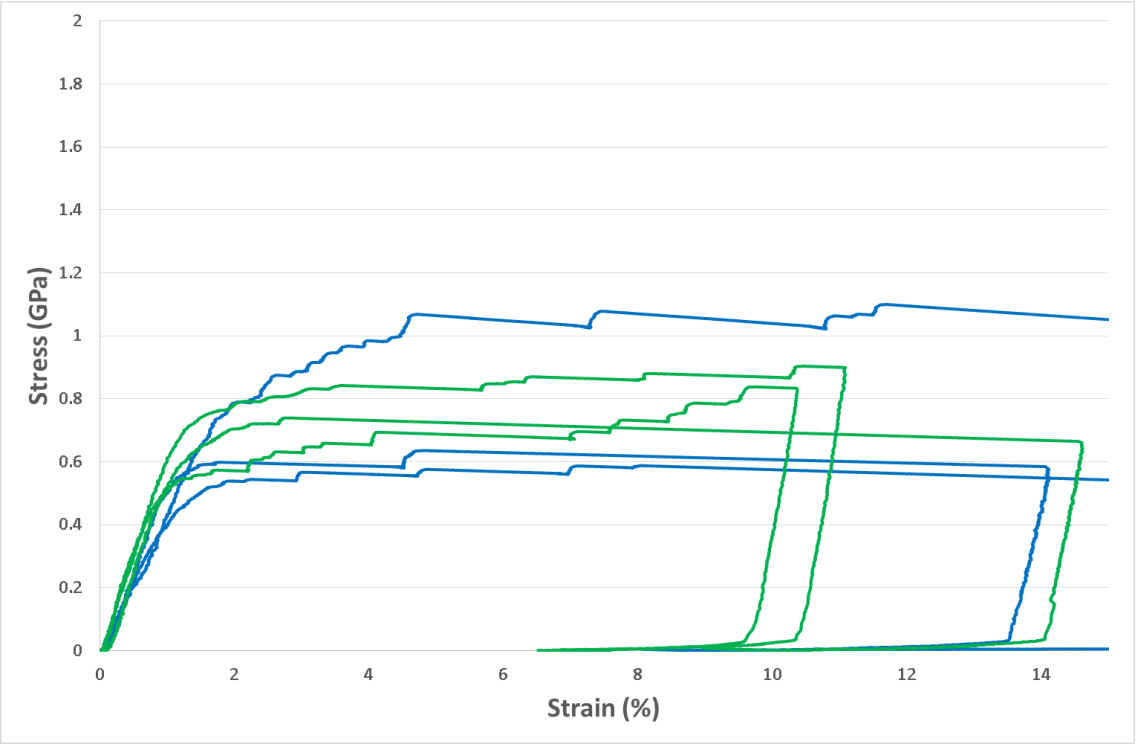

Figure 87 - Fe-14wt%Cr, Unimplanted blue, implanted green (up to 15% strain)

Table 14 - Number and length of strain bursts up to 10% strain.
Brackets indicate unusual behaviour and the associated inclusive averages.

Fe-14wt%Cr	Number of bursts per line	Average number of bursts	Average length of burst
Unimplanted	5, 4, 2	3.67	2.2%
2000appm He + 4.5dpa Fe	10, 9, (3)	9.50 (7.33)	0.8% (1.1%)

Figure 87 compares the results of compressions of unimplanted and implanted Fe-14wt%Cr micropillars. The elastic sections of all curves are approximately parallel, suggesting that the implantation does nothing to change the elastic modulus of the material (discussed further in Section 19.5). Similarly the range of yield strength within the implanted and unimplanted sets is approximately equal. The main difference between the sets is the mode of deformation after yield. Table 14 shows that the unimplanted material has fewer, longer strain bursts with a greater stress increase initiating each burst. The implanted Fe-14wt%Cr shows many more, shorter strain bursts (with the occasional long burst).

As these were tested in the SEMentor, video footage of the test is available. Correlating the graphs with the videos shows how the strain bursts physically manifest themselves on the pillars. In the unimplanted material each strain burst corresponds to a large slip in the pillar. Most of the slips occur on new lines for each burst. In the implanted pillars, the slip concentrates into a band, with subsequent slips occurring on the same or a very close parallel slip plane to an existing slip plane.

Figure 88 is a series of screen captures from two SEMentor videos. It shows the relative speeds of slip between unimplanted and implanted pillars – unimplanted pillars show massive displacement change in one second, whereas the implanted pillar slowly deforms over a minute. Full video footage can be viewed in Appendix A on the enclosed CD.

Unimplanted

99s

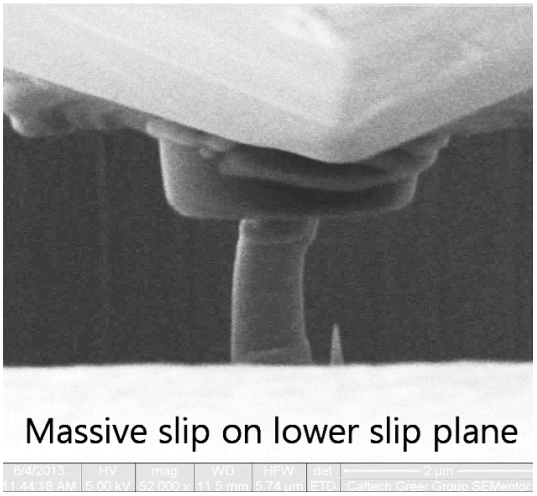

100s

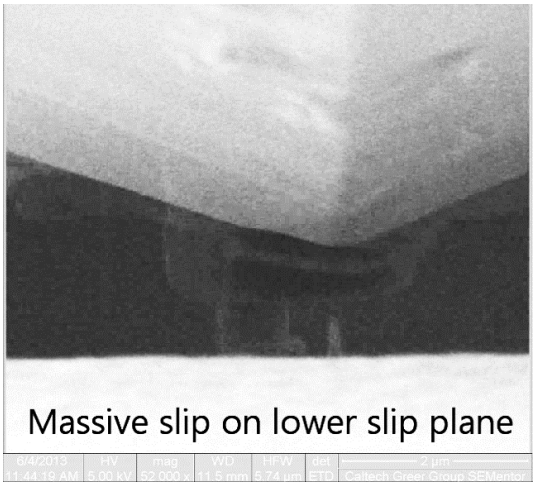

2000appm He + 4.5dpa Fe

39s

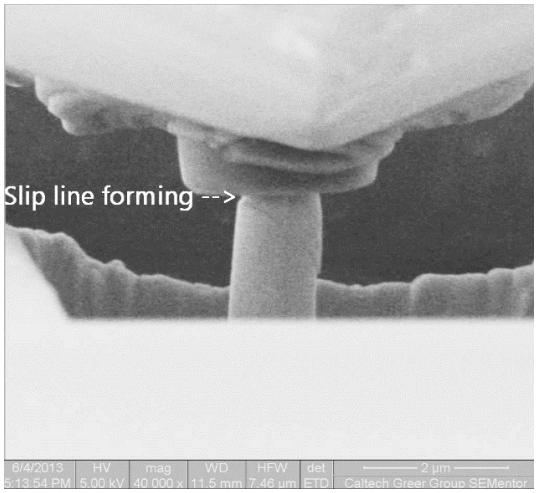

69s

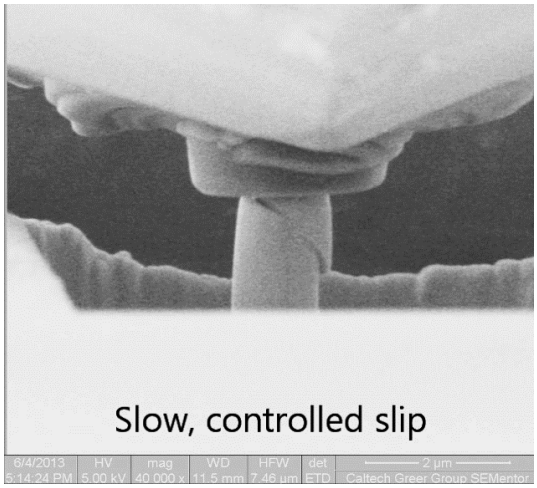

99s

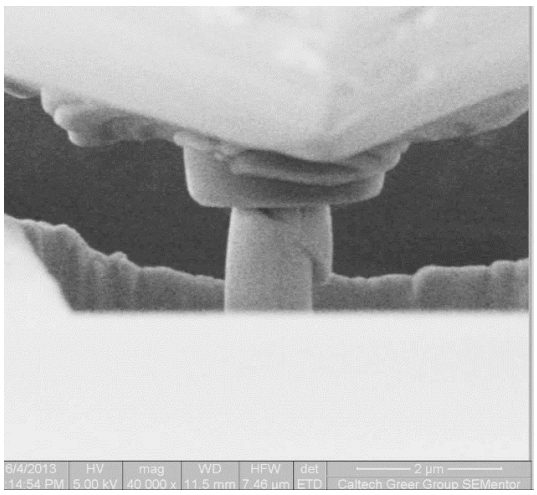

Figure 88 - Showing the difference in speed of slip between unimplanted and 2000appm He + 4.5dpa Fe pillars in Fe-14wt%Cr.
The unimplanted pillar undergoes a massive slip/indenter tip displacement in one second. The implanted pillar slip is slow and controlled over the course of a minute.
The times indicated are the number of seconds after the indenter tip makes contact with the pillar surface.
All images are screen captures from the SEMentor videos, (the full videos can be seen in Appendix A).

19.2 CEA ODS – Tested at CalTech

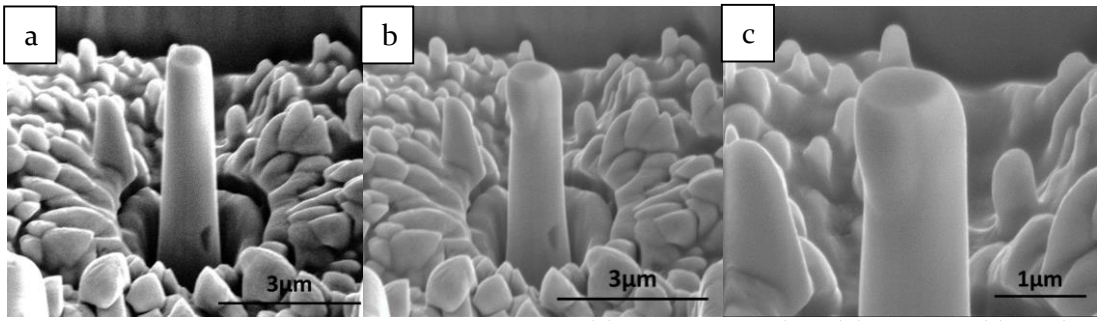

Figure 89 - Unimplanted CEA ODS pillar pre-test (a) and post-test (low (b) and high (c) mag) Deformation is seen only in the top 1.5µm of the pillar. The pillar sides are bowed out and the start of a slip line can be seen down the centre of the pillar from the top, curving left.

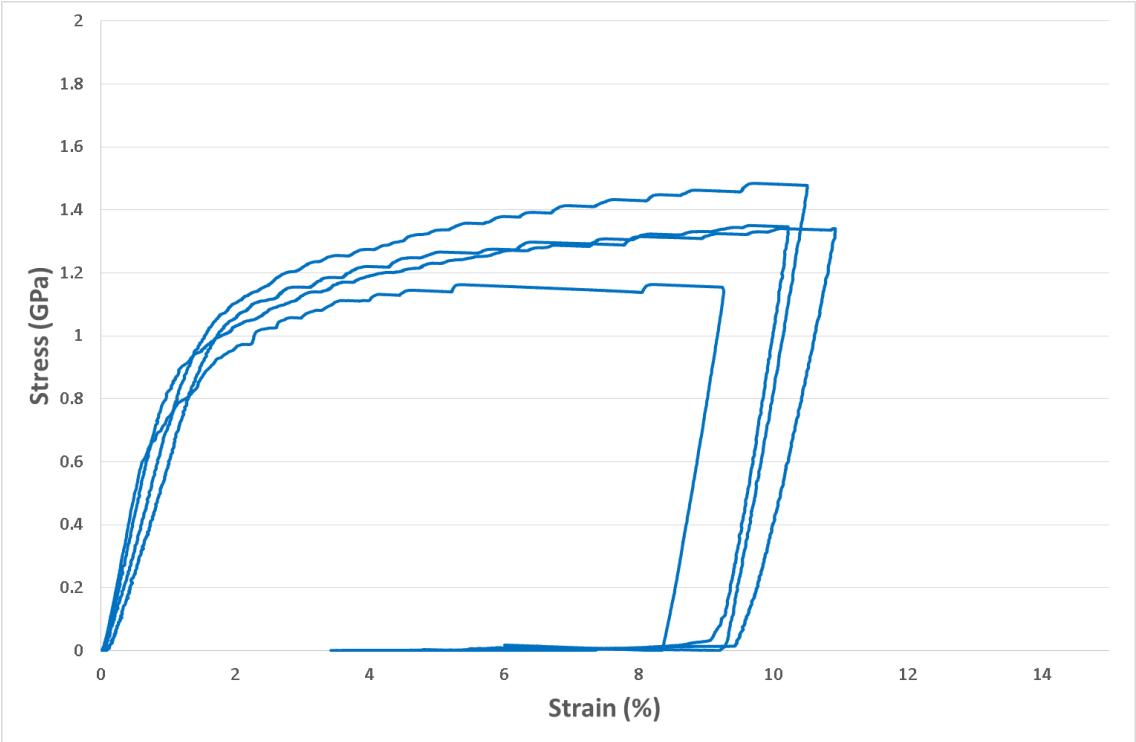

Figure 90 - CEA ODS Unimplanted – four pillars

The deformation of all the CEA ODS unimplanted pillars was very similar. The graph (Figure 90) shows almost equal elastic moduli (see Section 19.5) for all curves and yield stresses in the range ~0.7-1.0GPa. The plastic deformation occurs in a series of small strain bursts with stress increases of ~0.02GPa per strain burst.

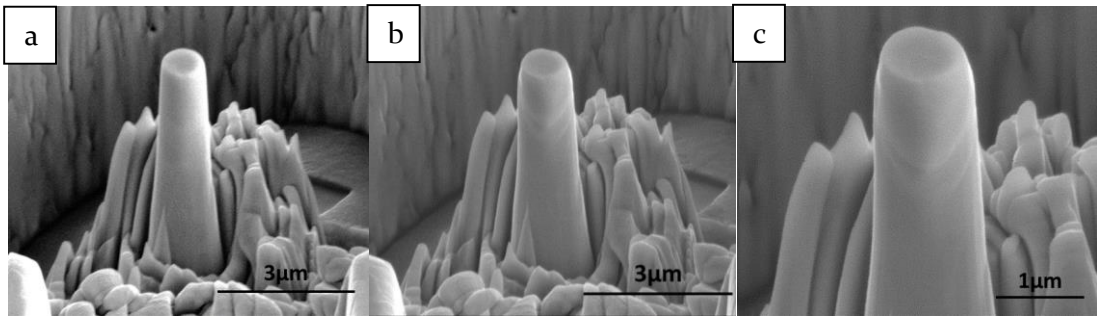

Figure 91 - Implanted CEA ODS pillar pre-test (a) and post-test (low (b) and high (c) mag) Deformation is limited to the top ~1.5µm, showing bowing out of the pillar sides and the start of formation of a couple of shallow slip bands.

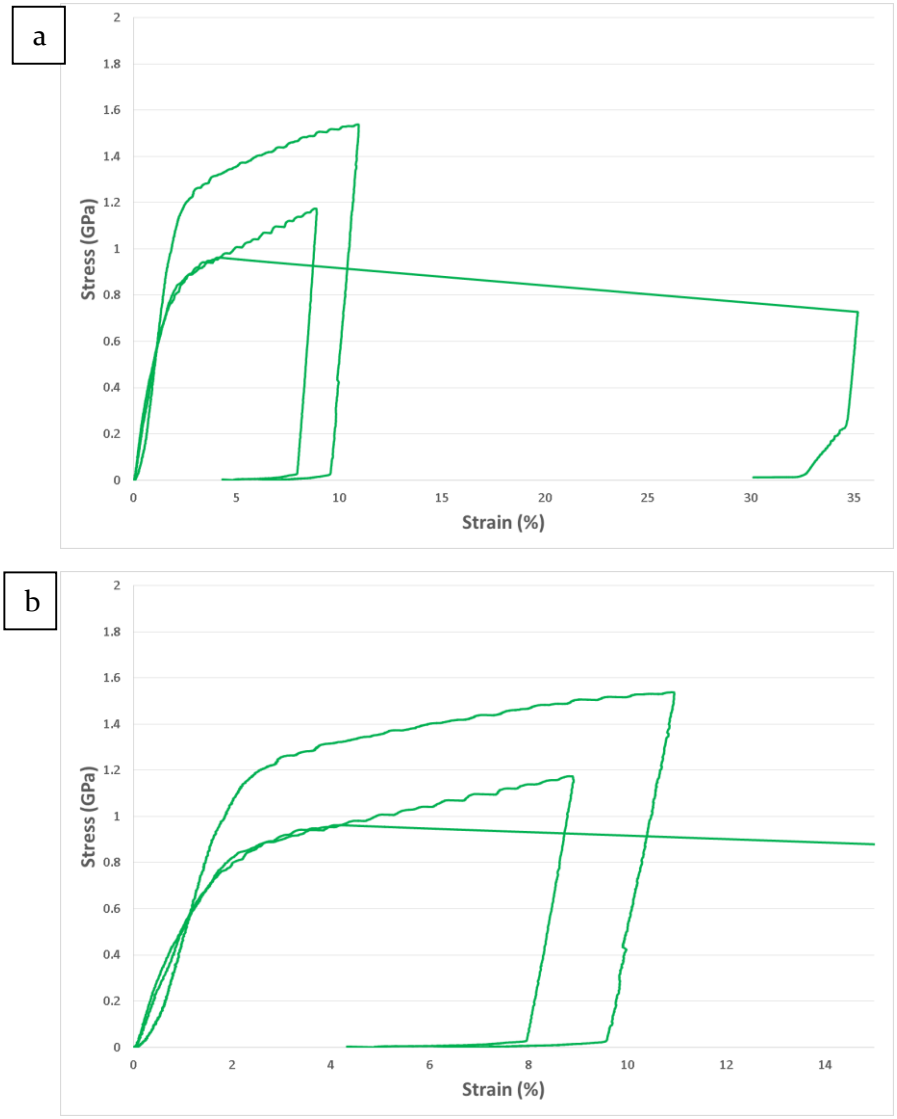

Figure 92 - CEA ODS Implanted - -three pillars (full extent of slip (a) and up to 15% strain (b))

Figure 92 shows one of the implanted pillars started to deform with small regular strain bursts then had a massive slip event. The other two both deformed with small regular strain bursts, one with higher yield stress (1.2 vs. 0.8GPa).

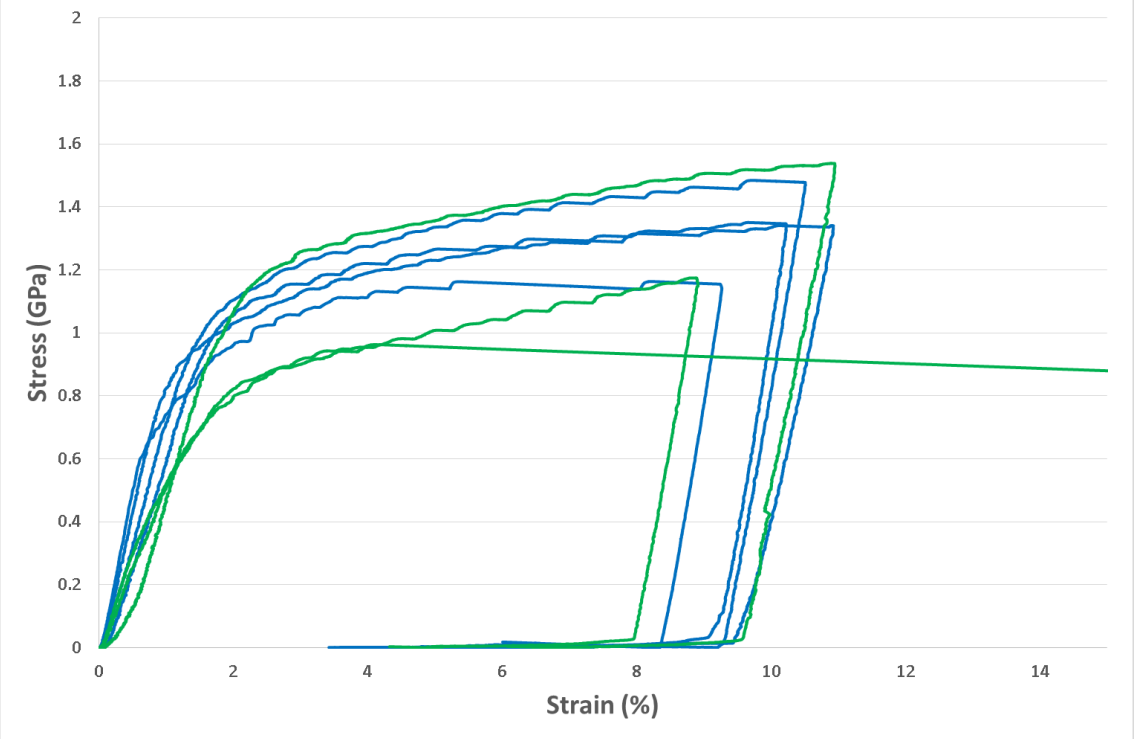

Figure 93 - CEA ODS, unimplanted blue, implanted green (up to 15% strain)

Table 15 - Number and length of strain bursts up to 10% strain. Brackets indicate unusual behaviour and the associated inclusive averages.

		Number of bursts per line	Average number of bursts	Average length of burst
CEA ODS	**Unimplanted**	15, 13, 12, 9	12.25	0.65%
	2000appm He + 4.5dpa Fe	14, 13, (4)	13.50 (10.33)	0.59% (0.77%)
Fe-14wt%Cr	**Unimplanted**	5, 4, 2	3.67	2.2%
	2000appm He + 4.5dpa Fe	10, 9, (3)	9.50 (7.33)	0.8% (1.1%)

Figure 93 compares the unimplanted and implanted stress-strain graphs of the CEA ODS pillars. All the curves show a similar elastic modulus and plastic deformation mode. The range of yield stress for both sets is approximately the same (unimplanted 0.7-1.1GPa, implanted 0.8-1.2GPa). Young's modulus will be discussed in Section 19.5.

Table 15 shows the strain burst characteristics of CEA ODS and Fe-14wt%Cr. Compared with Fe-14wt%Cr, CEA ODS has a much larger average number of strain bursts, and much smaller difference between implanted and unimplanted results.

The video footage of these tests showed both the implanted and unimplanted pillars deforming in a similar manner, barrelling of the pillar eventually leading to the formation of shallow slip lines visible on the surface. The unimplanted pillars only deformed in the top ~2μm of the pillar. The implanted pillars, however, barrelled down the whole length of the pillar, with elastic recovery occurring on indenter tip retraction leaving only the top section plastically deformed.

Videos of all the tests are available in Appendix A, on the enclosed CD.

19.3 EUROFER – Tested in Oxford

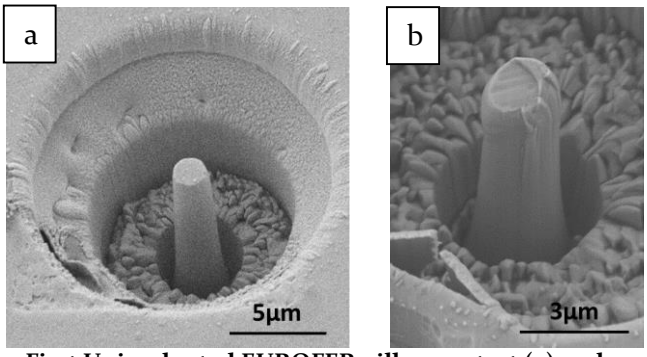

Figure 94 - First Unimplanted EUROFER pillar pre-test (a) and post-test (b)

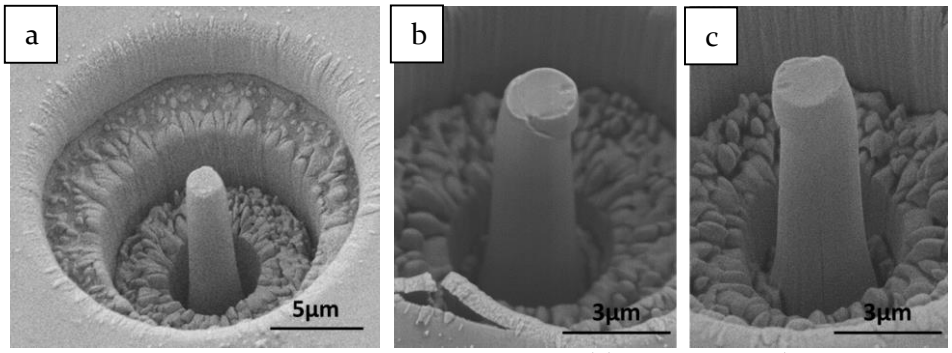

Figure 95 – Second Unimplanted EUROFER pillar pre-test (a) and post-test (b and c - two angles))

(N.B.: the stress axis on the EUROFER graphs is 0–3.5GPa, for all other materials it is 0–2GPa.)

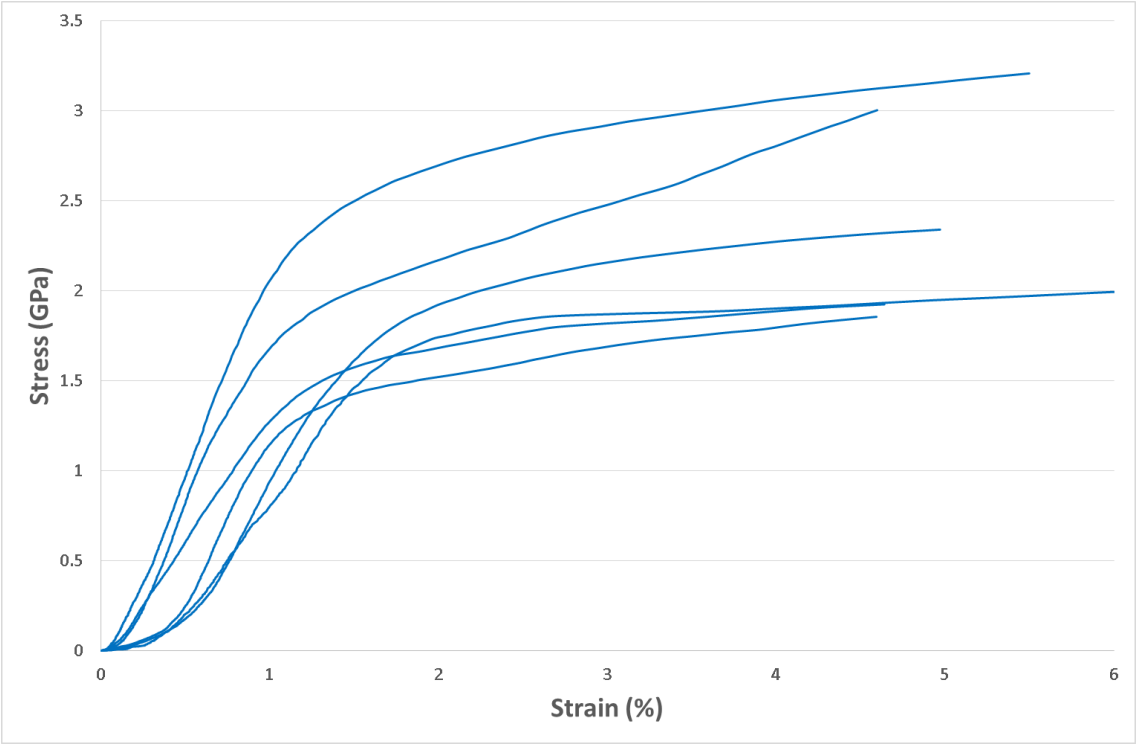

Figure 96 - EUROFER Unimplanted – six pillars

Deformation in both pillars above (Figure 94 and Figure 95) is confined to the top ~2μm. The first pillar (Figure 94) shows barrelling of the top section of the pillar. This deformation is characteristic of most of the pillars in this set. Two of the pillars, however, showed shallow but obvious slip in the top section of the pillar along a single slip band (Figure 95).

The graph (Figure 96) shows that all the pillars start by deforming elastically and then smoothly transition to plastic deformation; there is a range in yield stress. The gradient of the elastic portion of each curve (i.e. the elastic modulus) is fairly similar for all curves; three lines however, show a curved increase in strain at low stress before they reach the elastic region. Comparing this data with the SEM images of the specific pillars suggests that this was due to contact feedback errors between the pillar and the nanoindenter tip (i.e. the contact surfaces were not parallel (with a greater angle than ~1.5° see (Section 19.5)) or more likely (since no buckling of pillars was observed) the indenter tip did not have contact with the full pillar top surface. The curve up to the elastic portion would then be due to the small stress applied as the tip settles into full contact.

Figure 96 includes the lines for those pillars that exhibited visible slip bands. It appears that the mode of deformation (barrelling or slip) makes little difference to the stress-strain response.

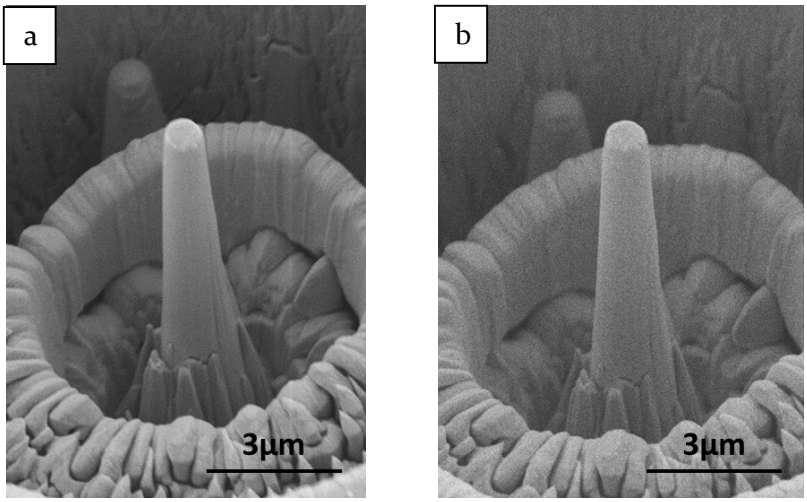

Figure 97 - Implanted EUROFER pillar pre-test (a) and post-test (b)

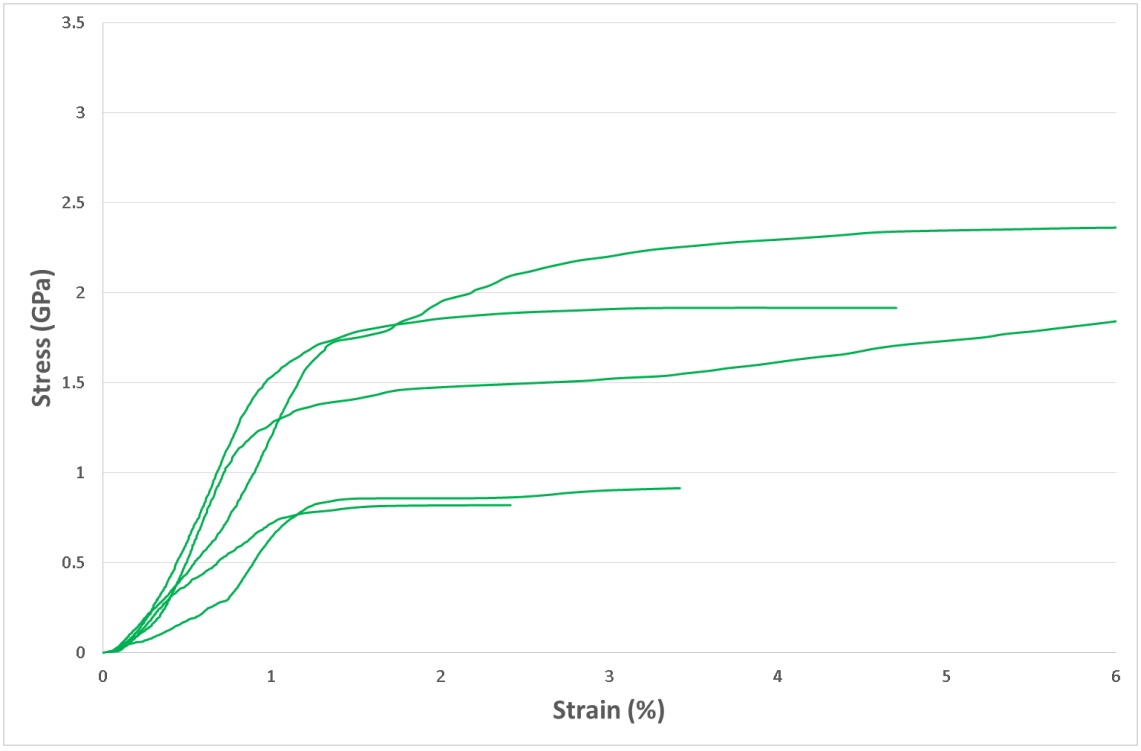

Figure 98 - EUROFER Implanted – five pillars

The implanted EUROFER pillars showed almost no visible slip lines on their surface post-deformation. As can be seen in Figure 97, the only difference between pre- and post-test pillars is a slight barrelling down the length of the pillar. A couple of lines in Figure 98 show ridged areas that indicate small strain bursts.

Similar to the unimplanted EUROFER pillars, the lines in Figure 98 show a contact curve up to an elastic region before smoothly transforming into plastic deformation. This may be due to misalignment of the tip and pillar surfaces.

It should be noted that these pillars are not parallel sided which will alter deformation. Discrete dislocation simulation of up to 5° taper in micropillars has, however, shown that increasing taper angle decreases the size effect and therefore should decrease the yield, but should make no changes to the Young's modulus [168][169]. The issue with stress calculations is the determination of the cross-sectional area of the pillars which changes down the length of a tapered pillar. The width of all the pillars in this project was measured at half the pillar height for consistency.

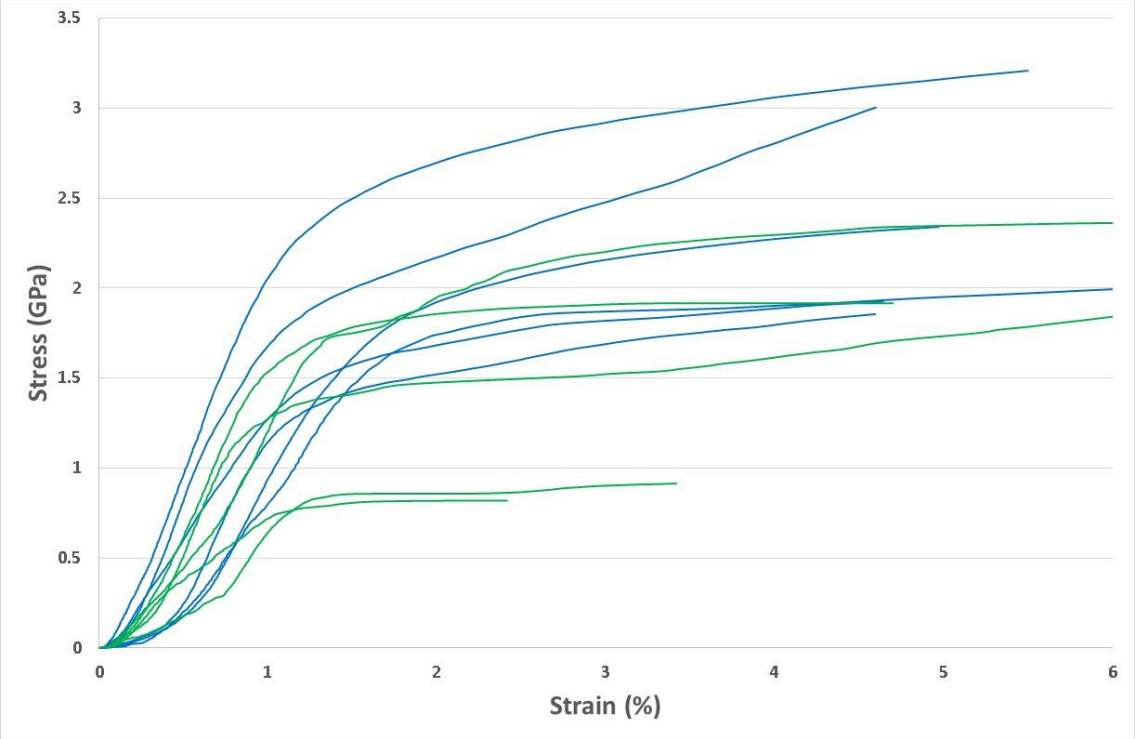

Figure 99 – EUROFER, Unimplanted blue, implanted green

Comparison of the unimplanted and implanted lines in Figure 99 shows no significant difference in the yield response between the conditions. The two highest outliers are unimplanted and the two lowest are implanted, but the majority of the curves fit with their plastic regions between 1.5 and 2.5GPa. Interestingly, the EUROFER pillars have significantly higher range of yield stresses (0.8-2.5GPa) than the other three materials (0.6-1.2GPa), which does not correlate with the previously mentioned taper effect. The gradient of the plastic deformation after yield, however, is generally flatter in the implanted results suggesting less overall work hardening. Unirradiated mean gradient: 16GPa (+15, -8), Irradiated: 5GPa (+4, -4).

These samples were tested in Oxford, therefore no video footage of the tests is available. Comparing the before and after SEM images shows the pillars mostly deform with barrelling to the pillar sides which corresponds to the smooth curves of all the lines.

19.4 EUROFER ODS – Tested in Oxford

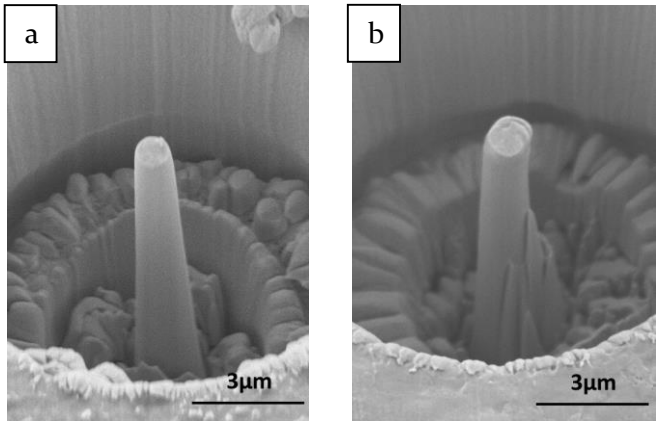

Figure 100 – First unimplanted EUROFER ODS pillar pre-test (a) and post-test (b)

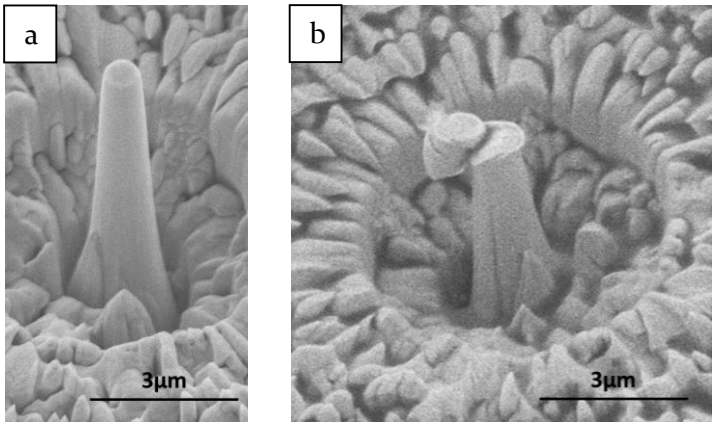

Figure 101 –Second unimplanted EUROFER ODS pillar pre-test (a) and post-test (b)

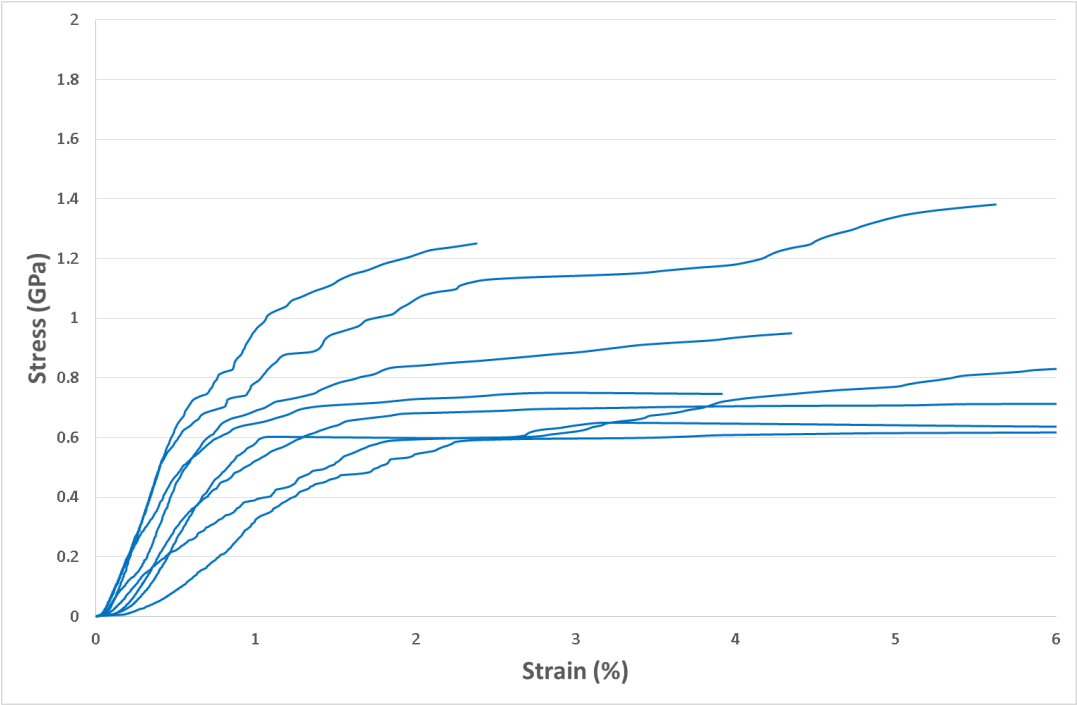

Figure 102 - EUROFER ODS Unimplanted – eight pillars

Figure 100 shows the deformation characteristics of most of the EUROFER ODS unimplanted pillars – barrelling and slight slip in the top ~1μm of the pillar. Figure 101 shows a massive slip in the top 1μm of the implanted pillar, and the whole top section has been sheared off – this only occurred in a few pillars.

Figure 102 shows there is a wide range of elastic moduli (Section 19.5) and yield stresses (Table 17) between the different pillars. There is still consistency in the progression of deformation between them, however – all start with a short elastic deformation region, which changes into a series of plastic deformation slip steps and then a massive strain burst occurs. These small slip steps are similar to those observed before in Fe-14wt%Cr and CEA ODS.

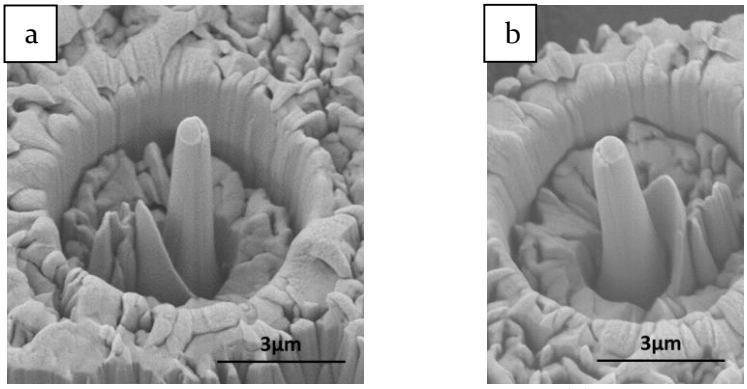

Figure 103 - Implanted EUROFER ODS pillar pre-test (a) and post-test (b)

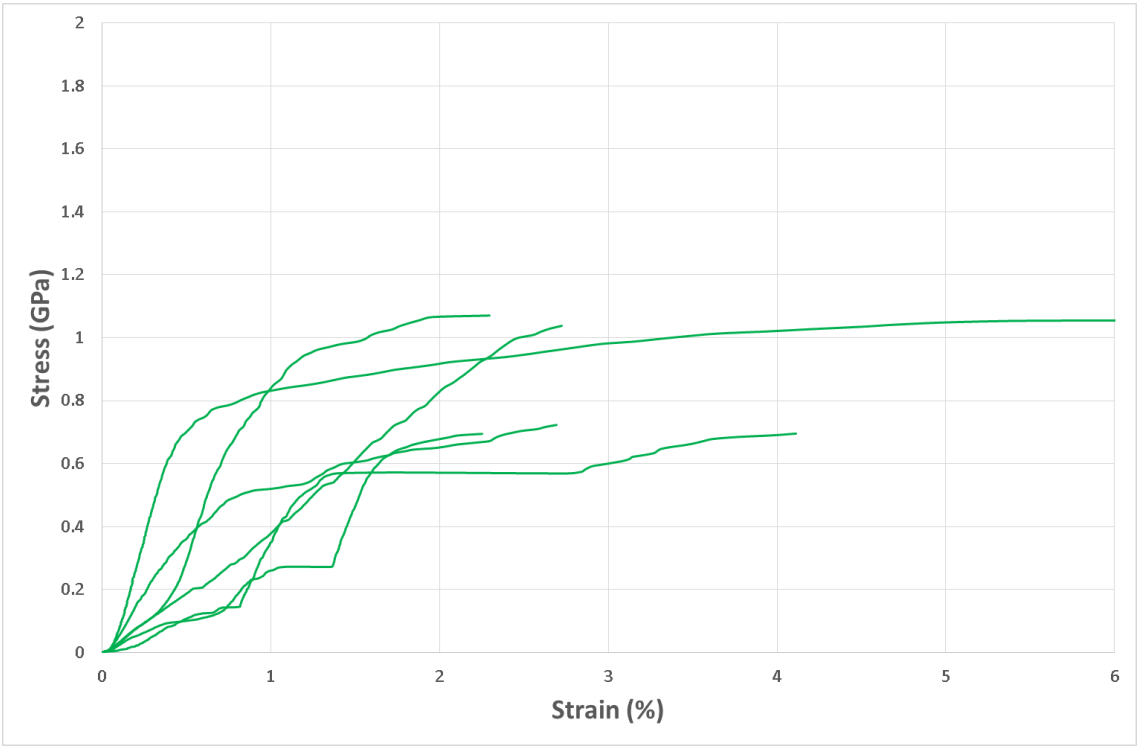

Figure 104 - EUROFER ODS Implanted – six pillars

Figure 103 shows deformation characteristic of the implanted EUROFER ODS pillars – slight barrelling along its length. This pillar also has a very small slip visible on the top surface, and is slightly bent to one side; this bend is due to non-flat contact with the indenter tip.

In the implanted graph (Figure 104) there is a wide scatter of elastic moduli (Section 19.5) and yield stresses (Table 17), but there does appear to be a band of results with similar moduli at the bottom. Most of the lines exhibit an elastic region that slowly curves over until a massive slip occurs. Two of the lines (with near vertical sections at ~1% and ~1.4% strain) show a couple of strain jumps before the final long slip.

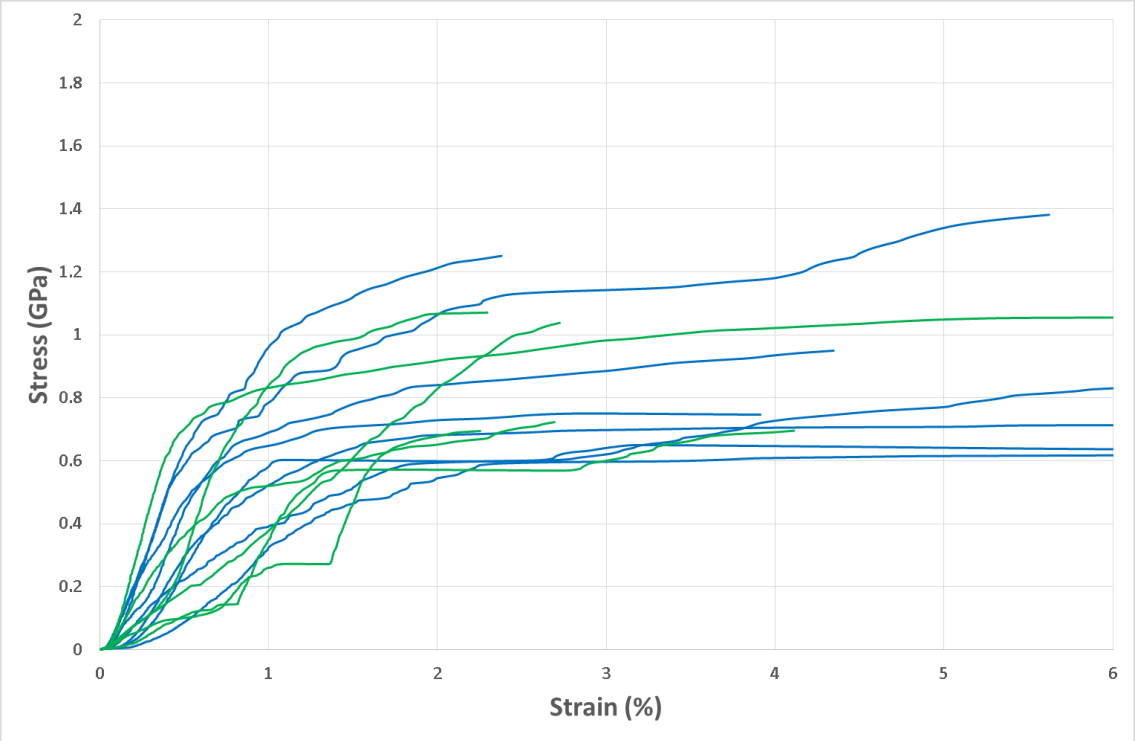

Figure 105 - EUROFER ODS, unimplanted blue, implanted green (up to 10% strain)

Comparing the results for unimplanted and implanted EUROFER ODS (Figure 105) the implantation appears to have very little effect on the range of elastic moduli (Section 19.5). The range of the yield strength appears to shift downwards slightly. The unimplanted lines exhibit more significant, visible small strain bursts, whereas the implanted lines have much smoother curves. All the lines show a massive strain burst by ~3% strain.

These samples were tested in Oxford: no video footage of the tests is available. The before and after SEM images show that the unimplanted pillars deform with a few small slip lines (visible on the pillar surface) which correspond to the small strain bursts seen in the graphs. Furthermore the top section of the pillar is sheared off corresponding to the massive strain burst and the end of the test (as the maximum test depth is passed).

Both sets exhibit barrelling down the length of the pillar and both sets exhibit slip, but it is significantly more pronounced in the unimplanted pillars (especially in the cases where the tip of the pillar has been sheared off).

19.5 Elastic Moduli Summary

Something to be noted in Figure 106 is that the measured elastic moduli for Fe-14wt%Cr, CEA ODS and EUROFER ODS are significantly less than those which would be expected for macro scale tests (Fe-14wt%Cr ~150GPa, CEA ODS and EUROFER ODS ~200GPa). The top of the scatter of EUROFER results reaches the predicted level (~200GPa), but many of the results are significantly lower. Modelling work on the design of accurate micropillar compression experiments [170] reveals that tapered pillar sides have an effect on modulus, but the opposite of the effect is seen here (increasing taper angle overestimates modulus). The same work [170] however did show that misalignment of the pillar top and indenter tip can cause underestimation of modulus. A misalignment of ~1.5° can reduce the modulus to ~35%, which would explain the discrepancy in recorded results.

All moduli for the Fe-14wt%Cr and CEA ODS pillars are similar within their materials/conditions, because the pillars in each set were milled in batches and tested in parallel. Each sample, however, may not have been loaded into the nanoindenter perfectly perpendicular to the indentation direction, causing misalignment of the indenter tip and pillar top surfaces. The EUROFER and EUROFER ODS pillars were not all milled in one batch per material/condition, leading to different misalignments for each pillar, thus causing the wide scatter of results. As we are unable to determine the misalignment angles for each pillar, the data cannot be calibrated. This is one of the reasons the quantitative data from micropillar compression should be treated tentatively.

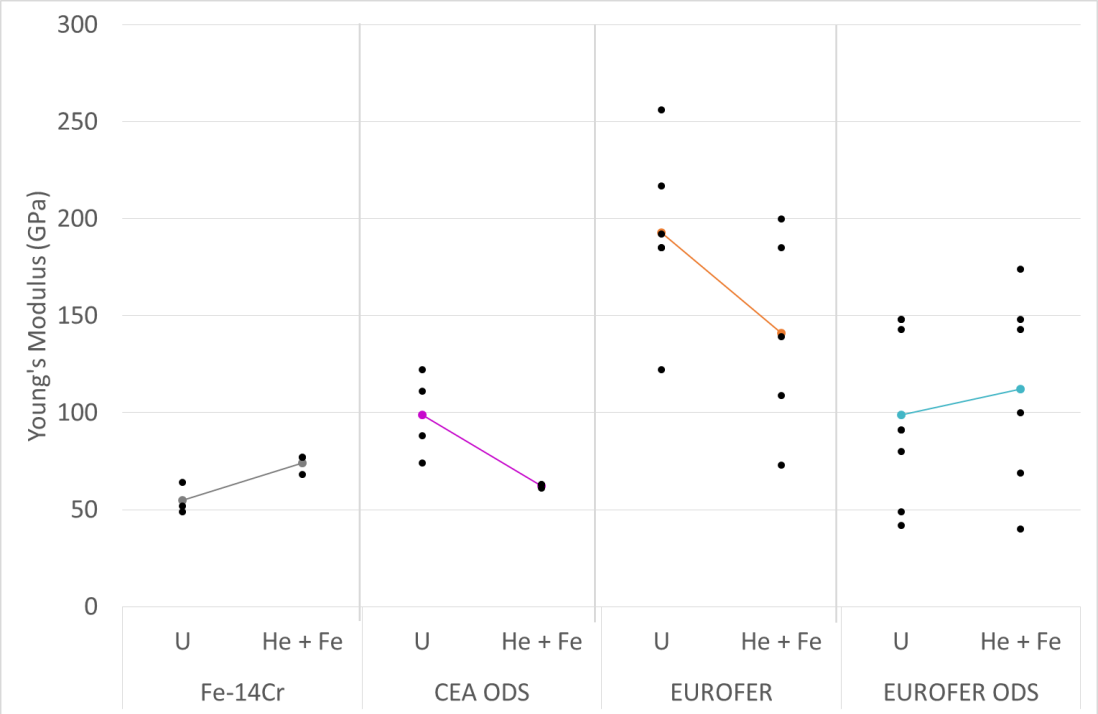

Figure 106 – Young's modulus of each micropillar with coloured points to denote mean modulus of each material/implantation condition

20 Discussion

The first consideration when analysing these data is whether the CalTech and Oxford tests are directly comparable. Therefore an extra pillar was cut in the Fe-14wt%Cr unimplanted material and tested in the Oxford system. From the results in Figure 107 it can be seen that the Oxford test lies within the range of the CalTech tests, has an almost identical elastic modulus and similar deformation/loading pattern. It can therefore be assumed that the data sets collected on the two different nanoindenters are comparable both qualitatively and quantitatively.

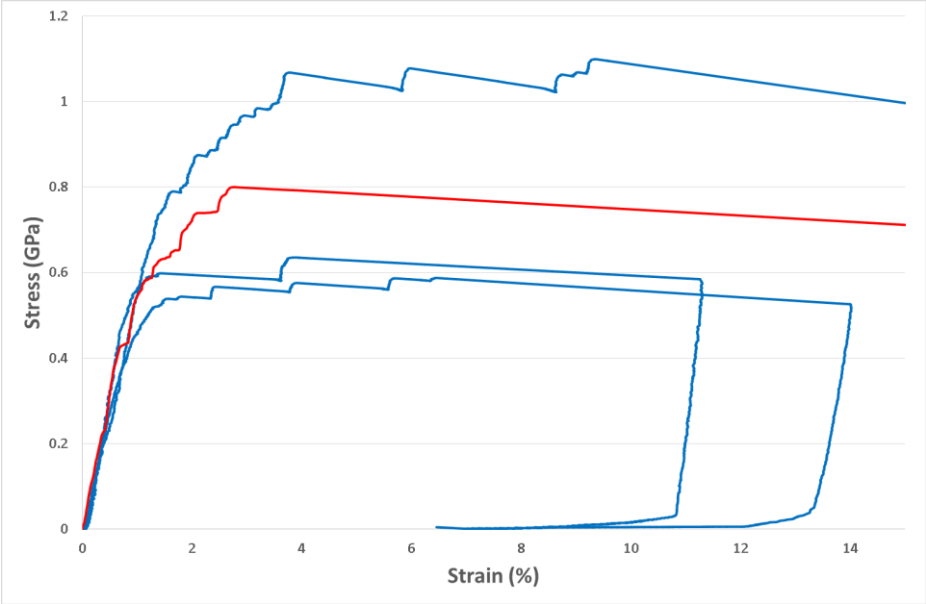

Figure 107 - Fe-14wt%Cr unimplanted - blue CalTech tested, red Oxford tested

Table 16 - Summary of deformation characteristics

Fe-14wt%Cr Unimplanted 3 pillars	Two or three individual deep slip lines.
Fe-14wt%Cr Implanted 3 pillars	Narrow band of shallow slip lines.
CEA ODS Unimplanted 4 pillars	Barrelling of top ~2μm of pillar.
CEA ODS Implanted 3 pillars	Barrelling down whole pillar length. One pillar also showed a single deep slip at the end of the test.
EUROFER Unimplanted 6 pillars	Barrelling of top ~2μm of pillar. Two pillars also showed shallow slip bands at the tip.
EUROFER Implanted 5 pillars	Barrelling down whole pillar length.
EUROFER ODS Unimplanted 8 pillars	Barrelling of top ~1μm of pillar. Four pillars showed shallow slip lines, or which three also had sheared off tips.
EUROFER ODS Implanted 6 pillars	Barrelling down whole pillar length. Two pillars showed shallow slip lines, or which one also had sheared off tip.

All the pillars show a period of elastic compression followed by a smooth transition into plastic deformation. The distinct deformation characteristics are summarised in Table 16. In Fe-14wt%Cr and CEA ODS plastic flow occurs in discrete strain bursts seen as horizontal lines on the stress/strain curves. In the EUROFER and EUROFER ODS, some strain bursts are visible, but many of the pillars have deformed with a smooth line and no obvious strain bursts; in unimplanted EUROFER there are no obvious strain bursts on any of the curves.

In Fe-14wt%Cr, the pillars are cut within a single grain. This means there will be very few dislocation sources within the pillar before ion implantation. As with the microcantilever testing (Chapter 5), the influence of the damage and introduction of dislocations caused by the gallium ions used for FIB milling should be considered. When FIB milling a specimen, some of the gallium ions used for removing material will become implanted in the surface. Previous work showed that this damage can cause marked changes in measured mechanical properties between the same materials produced by FIB and by non-FIB routes [171]. In this study all samples were manufactured using identical FIB routes, so all pillars will be affected to the same degree by the gallium damage. How the gallium interacts with the iron ion-irradiation damage is unclear, but the damage is limited to the top 30nm of the pillars. All marked differences in behaviour between implanted and unimplanted pillars are significantly below this level, which indicates that the deep iron ion damage (combined with implanted helium) rather than shallow gallium ion damage is likely controlling defect population.

In unimplanted Fe-14wt%Cr, slip is confined to a few discrete slip lines. This is similar to deformation seen in other single crystal pillar compression experiments [116][129]. This mode of slip is due to the small number of available dislocation sources within the pillars. With a typical dislocation density of $1x10^{14}m^{-3}$ in a well annealed

metal, it would be expected that each pillar would only contain at most a few dislocation sources. The size of the slip steps visible on the surfaces of the pillars (several hundred nanometres) indicates that several hundred dislocations have propagated from each active dislocation source.

CEA ODS, EUROFER and EUROFER ODS all have a much higher native dislocation densities than Fe-14wt%Cr (EUROFER ODS: 10^{15}–10^{16}m^{-3} [172]). With smaller grain sizes than Fe-14wt%Cr (Chapter 2, Section 9), there is also a greater chance of having grain boundaries contained within the pillars, meaning that a single slip plane cannot run from side to side across a pillar, as this will immediately suppress big strain jumps. Grain boundaries within the pillar can then act as dislocation sources [173]. The ODS materials also both contain oxide nanoparticles deliberately added as dislocation movement inhibitors.

As pillars in the small grained materials are compressed, dislocations will start to move to allow plastic deformation. Each dislocation will only be able to move a short distance, however, before it is restricted by other dislocations, ODS particles or a grain boundary, and it becomes energetically more favourable for another dislocation to move or source to propagate. This small movement of multiple sources is visible as the shallow slip lines and pillar barrelling.

The yield stress of each material was calculated as the stress at which there is significant deviation from the elastic deformation section of the curve. The mean value was then taken over all the pillars in each material and implantation condition.

20.1 Unimplanted/Implanted

As a material is implanted with heavy or self-ions (in this case Fe into Fe-Cr based alloys), the incident ions cause the formation of defects in the lattice. These defects can act as dislocation sources when the material is deformed. Implantation with light/small ions (in this case helium) fills interstitials, vacancies and defects in the material, which, at high enough concentrations, can lead to the formation of unstable bubbles and voids. During dual-beam implantation (e.g. He+Fe), the helium can fill the defects in the lattice as they are created by the incident iron ions. These helium and iron defects in the material can disrupt dislocation motion during mechanical testing and affect mechanical and deformation properties.

Table 17 - Mean yield stress (GPa)
(with min./max. range)
n is the number pillars tested in each condition.

	Unimplanted	n	U range	Implanted	m	I range	Difference
Fe-14wt%Cr	0.57	3	0.30 (-0.12, +0.18)	0.62	3	0.15 (-0.07, +0.08)	+0.05
CEA ODS	0.76	4	0.30 (-0.16, +0.14)	0.77	3	0.20 (-0.07, +0.13)	+0.01
EUROFER	1.57 *recalc. 1.40*	6 *4*	0.40 (-0.21, +0.19)	1.15 *recalc. 1.39*	5 *3*	0.45 (-0.24, +0.21)	-0.42 *recalc. -0.01*
EUROFER ODS	0.54	8	0.37 (-0.19, +0.18)	0.53	6	0.84 (-0.38, +0.46)	-0.01

Table 17 collates the mean yield stresses of each of the materials and implantation conditions and shows that there is no significant change in the mean yield stress in micropillars of any of the materials due to implantation except for EUROFER.

A closer look at the EUROFER data reveals two high outlying results in the unimplanted data and two low outlying results in the implanted data. These outliers were removed and the means re-calculated – noted *recalc.* in Table 17.

The updated mean data, without the outlying results, indicates EUROFER also has no significant change in yield stress due to implantation. The differences between unimplanted and implanted are all well within the scatter of results for each sample (U

range and I range in Table 17). It can therefore be assumed that implantation with 2000appm He + 4.5dpa of Fe ion damage has no significant effect on the yield stress of microcompression pillars. The yield stress data collected from these micropillar compression tests will be compared with the yield and hardness results of the other mechanical testing methods in Section 32, Table 36.

Despite the minimal changes in yield stress, there are, however, differences in the deformation modes of the different implantation conditions across the materials. The stress–strain graphs show strain-bursts in the deformation of most pillars. Each burst is due to rapid displacement during loading, corresponding to plastic flow along the visible slip lines. The correlation of the graphical strain bursts with plastic deformation of the pillar was verified using the live video imaging of pillar compression at CalTech.

Each strain burst corresponds to a dislocation source (or possibly a couple of sources) activating and allowing plastic deformation before a rise in stress to the next strain burst. In Fe-14wt%Cr the implanted material shows many more, and shorter, strain bursts than the unimplanted material. In CEA ODS, the bursts are almost equal in size between the implanted and unimplanted conditions. EUROFER shows no significant strain bursts at all (just a smooth curve). EUROFER ODS mostly only shows significant strain bursts in the unimplanted pillars.

In unimplanted Fe-14wt%Cr the pillars are sheared along a small number of widely spaced slip lines; video footage showed each slip propagating individually. In implanted Fe-14wt%Cr the slip tends to be concentrated in one or two wide dense bands, which propagated in quick succession, next to each other. This effect has been seen before in previous work on Fe-Cr alloys subject to self-ion implantation [164]. There it was concluded that the mechanical response in micropillar testing is controlled by the activation of dislocation sources, rather than dislocation propagation. Once a dislocation source is activated, slip will occur on a single slip plane. Once the

dislocation source is exhausted (possibly as a result of the nucleated dislocation segment leaving the pillar) sufficient stress must build up to nucleate another dislocation source. The dislocation source with the next lowest activation energy may not be adjacent to the previous slip, hence the randomly spaced gaps between slip bands. Recent MD modelling of iron micropillars has shown the formation of localised slip bands very similar to those seen here in the unimplanted pillars [174].

The deformation mode in the Fe-14wt%Cr implanted pillars is distinctly different from that in the unimplanted ones, with slip concentrated in a single set of parallel glide planes. Again, this follows the results seen before in other Fe-Cr alloys [164]. The increased frequency and reduced size of strain bursts indicates the presence of dislocation sources within the glide band operating at stresses not much higher than the current flow stress. The formation of this broad glide band in the implanted pillars may be due to the interactions between glissile and sessile dislocation loops and local stress concentrations due to pile-ups at dislocation loops. Once a dislocation source has been activated and started to run out, the lowest energy option is for a closely parallel slip plane to activate, possibly through the interactions of glissile and sessile dislocations in adjacent planes. Each slip plane only has to propagate a short distance before it becomes energetically more favourable for another to activate, leading to the closely spaced band seen here.

Unlike Fe-14wt%Cr, the other three materials show fewer significant differences between the deformation of implanted and unimplanted pillars. In Fe-14wt%Cr the size of the strain bursts decreases in the implanted condition. This effect can be seen to a much lesser degree in CEA ODS and EUROFER ODS, where the strain bursts become less obvious (and in the case of EUROFER ODS almost disappear). Unimplanted EUROFER shows no strain bursts at all and implanted EUROFER only shows very minimal kinks in the graphs indicating tiny strain bursts. Overall, the smaller size of

strain bursts in the small grained materials (compared with Fe-14wt%Cr) is most likely due to the grain structure of the pillars. Small grains mean grain boundaries within the pillars which will act as disruptions/blocks to slip; only a small amount of dislocation movement will be possible before a grain boundary is reached.

The decrease in size of the strain bursts between unimplanted and implanted in the ODS materials may also have a similar cause to the decrease seen in Fe-14wt%Cr – implantation increases the number of easily activated dislocations, and therefore it becomes more energetically favourable for small lengths of slip to occur on each plane before jumping to another.

In CEA ODS, both unimplanted and implanted sets exhibit bowing of the pillar sides and show surface slip lines starting to form. The only slight difference is that the unimplanted pillars barrelled only in the top ~2μm, whereas the implanted barrelled along their full length. For the two EUROFER materials the unimplanted pillars have a stronger propensity to form slip lines and the implanted pillars barrel down their length. In all three materials, however, there is no apparent significant effect like the single spaced/narrow band of slip lines seen in Fe-14wt%Cr. The most significant difference between Fe-14wt%Cr and the other three materials is in the microstructure: Fe-14wt%Cr has very large grains, no precipitates; others have small grains with precipitates and additional alloying elements. As with the stress-strain response discussed above, it is presumably the interaction between the implantation and the microstructure that has an effect on the deformation mode seen.

20.2 Non-ODS/ODS Materials

The materials in this project have such varied microstructures that direct comparison of numerical data between materials is inadvisable. Visual evidence of their deformation modes, however, can provide a useful insight into dislocation motion and its interaction with implantation and microstructural defects.

In the Fe-14wt%Cr materials there is a very noticeable difference in deformation between the model alloy and ODS variant (CEA ODS). The mean yield stress (Table 17) of the ODS pillars is 33% higher than Fe-14wt%Cr in the unimplanted condition. This difference is to be expected as the materials have very different microstructures which affect the mechanical properties. The difference between EUROFER and EUROFER ODS is the opposite, with the ODS variant yield stress 60% lower than ordinary EUROFER. In fact, the EUROFER ODS pillars have a mean yield stress comparable with the Fe-14wt%Cr pillars. The order of yield stresses of the materials does not correlate at all with the results from the other experiments (yield stress increasing through Fe-14wt%Cr, EUROFER, EUROFER ODS, CEA ODS – Section 31.2).

The EUROFER results in this chapter are anomalous. It has been demonstrated [170] that increase in taper angle of the pillar causes an decrease in measured yield stress, however, the taper of the EUROFER pillars is not significantly different to any of the other materials. It is possible that the increased yield is a local effect in the particular EUROFER sample (all pillars were located within an area 5mmx1mm). The samples revealed no obvious differences in microstructure under optical or SEM viewing; chemical and EBSD analysis was not performed. It may be that the particular area tested had a non-typical microstructure (such as significantly smaller grain size) leading to erroneous results. The EUROFER general EBSD map in Chapter 2, Section 9.3 shows how inhomogeneous the microstructure can be.

In Fe-14wt%Cr, the video footage can be used to correlate the big strain bursts and the slip band movement in the pillar. In CEA ODS, the multiple small strain bursts do not appear in the video as distinct slips, rather as a slow barrelling deformation of the sides of the pillar. For the EUROFER type materials, there is no video footage, but comparison of before and after images reveals that both EUROFER and EUROFER ODS exhibit barrelling of the pillar sides and show visible slip bands on the pillar surface in the unimplanted conditions. The conclusion that can be drawn from these results is that there appears to be no specific effect of the ODS particles on how the pillars deform. Since the material with the most different results is Fe-14wt%Cr, it is likely that it is the grain size and presence of general oxide/carbide particles that have more of an effect (CEA ODS, EUROFER and EUROFER ODS are all very similar in that respect).

Fe-14wt%Cr has very few dislocation sources, therefore the addition of damage through implantation makes a significant difference to the material properties and deformation mode. In the other materials, the pillars will contain grain boundaries; the CEA ODS pillars will all contain ~2 grains across the pillar diameter and ~8 grains down the pillar length, EUROFER and EUROFER ODS have slightly larger grains and therefore may not contain grain boundaries vertically within the pillar, but will contain three or four horizontal grain boundaries. These grain boundaries present in the pillars act as dislocation sources, so these materials will have a higher initial grain boundary density than Fe-14wt%Cr. Implantation still increases the number of sources, but the high number already present means there is less need for the implantation introduced sources to activate during mechanical deformation. This explains the minimal difference between the unimplanted and implanted pillar deformations. The more similar dislocation sources present in a material, the shorter distance each source will slip before it becomes more energetically favourable for another source to activate. Therefore, in materials with high dislocation source density, each strain burst is tiny,

eventually leading to a smooth curve (such as seen in the EUROFER materials). The differences between individual pillar graphs will be due to the exact local microstructure of each pillar.

21 Conclusions

Analysis of all the above data concludes that implantation with 2000appm helium and iron ions to cause 4.5dpa of damage has limited effect on the yield stress of all four materials when tested using micropillar compression. The implantation does have an effect on the deformation mode, and this is most obvious in Fe-14wt%Cr. The implantation increases the number of dislocations in the material, allowing easier propagation, leading to a greater number of small strain bursts than in the unimplanted equivalent pillars.

Chapter 5
Microcantilever Bend Testing

22 Methodology

Micromechanical testing enables very small amounts or thin films of material to be subjected to standard mechanical property tests (compression, tension, torsion etc.).

FIB machining is used to cut nano- and microscale cantilevers and pillars for bend and compression testing of thin films (e.g. an ion implanted damaged layer) [121][123][126][164][169]. These are then tested with a nanoindenter to determine mechanical property data on a small scale.

For information on specific grain orientations or grain boundaries, the dimensions, shape and notching of cantilevers can be adjusted according to the properties being tested. Tests can also be performed under a range of temperatures and loading conditions.

Microcantilevers are subject to various size effects which can cause changes in mechanical loading response as the cantilevers become smaller [136]. These are due to the restricted movement of dislocations within the test volume (compared with a bulk specimen) and the larger free surface area to volume ratio.

Hardie [175] investigated the size effect observed in cantilevers in similar materials to those in this study (Fe-Cr alloys). His work showed that proof stress rises as the height (thickness) of the microcantilever decreases below ~2μm. Below this threshold the size effects are dominated by the low to zero number of initial dislocations within the test volume. To produce relevant mechanical property data, the cantilever size should be maximised to reduce these size effects.

The maximum cantilever size is limited by FIB constraints and implantation depth. The speed of FIB machining is dependent on the beam current. A higher current (e.g. 3000pA) will remove material faster, but the beam will be wider, thus producing less accurate structures. The initial milling of a cantilever must be reasonably accurate, otherwise the final stages will take longer and/or the cantilever will be unsuitable for testing. Accuracy requires a lower current (~100pA) so the size of cantilever is limited by the FIB time available. In unimplanted materials, the size limit is dependent on the available microscope time. Additionally, in order for the mechanical property results to be representative of the implanted conditions, the entire cantilever must be contained within implanted material. Details of the implantations used in this project are discussed in Chapter 2, Section 11. The depth of the implantations was limited to 3μm in the 2000appm He and 1μm in the 75appm He experiments. To make analysis and comparison of the results in different materials easier, all the cantilevers were made to approximately the same dimensions. An equilateral triangle is a simple cross-section to manufacture and has the benefits of producing easily analysable, reproducible results using methods such as simple beam theory. All the cantilevers were cut to ~3μm side triangles giving a depth of ~2.6μm. This meant the whole of the 2000appm He cantilever was within the implanted layer, whereas the 75appm He implantation was only to a depth of 1μm. If cantilevers had been cut to fit within this layer, the difference in properties due to the size effect would have been very large. In a triangular cross-section cantilever, the neutral axis (the division between tensile and compressive during bending) is one third of the height down from the top surface. Therefore, although the 75appm implanted layer did not fill the entire cantilever, the whole tensile zone was within the damaged region. The maximum compressive stress is at the lower surface, and so, was not within the implanted layer. Quantitative results, therefore, will include

a contribution from the unimplanted bulk, but any differences visible in surface deformation can be attributed to the implantation.

Microcantilever testing is most commonly used to investigate yield stress, modulus and fracture toughness [126]. The original aim of the cantilever tests in this project was to examine how implanted helium concentration changes the fracture properties of grain boundaries. However, the intrinsic properties of the materials being tested meant that fracture testing was not possible. Even at large deflections of the beams, only plastic deformation was seen; no fracture was evident.

22.1 Sample Preparation

Samples of each material were prepared as described in Chapter 2, Section 10. The stub-mounted samples were then loaded into the FIB for cantilever milling.

22.2 Focused Ion Beam Milling of Microcantilevers

The cantilevers were milled using a combination of three Focused Ion Beam Microscopes due to the limited time available on each. The systems were a single beam FEI FIB 200, dual-beam Zeiss Auriga FIB-SEM and dual-beam Zeiss NVision 40 FIB-SEM.

Cantilevers were prepared in a set of stages at different milling currents. Initial deep trenches were cut perpendicular to the surface at a high milling current (3000pA). The outer trench dimensions did not need to be specific; they were cut to at least three times the width of the cantilever. The dimensions of the rough cantilever needed to be at least 1µm larger in all dimensions than the final desired cantilever to allow for the material cut off in the next steps (Figure 108 and Figure 109).

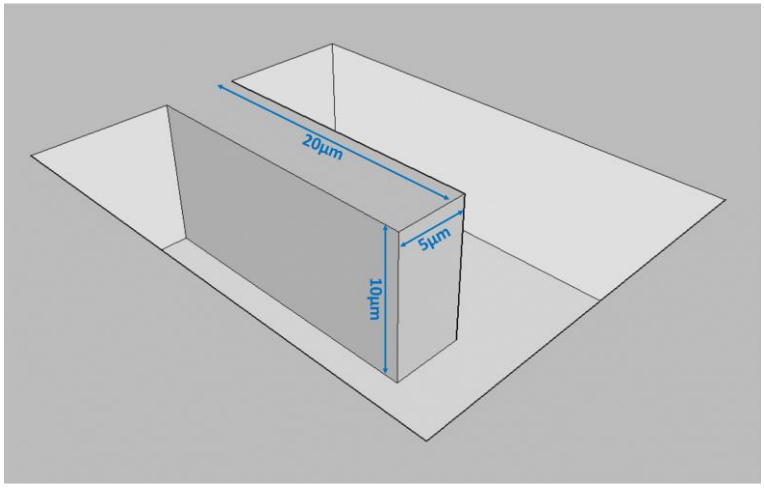

Figure 108 - Trenching dimensions

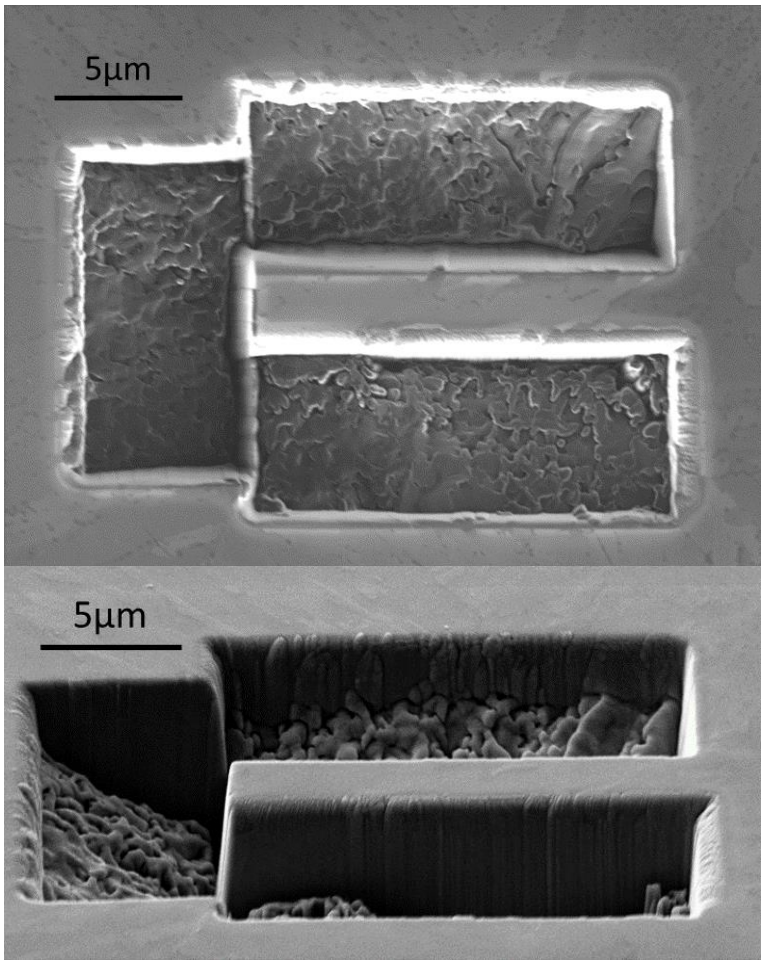

Figure 109 - Initial trenching in Fe-14wt%Cr unimplanted
(FIB imaged perpendicular to the surface and SEM imaged at 54° to perpendicular).

Once the initial trenching was performed, the milling current was reduced to ~600pA and the sample tilted by 30°. The cantilever was then undercut from both sides close to the final required dimensions (Figure 110 and Figure 111).

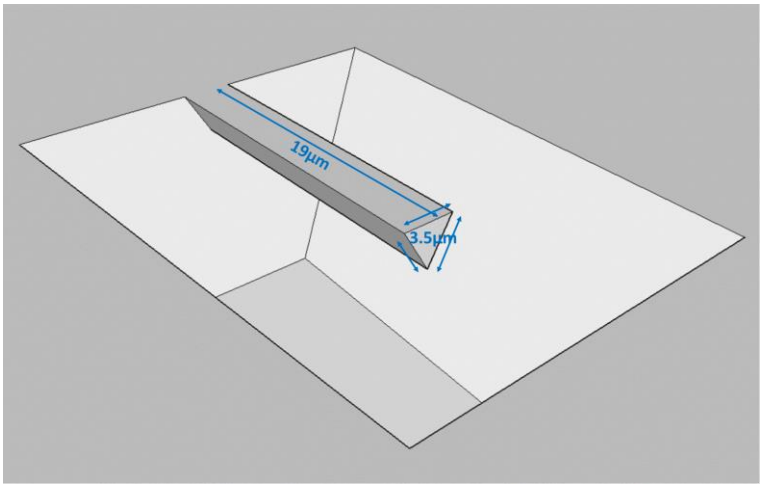

Figure 110 - Undercutting dimensions

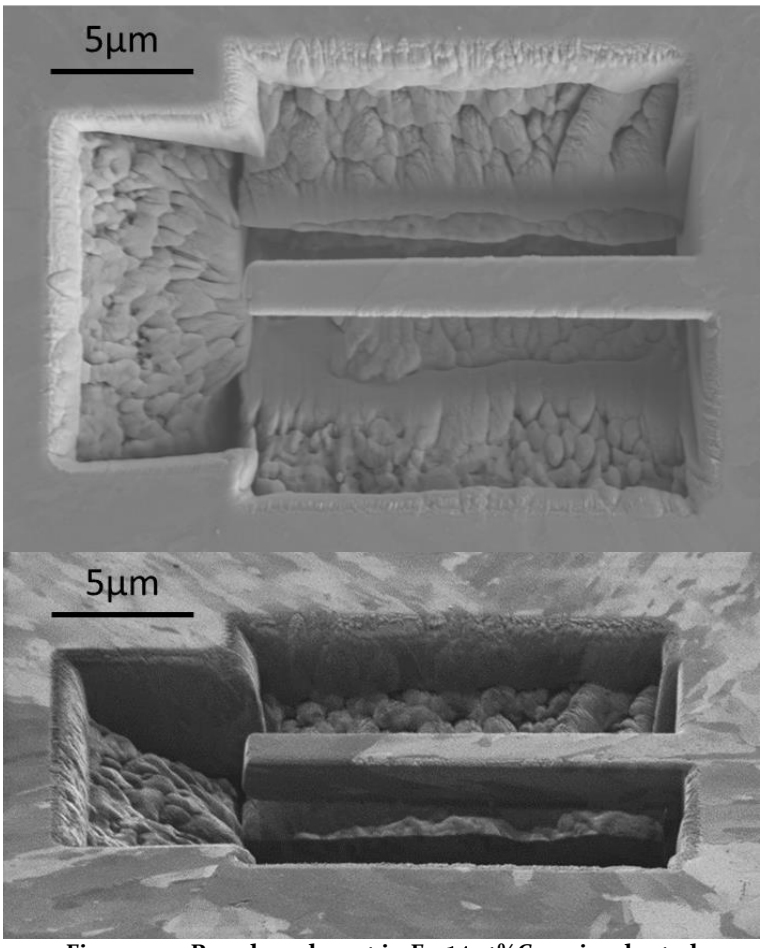

Figure 111 - Rough undercut in Fe-14wt%Cr unimplanted
(FIB imaged perpendicular to the surface and SEM imaged at 54° to perpendicular).

As the undercuts are made, some milled material will be re-deposited in the trench (which is not an issue) but some will also be deposited on the sides of the cantilever; the final step is to polish this off. The current is dropped again to ~100pA and final undercuts were made to give a smooth sided cantilever with an equilateral triangle cross-section. The finished cantilever was SEM imaged and the cross-section dimensions, measured using Gatan Digital Micrograph, were recorded for use in later analysis (Table 18). The cantilever height was measured with the sample viewed at 30° to perpendicular, therefore actual height equalled twice measured height.

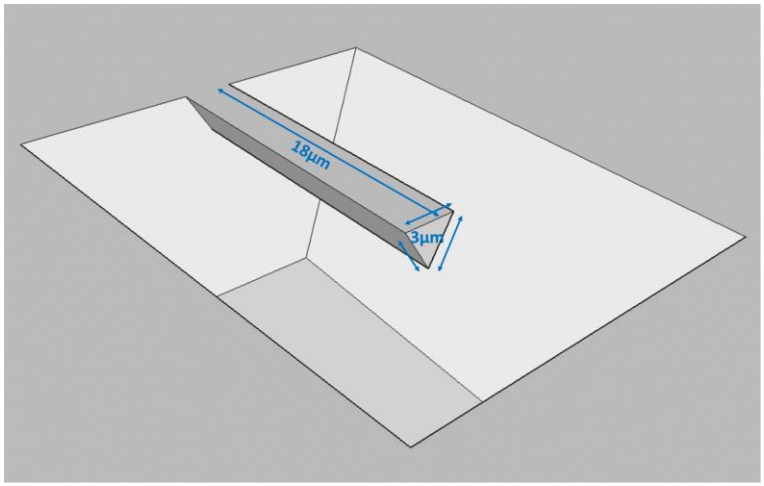

Figure 112 - Final dimensions

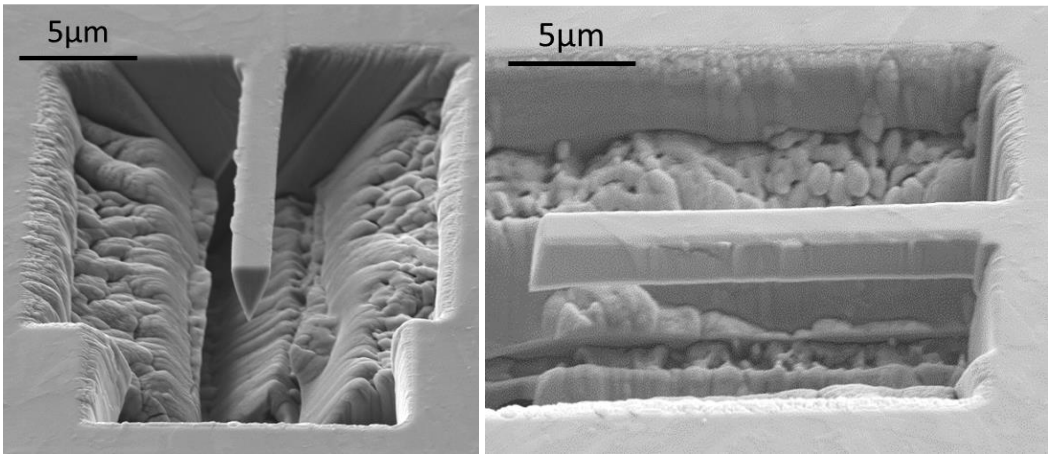

Figure 113 - Final polish in Fe-14wt%Cr unimplanted (SEM imaged at 54° to perpendicular).

22.3 Microcantilever Bending Using a Nanoindenter

The finished cantilevers were tested using an MTS Nanoindenter XP fitted with piezo-electric stage for fine scale X-Y movements. Using an optical microscope, locations could be placed to within an accuracy of ±0.5μm. This system was also used for hardness nanoindentation (Chapter 3). Using the piezo-electric stage, the sharp diamond tip can also be scanned across a surface to provide a topological map similar to an atomic force micrograph with sub-nanometre X-Y dimensional resolution.

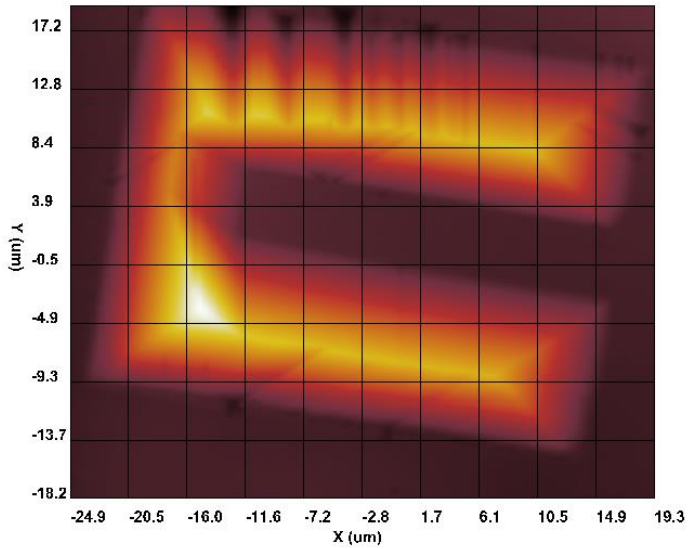

Figure 114 – Typical topographical cantilever map

This topographical map (Figure 114) was used to accurately position the nanoindenter tip over the free end of the cantilever, prior to controlled loading to a pre-set vertical displacement. In this project all cantilevers were tested under the same loading conditions: 2000nm maximum cantilever vertical displacement of the free end and strain rate target $0.02s^{-1}$. The vertical displacement and strain rate were measured by continuous stiffness feedback of the tip.

The tested cantilevers were SEM imaged again to locate the loading point on the beam. Following loading, a very small indentation is left in the cantilever surface from the sharp point of the indenter; finding this (Figure 115) allows for accurate measurement of the bending length of the cantilever. Bending length is measured as the distance from nanoindenter contact (i.e. visible surface indentation) to the fixed end of the cantilever.

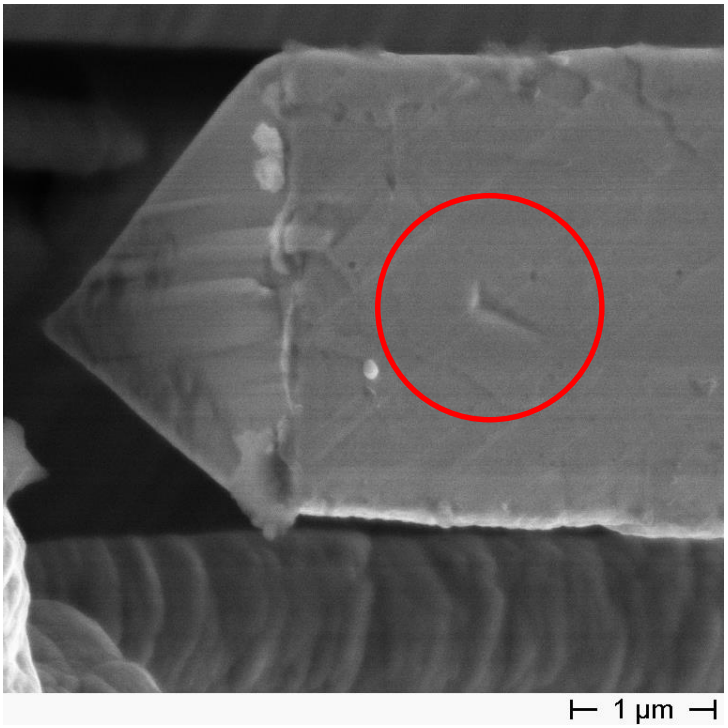

Figure 115 - Unimplanted EUROFER ODS cantilever with surface nanoindentation circled.

SEM images were also used to see the plastic deformation resulting from the bending. In Figure 116, the top cantilever is in the 'As-milled' state, ready to test. The bottom cantilever has been tested and the top surface is no longer parallel to the bulk surface; testing has caused plastic deformation.

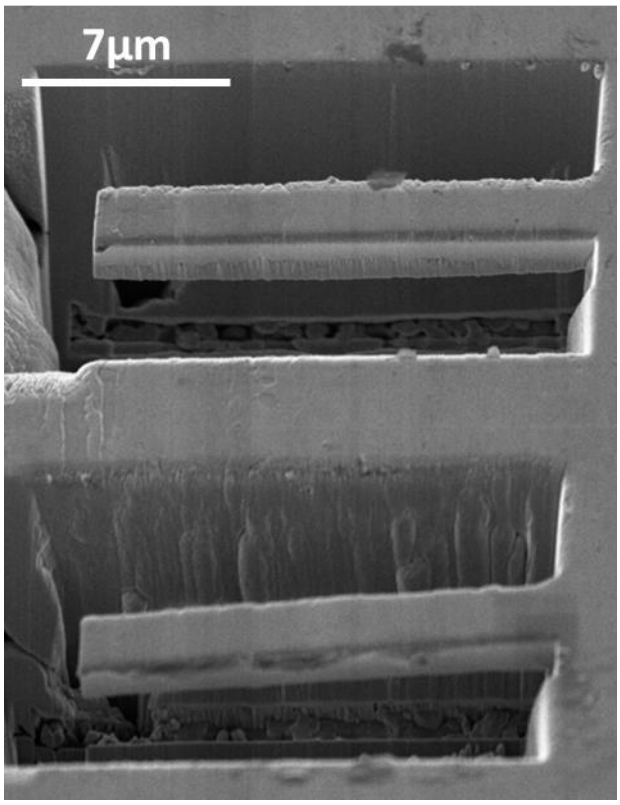

Figure 116 - CEA ODS + 2000appm He – top cantilever as-milled, bottom cantilever as-tested – Note the bottom cantilever is no longer parallel with the sample surface.

23 Results

23.1 Load-Displacement

The nanoindentation software outputs load-displacement data to Microsoft Excel for analysis. The nanoindenter was set to displace each cantilever by 2000nm, measured from the point when the tip touched the surface, and recognised as a significant sudden hardness increase. The loads required to deform these cantilevers, however, are sufficiently small that the surface find calculation does not always work effectively. Graphs were drawn from the raw data and the surface position manually determined where required (tip contact with the surface was taken as the point of sudden gradient increase). This means that the actual displacements in the tests vary from 1000nm to >2000nm.

In some tests, the trench around the cantilever was not wide enough and the indenter tip hit the sides during the deformation (Figure 117). The load required for displacement in the bulk material was significantly higher than for cantilever displacement. Once the tip hit the surface, the load rapidly increased and data from the cantilevers was obscured. In these cases, the data was cut off at the point where the load started to rise, hence some lines of data show less than 1000nm displacement.

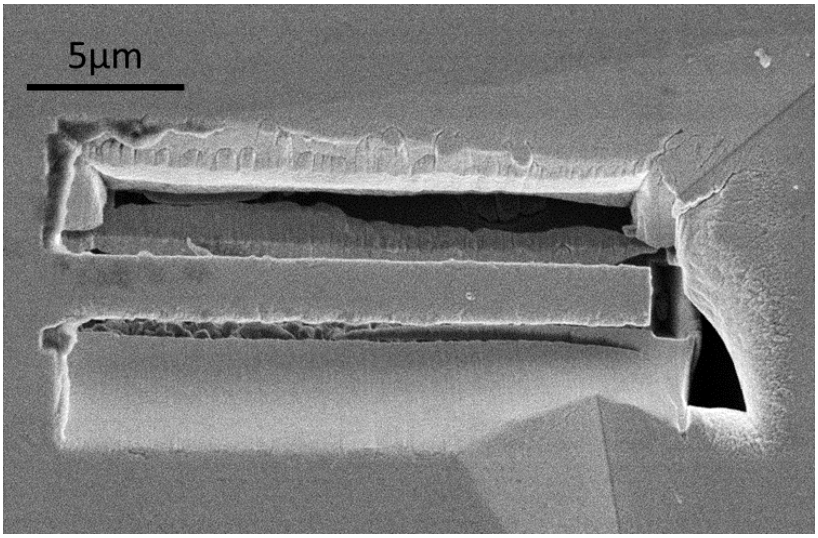

Figure 117 - A test where the indenter tip has hit the sides and started to indent bulk material.

Figure 118 shows a specimen load-displacement graph – Fe-14wt%Cr unimplanted cantilevers. Table 18 contains the measured dimensions of each of the cantilevers the tests of which are shown on the graph. All the graphs can be found in Appendix B. Cantilevers were cut in each of the four materials, in each of three implantation conditions – unimplanted, 75appm He and 2000appm He (except for 75appm He in Fe-14wt%Cr where no sample was produced).

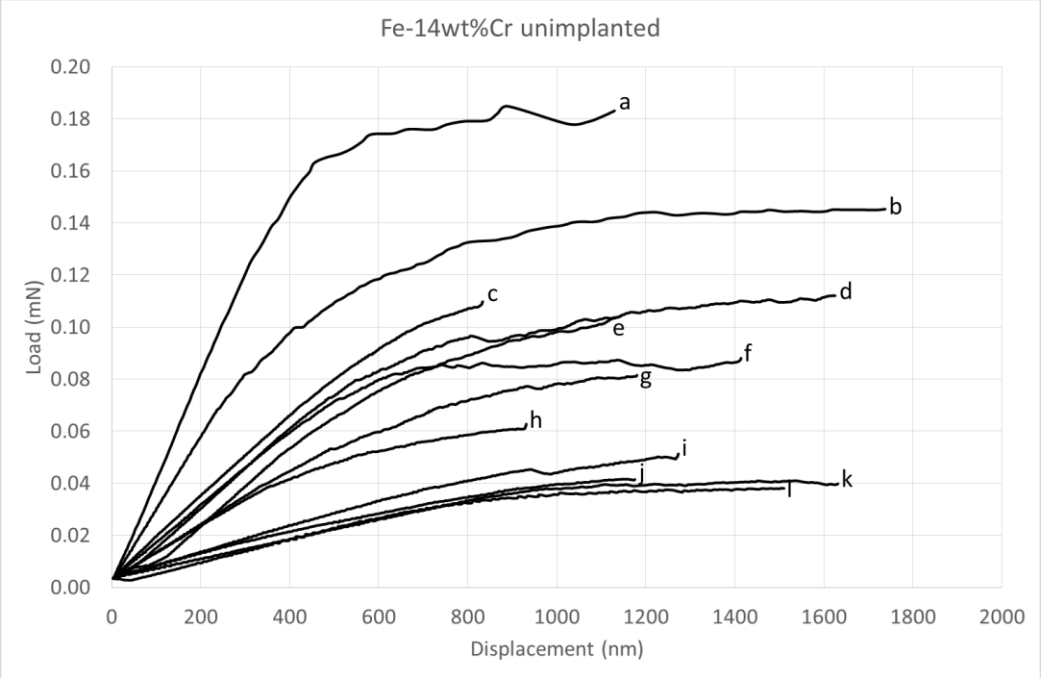

Figure 118 – Load vs. Displacement example graph

Table 18 - Fe-14wt%Cr unimplanted cantilever dimensions

Line	***Width (μm)***	***Height (μm)***	***Length (μm)***
a	2.52	3.02	16.78
b	2.71	3.16	14.91
c	2.74	3.14	16.23
d	2.71	3.68	18.65
e	3.59	4.28	15.94
f	2.38	2.90	16.20
g	2.09	2.84	14.39
h	2.50	3.10	15.65
i	3.11	3.64	16.39
j	2.62	3.26	18.30
k	2.45	3.04	15.58
l	2.56	3.02	14.13

23.1.1 Load-Displacement Summary

The usual method of comparing deformation curves would be to record the yield load of each cantilever by taking the load point at which the graph significantly curves away from a straight line (i.e. at the change between elastic recoverable and plastic permanent deformation). As seen in Figure 118 and the other load displacement graphs in Appendix B, many of the curves show no clear transition from elastic to plastic. Therefore, to allow for direct comparison of the raw data of all the materials and implantation conditions, the load at 1000nm displacement was recorded for each line instead of the yield load. Figure 119 plots load recorded at 1000nm displacement for all tested cantilevers. The coloured lines join the mean load value of each implantation condition.

Figure 119 shows the full range of load results. CEA ODS in the unimplanted and 75appm He conditions has several outlying results above 1mN (the lines of these points are indicated with red arrows in Figure 193 and Figure 195 in Appendix B). A first assumption would be that these cantilevers have larger dimension than average, thereby requiring a correspondingly higher load to displace them. SEM imaging/measurements, however, showed no significant differences, therefore it must be assumed that these load differences are due to variations in localised microstructural properties – this will be further analysed and discussed in Section 24.1.

To allow for better comparison of the materials, the range of load data plotted is reduced to load points below 1mN, resulting in Figure 120. The coloured points show the mean of each data set with lines joining the mean values to investigate any correlation in the trends within each material (in CEA ODS, it is the mean of the data below 1mN shown).

U = unimplanted, 75 = 75appm He, 2000 = 2000appm He.

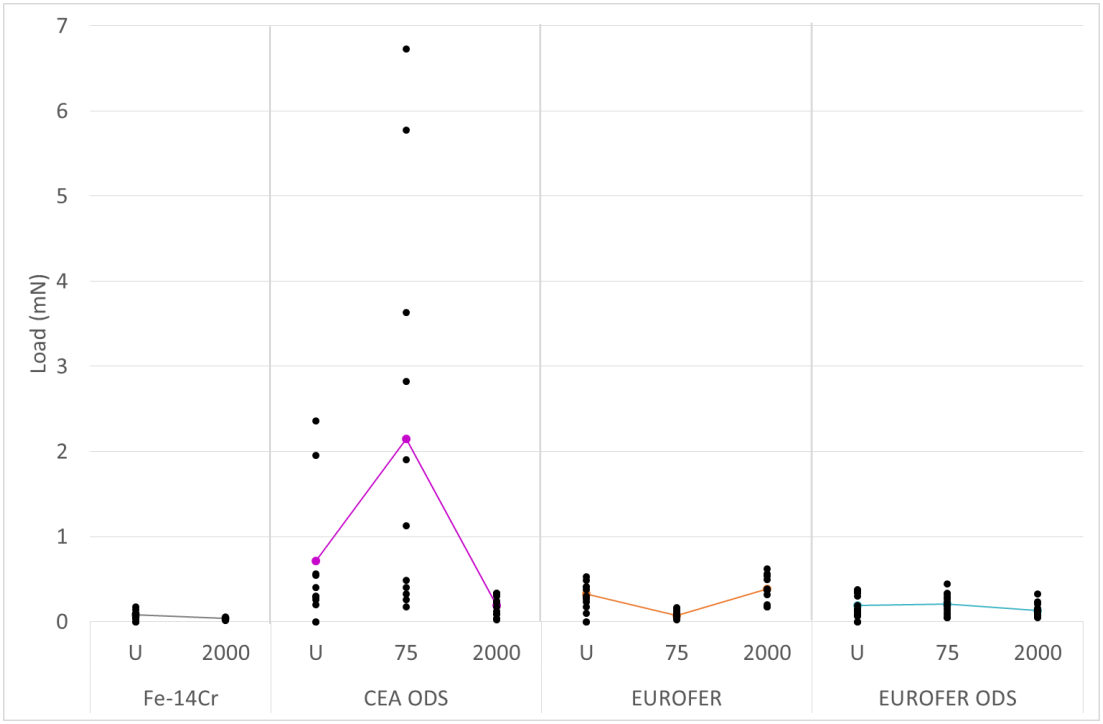

Figure 119 - Load on each cantilever at 1000nm displacement with coloured points to denote mean load of each material/implantation condition.

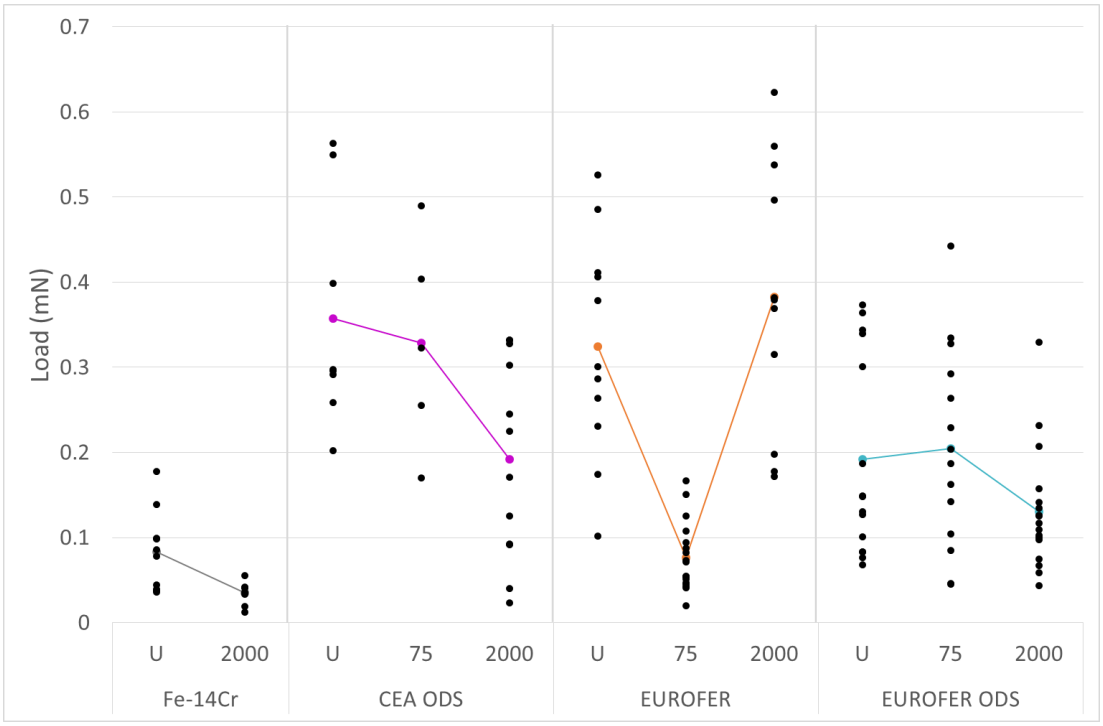

Figure 120 - Reduced load range without high anomalous outliers.

23.2 Stress-Strain

Although efforts were made to make all the cantilevers identical, inconsistencies in FIB milling and material microstructure mean that there was some variation in beam sizes. To compare the data across all the cantilevers, therefore, the load-displacement data must be normalised to stress-strain using simple beam theory.

23.2.1 Simple Beam Theory

Simple beam theory allows stress and strain to be calculated using the following relationship:

Equation 3

$$\frac{\boldsymbol{\sigma}}{\boldsymbol{y}} = \frac{\boldsymbol{M}}{\boldsymbol{I}} = \frac{\boldsymbol{E}}{\boldsymbol{R}}$$

σ = stress in the beam

y = perpendicular distance, neutral axis to beam edge;

for an equilateral triangular beam: $y = \frac{2}{3}h$

M = bending moment; load (P) * length (l)

I = second moment of area (see below)

E = Young's modulus

R = radius of curvature of the neutral axis of the beam due to bending moment M

For the triangular cantilever beams the neutral axis is one third of the height down from the top surface and the second moment of area is:

Equation 4

$$I = \frac{wh^3}{36}$$

w = beam width

h = beam height

Using these equations the stress (σ) in the beam can be calculated:

Equation 5

$$\sigma = \frac{24Pl}{wh^2}$$

Absolute strain (ε) is calculated by:

Equation 6

$$\varepsilon = \frac{2\delta h}{l^2}$$

δ = displacement of the beam

Figure 121 to Figure 133 show load-displacement data for each material and condition converted to stress-strain curves. All values are in absolute strain i.e. 0.02 absolute strain =2% strain.

23.2.2 Fe-14wt%Cr

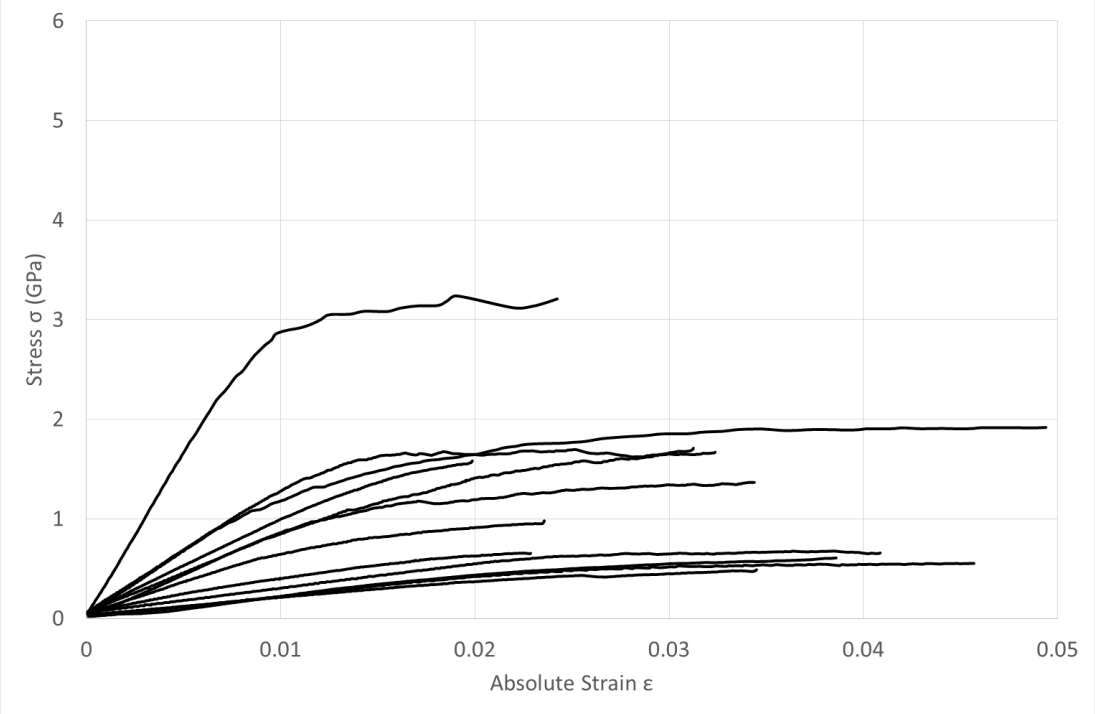

Figure 121 - Stress vs. Strain - Fe-14wt%Cr unimplanted

Although cantilevers were tested in Fe-14wt%Cr 2000appm, the conversion to stress-strain revealed an error in the testing. Imaging of the tested cantilevers revealed plastic bending, however, the stress-strain graph suggested only elastic deformation with non-zero intercepts. Unfortunately there was not time to repeat these experiments and this data has been omitted from further analysis.

23.2.3 CEA ODS

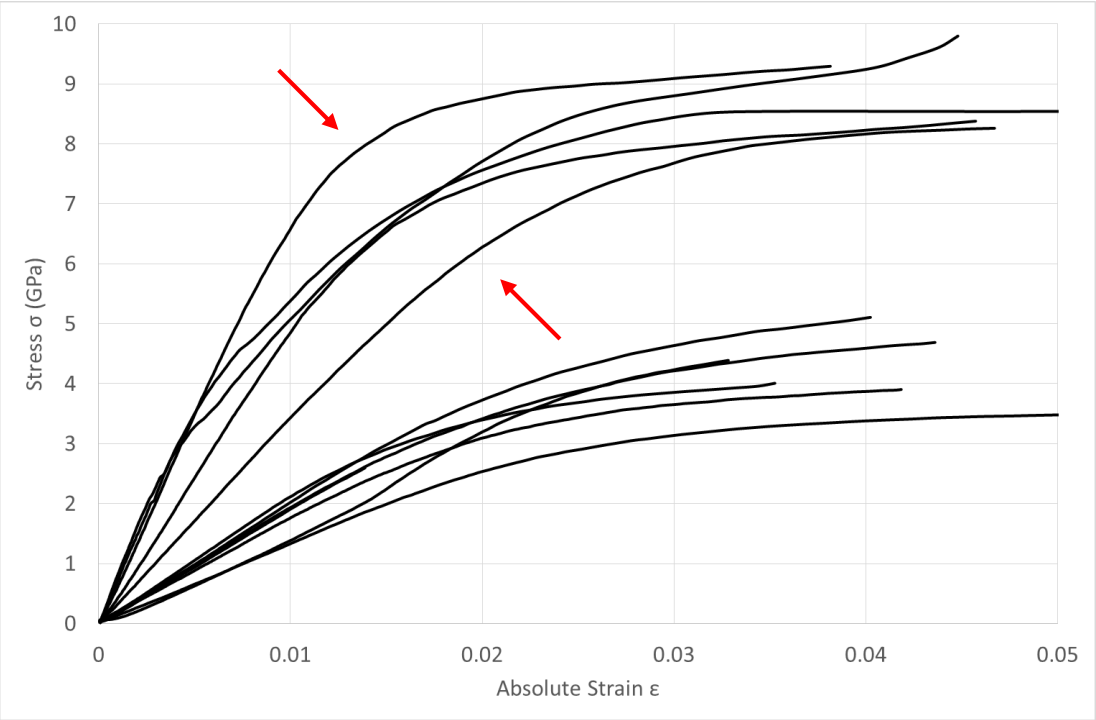

Figure 122 - Stress vs. Strain - CEA ODS unimplanted, full range
Red arrows indicate the tests with stress greater than 6GPa at a strain of 0.02 – these results are anomalous and will be discussed later in Section 23.2.6.

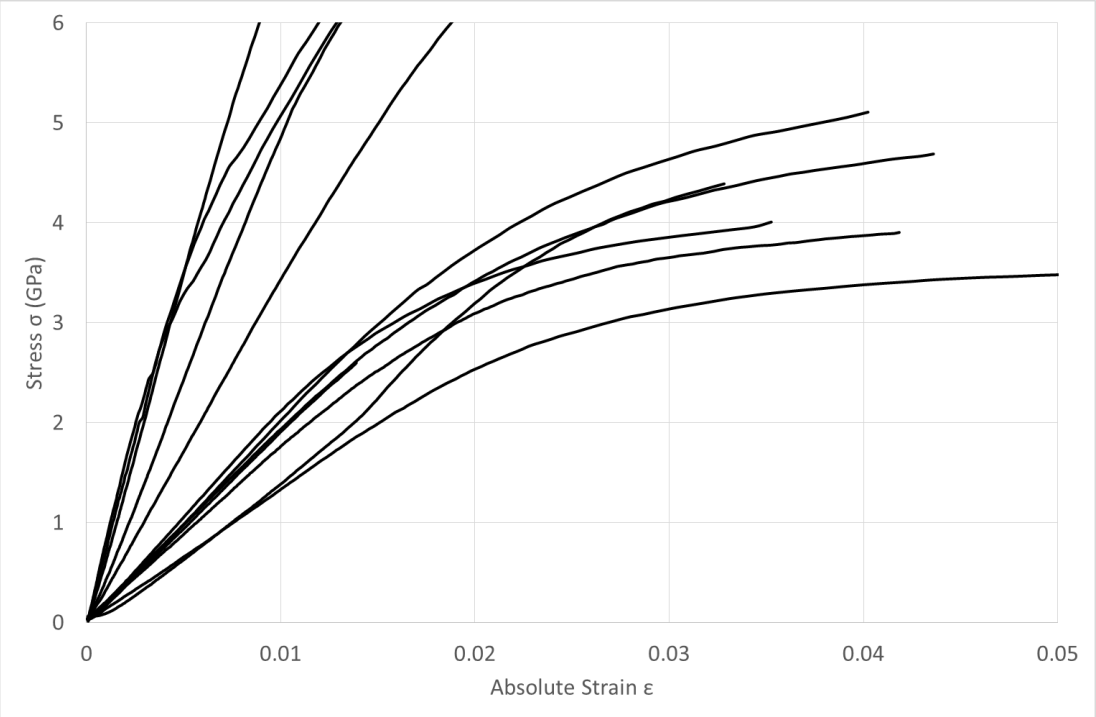

Figure 123 - Stress vs. Strain - CEA ODS unimplanted, reduced range

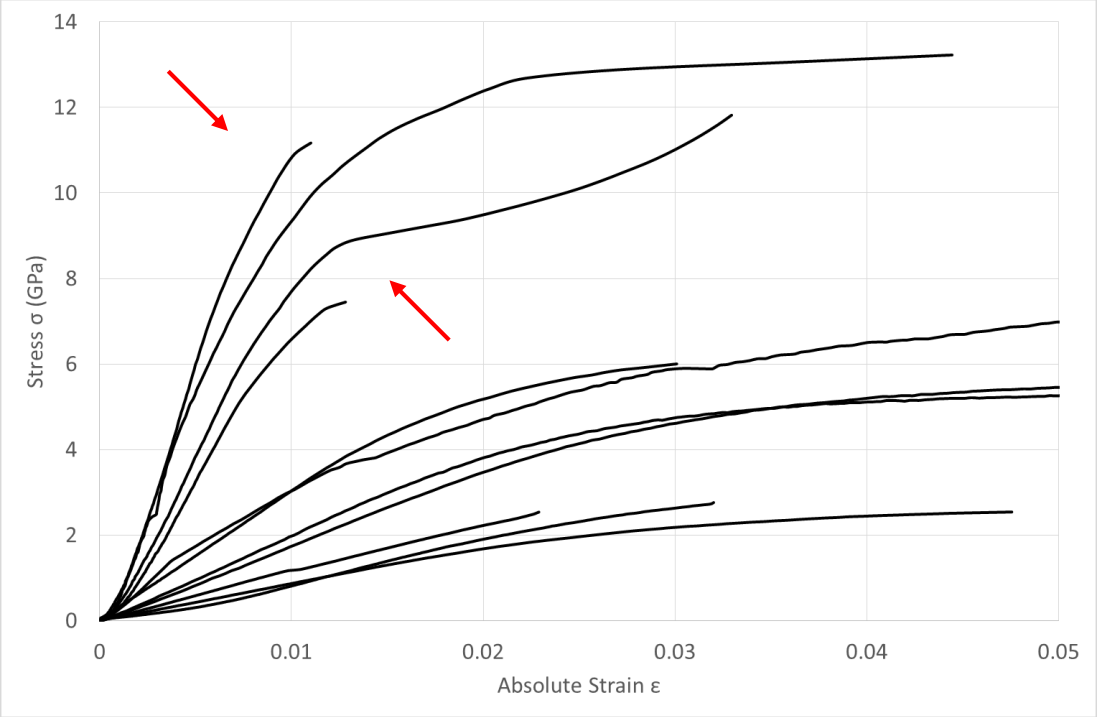

Figure 124 - Stress vs. Strain - CEA ODS 75appm He, full range
Red arrows indicate the anomalous tests with stress greater than 6GPa at a strain of 0.02.

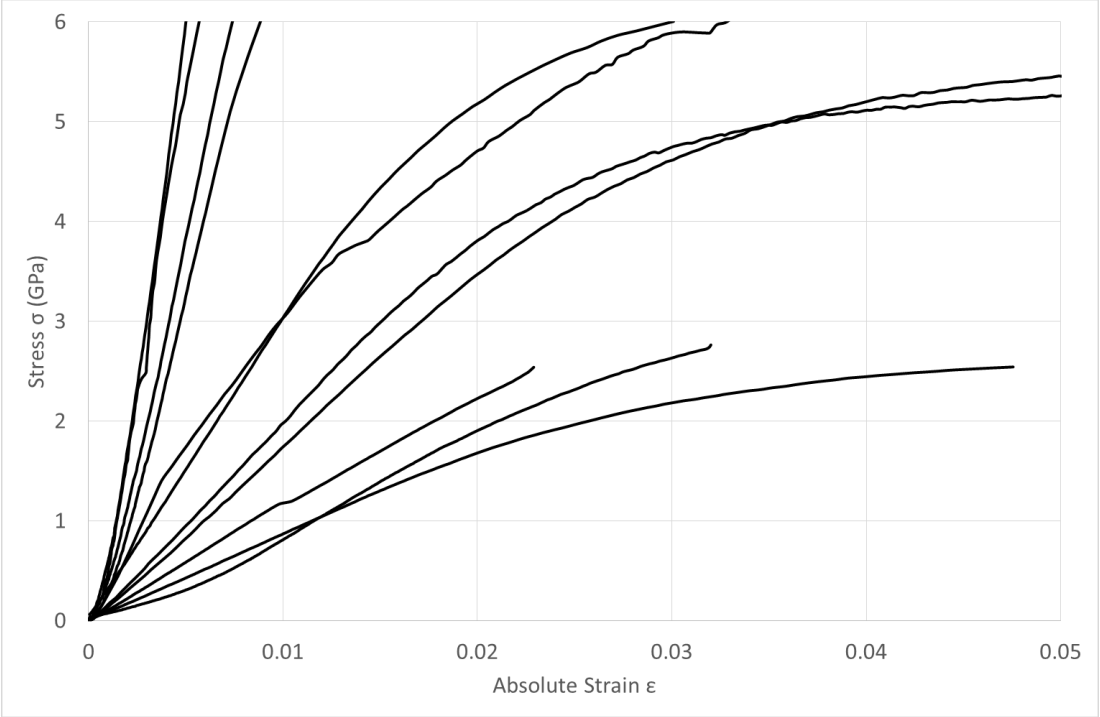

Figure 125 - Stress vs. Strain - CEA ODS 75appm He, reduced range

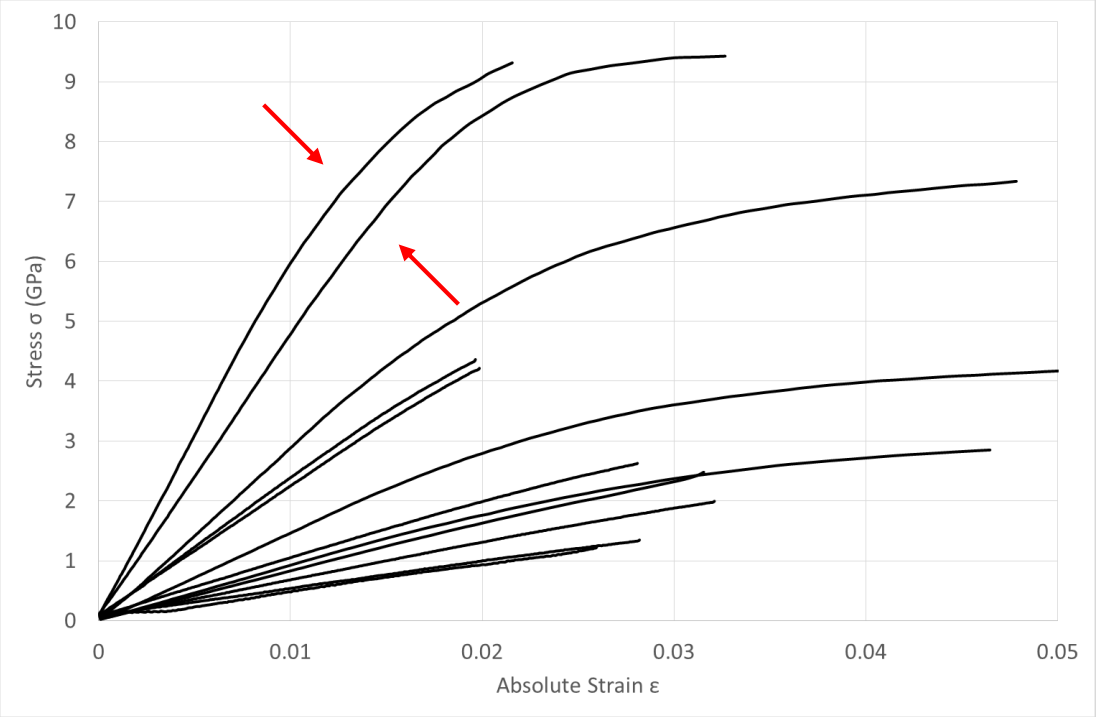

Figure 126 - Stress vs. Strain - CEA ODS 2000appm He, full range
Red arrows indicate the anomalous tests with stress greater than 6GPa at a strain of 0.02.

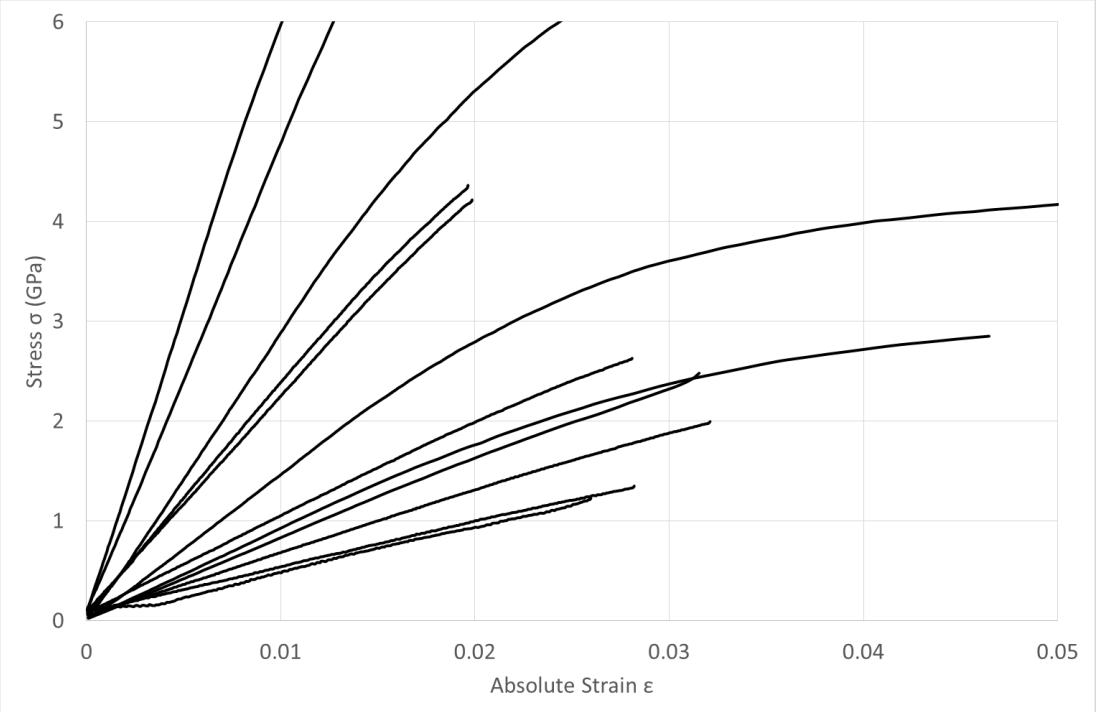

Figure 127 - Stress vs. Strain - CEA ODS 2000appm He, reduced range

23.2.4 EUROFER

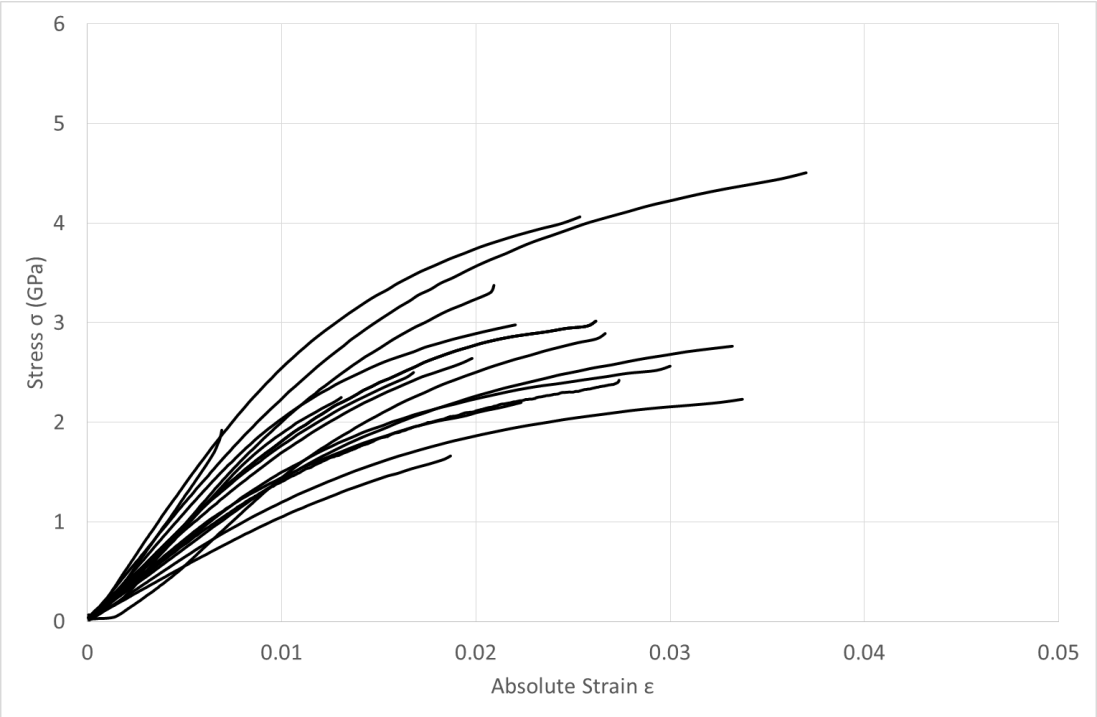

Figure 128 - Stress vs. Strain - EUROFER unimplanted

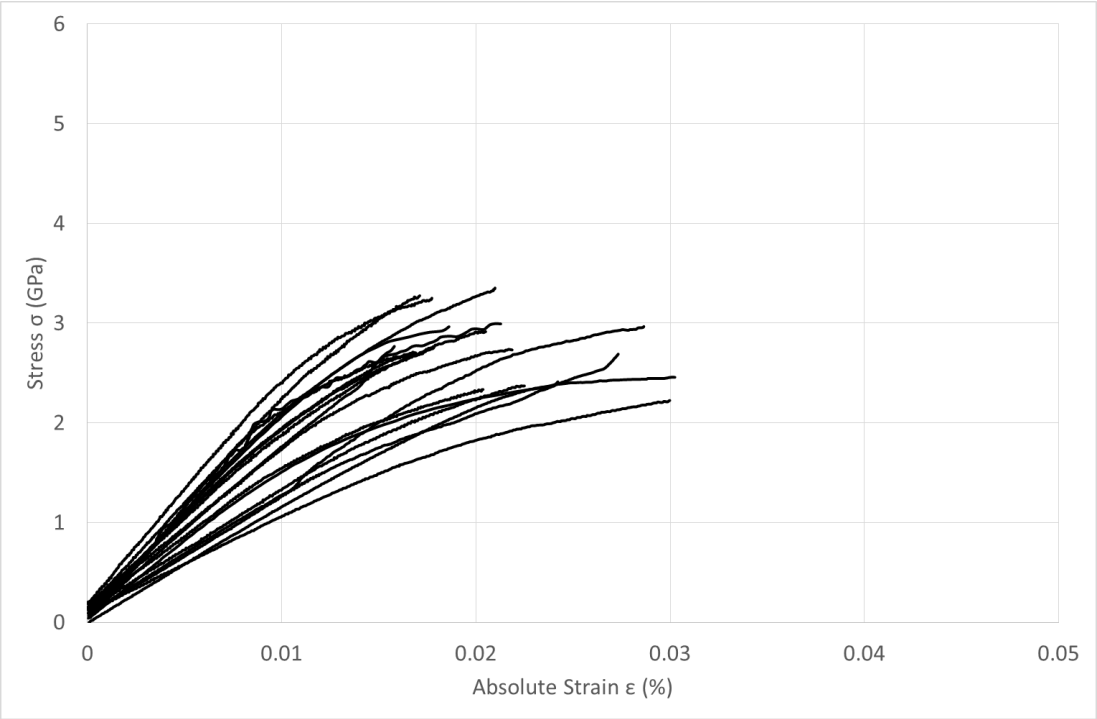

Figure 129 - Stress vs. Strain - EUROFER 75appm He

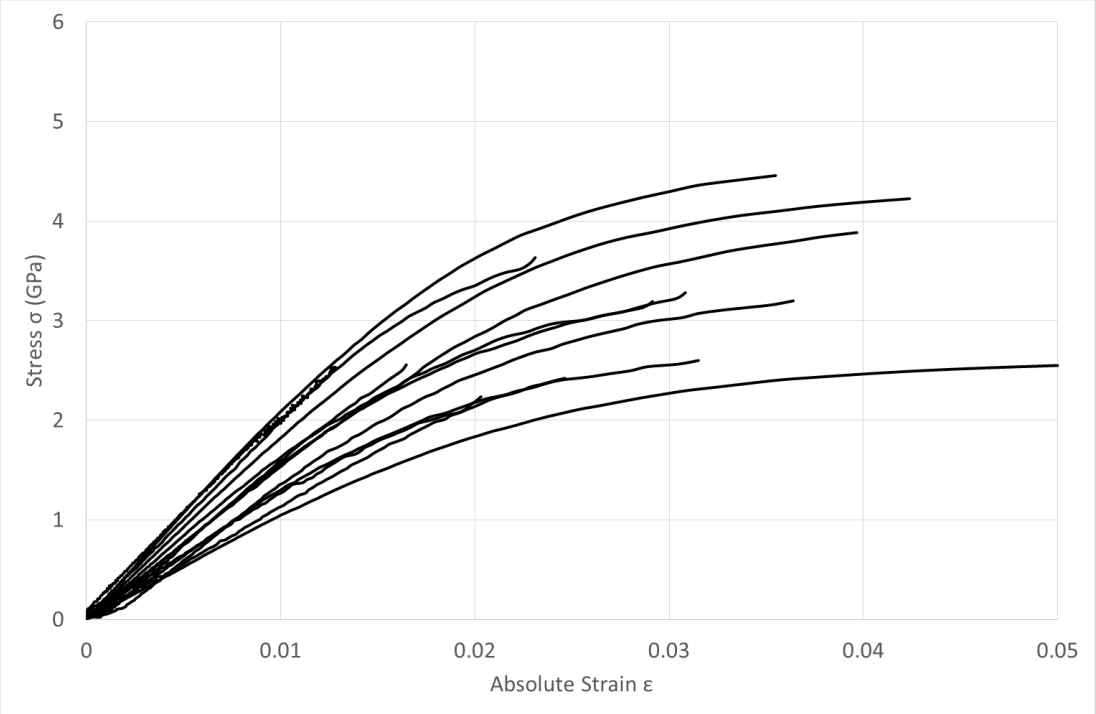

Figure 130 - Stress vs. Strain - EUROFER 2000appm He

23.2.5 EUROFER ODS

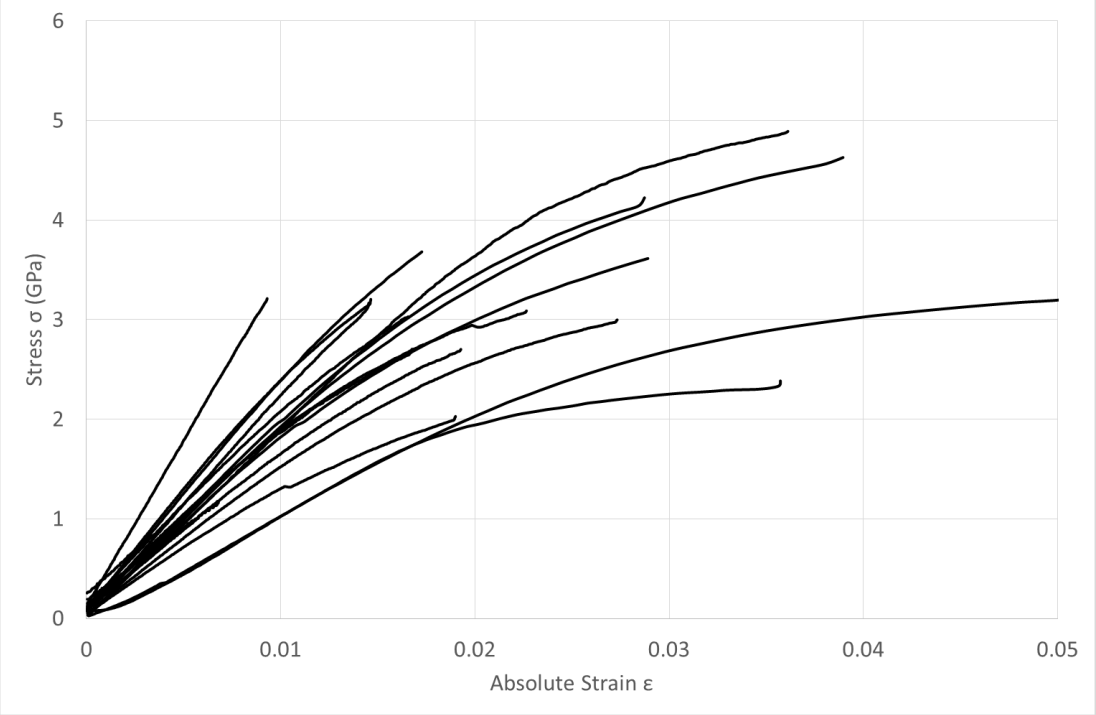

Figure 131 - Stress vs. Strain - EUROFER ODS unimplanted

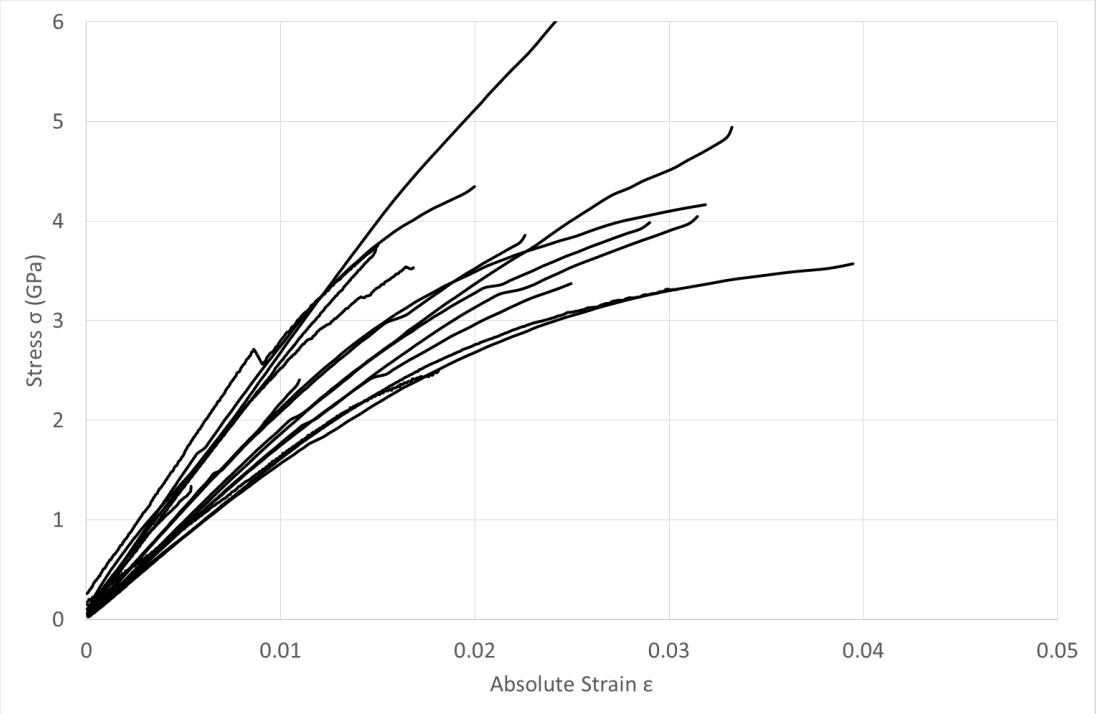

Figure 132 - Stress vs. Strain - EUROFER ODS 75appm He

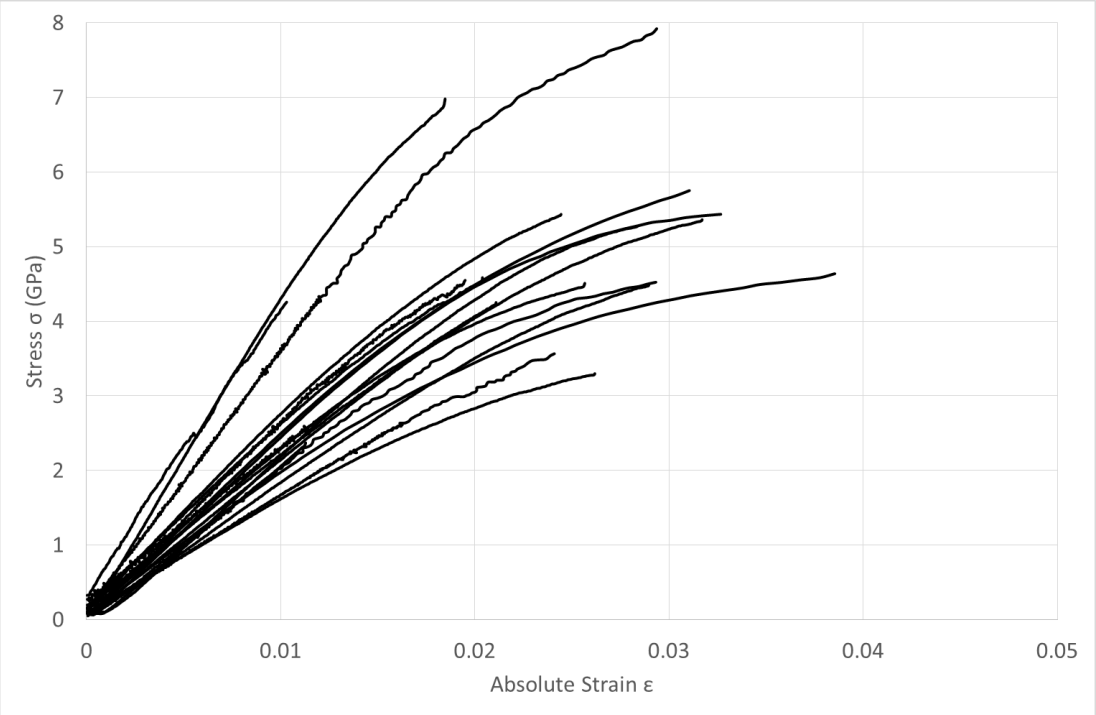

Figure 133 - Stress vs. Strain - EUROFER ODS 2000appm He

23.2.6 Stress-Strain Summary

As with the load-displacement data, there is no obvious yield stress in many of the graphs, therefore the way to compare the data sets is to look at the stress required to bend each to a given point. Cantilevers in this project were displaced by 1000nm which equates to a strain of ~2%. The stress at 2% strain was recorded for every line. The coloured lines join the mean load value of each implantation condition.

Figure 134 shows the full range of stress results. As seen before in the load displacement data (Figure 119), CEA ODS has several outlying results. The lines of these points are indicated with red arrows in Figure 122, Figure 124 and Figure 126. As these data have been converted to stress-strain (therefore negating any effect of cantilever dimension differences), it must be concluded that these differences are due to localised microstructural properties. This is analysed below.

To allow better comparison of the lower GPa data points, Figure 135 shows only the points below 6GPa. The Fe-14wt%Cr, EUROFER and EUROFER ODS results all fit into close bands of stress and all three show an increase in stress as the level of helium implantation increases. The mean line of CEA ODS appears to show a decrease with increasing helium concentration, but looking at the individual data points, it is actually an increase in scatter.

U = unimplanted, 75 = 75appm He, 2000 = 2000appm He.

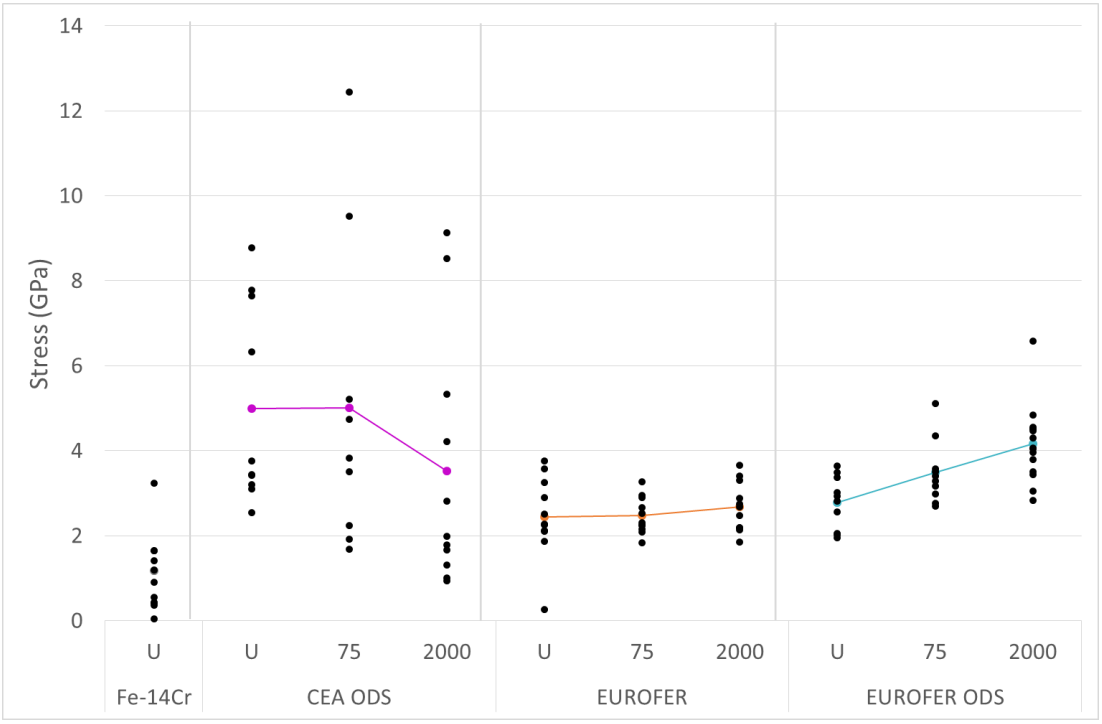

Figure 134 - Stress on each cantilever at 2% strain with coloured points to denote mean stress of each material/implantation condition.

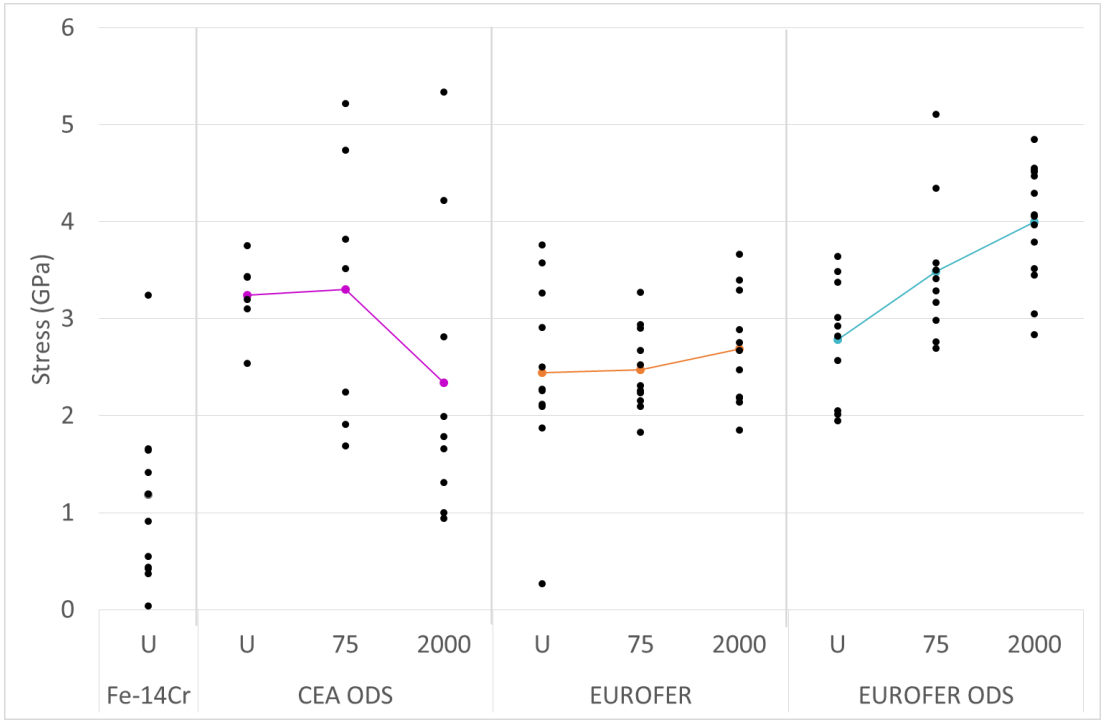

Figure 135 - Reduced stress range only showing points below 6GPa

Table 19 collates the mean stress values, stress ranges and the number of cantilever tests in each set. Table 20 shows the difference between the mean stress of the unimplanted and 2000appm He samples of each material as a percentage of the highest mean for each material (i.e. 2000appm for all but CEA ODS).

Table 19 - Mean stress and range (GPa) at 2% strain and number of tests (n) in each condition

	Fe-14wt%Cr	***n***	**CEA ODS**	***n***	**EUROFER**	***n***	**EUROFER ODS**	***n***
Unimplanted	1.18 (-1.14,+2.06)	*11*	3.24 (-0.70,+0.51)	*6*	2.44 (-2.18,+1.32)	*11*	2.78 (-0.84,+0.86)	*10*
75appm He	-	-	3.30 (-1.62,+1.91)	*7*	2.47 (-0.65,+0.80	*11*	3.48 (-0.79,+1.62)	*10*
2000appm He	-	-	2.34 (-1.40,+3.00)	*9*	2.68 (-0.83,+0.98)	*11*	4.00 (-1.16,+0.85)	*14*

Table 20 – Percentage change in mean stress between unimplanted and 2000appm He

	Fe-14wt%Cr	**CEA ODS**	**EUROFER**	**EUROFER ODS**
Percentage change	-	-28	+9	+30

Both EUROFER and EUROFER ODS show an increase in measured stress with increasing helium content; the biggest change in mean stress is seen in EUROFER ODS. CEA ODS shows a negative percentage change in the mean flow stress from unimplanted to 2000appm. The scatter of data points, however, suggests that the mean may not be the optimum method of analysing this material. As concluded above (Sections 23.2.1 and 23.2.6), the wide range of results in CEA ODS must be due to some microstructural effect. In Chapter 2, Section 9.2 it can be seen that the microstructure of this material is not homogeneous. Therefore further investigation into the local microstructure of each cantilever was required as is discussed in Section 24.1. Looking at the scatter of results for EUROFER and EUROFER ODS, (Figure 135), the overlap in result ranges between implantation conditions is very wide.

In all cases (CEA ODS, EUROFER and EUROFER ODS), change in stress from unimplanted to 2000appm He is less than the scatter seen in the data under each condition. The EUROFER results in particular show an almost constant stress range for

all implantation conditions (~1.8-3.7GPa – excluding the single very low unimplanted value). Even in the EUROFER ODS with a 30% increase in mean value, there is an overlap of ~1GPa between the unimplanted and 2000appm He bands of results. This suggests that any apparent trend in stress with helium content is simply due to a variation in scatter within the band of results. To determine whether the increase in stress with helium content seen in EUROFER and EUROFER ODS is a true trend, a greater number of data points are needed, at each condition and ideally over an expanded range of irradiation conditions (e.g. 500, 1000 and 1500appm He).

23.2.7 Young's Modulus

Another significant feature of the stress-strain graphs is the wide scatter of Young's modulus observed. The gradient of each line on the graphs was measured $\left(Young's\ Modulus = \frac{Stress}{Strain}\right)$ and the values plotted in Figure 136. As with the measured stresses, there are some high outliers in the CEA ODS; Figure 137 shows only moduli less than 450GPa. Table 21 presents the mean values.

Table 21 – Young's modulus average and range (GPa) and number of tests (n) in each condition

	Fe-14wt%Cr	*n*	CEA ODS	*n*	EUROFER	*n*	EUROFER ODS	*n*
Unimplanted	98 (-76,+233)	*12*	343 (-200,+323)	*12*	186 (-72,+91)	*16*	197 (-102,+156)	*15*
75appm He	-	-	505 (-420,+771)	*10*	177 (-70,+60)	*19*	177 (-10,+152)	*15*
2000appm He	-	-	204 (-157,+421)	*13*	157 (-49,+55)	*13*	250 (-85,+176)	*19*

Although large, the scatter is not unusual. Previous work by Hardie [175] observed an increase in modulus scatter with decreasing cantilever size. At a cantilever height of ~3μm, Hardie showed a modulus range of ~130-280GPa for pure iron attributed to variations in crystal orientation across each test. Halliday's irradiated Fe-Cr alloy microcantilevers [176] show datasets up to 190GPa scatter range, and Gibson's irradiated tungsten microcantilevers [177] showed scatter range up to 180GPa.

There are several possible reasons for the high scatter in microcantilever moduli. Inhomogeneous microstructure has been discussed with respect to anomalous CEA ODS yield, this may contribute to the modulus scatter – see Section 24.1. The scatter in other materials, however, is better attributed to nanoindenter thermal drift – the change in indenter/specimen dimensions due to temperature change during testing. Although nanoindentation test methods stabilise for thermal drift, microcantilever methods do not and a vertical drift of ~1nms^{-1} (average seen in unstabilised indentations) over a test period of ~200s gives a huge (10%) displacement error. Even a low drift of 0.1-0.2nm/s gives 1-2% displacement error. As thermal drift is not recorded and hard to regulate, the errors cannot be quantified.

U = unimplanted, 75 = 75appm He, 2000 = 2000appm He.

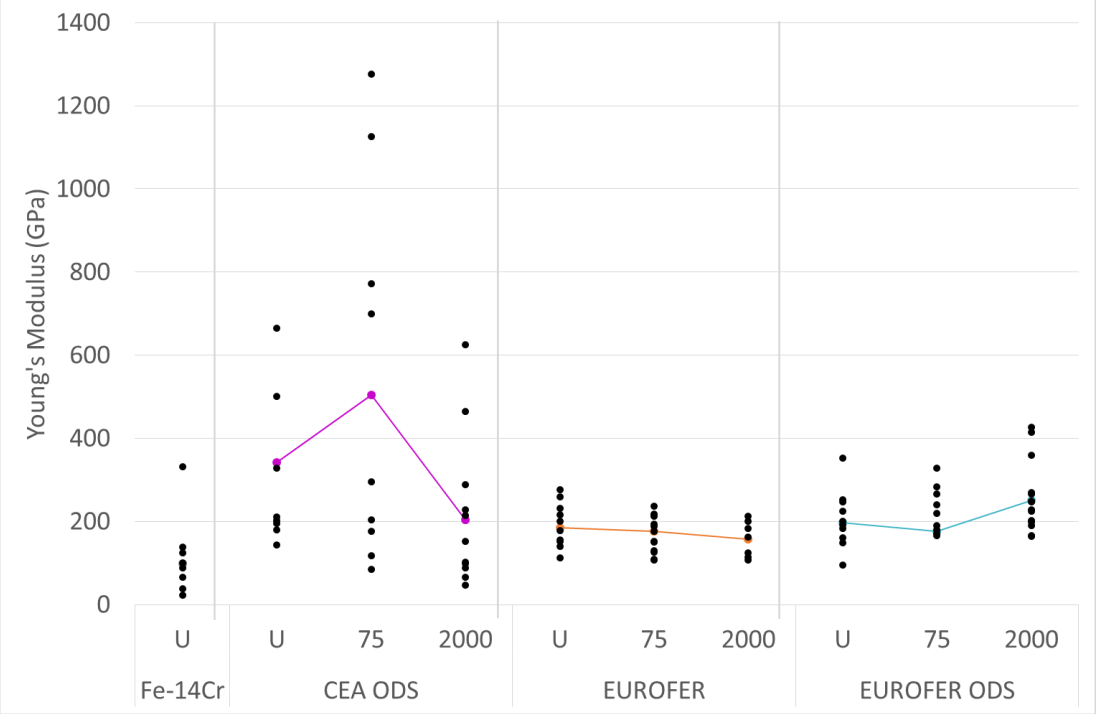

Figure 136 – Young's modulus for each cantilever.
Coloured points to denote the mean Young's modulus of each material/implantation condition.

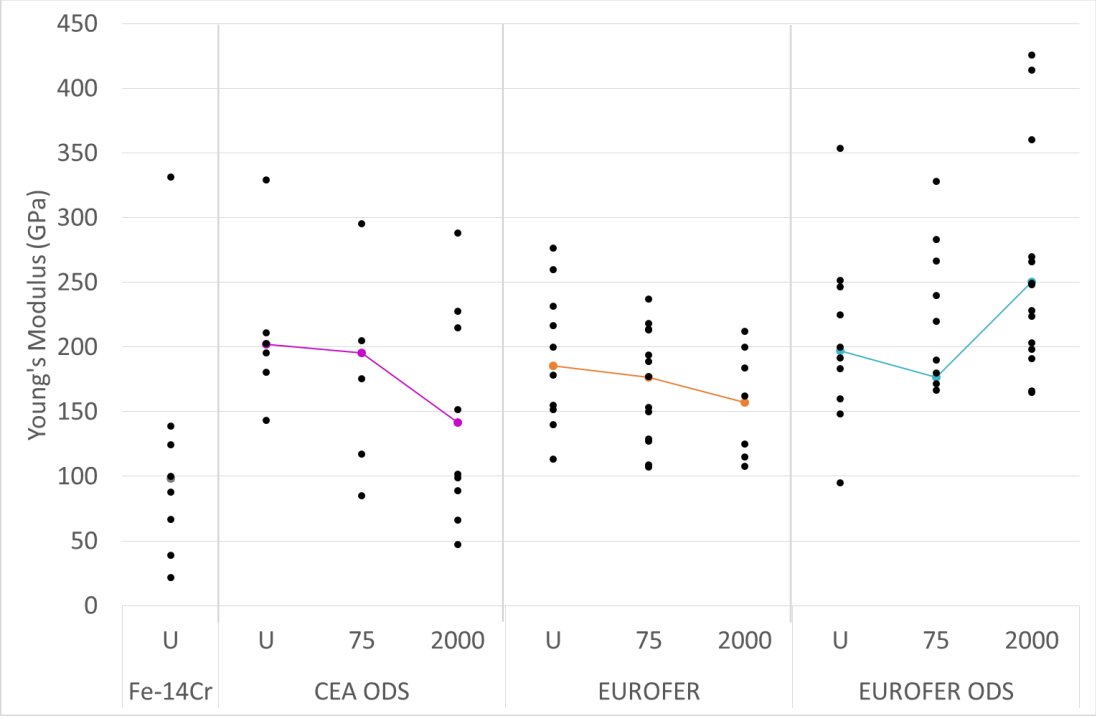

Figure 137 - Reduced stress range only showing points below 6GPa.

24 Discussion

The raw graphical data (Figure 118 and Appendix B) show that the load-displacement response can vary hugely within each material and implantation condition. Summarising the load-displacement data by taking load at 1000nm displacement for each cantilever allows for simple comparison of all the material conditions (Figure 119). Converting the load-displacement data to stress-strain using simple beam theory (Section 23.2.1) removes the effects of cantilever size variation from the data. In this project, the application of simple beam theory has (in all but CEA ODS) concentrated the results into a tight band. This shows that even small differences in cantilever dimensions can cause big discrepancies when analysing load-displacement data. For the most accurate comparison of the data, it must be normalised by converting to stress-strain.

24.1 Scatter in CEA ODS Results

All the materials show reasonably tight bands of stress and modulus data points with the exception of CEA ODS, where a range of higher loads are scattered above the expected lower band. Converting from load-displacement to stress-strain converges the data points into narrow bands where the scatter in results can attributed to minor local microstructural and experimental differences and measurement inaccuracies.

CEA ODS, however, still shows a scatter of higher than expected outlying results (Figure 134 and Figure 136). These outliers may be caused by the material's microstructure and therefore further characterisation of the grain structure was required. Initially EBSD scans were considered, however, the sputtering effects of the FIB Ga^+ ion beam used for cutting the cantilevers had degraded the polished surface quality and the EBSD scans produced were incomplete with uncharacterisable areas.

During cantilever production, the sample has to be imaged with the FIB beam to check milling progress. Some of these FIB images (e.g. Figure 138) show significant

grain contrast on the material surface and could be used to make grain maps (without grain orientation information). FIB scanning, however, is a destructive technique (the surface is sputtered away as the sample is scanned and therefore not suitable for large area mapping of a sample that will be needed in future). A similar SEM technique, Angle-selective Backscattered imaging (AsB), is non-destructive and uses channelling. Using a Zeiss Merlin SEM, H. Abdolvand (Oxford Materials) produced AsB scans of the region of cantilevers on three CEA ODS samples (unimplanted, 75appm He and 2000appm He).

Figure 139 shows an AsB image of a single cantilever with the elongated grain structure of the CEA ODS clearly visible. All cantilevers were cut in the same orientation with the elongated grains perpendicular to the cantilever length. The grains are approximately cylindrical (rather than flattened discs) therefore cantilevers will be ~2-3 grains deep. The material has a bimodal grain structure however, therefore some cantilevers will contain regions with larger grains. One such larger grain is indicated on Figure 139 with red brackets. High resolution AsB scans of all cantilevers were taken to determine the location of the larger grains with respect to the individual cantilevers.

Correlating these AsB scans with the individual cantilever data sets showed that the outlying data points are the results from cantilevers where the bimodal grain structure has caused the fixed end of the cantilever to be within one of the randomly spread larger grains rather than the smaller grains that make up most of the material (see Figure 140). Cantilever 1 (left) shows a uniform small grained structure along the length of the cantilever and in the region of the fixed end. Cantilever 2 (right) shows one of the bimodal grain structure's large grains encompassing the fixed end of the cantilever (indicated with red brackets in the figure). The stress-strain data for these particular cantilevers gives the stress at 2% strain as 3.09GPa for cantilever 1 and 7.39GPa for cantilever 2. Cantilever 1 is therefore in the middle of the lower band of results (2.54-

3.75GPa), and cantilever 2 is in the middle of the high outlying results (6.33-8.77GPa). The large grain at the fixed end of cantilever 2 is the only visible significant microstructural difference between the cantilevers, which suggests that this is the reason for the discrepancy in stress results.

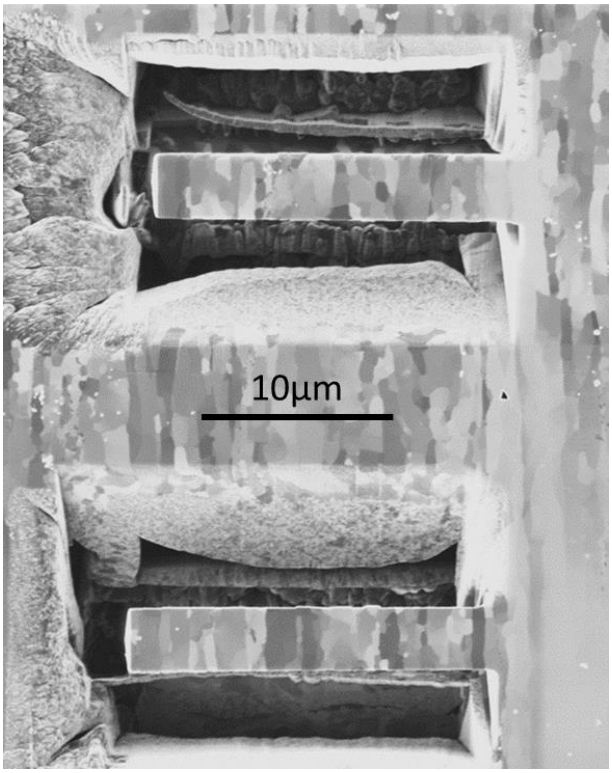

Figure 138 - FIB scan of a cantilever in CEA ODS unimplanted showing the grain structure imaged with a 50pA beam to minimise surface damage

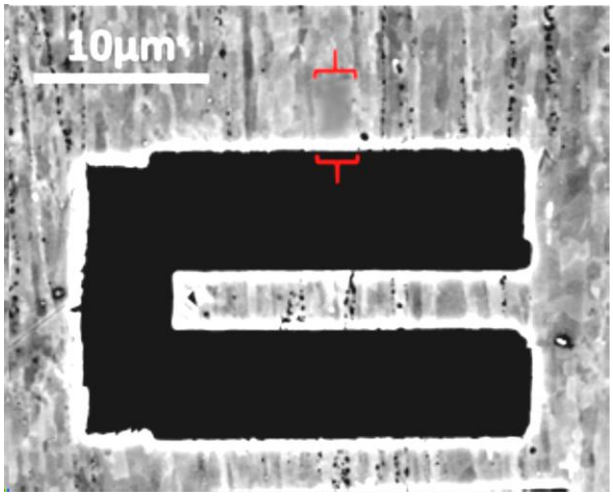

Figure 139 - AsB scan of a cantilever in CEA ODS unimplanted showing the grain structure. AsB has the advantage over FIB of being non-destructive. Red brackets indicate one of the larger grains present in the bimodal microstructure.

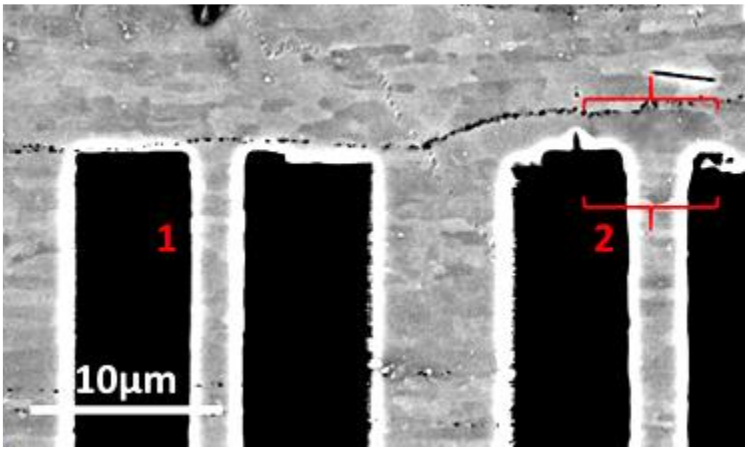

Figure 140 - AsB scan of the fixed end of two CEA ODS unimplanted cantilevers. The red brackets on cantilever 2 indicate a large grain.

Investigating all the other cantilevers showed a trend of the high outlying data points correlating with cantilevers of similar microstructure to cantilever 2 (Figure 140) i.e. with a large grain surrounding or significantly covering the fixed end.

Microstructural differences, however, only explain the high outlying results. All the cantilevers were investigated and at the lower end of results (below ~4GPa) there are no significant differences in the microstructures between cantilevers; therefore no specific microstructural influence can be attributed to the scatter of lower (<4GPa) results seen in CEA ODS (Figure 135).

The increase of scatter with increasing helium concentration in CEA ODS will be discussed further (Section 24.3).

24.2 Deformation

None of the beams fractured during testing. All the load-displacement curves show a section of elastic deformation that slowly merges into plastic bending deformation of the cantilever. SEM imaging of the cantilevers shows that this plastic deformation is a uniform bending along the cantilever (Figure 116).

Close inspection of the fixed end of the cantilevers shows one of three types of deformation. The following images (Figure 141, Figure 142 and Figure 143) show typical deformation structures; these pictures are all in CEA ODS, a full set of the deformations is in Figure 144. The images show the sides of the cantilevers at their fixed ends.

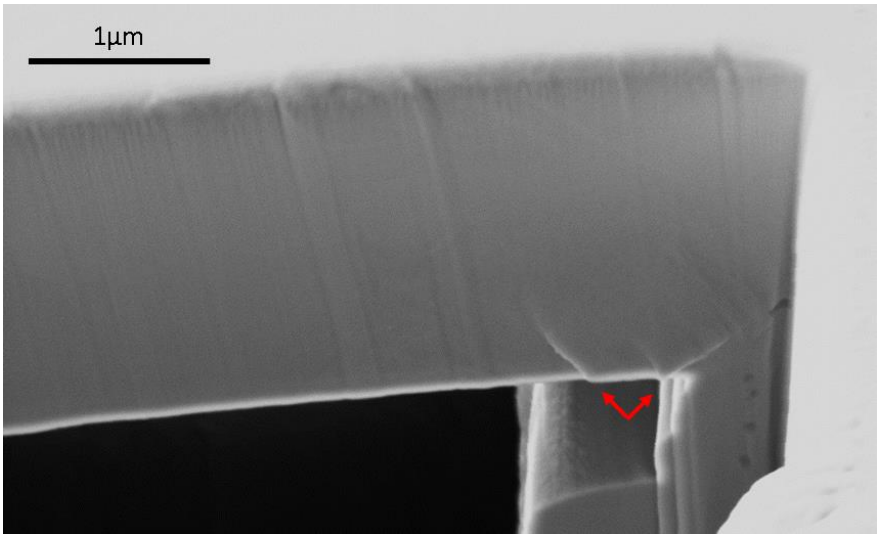

Figure 141 - CEA ODS unimplanted cantilever showing slip at ~45° indicated by the red arrows.

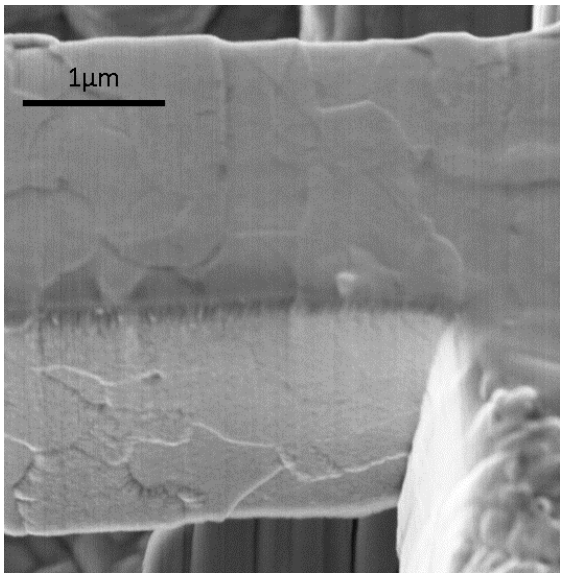

Figure 142 - CEA ODS + 2000appm He cantilever showing grain boundary slip.

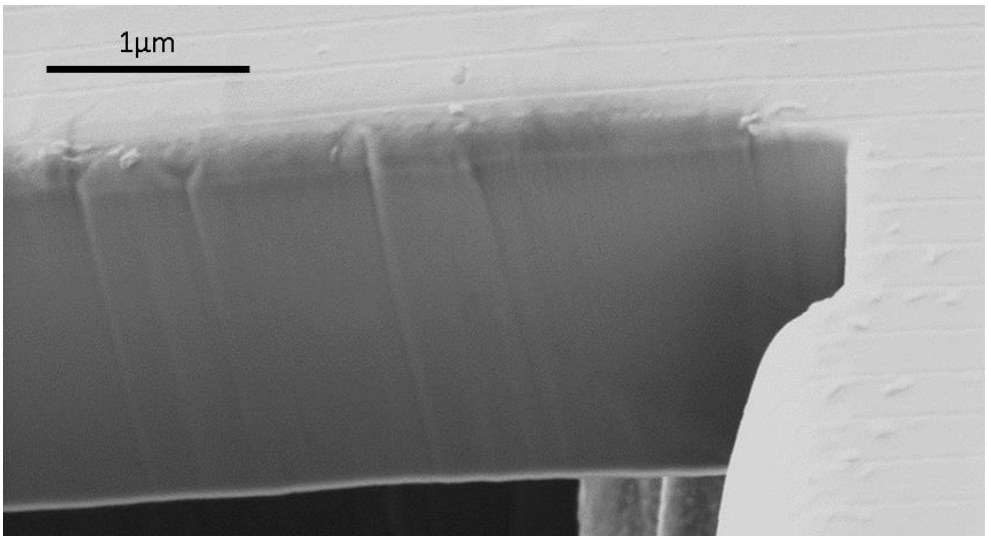

Figure 143 - CEA ODS unimplanted cantilever showing no form of slip.

Figure 141 shows slip line formation at approximately 45° to the cantilever surface. These slip lines have formed within the first 0.5μm from the fixed end and propagate less than one third up the height of the cantilever.

Figure 142 shows deformation by grain boundary slip. In the finer grained materials (CEA ODS, EUROFER and EUROFER ODS), the grain boundaries near the fixed end of some cantilevers became more pronounced after testing. If slip within the grains is homogeneously distributed it will be difficult to see. The build-up of slips within the grains can then lead to grain boundary sliding.

The ODS materials made by M. Gorley (Oxford Nuclear Materials) [107] have a bimodal grain size structure very similar to CEA ODS. In these it has been observed that grain boundary sliding occurs on the boundaries between the large grains and areas of small grains, but not within the small grain regions. If the cantilevers are cut over one of these boundaries, this will affect the observed deformation mode. This difference in deformation around the large grains helps to explain the scatter of stress results seen in CEA ODS (Figure 135) – if a cantilever is cut with large grains around the fixed end, grain boundary slip is less likely to occur, and therefore deformation must follow a different mechanism potentially requiring a greater load, thus resulting in the high stress results.

Figure 143 shows the most common deformation type across all the materials and implantations conditions: plastic bending deformation with no obvious slip. The vertical lines on the cantilever side are river lines due to FIB milling and the horizontal lines on the top surface are scanning lines from the AFM-type indenter scanning of the cantilevers; neither result from deformation. On the majority of cantilevers, the only deformation seen is an overall plastic bend in the cantilever (as in Figure 116). Comparing the deformation types of the cantilevers and their respective graphs shows no particular correlation of deformation with graph shape or load at 1000nm. The

deformation differences, therefore, are probably due to local microstructural variations within each cantilever, allowing another mode to be predominant depending on the local loading conditions.

Each of the three deformation types was seen in all materials except for no grain boundary sliding in Fe-14wt%Cr, as these cantilevers contained no grain boundaries. All these deformation types can be explained in the small, multigrained materials (CEA ODS, EUROFER and EUROFER ODS), since the prevalence of several grain boundaries within each cantilever allows for many tiny plastic slips leading to an overall plastic bend deformation. In the large grained Fe-14wt%Cr, however (Chapter 2, Section 9.1), there are no grain boundaries to slip, so plastic deformation must be homogenously distributed down the length of the cantilever, giving rise to either 45° slip or no obvious slip lines.

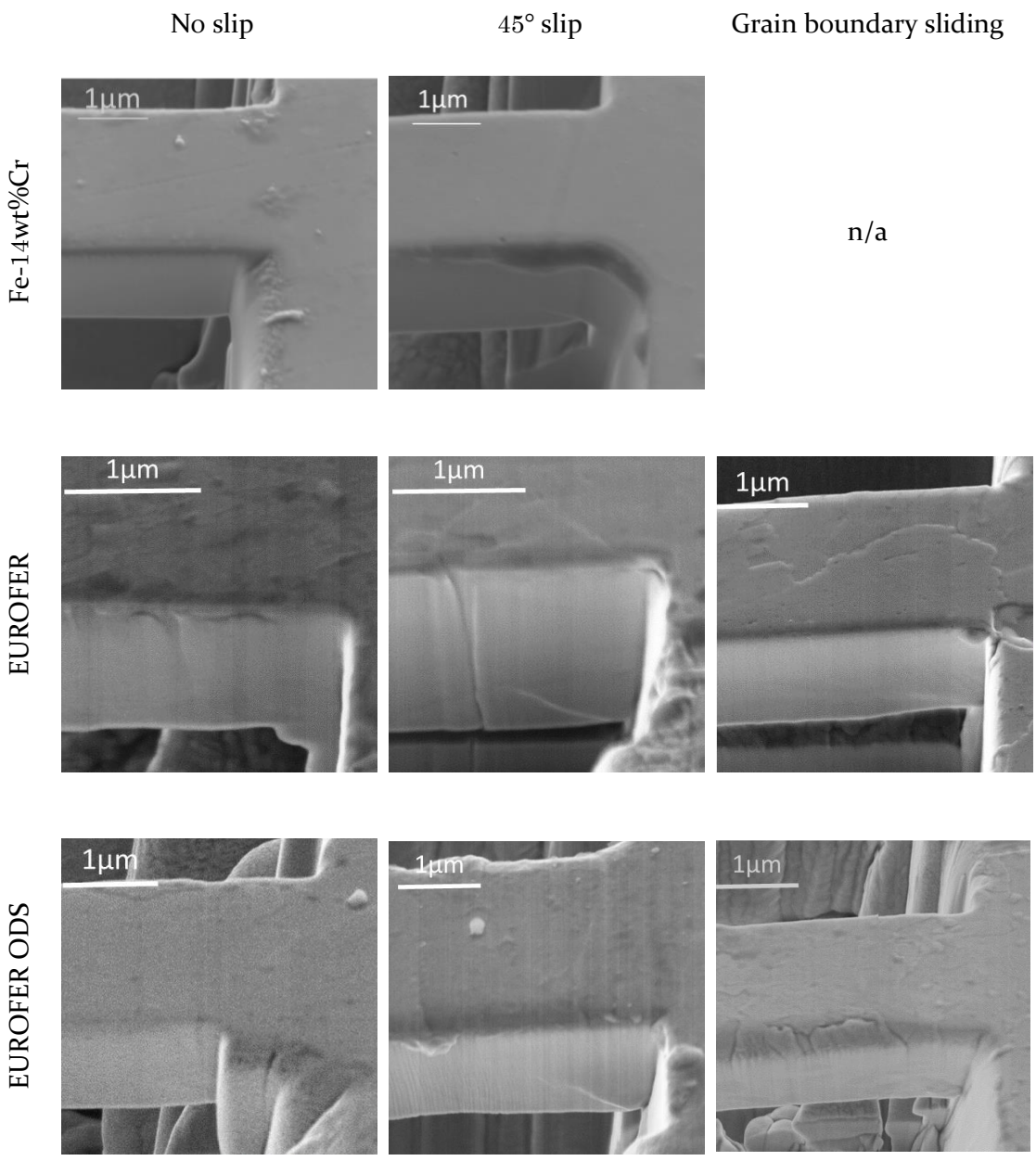

Figure 144 - Deformation patterns seen in all materials

24.3 Effect of Helium

In the EUROFER and EUROFER ODS alloys, the addition of helium causes an increase in the stress measured at 2% strain ($\sigma_{2\%\varepsilon}$). In CEA ODS the implantation of helium causes a scatter in $\sigma_{2\%\varepsilon}$, rather than an increase, but this is probably due to the grain microstructure issues mentioned previously (Section 24.1).

As helium is implanted into the materials, it will collect in low energy sites as interstitials, in voids/bubbles and at grain boundaries. As the implanted cantilevers are tested, dislocation motion through the grains will be disrupted by voids in the matrix, and grain boundary motion will be reduced due to the collected helium causing pinning of the grain boundaries.

Fe-14wt%Cr has very large grains compared with EUROFER (Chapter 2, Section 9). The higher percentage of grain boundaries in EUROFER already acts as a dislocation movement inhibitor, hence its higher baseline yield stress and hardness.

An ideal nuclear reactor material is one that is minimally affected by helium implantation. According to these microcantilever tests EUROFER is the most suitable material as it shows only a 9% increase in $\sigma_{2\%\varepsilon}$between the unimplanted and 2000appm helium samples (cf. 30% or more in other samples – Table 20, p187). It is interesting to note that the non-ODS EUROFER variant shows the best response, when it is the addition of the oxide dispersion that is designed to deal with the incident helium in a reactor. The greater increase in the $\sigma_{2\%\varepsilon}$in EUROFER ODS can be explained, however, by the following theory.

The oxide nanoclusters in EUROFER ODS are of the order of ~2-5nm in diameter. These are, therefore, too small to provide any significant disruption to dislocation motion within the material. The main purpose of the clusters, however, is to act as sinks for the helium. As the helium bubbles cluster around the oxides, they increase the size of the obstacle and therefore start to have an effect on dislocation motion. This would

appear as an increase in yield stress with increasing helium concentration (as more helium clusters around the oxides).

The mean points of the CEA ODS plots show a decrease in $\sigma_{2\%\varepsilon}$ as helium concentration increases, but taking the scatter of outliers into consideration, this is probably a misleading result. As with EUROFER ODS above, the oxide particles are too small to disrupt dislocation motion. In CEA ODS, the particles are even smaller, in the range of 1-2nm and therefore, even with the added helium clustering to the precipitates, they may not be large enough to cause any form of yield stress increase.

25 Conclusions

When investigated using microcantilever bend testing, implantation of helium up to 2000appm appears to causes an increase in the average stress at 2% strain and Young's modulus measured in EUROFER and EUROFER ODS. The effect is smallest in EUROFER. In CEA ODS, irregular grain size has a significant effect on scatter in the results which masks any helium effects. The observed trends of stress with helium however, all have stress ranges that are narrower than the observed bands of results. This means that the trends may simply be due to the distribution of scatter. To determine whether they are true trends, a greater number of data points are needed, at each condition and ideally over an expanded range of irradiation conditions (e.g. 500, 1000 and 1500appm He).

Chapter 6
Transmission Electron Microscopy and Energy Dispersive X-ray Spectroscopy

26 Transmission Electron Microscopy Methodology

TEM foils were prepared for each material in order to investigate how the deformation caused by mechanical testing interacts with the microstructure of the materials and how this changes with ion implantation. The mechanical deformation used was shallow nanoindentation (~100nm deep) into the material surface and cross-section TEM foils were prepared using FIB cross-section lift out.

26.1 Sample Preparation

- Nanoindentations were used to create mechanical deformation in the samples. The MTS Nanoindenter XP with a Berkovich diamond tip was used to create 100nm deep indentations in the surface of bulk specimens (Figure 145a).
- Using a Zeiss Auriga FIB-SEM, these nanoindentations were covered with a ~200nm thick protective layer of platinum to act as a protective layer during FIB milling (b).
- Deep wide trenches (~22x10x15µm) were cut on both sides of the protected area using a high beam current (~1nA) (c and d).
- Fine trenching on the two long sides achieved the approximate shape and size of the lift-out to be performed (e and f).

- Undercutting was performed from both sides at 40° from the material surface and the final fixed end cut until only a small amount of material remained attaching the lift-out to the bulk (g and h).
- Using a Kleindeik Nanotechnik system, a micromanipulator needle was brought into contact with the free end of the lift-out and attached using platinum (i).
- The lift-out attachment was cut through so the sample could be lifted out of the bulk surface (j).
- An Omniprobe 4-post Cu lift-out grid was positioned under the micromanipulator and the lift-out carefully lowered into position touching the surface with the two bottom points in contact with the copper. The lift-out was then attached to the copper post by platinum deposition and the micromanipulator cut off from its platinum attachment (k). The lifted-out block was thinned down to TEM transparency through a series of mills dropping in beam current from 240pA to 50pA for a final polish. Once the lift-out was ~100nm thick it was ready for TEM imaging (l) – the blue arrow indicates the surface depression of the indentation.

The lift-outs in this project were all examined using a JEOL JEM-2010 TEM or a JEOL JEM-2100 TEM. Images were taken at lower magnifications (~5,000-10,000x) to investigate the deformation characteristics and higher magnifications (~200,000x) to investigate bubble formation in the implanted specimens.

Figure 145 – FIB lift out process

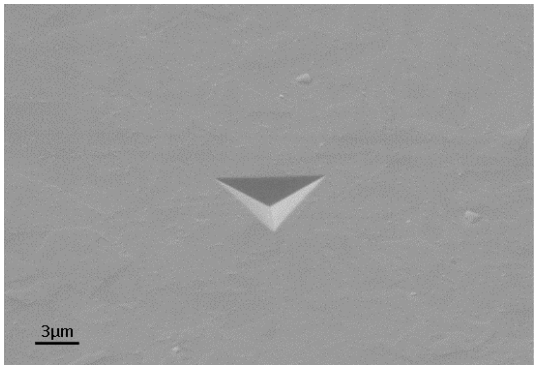

a) SEM of indentation

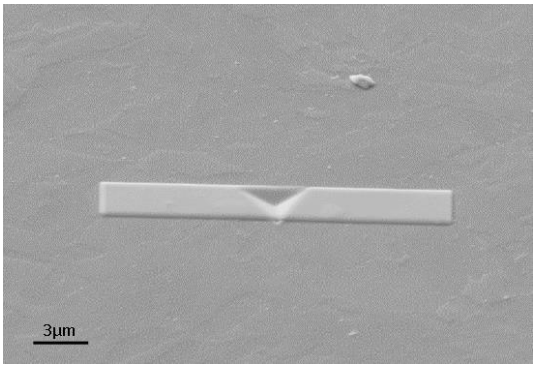

b) SEM of platinum protective layer

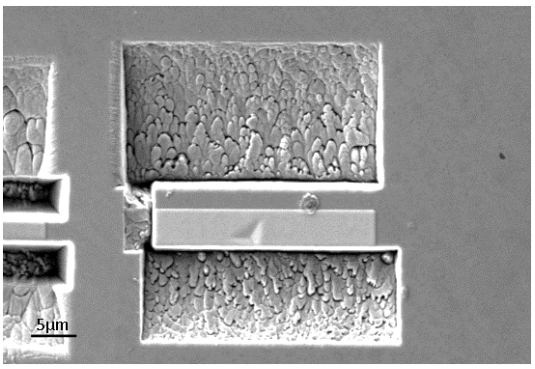

c) SEM of coarse trenches

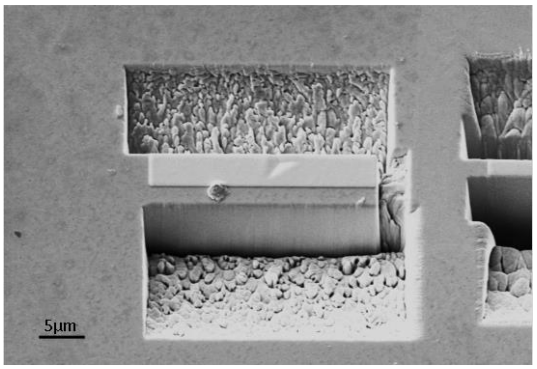

d) FIB of coarse trenches

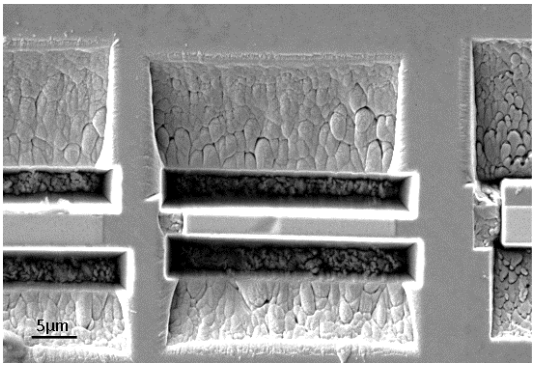

e) SEM of fine trenches

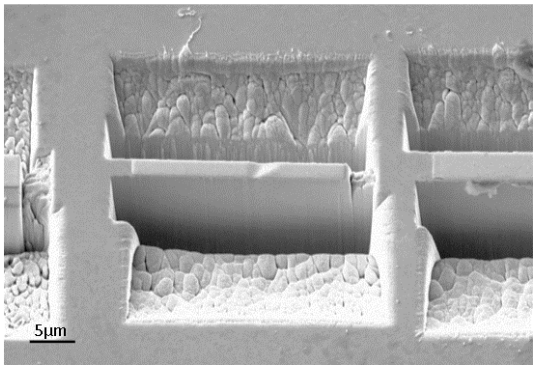

f) FIB of fine trenches

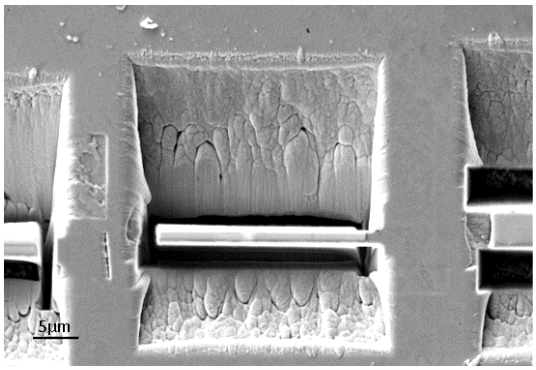

g) SEM of undercut, ready to lift sample

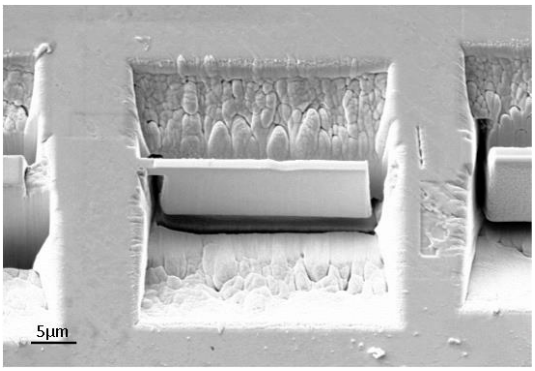

h) FIB of undercut, ready to lift sample

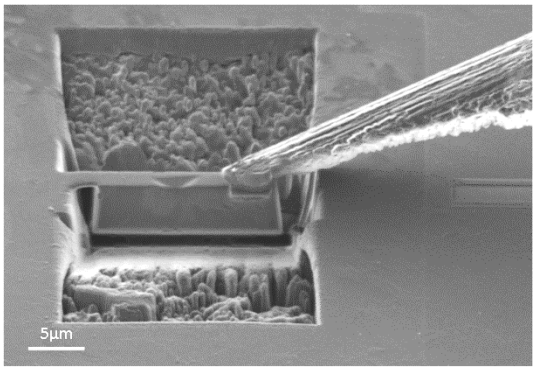

i) SEM of lift-out attached to needle

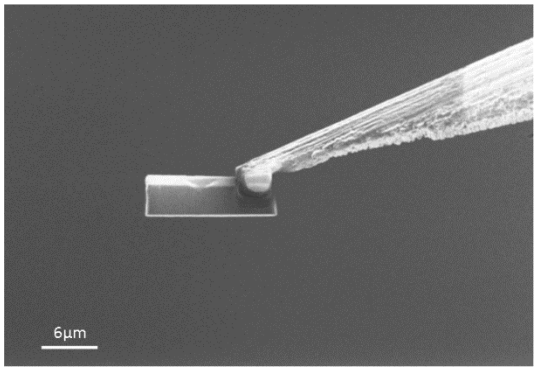

j) SEM of lift-out cut free from sample

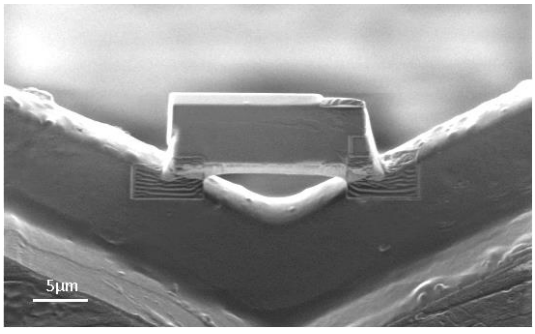

k) SEM of lift out on copper grid

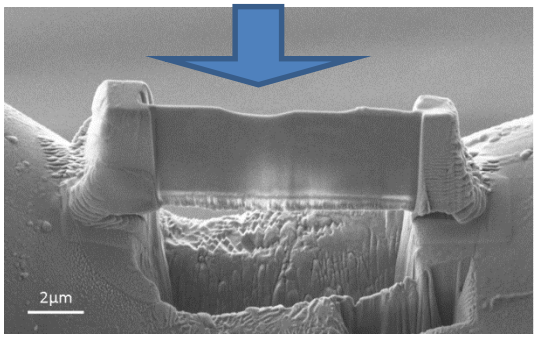

l) SEM of thinned lift out
Blue arrow indicates position of indentation.

27 Transmission Electron Microscopy of Indentations

Nanoindentation causes plastic deformation of the material below the surface. Microstructural features and dislocations can be seen using TEM when cross-section samples have been reduced in thickness to ~100nm. This sample preparation method has been used in previous similar works investigating geometrically necessary dislocations (GNDs), plastic zone sizes [178] and dislocation/grain boundary interactions [179].

The following pages contain TEM images for each material, showing microstructures and examples of bend contours. The images are annotated with comments on significant features. All the images are orientated with the indentation at the top of the frame, although many are slanted because of the sample orientation in the TEM during imaging. The position and orientation of each indentation is marked with a blue arrow. Dark field imaging was used on many of the samples to facilitate viewing the dislocations. In all materials the 2000appm He and He+Fe implanted layer is 3μm deep and the Ne implantation is 1.2μm deep. Implantation depth is marked with a red bracket or arrow (if the implanted layer is deeper than the image).

Note that the subtle contrast differences in the images do not reproduce well in print and are best viewed on a backlit computer screen; see enclosed CD. Each image set is accompanied by a schematic indicating significant features. The surface is marked with a thick line, hatchings denote areas where high dislocation density is visible, shaded areas show the surface platinum strip and lines indicate grain boundaries.

27.1 Microstructure

Fe-14wt%Cr

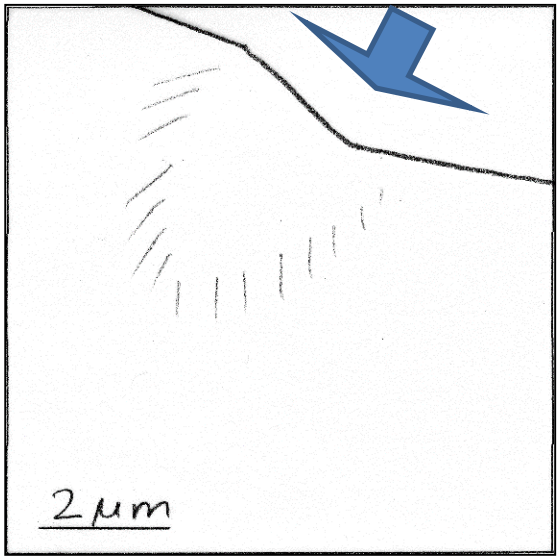

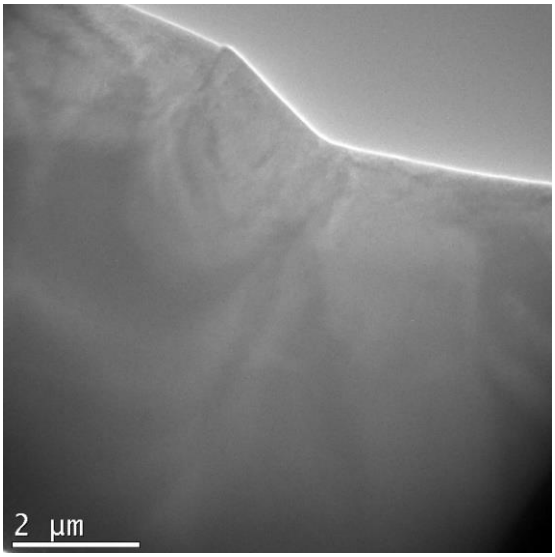

Figure 146 - Fe-14wt%Cr unimplanted
No visible grain boundaries.

CEA ODS

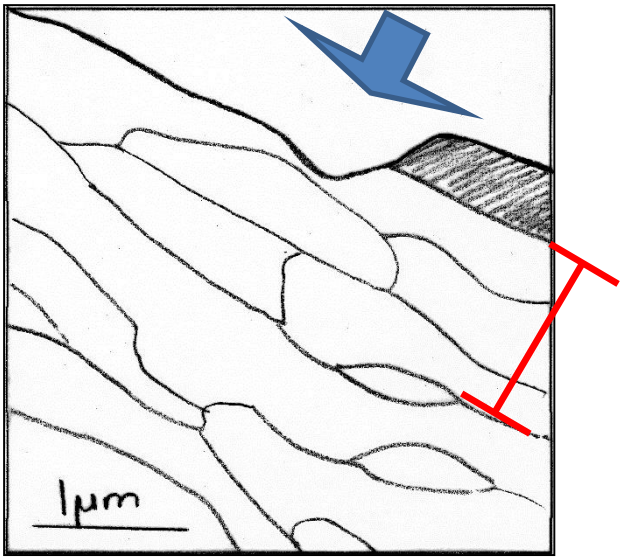

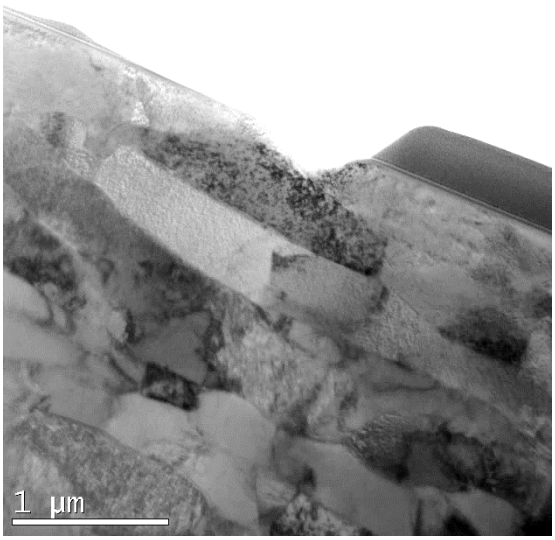

Figure 147 - CEA ODS 2000appm Ne
(Bright and dark field)
Clear elongated grain structure.

EUROFER

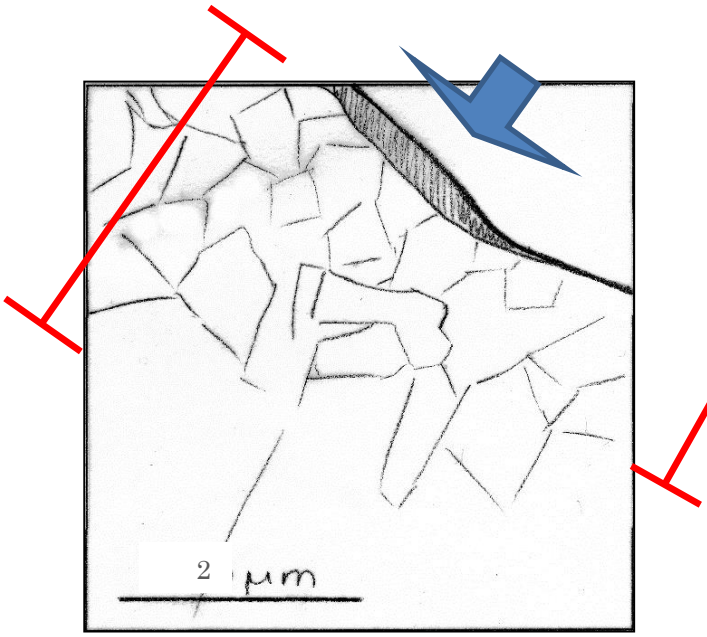

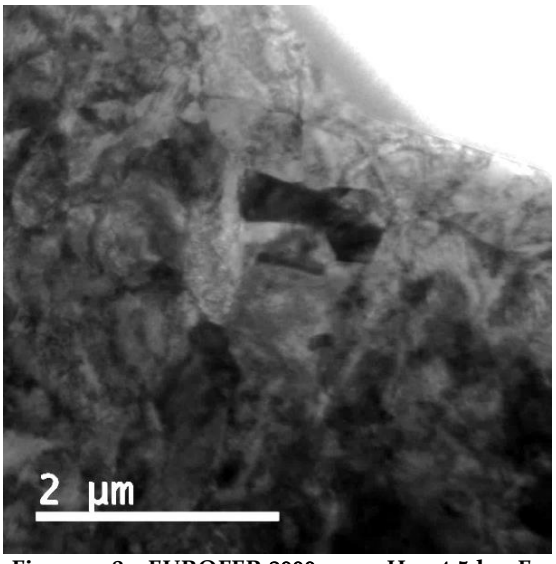

Figure 148 – EUROFER 2000appm He +4.5dpa Fe Complicated, approximately equiaxed grain structure.

EUROFER ODS

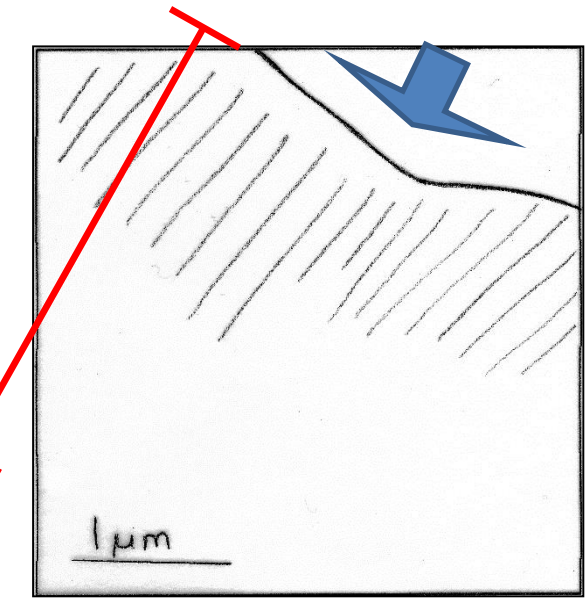

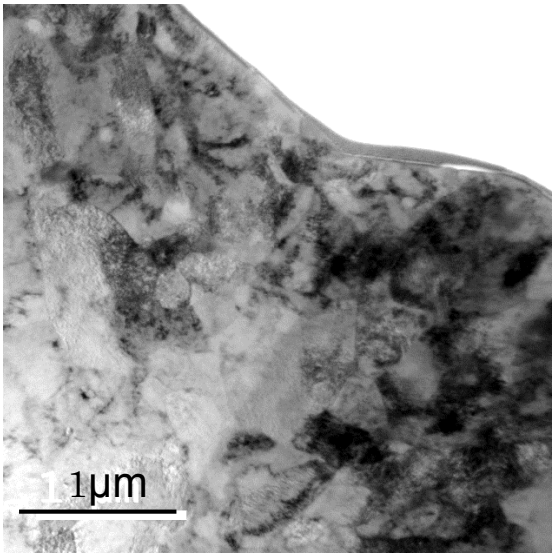

Figure 149 - EUROFER ODS 2000appm He Equiaxed grain structure similar to EUROFER..

TEM images were taken of all four materials, in each of all four implantation conditions (unimplanted, 2000appm He, 2000appm He + 4.5dpa Fe and 2000appm Ne). Figure 146 to Figure 149 show the microstructure observed in each of the materials. The best available image was used for each material, and they cover a variety of implantation conditions. At the lower magnification used to view the overall microstructures, however, there were no visible differences in the microstructures between implantation conditions, so these can be taken as showing the typical grain and dislocation structures for each material.

Fe-14wt%Cr (Figure 146) has very large grains (~200μm), therefore each TEM foil cut only contained a few grains. Figure 146 contains no grain boundaries. There is, however, a visible arc around the surface indentation; this is a bend contour and will be discussed further in Section 27.2.

CEA ODS (Figure 147) has a much smaller grain size (1-4μm) than Fe-14wt%Cr (~200μm). It also has a more complicated in-granular microstructure due to the addition of multiple alloying elements and precipitates not present in Fe-14wt%Cr. The effects of the various alloying elements will be discussed in Section 31.1. During its production the CEA ODS was extruded; the elongated grain structure is clearly visible in Figure 147. Extrusion increases the initial dislocation content of the material.

The orientation of lattice defects with respect to the incident TEM beam has an effect on the features seen in the resultant image. If the lattice and inherent defects are lined up parallel to the beam, diffraction will be greater and the area will appear darker in bright field imaging (or brighter in dark field imaging). The sample can be tilted (e.g. Figure 151) to change which grains show the most contrast. This effect also shows that the grains in CEA ODS have high angle grain boundaries.

The two EUROFER materials (Figure 148 and Figure 149) have very similar microstructures – small (2-5 μm), approximately equiaxed grains. Although implantation will increase the number of dislocations, this effect is minimal compared to their high initial

dislocation content, and therefore no change is visible between unimplanted and implanted micrographs at this magnification.

27.2 Bend Contours

Bend contours were seen to some degree in all four materials, but their appearance was not affected by implantation conditions. They were most visible in Fe-14wt%Cr where samples (at all implantation conditions) strongly showed curved bands at ~700-800nm below the surface nanoindentations. This is obvious for all samples in both bright field and dark field conditions; the band appears black in bright field and white in dark field. Figure 150 shows a particularly good example. Beneath this thick band, thinner stripes continue to follow this roughly semicircular shape down to ~1500nm depth. The visibility of these bands changes with the tilt condition of the sample (see the neon implanted tilt series – Figure 151); they first become visible at ~100nm depth under the indentation and spread out deeper than 4µm.

In CEA ODS, the bend contours are visible as a semicircle around the indentation. The grain structure, however, makes this much less visible; it can be best seen as a pale semicircle in the dark field image Figure 152.

The grain structure in EUROFER makes it much harder to pick out the bend contours. With many grains of differing orientations present, the bend contour will not appear as a smooth curved line. In Figure 153 they can be seen as darker lines running approximately parallel to the left side of the image and faintly horizontal lines across the centre right of the image.

Most of the EUROFER ODS images appeared very similar to the EUROFER images, with ragged contours disrupted by the grain structure. Figure 154 however, magnifies an area of a few grains and shows how bend contours are only visible under certain grain orientations as it passes through the grain central to the image.

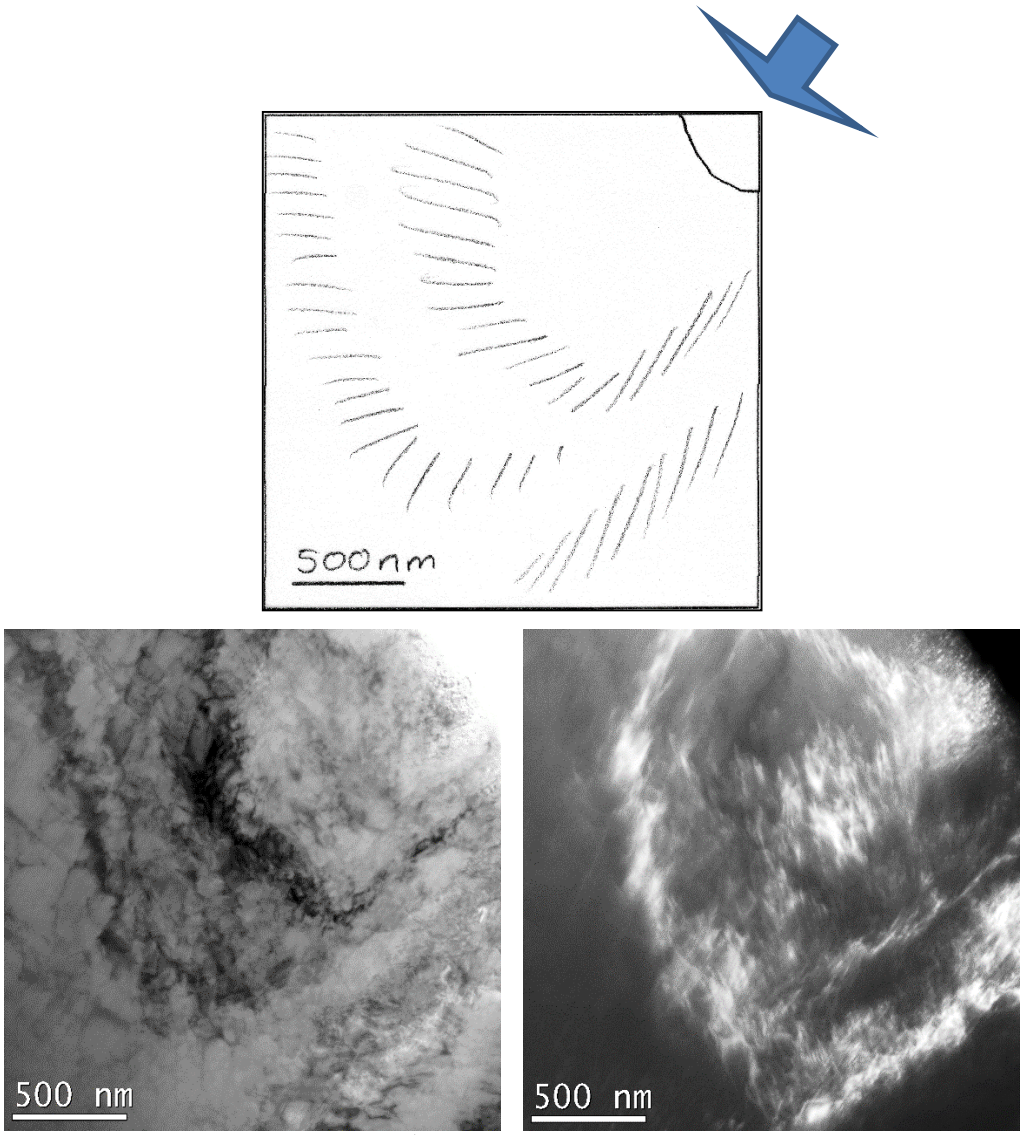

Figure 150 - Fe-14wt%Cr unimplanted (bright field and dark field under indentation top right) Semicircular bend contours spread out from the indentation.

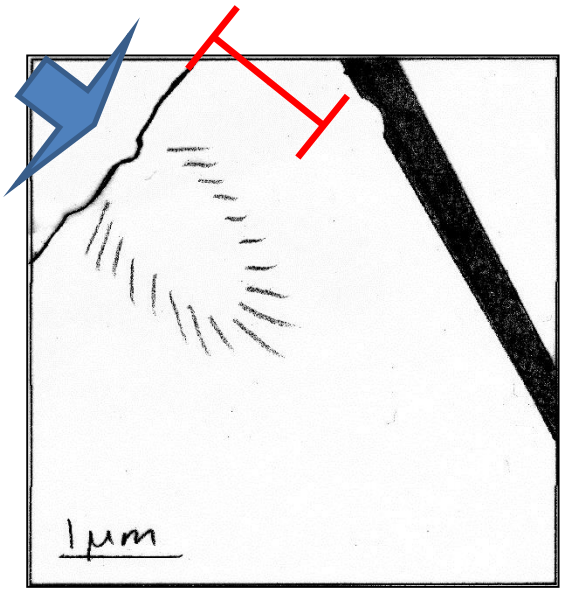

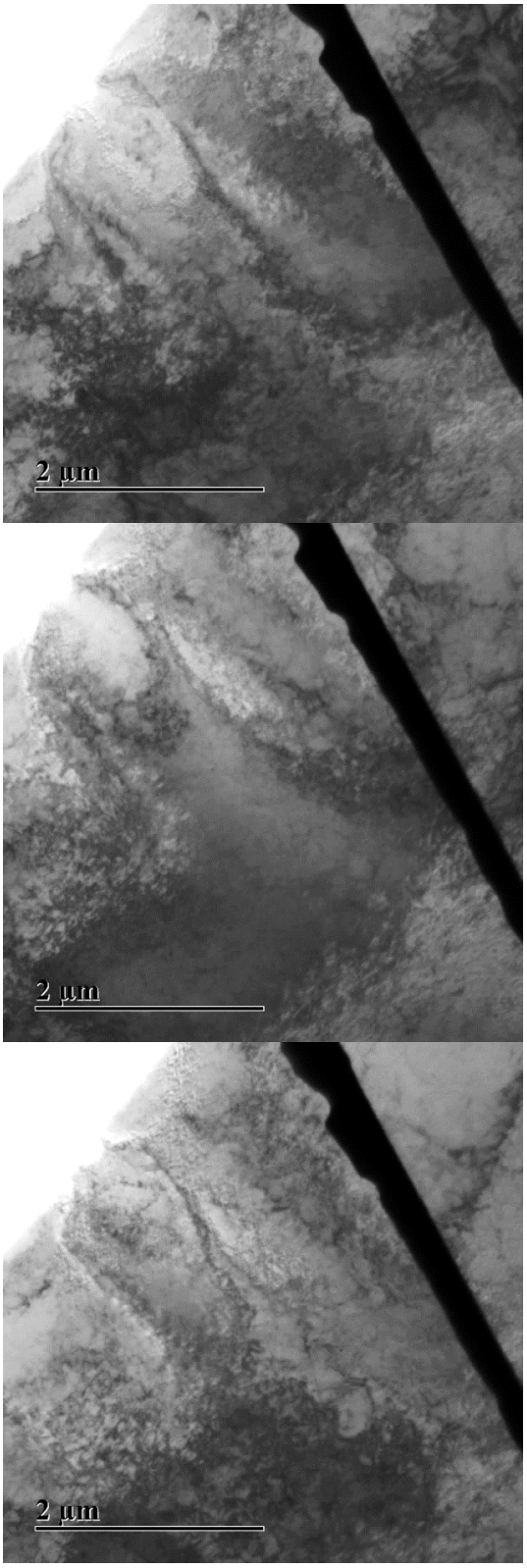

Figure 151 - Fe-14wt%Cr 2000appm Ne (-2°, 0°, +2° tilt) Note the bend contours spreading out around the indentation, and how they change position with tilt. (The black line is a sample preparation defect)

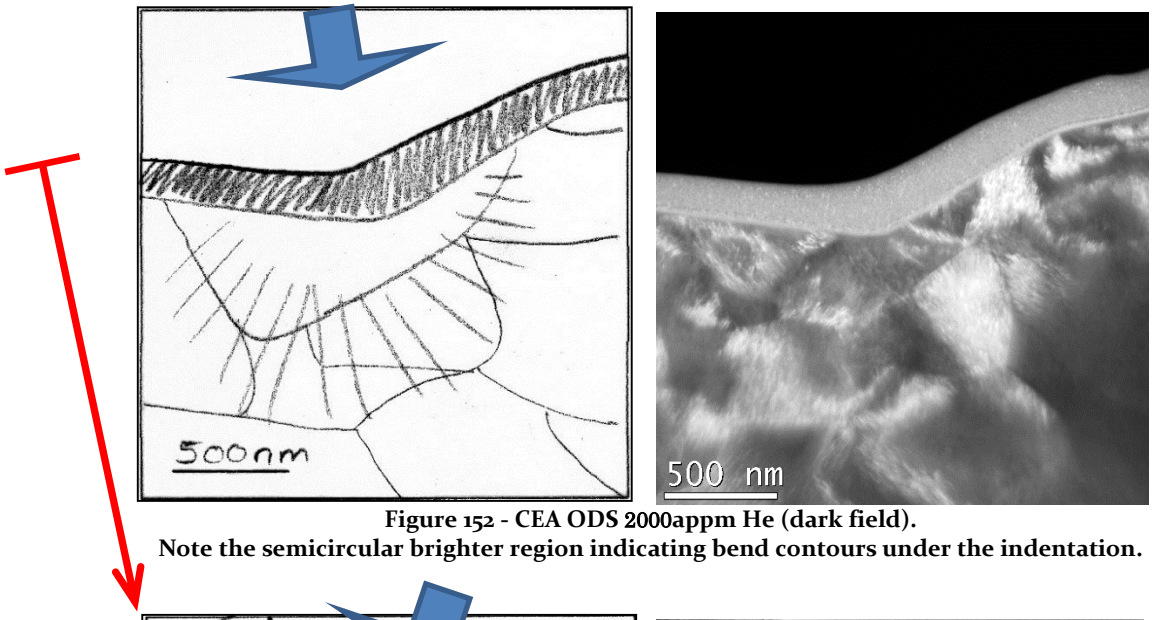

Figure 152 - CEA ODS 2000appm He (dark field).
Note the semicircular brighter region indicating bend contours under the indentation.

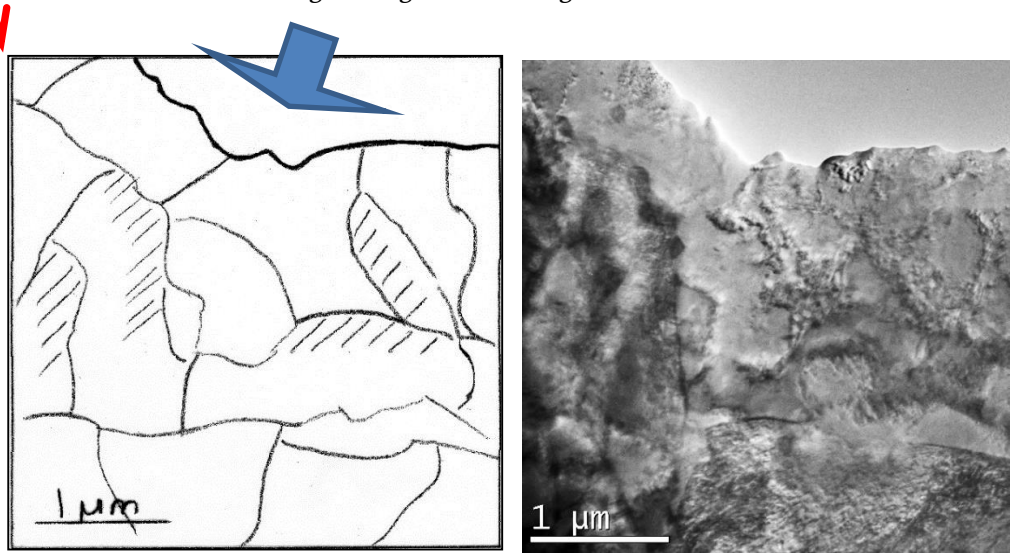

Figure 153 - EUROFER unimplanted
Note the complicated grain structure causing the bend contours to appear ragged; they are easiest to see approximately parallel to the left of the image.

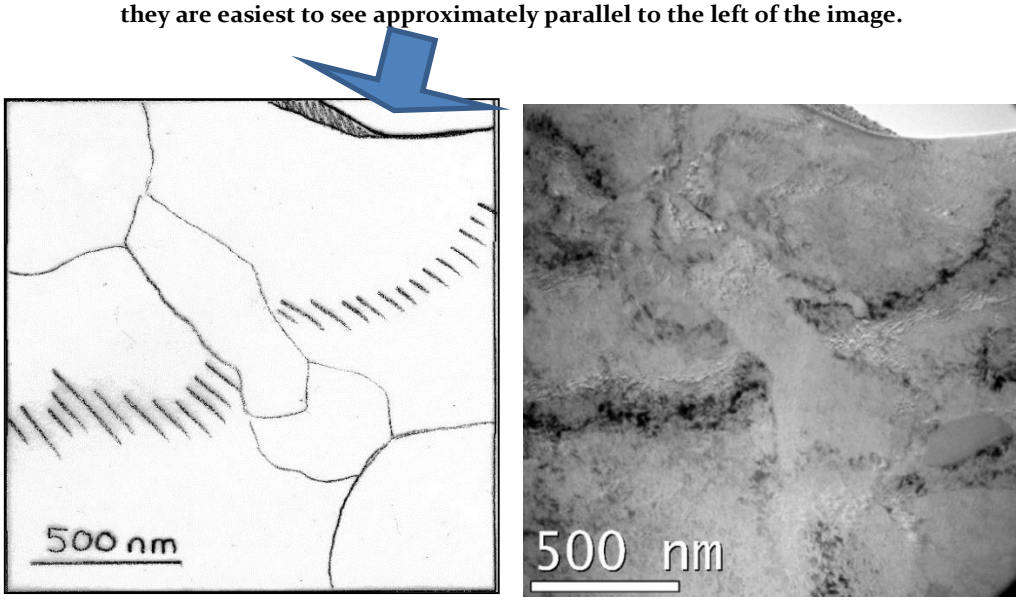

Figure 154 - EUROFER ODS unimplanted
Note that the dark bend contour appears cut off by an intermediate grain with a different orientation.

27.3 Discussion

When an elasto-plastic material is indented, the mechanical deformation leaves a plastically deformed zone after the indenter is unloaded; this plastic zone is approximately hemispherical down from the surface (Figure 155) [180]. This plastically deformed region retains residual stresses after the indenter tip is removed. When TEM samples are cut through this stressed region, the physical material constraints are reduced and the residual stresses can relax causing the thin foil to buckle.

Imaging in a TEM relies on the different features in a sample causing differing amounts of scattering and diffraction to produce a range of contrast on the image. For two beam imaging in TEM, diffraction contrast will only be seen if the lattice planes in the materials corresponding to the diffracted beam are perturbed by some form of lattice defect, e.g. a dislocation. Similarly to dislocation contrast, bend contours can also be seen in a buckled foil as the lattice orientation with respect to the beam changes the diffraction condition, i.e. a particular set of diffracting planes is not parallel everywhere. Figure 156 shows the lattice planes parallel to the incident beam at the centre and edges of the figure. The beams marked A, however, where the foil has bent, hit the foil exactly in the Bragg condition and diffract. Below these diffracted beams a dark region appears in the image. These dark lines follow the contours of the bent specimen. In dark field imaging, the incident beams are diffracted into view, and therefore appear as bright lines on the image.

Distinguishing bend contours from real line defects in a sample is simple; bend contours do not have a fixed position with respect to the sample as it depends on the angle between the incident beam and lattice planes. Therefore, when a sample is tilted, bend contours will appear to move, as seen in Figure 151.

In these indented samples, the residual stresses left by indentation cause the thinned foil to buckle around the point of the indentation, leading to the approximately semicircular bend contours seen in the TEM images.

In the Fe-14wt%Cr, there are no grain boundaries near the indentation, therefore the residual stresses can relax in all directions which leads to much smoother contour lines. In the other materials the multiple grain orientations present mean that the Bragg condition will not be met by the incident beam the whole way round the bent region, and therefore the bend contour will not appear as a smooth line. A good example of this is Figure 154 where the bend contour disappears as it passes through the grain centre of the image, and then reappears in the next grain where the Bragg condition is met again. The many small grains present in CEA ODS, EUROFER and EUROFER ODS will also affect the residual stress relaxation, grain boundaries sliding becomes a possible mode of relaxation, potentially reducing the bend in the material and therefore less contouring is seen.

This difference in bend contouring seen between Fe-14wt%Cr and other materials is therefore due to the material microstructure. This equates with the results seen in hardness (Chapter 3), micropillar (Chapter 4), and microcantilever (Chapter 5) work: where CEA ODS, EUROFER and EUROFER ODS all yielded similar results that as a group were significantly different to those of Fe-14wt%Cr. For example, in microhardness testing of the unimplanted materials, the two ODS variants have very similar high hardnesses, and although the EUROFER hardness is less, it is still high compared with the low Fe-14wt%Cr (microhardness at ~6μm depth: CEA ODS and EUROFER ODS ~4GPa, EUROFER ~2.5GPa, Fe-14wt%Cr ~1.5GPa). The microcantilever testing results show a similar trend to the hardness. Stress measured at 2% strain gave CEA ODS 3.2GPa, EUROFER ODS 2.8GPa and EUROFER 2.4GPa, compared to Fe-14wt%Cr 1.2GPa. In the micropillar compression testing, the deformation modes seen

in the compressed pillars group together the CEA ODS, EUROFER and EUROFER ODS. These showed bowing of the micropillar sides and small, surface slip lines, compared with distinct, separate, cross-pillar slip in Fe-14wt%Cr. Full comparison of the results from each technique will be presented in Chapter 7.

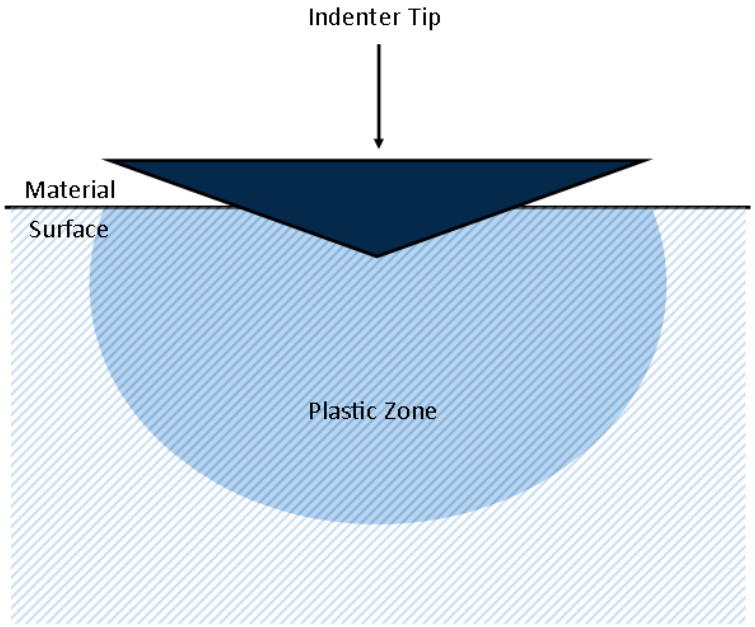

Figure 155 - Showing the approximate shape of the plastic zone formed under an indentation.

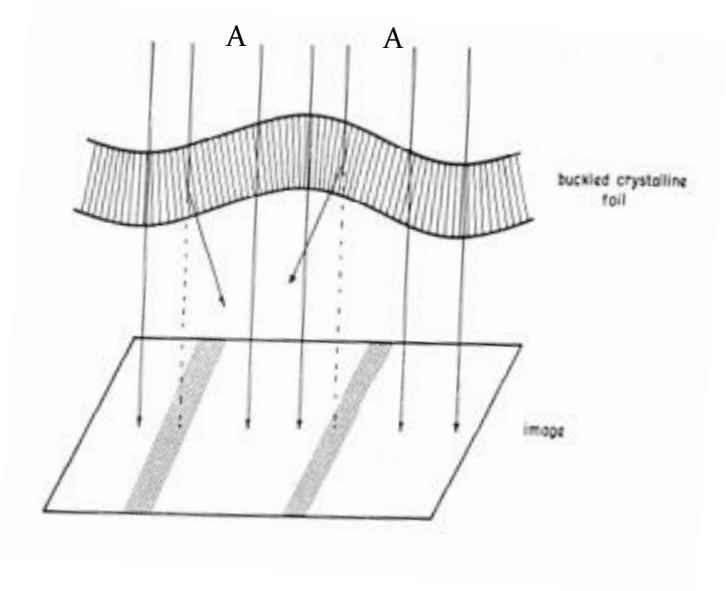

Figure 156 – Origins of bend contours [181]

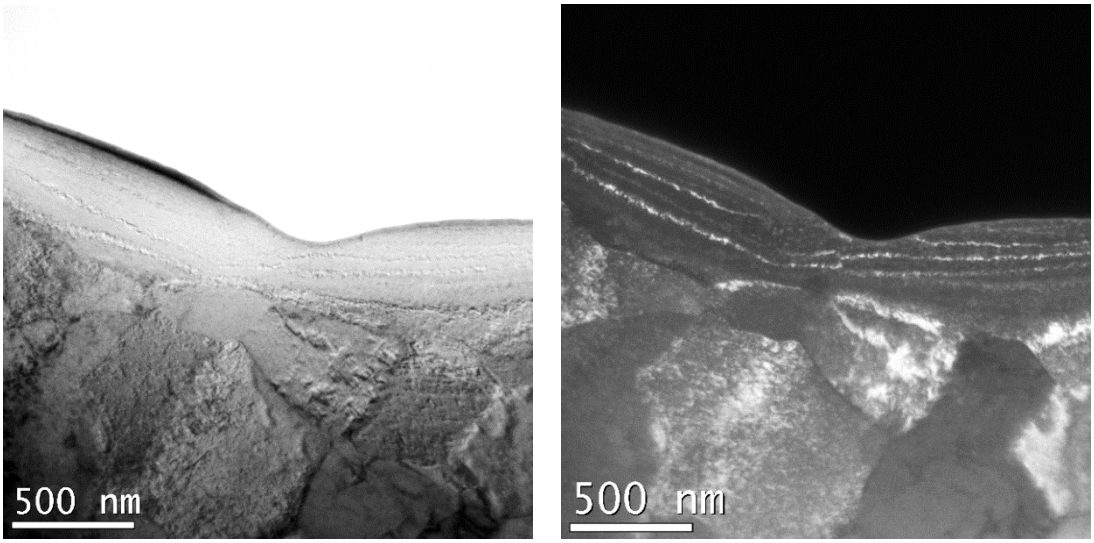

Figure 157 - CEA ODS unimplanted

In one sample (Figure 157), a set of contrast contours was seen in the surface layer, predominantly visible in the dark field image. This surface layer is the platinum protective layer, laid down on the surface during FIB machining before the TEM foil is extracted; deposited by ion beam assisted chemical vapour deposition. The deposit contains nano-crystals, but usually appears in TEM images with a single contrast along the layer (see Figure 152). In this image, the bright contrast in a dark field image means the diffraction condition is being satisfied there, ergo the bright bands must be crystalline. It is possible that if this deposition were performed at the end of the life of the FIB platinum source, the deposition may not have been laid down evenly; and if the incident gallium beam caused local heating, the platinum could have crystallized somewhat while it was being deposited. This would lead to the irregular layer structure seen in this image.

These set of low magnification TEM images were taken to enable comparison between the implantation conditions within each material (as well as comparison across materials); however, at this magnification, there are no obvious differences due to implantation in any of the samples.

28 Transmission Electron Microscopy of Bubbles

The second purpose of cutting TEM foils from the surface of the bulk implanted materials was to investigate whether the gas implantations of helium and neon had caused bubble formation in these materials, and how the oxide dispersion content of CEA ODS and EUROFER ODS affects bubble formation.

Bubbles are not easily detected in TEM, because when a sample is in focus, the bubble causes no disruption to the imaging electron beam and therefore no shape appears on the image. However, when viewed in a bright field underfocus condition, bubbles appear surrounded by a bright Fresnel fringe; in overfocus this contrast is reversed and a dark Fresnel fringe appears [33][182]. The optimum way to find bubbles is therefore to image an area at focus, underfocus and overfocus – if dark spots appear in underfocus and bright spots are present in the same locations at overfocus, these are likely to be bubbles (or voids).

TEM lift-outs of all the materials were imaged in all implantation conditions. The following images were taken in the region of the samples that should contain implanted ions (top 3μm in 2000appm He and 2000appm He + 4.5dpa Fe, top 1.2μm in 2000appm Ne). The images of unimplanted material were also taken within the top few microns to ensure consistency of sample depth. Bubbles start to be visible at ~±200nm defocus, but should be clearly visible at ±500nm [183]. All samples were imaged over a range of defocus to determine the existence (or not) of bubbles. The images below, however, were mostly taken at ±500nm defocus for consistency. The samples used did not perform well above 200,000x magnification (magnetic distortion was difficult to overcome); hence all the images were taken at 200,000x. Full discussion of these images follows in Section 28.2.

28.1 Results

28.1.1 Unimplanted

No bubble-like structures can be seen in any unimplanted materials at 200,000x magnification.

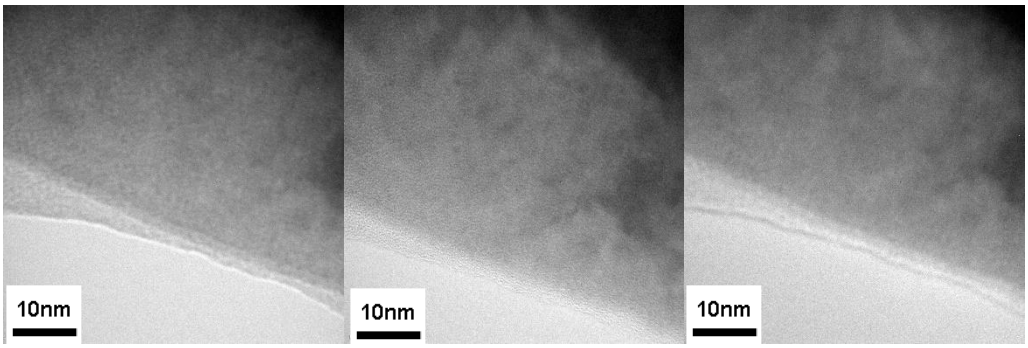

Figure 158 - Fe-14wt%Cr unimplanted (focus: -500nm, 0, +500nm)

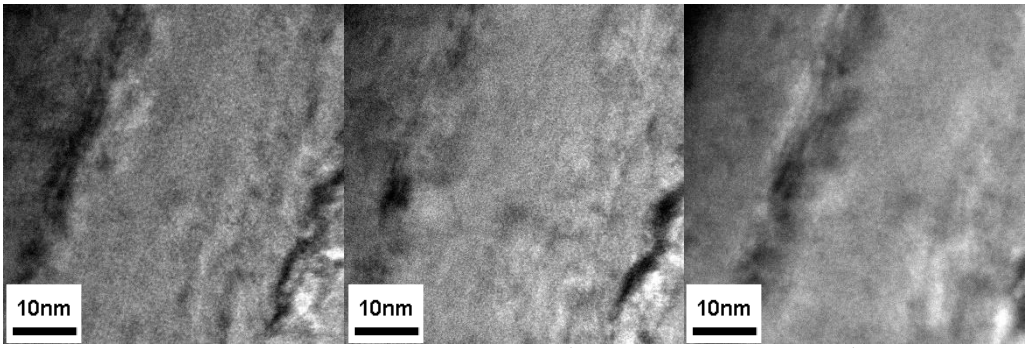

Figure 159 - CEA ODS unimplanted (focus: -500nm, 0, +500nm)

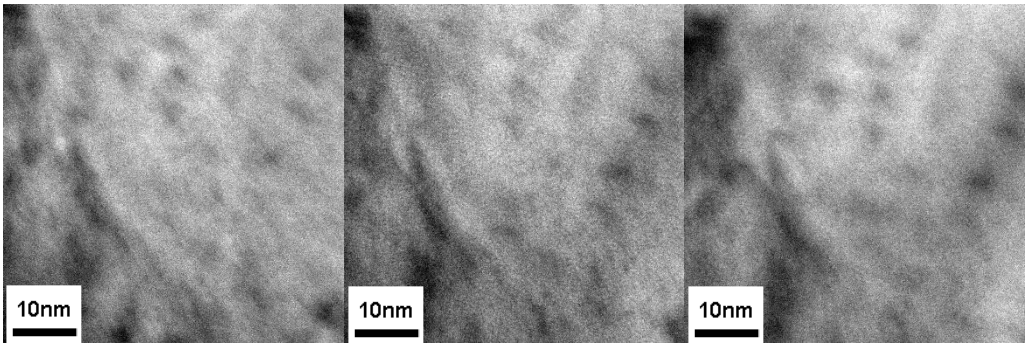

Figure 160 - EUROFER unimplanted (focus: -500nm, 0, +500nm)

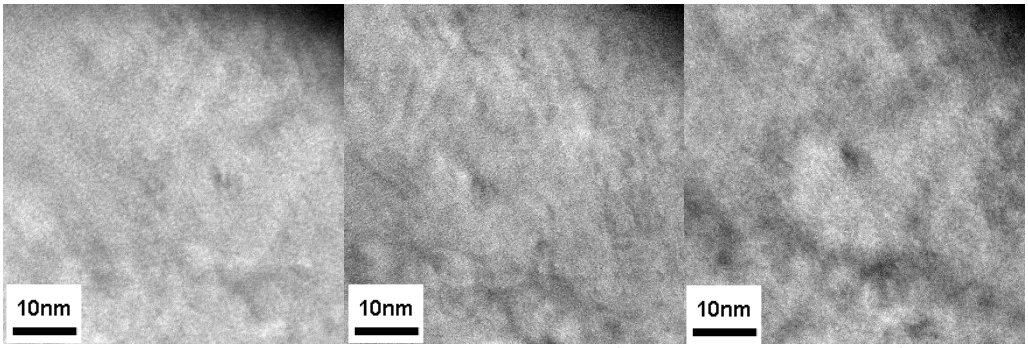

Figure 161 - EUROFER ODS unimplanted (focus: -500nm, 0, +500nm)

28.1.2 2000appm He

In Fe-14wt%Cr +2000appm He bubble-like structures can be seen (best viewed on a backlit screen; see enclosed CD).

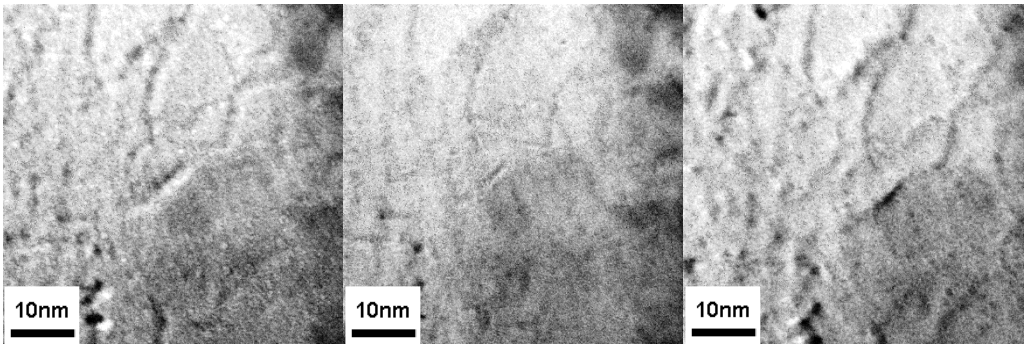

Figure 162 - Fe-14wt%Cr 2000appm He (focus: -500nm, 0, +500nm)
(Figure 175 magnifies this image and indicates the bubble locations).

None of the other materials showed any bubble-like structures.

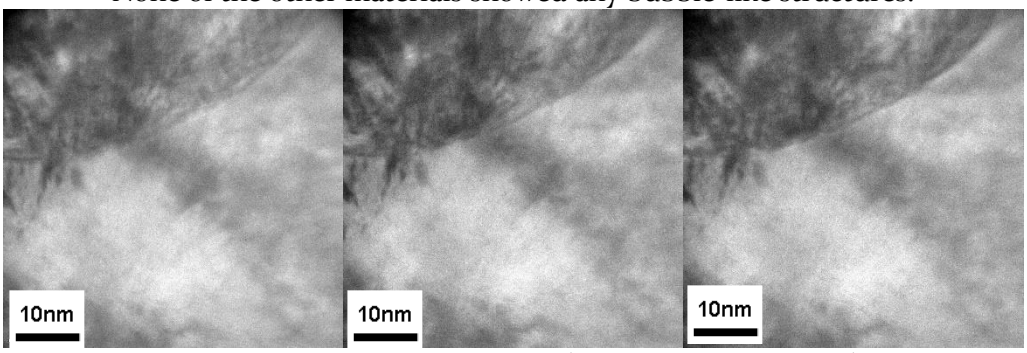

Figure 163 - CEA ODS 2000appm He (focus: -500nm, 0, +500nm)

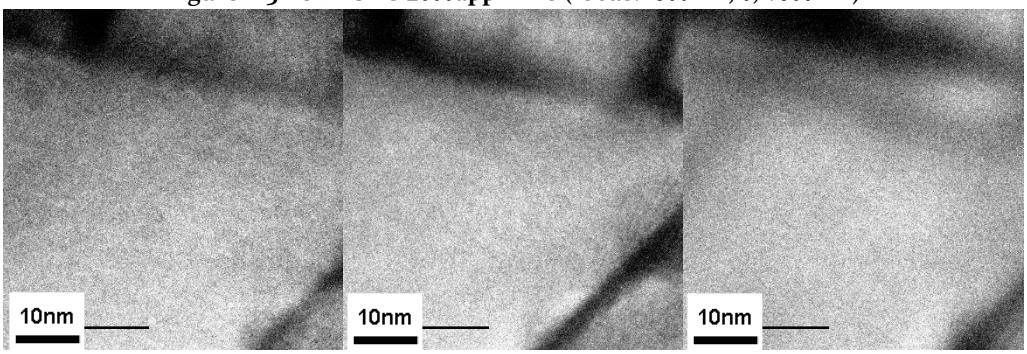

Figure 164 - EUROFER 2000appm He (focus: -500nm, 0, +500nm)

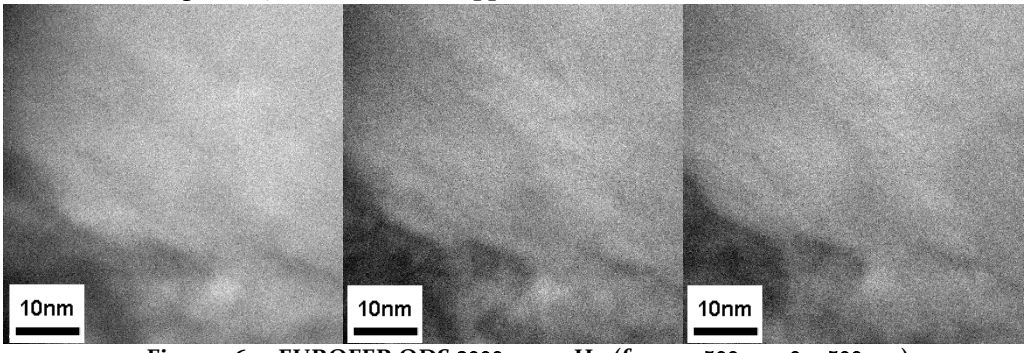

Figure 165 - EUROFER ODS 2000appm He (focus: -500nm, 0, +500nm)

28.1.3 2000appm He + 4.5dpa Fe

No bubble-like structures are visible in any of the 2000appm He + 4.5dpa Fe materials at 200,000x magnification.

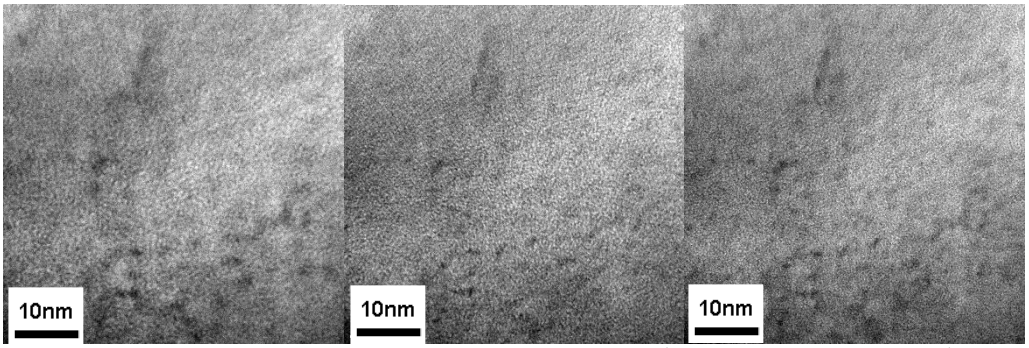

Figure 166 - Fe-14wt%Cr 2000appm He + 4.5dpa Fe (focus: -500nm, 0, +500nm)

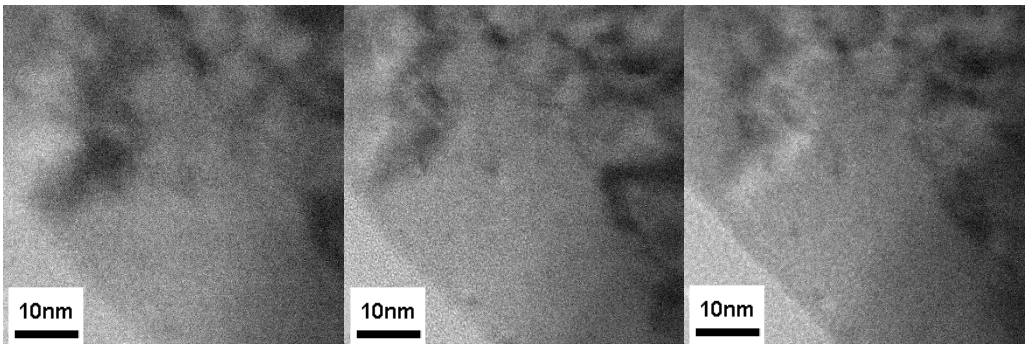

Figure 167 - CEA ODS 2000appm He + 4.5dpa Fe (focus: -500nm, 0, +500nm)

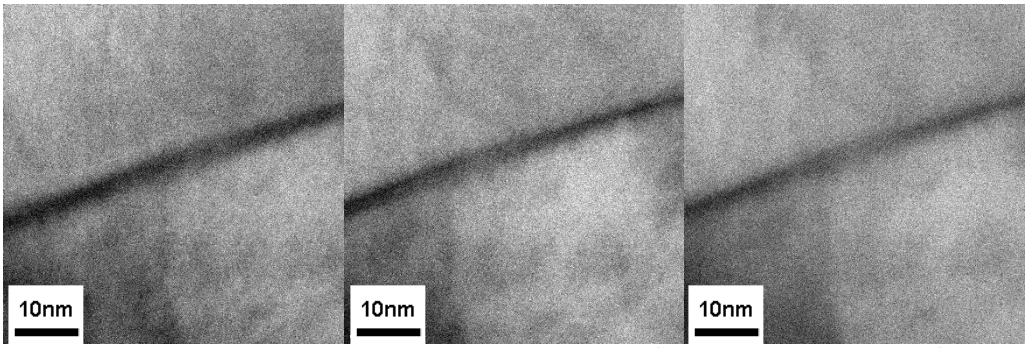

Figure 168 - EUROFER 2000appm He + 4.5dpa Fe (focus: -500nm, 0, +500nm)

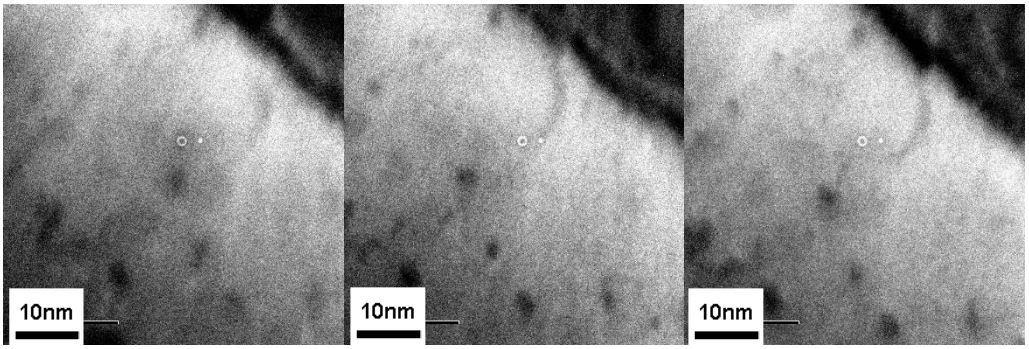

Figure 169 - EUROFER ODS 2000appm He + 4.5dpa Fe (focus: -500nm, 0, +500nm)
(The white circle and spot centre frame are camera artefacts)

28.1.4 2000appm Ne

In Fe-14wt%Cr +2000appm Ne, bubble-like structures are visible (best viewed on a backlit screen, see enclosed CD). Figure 176 magnifies Figure 170 and indicates the bubble locations).

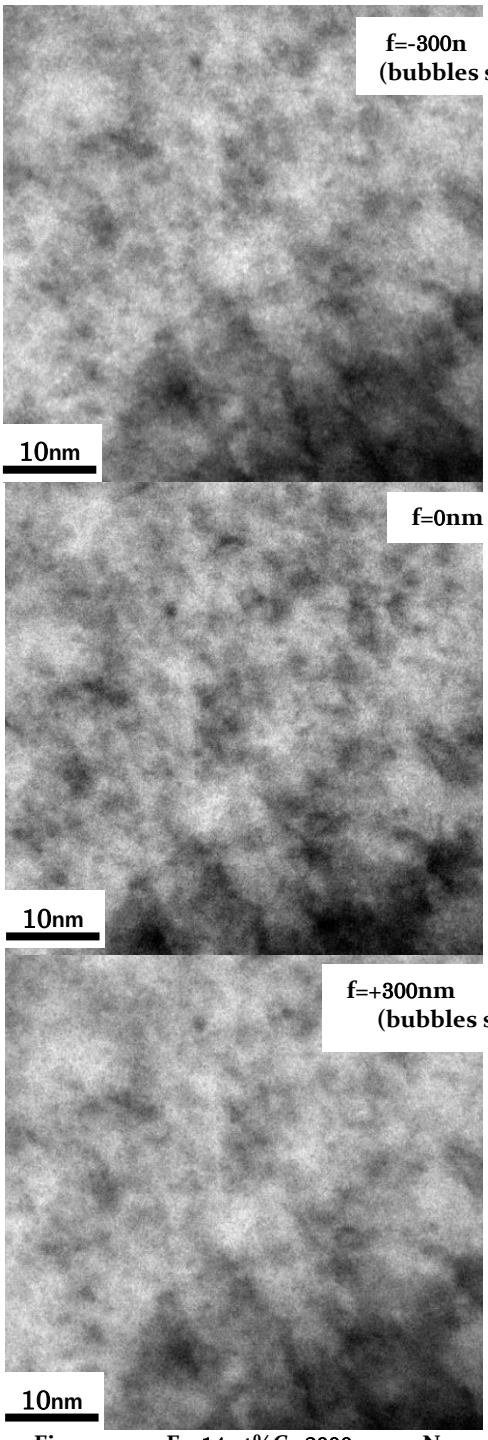

Figure 170 - Fe-14wt%Cr 2000appm Ne (focus: -300nm, 0, +300nm) Showing bubble-like features

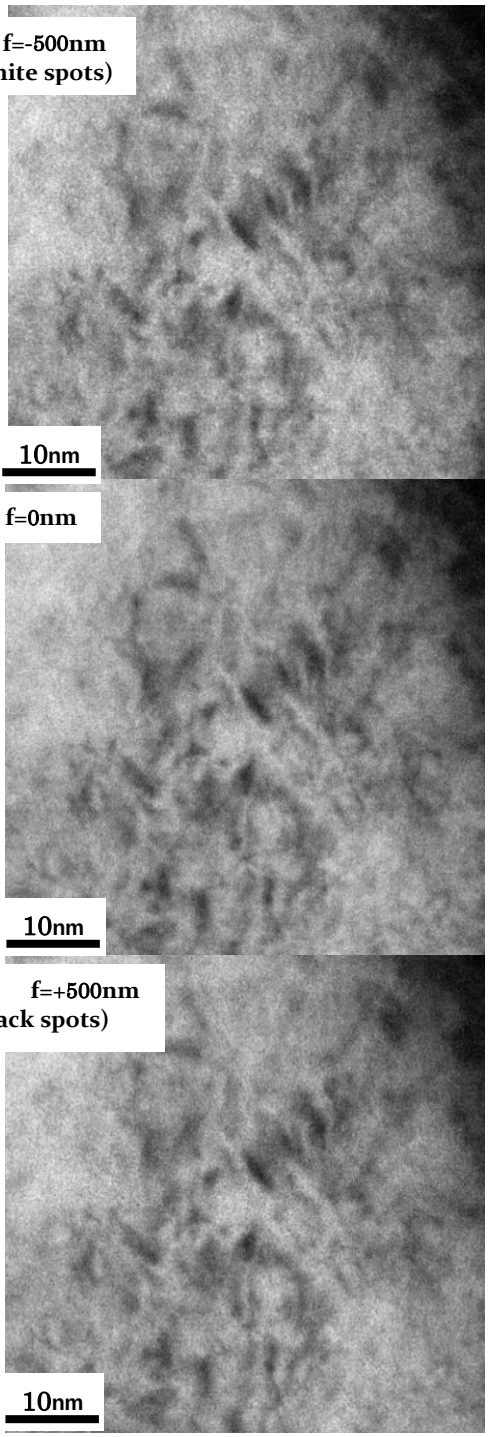

Figure 171 - Fe-14wt%Cr 2000appm Ne (focus: -500nm, 0, +500nm) Showing bubble-like features

None of the other materials (CEA ODS, EUROFER and EUROFER ODS) showed any bubble-like structures.

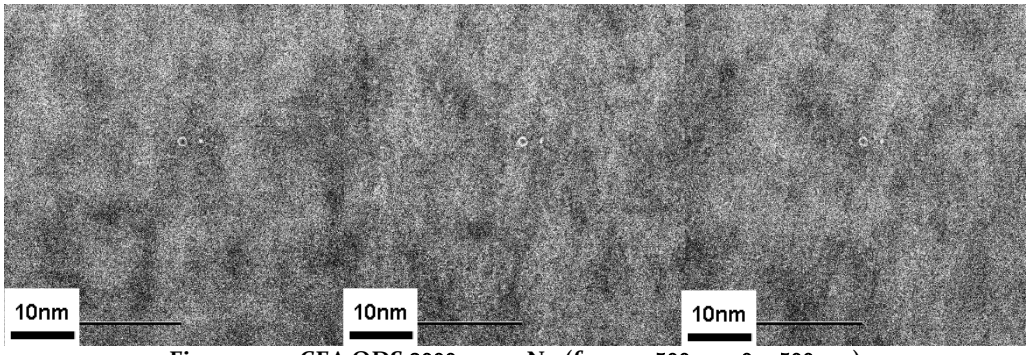

Figure 172 - CEA ODS 2000appm Ne (focus: -500nm, 0, +500nm)
(The white circle and spot centre frame are camera artefacts).

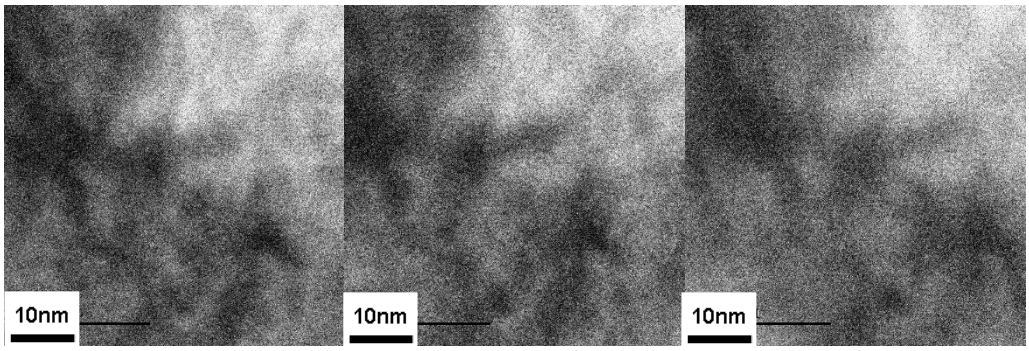

Figure 173 - EUROFER 2000appm Ne (focus: -500nm, 0, +500nm)

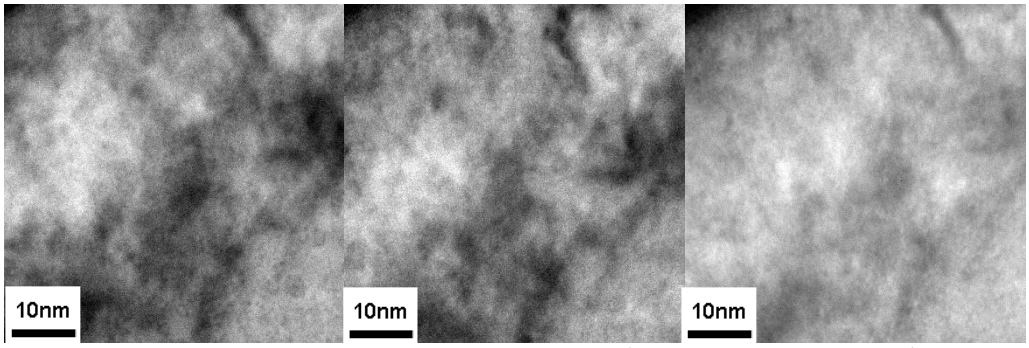

Figure 174 - EUROFER ODS 2000appm Ne (focus: -500nm, 0, +500nm)

28.1.5 Bubble Summary

Table 22 - Visible bubble-like features at 200,000x magnification

	Unimplanted	*2000appm He*	*2000appm He + 4.5dpa Fe*	*2000appm Ne*
Fe-14wt%Cr	✘	✓	✘	✓
CEA ODS	✘	✘	✘	✘
EUROFER	✘	✘	✘	✘
EUROFER ODS	✘	✘	✘	✘

The only samples where bubble-like features were seen at 200,000x magnification were Fe-14wt%Cr in 2000appm He and 2000appm Ne implantation conditions. The term 'bubble-like features' is used to describe the points seen in these images because without very high resolution microscopy and chemical analysis of the contents of these points, their true nature cannot be determined. The features were formed during gas implantations and appear circular (therefore presumably spherical), so are assumed to be gas-filled bubbles; they may, however, simply be spherical voids in the lattice, not filled with gas and therefore technically not bubbles.

Figure 175 and Figure 176 show the underfocus and overfocus image pairs from Figure 162 and Figure 170 respectively. Each pair of images is vertically offset to align the microstructural features – a selection of the most obvious bubble-like features has been highlighted with red circles. When the images are backlit (i.e. on a computer screen), the contrast enables many more bubble-like features to be identified that are less visible in the print copies.

To confirm that these features match in the under and overfocus images, the overfocus images of Figure 175 and Figure 176 were black/white inverted and overlaid at 50% transparency onto the underfocus images. This causes most features to be greyed out except for the bubble-like features (white in underfocus; black in overfocus, inverted to white), which appear as pale spots. Figure 177 and Figure 178 show the overlaid images of Fe-14wt%Cr implanted with 2000appm He and 2000appm Ne respectively, and an enlarged section of each image contains visible pale spots indicating bubble-like features.

There is a range of size and image contrast across the visible bubble-like features, including features that are barely distinguishable from the background noise of the material lattice (~1nm diameter). The number and density of the bubble-like features cannot be accurately determined due to this fading range at the lower end of the feature size. Similar previous work has noted that helium bubble clusters less than 0.8nm diameter cannot be observed by normal through-focus TEM techniques [184].

This range of size of bubble-like features in the two Fe-14wt%Cr materials suggests that, although not visible at 200,000x magnification, there may be similar smaller features present in the other materials. It cannot be assumed that no bubble-like features have formed, therefore further analysis can only apply to those features visible at 200,000x magnification (Table 22).

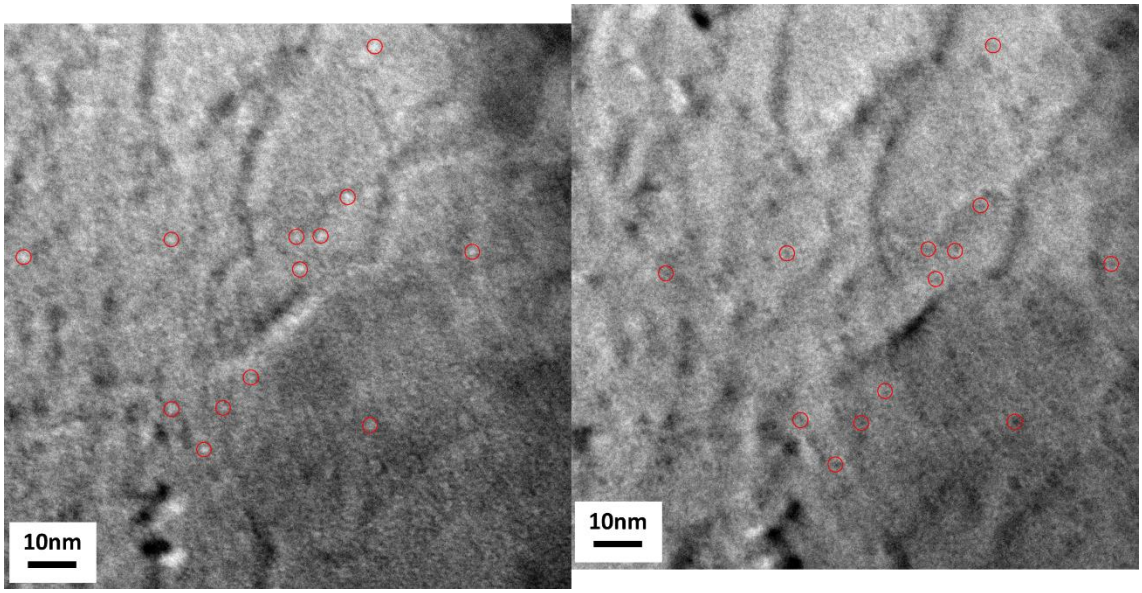

Figure 175 - Fe-14wt%Cr 2000appm He (focus: -500nm, +500nm)
Bubble-like features indicated by red circles .
Only the most distinct bubbles have been picked out; there are many more less distinct within this area.
Bright spots in underfocus corresponding with dark spots in overfocus indicate bubble-like features.

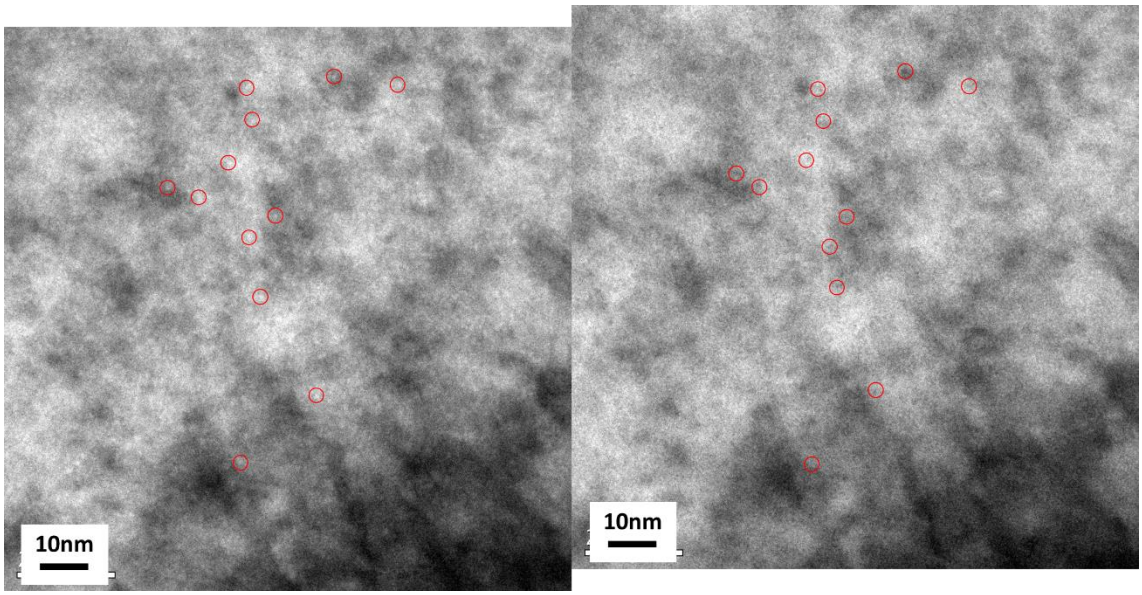

Figure 176 - Fe-14wt%Cr 2000appm Ne (focus: -300nm, +300nm)
Bubble-like features indicated by red circles
Only the most distinct bubbles have been picked out; there are many more less distinct within this area.
Bright spots in underfocus corresponding with dark spots in overfocus indicate bubble-like features.

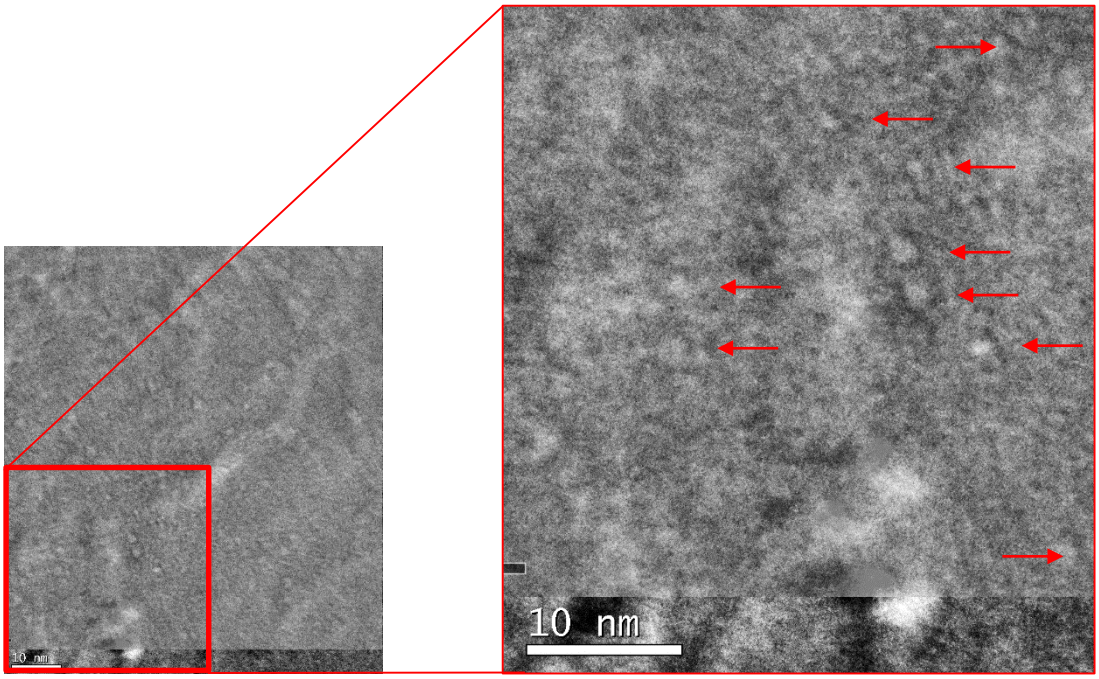

Figure 177 - Fe-14wt%Cr 2000appm He
Enlarged area of overlaid original -500nmand inverted +500nm images. The arrows point to the most obvious pale ~2nm diameter spots which are the bubble-like features.

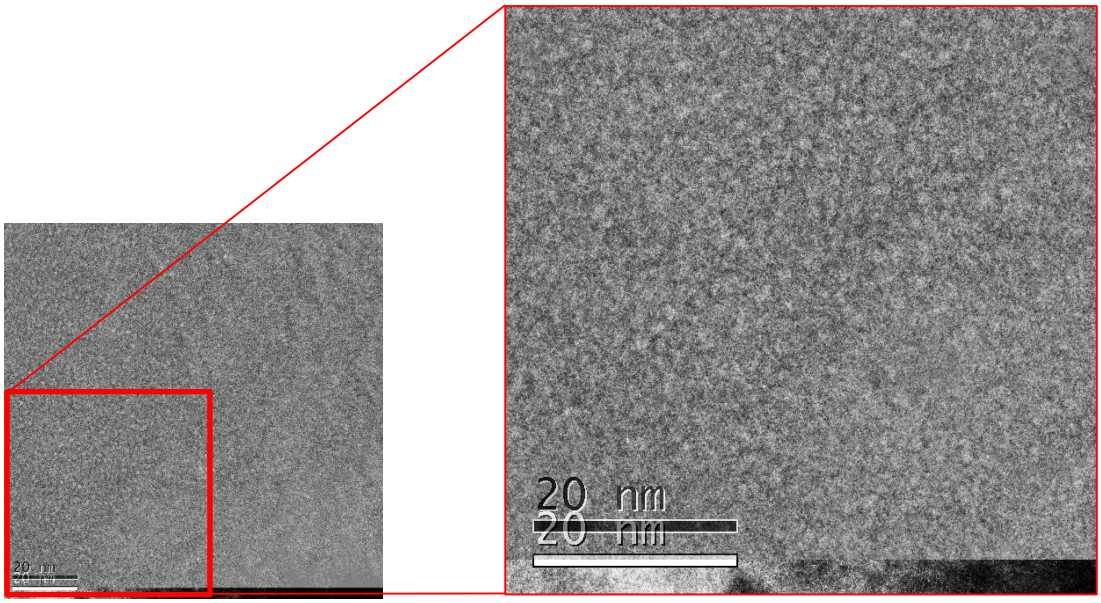

Figure 178 - Fe-14wt%Cr 2000appm Ne
Enlarged area of overlaid original -300nm and inverted +300nm images. The pale ~2nm diameter spots filling the whole image are the bubble-like features.

28.2 Discussion

It is immediately obvious from the high magnification (200,000x) bubble-imaging results that no bubble-like features were seen in any of the unimplanted specimens. Special care was taken to hunt for any form of features across each of the TEM lift-out samples to ensure it was not simply a single bubble-free area, but that the entire lift-out contained no bubbles. This complete lack of bubble-like features in all the unimplanted specimens means that any features observed in the implanted specimens are almost certainly due to the implantation to which they were subjected.

Bubble-like features large enough to be visible at 200,000x magnification were only seen in Fe-14wt%Cr in the 2000appm He and 2000appm Ne implantation conditions. Fe-14wt%Cr has the simplest microstructure of the materials in this project, with large grains (and therefore low grain boundary density) and no in-granular precipitates of any sort acting as low energy sites at which implanted ions could collect. The implanted gas will, therefore, initially enter the material lattice as interstitials, filling any voids and point defects already present. As the gas ion concentration increases in the lattice, it becomes more energetically favourable for the helium to coalesce and form bubbles (as discussed in Chapter 1, Section 4.3.4 [32]).

The bubbles formed will interact with dislocations in the material when it is plastically deformed and act as obstacles to dislocation motion. Weak obstacles will allow dislocations to pass perpendicular to the movement direction ($Ø_c$=90°). Dislocations must bow around strong obstacles, at their strongest $Ø_c$=0°. Bubbles are relatively weak obstacles, therefore estimated as $Ø_c$=75°. The breakaway angle, combined with estimated bubble-spacing from the images, can be used to calculate the hardening with the following equations [185]:

$$\Delta\tau = \frac{Gb}{\Lambda}(\cos \emptyset_c)^{\frac{3}{2}}$$

$$\Delta\tau \approx \frac{\Delta\sigma_y}{2} \approx \frac{\Delta H}{6}$$

$\Delta\tau$ = change in dislocation line stress
G = shear stress (typically 90GPa for steels)
b = Burgers vector (typically 0.25nm for steels)
Λ = mean obstacle spacing
$\emptyset_c$ = critical angle for breakaway (75°)
$\Delta\sigma_y$ = change in yield stress
$\Delta\tau$ = change in hardness

Table 23 - Calculating hardening due to bubbles with a critical breakaway angle of 75°

Fe-14wt%Cr	Measured Spacing (nm)	Calculated Δτ (GPa)	Calculated ΔH (GPa)	Measured ΔH (GPa)
2000appm He	6.6	0.45	2.7	2.6
2000appm Ne	5.0	0.59	3.6	4.1

The measured spacing was calculated in the 2000appm He sample by averaging the nearest neighbour distances for the obvious bubble-like features measuring from the centre of each feature (indicated with red arrows in Figure 177). This method gave a good estimate of hardening due to helium, but underestimated the hardening due to neon (compared with hardness results Chapter 3), suggesting that neon bubbles have a stronger dislocation-retarding effect than the helium bubbles. Calculating the theoretical breakaway angle from the measured ΔH, however, gives 75.4° for He and 73.5° for Ne showing there is very little difference between bubble strengths.

Bubble-like features were only seen in Fe-14wt%Cr. The other materials have significantly smaller grain sizes than Fe-14wt%Cr (CEA ODS ~1x5μm, EUROFER ~4x4μm, EUROFER ODS ~2x2μm compared with Fe-14wt%Cr ~200x200μm). Therefore, there is a much greater length of grain boundary per volume of material (grain boundary densities: Fe-14wt%Cr ~$1.5\text{x}10^{4}\text{m}^{2}\text{m}^{-3}$, CEA ODS ~$2.2\text{x}10^{6}\text{m}^{2}\text{m}^{-3}$, EUROFER ~$7.5\text{x}10^{5}\text{m}^{2}\text{m}^{-3}$, EUROFER ODS ~$1.5\text{x}10^{6}\text{m}^{2}\text{m}^{-3}$; Chapter 2 Section 9). This grain boundary area acts as a low energy site for the implanted gas to settle (causing a lower concentration in the lattice as interstitials etc.). The two EUROFER materials

contain vanadium and tantalum, which form fine carbide distributions [186]; CEA ODS and EUROFER ODS contain yttrium, which precipitates out in various oxide forms (e.g. Y_2O_3 and $YTiO_2$ [33]). The CEA ODS titanium content may also form titanium carbides if the carbon content is not controlled and the titanium is not completely confined to oxide complexes [187]. All these precipitates act as low energy trapping sites for gases, particularly the oxide particles (gas-trapping is their design purpose). As the implanted helium is attracted to and trapped by these precipitates, less remains free in the lattice to form bubbles and voids.

The ODS materials are designed with a high number density of very small particles, which lead to the dispersion of lots of small bubbles, rather than the smaller number of large bubbles seen in Fe-14wt%Cr. The dislocation motion retardation effect of these particles does not change significantly whether they have trapped He (or Ne) or not. The fine carbide distribution in EUROFER works similarly.

In the implanted specimens of CEA ODS, EUROFER and EUROFER ODS, bubbles have either formed below the resolution of the TEMs used in this project (i.e. less than ~0.8nm diameter [184]), or the helium is of sufficiently low concentration inside the grains that no bubbles form. If helium is settling at the grain boundaries and precipitates, the surface area density should affect the helium distribution. Using average oxide particle densities ($4.6x10^{23}m^{-3}$) and diameters (1.3nm) for ODS materials [102], the total particle surface area can be calculated as $2.44x10^{6}m^{2}m^{-3}$ (Appendix C). Helium has an atomic radius of 31pm, which would give full coverage of atoms as ~280 atoms per nm^2. 2000appm helium equals 353 helium atoms per oxide particle, or 66 helium atoms per nm^2 particle surface area, indicating that the helium could form as a monolayer around the oxide particles. Grain boundaries also provide low energy sites to which the helium could be attracted. The surface area of

grain boundaries is significantly larger than the surface area of the particles (grain boundary densities: Fe-14wt%Cr ~$1.5 \times 10^{4} m^{2} m^{-3}$, CEA ODS ~$2.2 \times 10^{6} m^{2} m^{-3}$, EUROFER ~$7.5 \times 10^{5} m^{2} m^{-3}$, EUROFER ODS ~$1.5 \times 10^{6} m^{2} m^{-3}$); therefore providing further helium trapping sites. Fe-14wt%Cr has significantly less grain boundary surface area than the other materials (and no oxide or carbide precipitates); therefore helium has fewer accessible lower energy sites. It therefore collects in the lattice, ultimately coalescing, forming bubbles and voids.

The lack of bubbles in the dual-beam 2000appm He + 4.5dpa Fe implanted Fe-14wt%Cr sample should be noted. As bubble-like features were seen in the single beam 2000appm He implantation, it would be expected that they should be present from the 2000appm He + 4.5dpa Fe implantation. Special further TEM investigations were performed on the Fe-14wt%Cr 2000appm + 4.5dpa Fe sample to ensure that no bubble-like features were visible anywhere in the sample (and the first investigation was not limited to a bubble-free area). It was concluded that no bubble-like features could be found at 200,000x magnification.

This may be because the incident iron ions create sites for the helium to fill. The implanted iron will cause point defects such as interstitials and vacancies to form. With an implantation dose of ~7×10^{15} ions cm^{-2}, the defect population created within the material will be significant, although TEM of the surface region showed no particular differences between the He only and He+Fe implantations in any of the materials. The dual-beam implantation runs simultaneously; therefore the incident helium is implanted into the material lattice as the iron is forming the defects. It is therefore likely that the helium fills the defects rather than dispersing throughout the lattice as with the single beam helium implantation. As discussed previously, providing low energy sites (in this case point defects, rather than grain boundaries or

precipitates) will reduce the helium sitting as interstitials in the lattice. With a high density of defects to fill, there is no energy incentive for the helium to coalesce and form large bubbles, therefore the helium remains below the bubble-size detection limit. It would be expected that this process also occurs in CEA ODS, EUROFER and EUROFER ODS, as any bubbles forming are already below the detection limit; however this effect is not visible in the TEM images.

This effect may help to explain the nanoindentation hardness results seen previously (Chapter 3). In all materials tested, the increase in hardness due to dual-beam 2000appm He + 4.5dpa Fe is less than the single beam 2000appm He. In the Fe-14wt%Cr sample the 2000appm He implantation increased the hardness from 2.85GPa to 5.43GPa; the 2000appm He + 4.5dpa Fe sample only has an increase in hardness to 3.3GPa (almost one sixth of the 2000appm He increase). The difference in increase in the other materials is similar, as is shown in Table 24.

Table 24 - Increase in hardness in GPa from Unimplanted, measured at 400nm depth

	Fe-14wt%Cr	CEA ODS	EUROFER	EUROFER ODS
2000appm He	2.58	1.19	1.05	1.35
2000appm He + 4.5dpa Fe	0.45	0.24	0.40	0.69

A possible reason for the lower observed increase in hardness in the dual-beam implanted samples is that the iron ion implantation adds significantly more damage (dpa) than the single gas implantation (the helium implantation will cause damage itself, but only minimally (~0.05dpa) compared with the iron implantation (4.5dpa)). The increased damage manifests itself as a greater number of point defects, (i.e. available sites for the helium). This means the overall defect distribution after implantation causes a higher number of smaller lattice defects/bubbles than would be seen in a single gas implantation. These smaller defects cause less disruption to

dislocation motion through the sample and therefore less hardening is observed. Unfortunately, due to resolution limits, the TEM imaging was unable to support or reject this theory. The effect is seen in all materials tested, but is obviously less in EUROFER and ODS materials wherever there are already other processes reducing the bubble defect size (e.g. carbide and oxide precipitates).

29 EDX Neon Detection

Energy Dispersive X-ray spectroscopy (EDX) is an analytical technique used for the elemental analysis of samples. An incident X-ray to the sample causes excitation of the surface atoms, stimulating the emission of further X-rays with wavelengths characteristic of individual elements – each element has a unique atomic structure giving a unique set of peaks in its X-ray spectrum.

Helium has a very low atomic mass and is therefore unsuitable for identification via EDX. In order to determine where the implanted ions come to rest in the samples, one set was implanted with neon as an analogue for helium [147]. The neon implantation was designed to produce lift-out samples for EDX analysis with the aim of recording a two-dimensional element distribution map perpendicular to the surface of the bulk material.

29.1 Results

The implantation of 2000appm neon has a definite physical effect on all the materials tested, notably an increase in hardness (Chapter 3). In Fe-14wt%Cr, bubble-like structures are seen to form (compare unimplanted Figure 158, with 2000appm Ne Figure 170 and Figure 171).

Using a JEOL-2100 TEM with an EDX detector, large areas scans (~1.5x1.5µm) were taken in the sub-bulk-surface region (neon implantation depth ~1.2µm) of the

Fe-14wt%Cr material. Multiple scans were performed on different areas, particularly where there were clearly bubble-like structures, and each scan was left to run for ten minutes to ensure the collected data was fully representative of the scanned area.

Only Fe-14wt%Cr was scanned as the more complicated chemical compositions of the other materials would produce a greater number of peaks in the spectrum, making identification of implanted elements more difficult.

The characteristic Kα peak of neon is at 0.848keV. The characteristic Lα peak of iron is at 0.705keV. 2000appm is 0.2at% and therefore almost at the EDX detection limit (~0.1at% [188]). However, the neon should still be just visible as a small individual peak or broadening of the iron peak. As the material is 86wt% Fe, the iron peak is significant and fairly broad. The presence of neon should be visible as a shoulder on the right hand side of the iron peak. In Figure 180, there is no visible peak or shoulder at 0.848keV (marked with a red arrow). No neon peak or shoulder was seen in any of the scans on the Fe-14wt%Cr lift-out. Because these scans were taken on a FIB lift-out foil, it is possible that the milling process has caused some of the neon to diffuse out of the sample (causing the concentration to be below the visible limit).

To assess whether the milling process caused a loss of neon, a second set of EDX experiments was performed on bulk specimens using a JEOL JSM SEM 5510LV with EDX. These scans were taken over ~5x5mm areas to maximise the possible detection area.

Fe-14wt%Cr specimens in both unimplanted and 2000appm Ne conditions were tested to provide data for comparison. On the following graphs, 0.848keV is marked with a red arrow to show where an expected neon peak should be.

Figure 181 only shows peaks for iron and chromium (as expected). Figure 182 (the neon implanted specimen) shows the same iron and chromium peaks as the unimplanted. There are also peaks for aluminium (Al) and silver (Ag); the aluminium peak is due to the aluminium stub the sample was mounted on, and the silver peak is due to the silver electrodag used to glue the sample to the stub. There is no peak at 0.848keV, nor any broadening or shoulder on the right hand side of the iron peak (at 0.705keV). Zooming in on the lower keV end of the spectrum (Figure 183) definitely shows no visible peak of any sort.

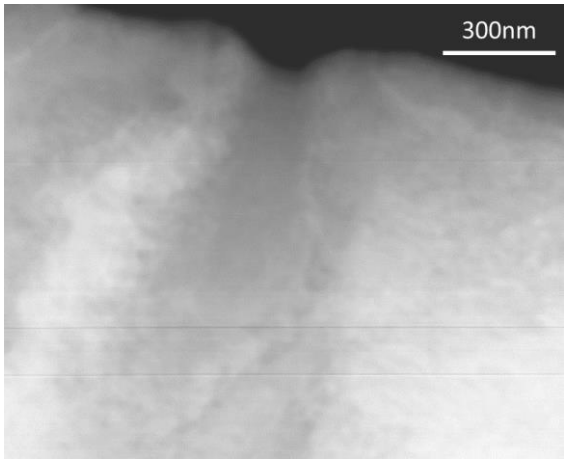

Figure 179 - TEM image of area of EDX scan (below nanoindentation)

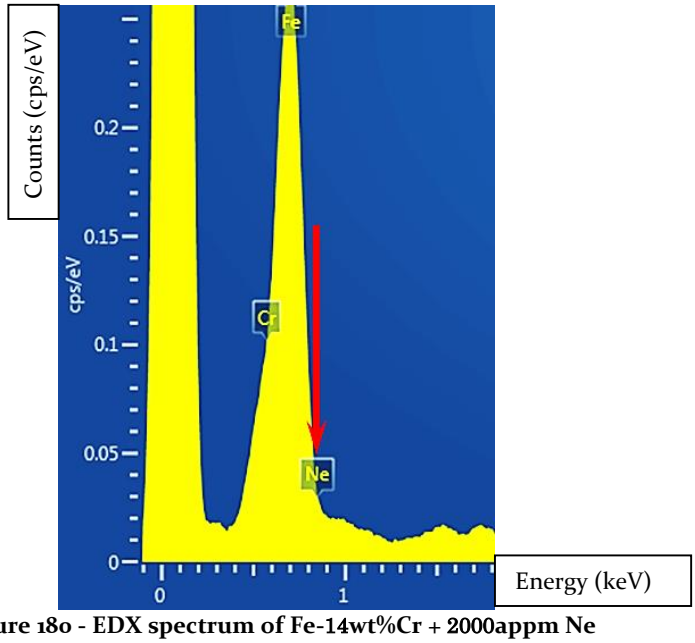

Figure 180 - EDX spectrum of Fe-14wt%Cr + 2000appm Ne
Iron and chromium peaks due to the bulk material are clearly visible, the position of the neon characteristic peak is marked with an arrow, and no neon peak is visible.

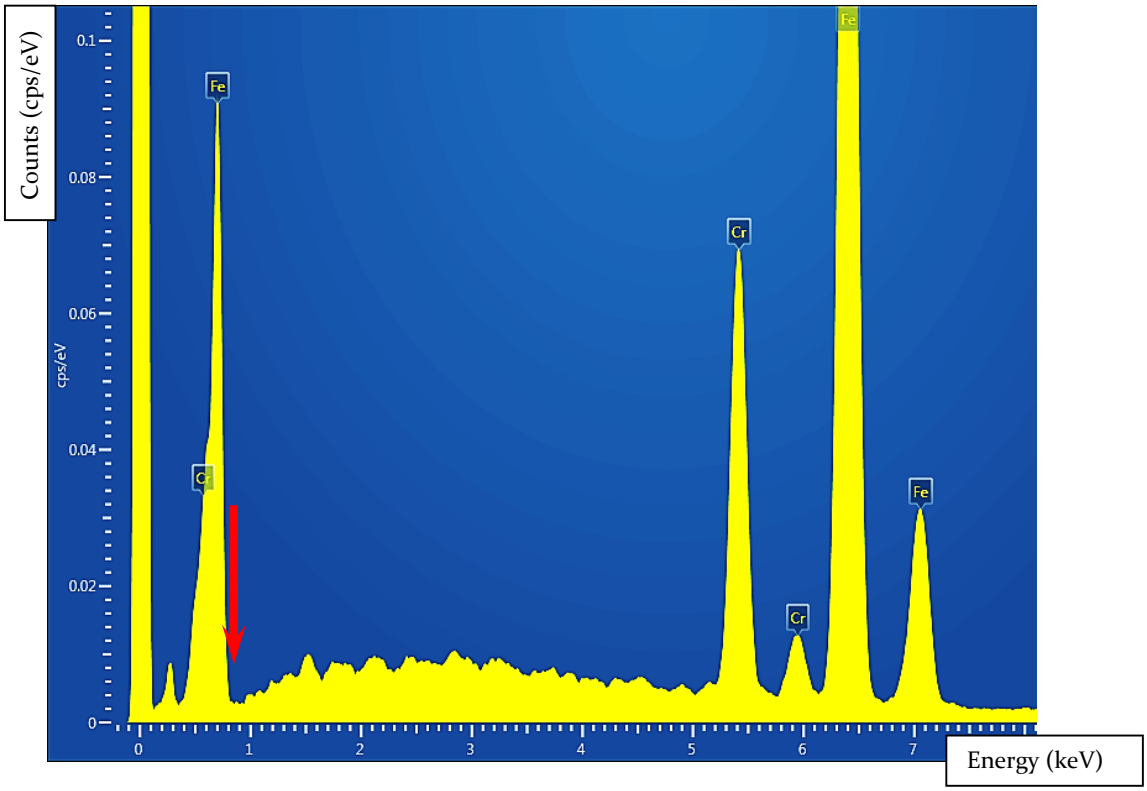

Figure 181 - EDX spectrum of Fe-14wt%Cr unimplanted

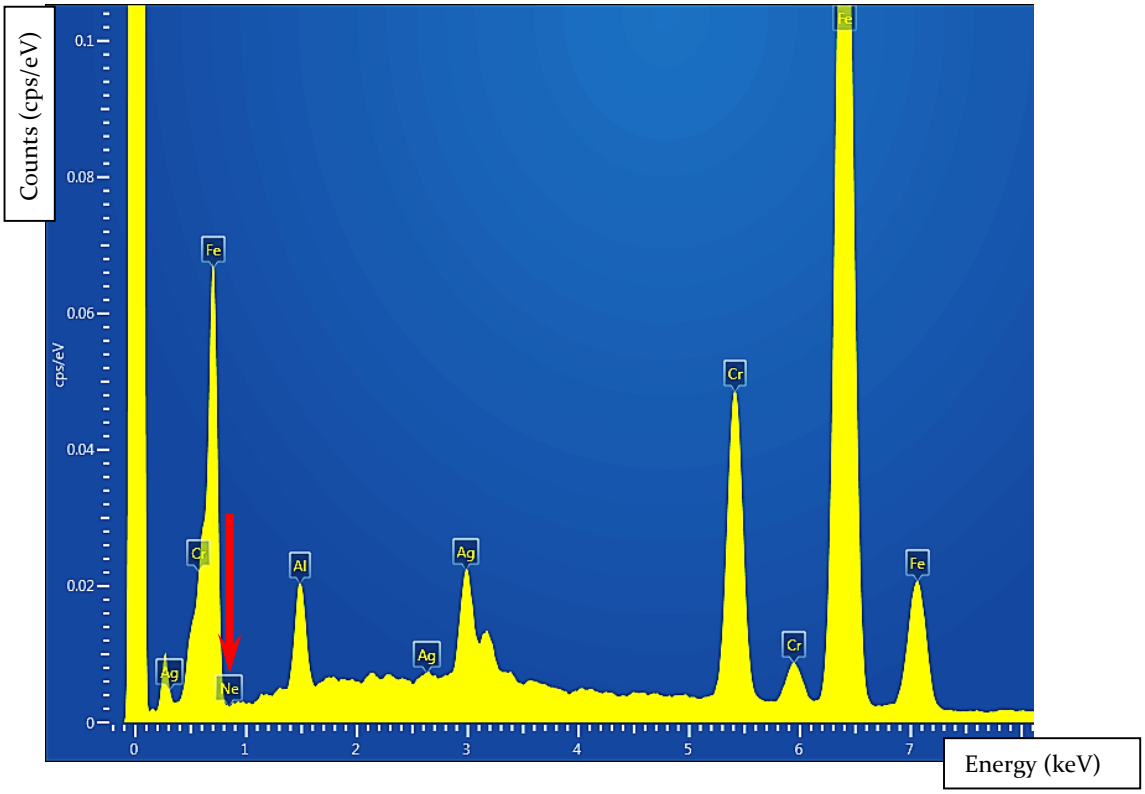

Figure 182 - EDX spectrum of Fe-14wt%Cr + 2000appm Ne

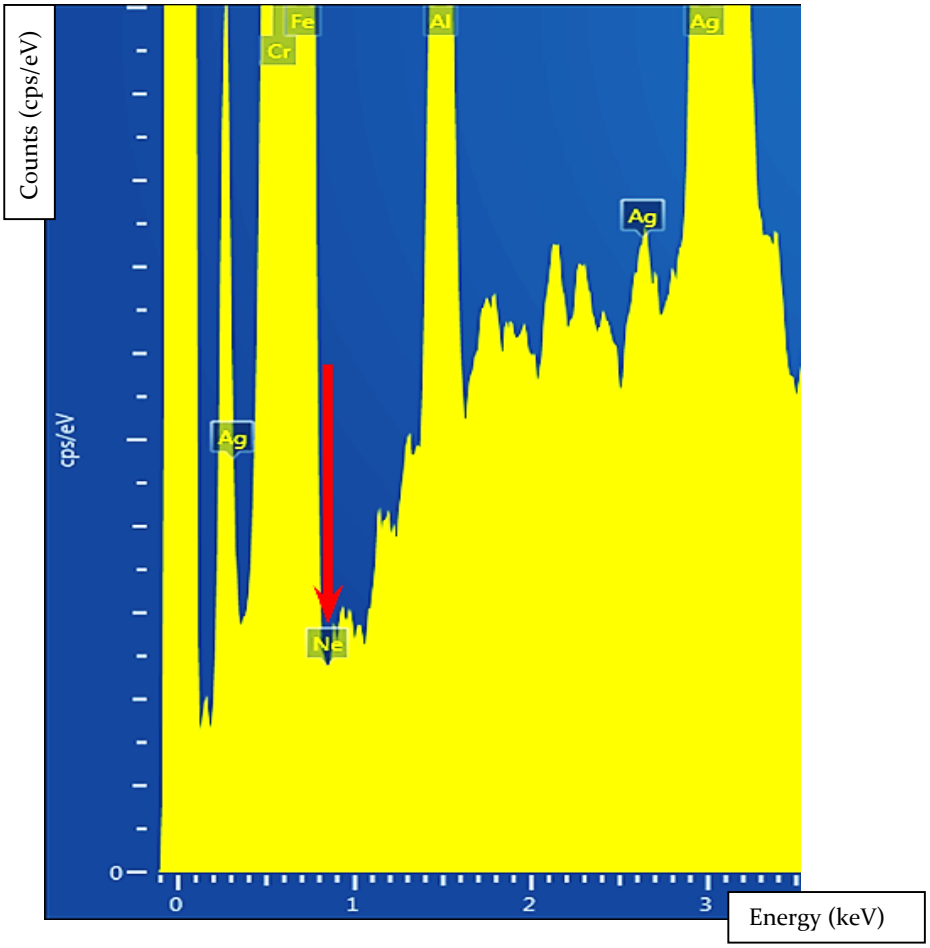

Figure 183 - EDX spectrum of Fe-14wt%Cr + 2000appm Ne (zoomed in)

Further EDX scans were also performed on the bulk samples of the other three materials: CEA ODS (Figure 184), EUROFER (Figure 185) and EUROFER ODS (Figure 186). None of these scans show a peak of any form at 0.848keV. The two EUROFER materials each contain 0.2% vanadium. This is visible on the graphs (with a peak at 4.949keV). Although detection increases with atomic mass (making V easier to pick up than Ne), the visible vanadium peaks show that small concentrations can be recorded and it would therefore be expected that some indication of neon should also be visible.

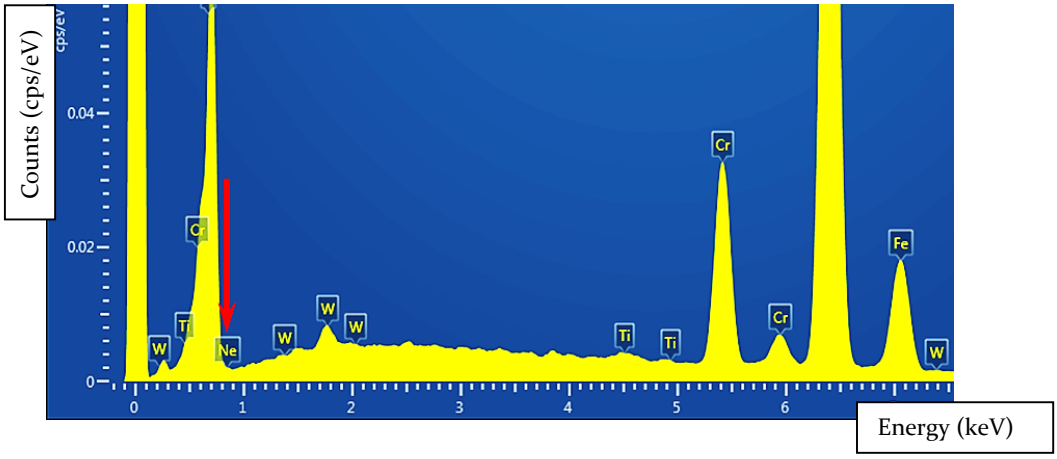

Figure 184 - EDX spectrum of CEA ODS + 2000appm Ne

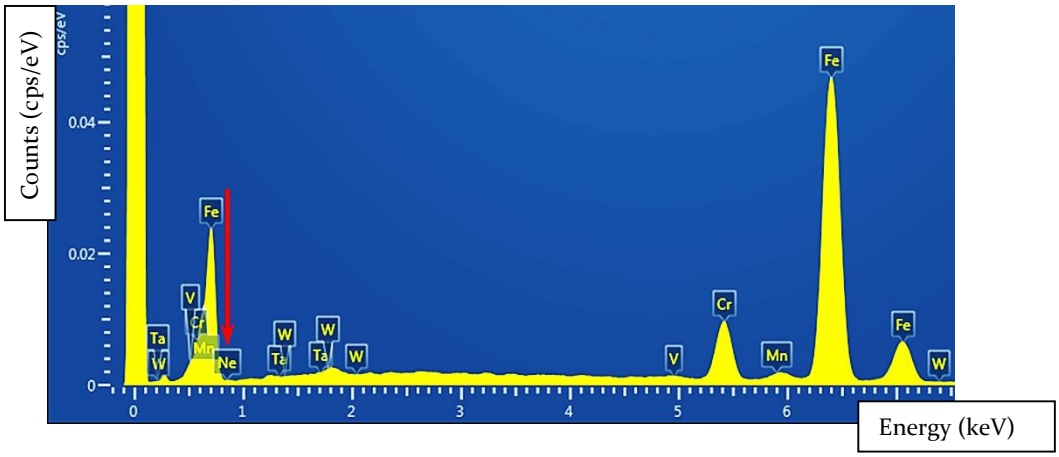

Figure 185 – EDX spectrum of EUROFER + 2000appm Ne

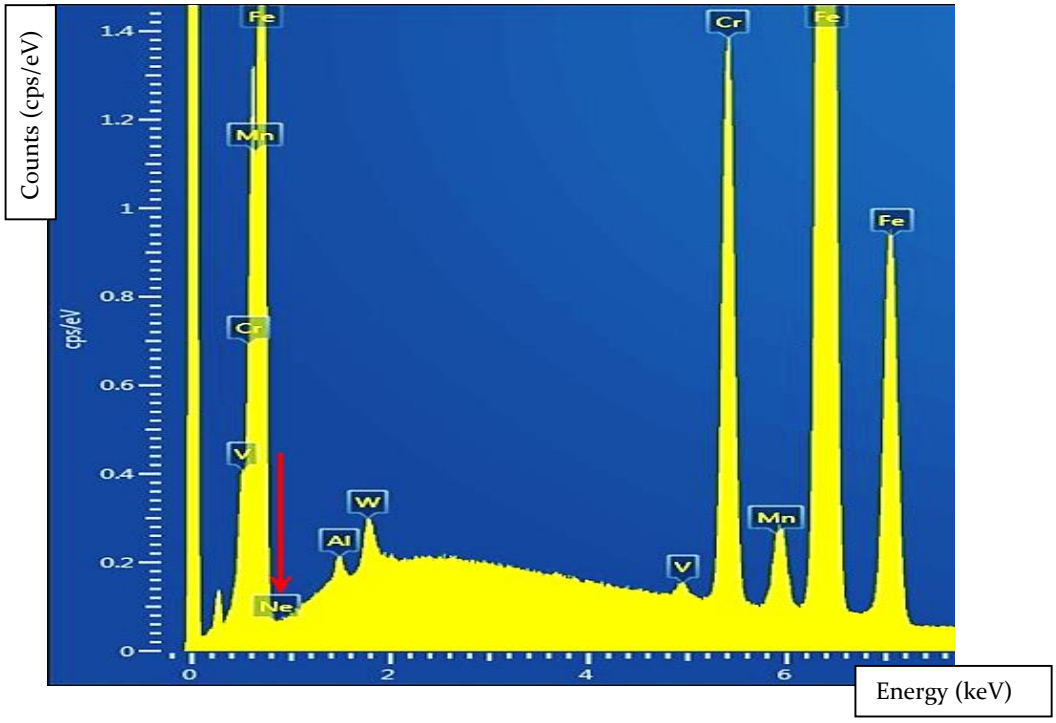

Figure 186 - EDX spectrum of EUROFER ODS + 2000appm Ne

29.2 Discussion

The implanted neon is not visible on any EDX scans performed (either on TEM cross-section or SEM bulk samples). Evidence of the formation of bubble-like structures is, however, visible in the Fe-14wt%Cr specimen (Figure 175 and Figure 176), and there was a noticeable increase in hardness in the implanted samples (Chapter 3), confirming that implantation definitely occurred and had a physical effect on the material.

There are various possible explanations for the lack of neon signal: the original implantation, although designed to implant 2000appm neon (Chapter 2, Section 11.1.3), might not have run exactly to plan and the initial concentration was lower than expected. Some proportion of the neon may have diffused out of the sample in the interval between implantation and EDX scanning; or it may be that the EDX scan was not efficient enough/run for a sufficient amount of time to pick up any neon signal due to its low atomic mass.

The original implantation experiment was carefully designed using SRIM to implant 2000appm neon in an approximately flat profile to a depth of ~1.2μm into the surface. The implantation run data provided by the Surrey Ion Beam Centre suggests that the run was completed as expected and therefore, unless SRIM calculated incorrectly, the implantation ran to provide the expected result.

Since implantation, the samples were stored in a low-vacuum desiccator and then were tested in microscopes operating under vacuum of the order of 10^{-7} mbar. All storage and testing was at room temperature. Directly after implantation, the samples were cooled down over six hours, from the ~300°C implantation temperature to room temperature, whilst still in a vacuum of ~10^{-7} mbar. During this period the higher temperature would cause an increased neon diffusion rate and there would be a high

concentration gradient from the 2000appm in the sample to the vacuum chamber. The neon could therefore potentially diffuse out of the sample (having already formed the bubble-like structures in the lattice during the implantation). However, as the bubble-like features form as low energy trapping sites, the thermal energy of the sample is likely to be less than the activation energy required for the gas to escape the bubble-like feature (and diffuse out of the samples). Modelling the diffusion of helium-vacancy clusters in iron shows that the larger the helium-vacancy cluster, the lower the diffusion coefficient. At 300°C a He_4v_5 cluster (4 helium atoms and 5 vacancies) has a diffusion coefficient of $0.3 nm^2 s^{-1}$ compared with a single vacancy diffusion coefficient of $1.04\ nm^2 s^{-1}$ [189]. Six hours diffusion at 300°C of a large He-v cluster would give diffusion over ~6.5μm. Ne-vacancy clusters are larger than their helium equivalents and therefore the diffusion coefficient would be even lower. As the temperature drops from 300 to 20°C over the six hours and the diffusion coefficient would be lower, it can therefore be assumed that the majority of the implanted neon will still be present in the samples, but not detected by EDX.

The neon implantation was originally performed to allow for chemical mapping of the implanted gas' final resting points for comparison with SRIM predictions. Since the neon could not be detected by EDX, this was not possible. Neon was originally chosen as an analogue for helium because it has a visible Kα peak (helium has no Kα peak), but at the low implantation dose used, the concentration was not sufficient to be visible.

There are two other possible methods that might be used to determine the location of the neon: electron microprobe (EMP) and electron energy loss spectroscopy (EELS). EMP works in a similar way to EDX, using characteristic X-rays to analyse which elements are present, but can detect elements in concentrations as

low as 100appm. EELS interprets the scattering that an electron beam undergoes when it is incident on a sample. Different elements cause varying energy loses and therefore careful analysis can determine the elements present in a sample. EELS works best for low atomic numbers. Both of these, however, are point analysis techniques, therefore producing a concentration map of the size required is not feasible.

In conclusion, the neon work proved that neon can be used as an analogue for the damage structures and effects seen in helium implantation (e.g. similar hardness results as discussed in Chapter 3). For chemical mapping of the location of implanted ions, however, either a higher concentration of neon needs to be used (although this would change the effects and bubble formation seen) or implantation should be done with a different substitute gas with a more recognisable characteristic X-ray peak (e.g. argon Kα 2.957keV).

Imaging of cross-sections of nanoindentations allowed bend contours caused by the relaxation of residual stresses from indentation to be viewed. Fe-14wt%Cr shows much clearer bend contours than the other materials which is likely due to the differences in grain size. Multiple grains of differing orientations mean the visible contours are unlikely to be continuous, and the presence of many grain boundaries that can accommodate some of the residual stress through grain boundary sliding. The results equate with those seen in the hardness, microcantilever and micropillar work of previous chapters, where CEA ODS, EUROFER and EUROFER ODS materials all yielded similar results which were significantly different to Fe-14wt%Cr.

This TEM work indicates that none of the unimplanted specimens have any visible bubble-like features at 200,000x magnification and therefore any features seen in the other samples must be due to the effects of implantation. The only effects seen were the appearance of bubble-like features in the Fe-14wt%Cr samples that had been implanted with 2000appm He and 2000appm Ne. In these samples, a range of bubble sizes was seen including down to the limit of distinguishing features from background noise. This suggests that bubble-like features exist below the limit of the microscopy performed. There may well be bubble-like features present in the other materials and implantation conditions that cannot be seen. It is suggested that the small size of these supposed below resolution bubbles is due to the greater number of defects/oxide and carbide precipitates/higher grain boundary density present in the other samples that capture the implanted gas in a greater number of smaller bubbles.

Using the visible bubbles in Fe-14wt%Cr, hardening due to the bubble-like features was estimated (assuming the bubbles act as weak obstacles to dislocation motion). It was determined that the bubbles have a critical dislocation breakaway

angle of ~75° (where strong precipitates are 0° and weak 90°) showing that they are a relatively weak obstacle.

Other than the appearance of bubbles in the Fe-14wt%Cr 2000appm He and 2000appm Ne samples, there were no significant effects on the structure and distribution of dislocations beneath surface nanoindentations caused by different levels of implantation or the appearance of the bend contours.

Implantation of neon as an analogue for helium worked in that it simulated the hardening effect and showed a similar array of bubbles in Fe-14wt%Cr. However, at the concentrations implanted it was not suitable for chemical mapping of the implantation depth profile as originally hoped.

Chapter 7
Discussion and Conclusions

Table 25 summarises the results of all the experiments performed during this project. A range of techniques were used to examine four different steel alloys. Nanoindentation is simple to perform and provides valuable and immediately comparable data, therefore it was used to test all the materials and implantation conditions. Vickers hardness, with its deep testing volume, was only suitable for investigating the unimplanted materials. Micropillars and microcantilevers were used to look at specific deformation and yield properties. TEM and EDX were used for investigating bubble formation. These techniques were only applied to limited ranges of the materials/conditions. As the neon implantation was performed for chemical mapping and this was as fully discussed in Section 29, those results will not appear in this chapter.

This chapter compares and contrasts the results and comments on the applicability of the techniques used. Section 31.1 predicts the theoretical material strengths for comparison with the experimentally derived values.

Table 25 - Summary of all experiments performed for this thesis.
U= unimplanted, 75= 75appm He, 2000= 2000appm He,
He+Fe= 2000appm He+ 4.5dpa Fe, Ne= 2000appm Ne

		Nanohardness	Vickers Hardness	Micropillars	Microcantilevers	TEM	EDX
Fe-14wt%Cr	U	✓	✓	✓	✓	✓	✓
	75	×	×	×	×	×	×
	2000	✓	×	×	✓*	✓	×
	He+Fe	✓	×	✓	×	✓	×
	Ne	✓	×	×	×	✓	✓
CEA ODS	U	✓	✓	✓	✓	✓	✓
	75	✓	×	×	✓	×	×
	2000	✓	×	×	✓	✓	×
	He+Fe	✓	×	✓	×	✓	×
	Ne	✓	×	×	×	✓	✓
EUROFER	U	✓	✓	✓	✓	✓	✓
	75	✓	×	×	✓	×	×
	2000	✓	×	×	✓	✓	×
	He+Fe	✓	×	✓	×	✓	×
	Ne	✓	×	×	×	✓	✓
EUROFER ODS	U	✓	✓	✓	✓	✓	✓
	75	✓	×	×	✓	×	×
	2000	✓	×	×	✓	✓	×
	He+Fe	✓	×	✓	×	✓	×
	Ne	✓	×	×	×	✓	✓

* Microcantilevers were tested in Fe-14wt%Cr, but experimental errors meant the results were not quantitatively viable and therefore were omitted from further numerical analysis, see Section 23.2.2.

31 Unimplanted Materials

31.1 Contributions to Strengthening

Pure iron (less than 60ppm impurities) is extremely weak. The resolved shear stress of a single crystal at room temperature can be as low as 10MPa, while the yield stress of a polycrystalline sample at the same temperature can still be well below 150MPa [190]. Iron can be strengthened through several mechanisms, the most important of which are grain size (Hall-Petch Effect) and alloying, causing solute and precipitate effects. Alloying can cause hardening effects for many different reasons depending on the alloying element and its concentration in the material.

The following sections outline the likely contributions to hardness of grain size and alloying for the materials in this project.

31.1.1 Hall-Petch

Increase in yield stress according to the Hall-Petch relationship is inversely proportional to the square root of grain size (Equation 7).

Equation 7 - Hall-Petch Relationship

$$\Delta\sigma = \frac{K}{\sqrt{d}}$$

K = strengthening coefficient (for mild steel $K \approx 0.74$MPa $m^{1/2}$ [191])

d = average grain diameter (m)

The grain sizes of the materials in this project were discussed in Section 9. CEA ODS and EUROFER have a bimodal grain structure, so the hardening has been calculated for the average large and small grain sizes, then a weighted average (by volume) has been used to calculate the overall Hall-Petch contribution to hardening.

Table 26 - Grain size and calculated hardening contribution for all materials

Material	Fe-14wt%Cr	CEA ODS		EUROFER		EUROFER ODS
Average grain size d (μm)	200	1	5	4	10	2
Volume %	100	95	5	75	25	100
Hardening contribution Δσ (MPa)	52	740x95% + 330x5% 720		370x75% + 230x25% 335		520
Hardening error (MPa)*	±3	±36		±17		±26

*Assuming an error of ±10% in average grain size measurement the error in hardening contribution is ~5%.

31.1.2 Alloying

The most common alloy hardening mechanisms are solution strengthening and precipitate hardening. Most elements at low concentrations (<20wt%) show a linear relationship between weight percentage of alloying element and the hardening effect produced in the material. This applies to both precipitation and solution strengthening and can be summarised as follows:

Equation 8 - Strength Contributions from Alloying

$$\Delta\sigma = \sum_i A_i \times wt\%_i$$

Using pre-determined contribution values for the different elements, the strengthening due to alloying can be estimated for each material. The solution and precipitation strengthening contributions can be combined in the same calculations.

Table 27 - Contributions to hardness from alloying elements per weight percentage addition [192][193][194][195][196]

	Solution Strengthening						***Precipitation Strengthening (*)***	
Element	***Cr***	***Mn***	***Ni***	***Si***	***Ta***	***W***	***Ti****	***V****
MPa/wt%	23	34	34	83	50	40	1450	1520

Table 28 - Fe-14wt%Cr

Element	***Cr***	
MPa/wt%	23	
wt%	14.25	
Δσ (MPa)	328	328 ≈ 330

Table 29 - CEA ODS

Element	***Cr***	***Ni***	***Si***	***Ti****	***W***	
MPa/wt%	23	34	83	1450	40	
wt%	13.65	0.16	0.27	0.3o	1.17	
Δσ (MPa)	312	5.5	22.5	435	47	822 ≈ 820

Table 30 - EUROFER

Element	***Cr***	***Mn***	***Ta***	***V****	***W***	
MPa/wt%	23	34	50	1520	40	
wt%	9	0.4	0.12	0.2	1.1	
Δσ (MPa)	207	13.5	6	304	44	574.5 ≈ 575

Table 31 - EUROFER ODS

Element	***Cr***	***Mn***	***Si***	***Ta***	***V****	***W***	
MPa/wt%	23	34	83	50	1520	40	
wt%	8.25	0.35	0.33	0.13	0.24	0.9	
Δσ (MPa)	190	12	27.5	6.5	365	36	637 ≈ 635

31.1.3 Nanoprecipitates

Two of the materials being tested also contained an extra strengthening mechanism – a dispersion of fine oxides. According to the Orowan dislocation by-pass process [197], strengthening due to non-shearable, incoherent particles increases approximately with the square root of particle volume fraction and increases more strongly with decreasing mean particle size. For an optimum particle size and distribution (fine and high volume fraction), as is present in CEA ODS and EUROFER ODS, the nanoparticles can contribute ~450MPa to the yield stress, although the exact value is dependent on particle distribution [197] (450MPa is an average of the 200-700MPa range observed in EUROFER ODS and other ODS alloys tested by Preiniger [197] – particle size range 3-14nm with volume fraction 0.01-0.05).

31.1.4 Combining Contributions

Contributions to hardening through the different mechanisms can be combined linearly and, if all parts have been taken into account, the resulting answer should approximate the mechanically measured yield stress of the bulk material.

Table 32 - Contributions to hardening from different sources (MPa)

Material	*Fe-14wt%Cr*	*CEA ODS*	*EUROFER*	*EUROFER ODS*
σ_y	150	150	150	150
Hall-Petch	52	720	335	520
Alloying	330	820	575	635
Nanoprecipitates	-	450	-	450
Total	532	2140	1060	1755
5% error	±27	±107	±53	±88

In this project, the materials have been mechanically tested by various methods. Nanoindentation provides a hardness result. This can be converted to an approximate yield stress by dividing by three [155]. The micropillar compression yield stress was calculated as the first significant deviation from elastic deformation (and averaged across the number of pillars in each material). The microcantilevers showed a slow

change from elastic to plastic, and therefore the stress at 2% strain was taken instead as an indicator – these cannot be numerically compared with the other yield stresses, but do allow for comparison of the relative strengths between materials (Table 33 and Table 34).

From their composition and microstructure, the ODS materials are expected to have the highest strength, with EUROFER lower than its ODS variant, and the large grained, pure Fe-14wt%Cr to have the lowest strength due to its lack of added hardening mechanisms. This ranking is distinct in the calculated results and the microcantilever data. There is an obvious discrepancy in the micropillar results, as the EUROFER value is significantly higher than all the others; this was discussed further in the micropillar chapter (Section 20).

Table 33 - Comparison of calculated and experimentally measured strengths in MPa (hardness values in brackets)

Material	*Fe-14wt%Cr*	*CEA ODS*	*EUROFER*	*EUROFER ODS*
Calculated total	532	2140	1060	1755
Nanoindentation σ_y (hardness at 400nm)	950 (2850)	1840 (5520)	1310 (3930)	1750 (5250)
Vickers σ_y (hardness at 7000nm)	420 (1260)	1260 (3780)	790 (2370)	1190 (3570)
Micropillar σ_y	570	760	1400	540
Microcantilever $\sigma_{(2\%\,\varepsilon)}$	1180	3240	2440	2780

Table 34 - Ratio of strengths in MPa relative to the Fe-14wt%Cr value

Material	*Fe-14wt%Cr*	*CEA ODS*	*EUROFER*	*EUROFER ODS*
Calculated total	1.0	4.0	2.0	3.3
Nanoindentation σ_y	1.0	1.9	1.4	1.8
Vickers σ_y	1.0	3.0	1.9	2.8
Micropillar σ_y	1.0	1.3	2.5	0.9
Microcantilever $\sigma_{(2\%\,\varepsilon)}$	1.0	2.7	2.1	2.4

31.2 Comparison of Unimplanted Yield Stress

Figure 187 and Figure 188 compare the unimplanted yield stress measured for each material and experimental method. The values are: $\frac{nanohardness}{3}$, micropillar yield stress and microcantilever stress at 2% strain. With the exception of micropillar compression, all experimental methods show the same order of yield stress: Fe-14wt%Cr < EUROFER < EUROFER ODS < CEA ODS. The cause of the anomalous high EUROFER micropillar result is unknown, but is possibly due to the material's inhomogeneous grain structure, discussed in Section 20.2.

The stresses measured in the unimplanted state correlate with the hardening contribution predictions (Section 31.1). CEA ODS and EUROFER ODS are the strongest, EUROFER is slightly lower, and finally Fe-14wt%Cr yield stresses are approximately half of the ODS materials. In the unimplanted state, these mechanical property differences cannot be due to any form of ion damage, and therefore must be related to microstructure. One significant difference between the materials is their grain size: in Fe-14wt%Cr each of the mechanical tests is within a single grain, whereas the small grain size of the other materials means each test will be influenced by multiple grain boundaries, contributing to the observed higher yield stress. In the theoretical strength calculations this was taken into account via Hall-Petch (Section 31.1.1).

The measured hardness and yield stress of the materials will also be affected by their in-grain microstructure. Fe-14wt%Cr is a very pure material with only traces of a few impurity elements whereas the other three materials have much more complicated compositions (Section 9). Sections 31.1.2 and 31.1.3 took into account the various carbide and oxide formers that give CEA ODS, EUROFER and EUROFER ODS their higher strength.

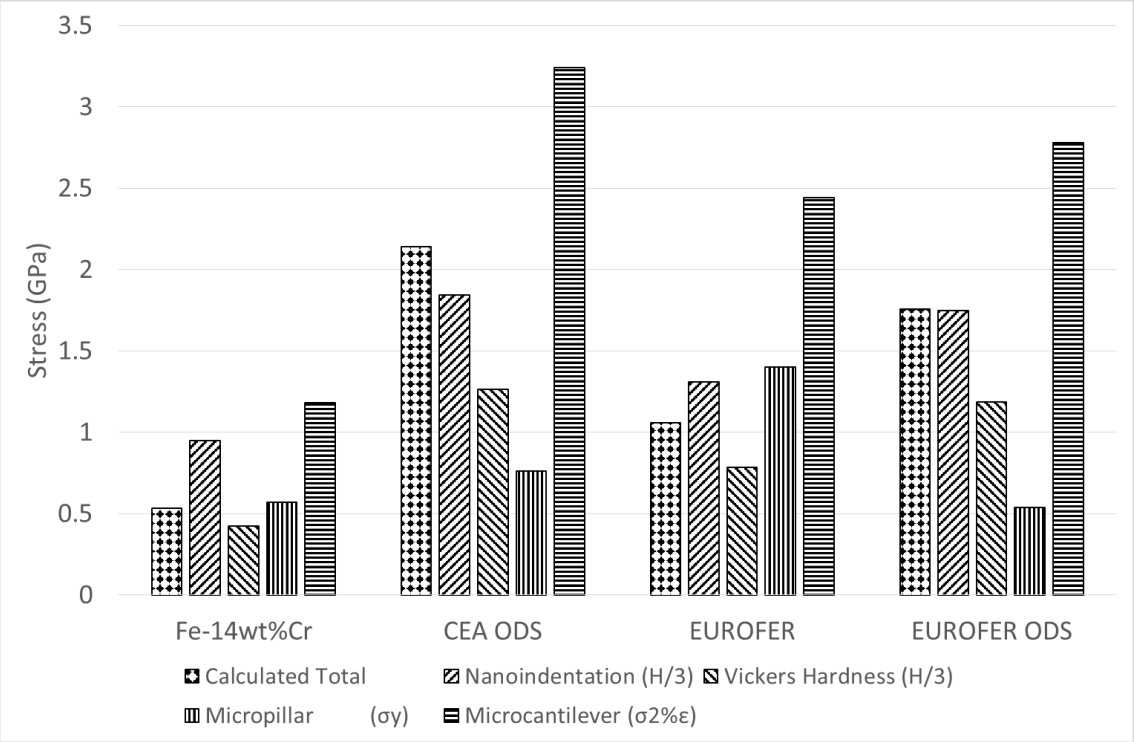

Figure 187 - Yield stress for all tests grouped by material

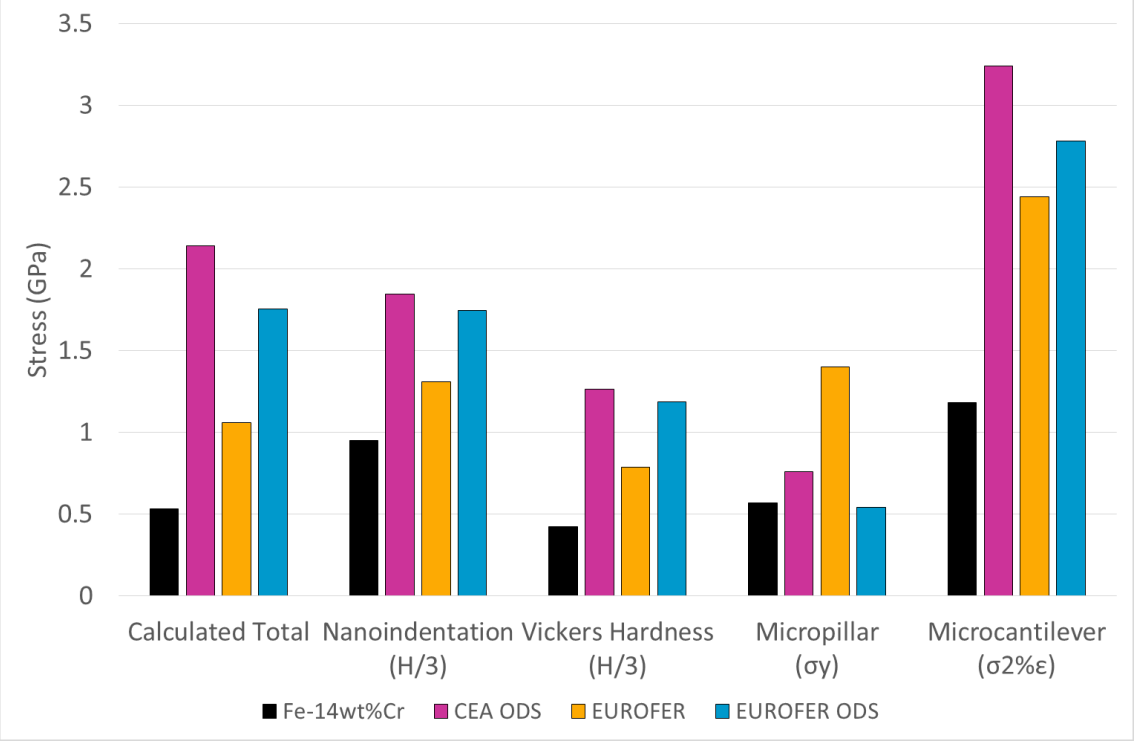

Figure 188 - Yield stress for all tests grouped by experimental method

32 Implanted Materials

Table 35 summarises the yield stresses recorded for all helium implantation conditions in each technique. The values in the table are: $\frac{nanohardness}{3}$, micropillar yield stress and microcantilever stress at 2% strain. These values are graphically represented in Figure 189 and Figure 190.

Table 36 gives the average change in yield stress for each implantation condition. Part a) averages all values across all experimental methods, whereas part b) excludes the CEA ODS 2000appm He and EUROFER ODS 75appm He microcantilever results, as these appear to be anomalous. Figure 134 showed huge scatter in the CEA ODS results; this is due to the bimodal grain structure and was evaluated in Section 24.1. The high increase in this EUROFER ODS result is also due to scatter; two unusual, high lines which significantly skew the average yield stress can be seen on Figure 133.

Overall, implantation of 75appm helium has no effective impact on yield stress ($\Delta\sigma_y$=0.00GPa). This is to be expected as it is below 100appm, the concentration at which helium effects become significant [145], and single helium atoms or small (few atom) clusters are too small to have any dislocation motion retarding effect . Implantation of 2000appm helium causes significant increase in yield strength ($\Delta\sigma_y$=+0.60GPa), while combined 2000appm He + 4.5dpa Fe only produced a minor increase ($\Delta\sigma_y$=+0.08GPa).

It should be noted that while the 75appm He and dual He+Fe implantations caused similar levels of change across all materials, the 2000appm He implantation showed a higher yield stress increase in Fe-14wt%Cr compared to the other materials: 0.86GPa cf. ~0.5GPa (ignoring CEA ODS microcantilevers).

Fe-14wt%Cr has low unimplanted yield stress because it has a large grain structure, so tests are effectively within a single crystal area and there are no extra

alloying elements to form any precipitates or specific defects within the lattice, therefore dislocation motion is easy. When implanted, the lack of added low energy sites to attract helium means it will start to collect in lattice vacancies as bubbles, which grow to become unstable voids. These voids are large enough (>0.5nm [31]) to cause obstacles to dislocation motion, resulting in the measured large increase in hardness and stress.

CEA ODS has a much higher original yield stress due to small grain size and oxide particles acting as hardening agents. The oxide particles also act as low energy attraction sites for implanted helium. The bimodal grain structure, however, can cause significant scatter in the results, as was seen in the microcantilever work in Section 24.1. EUROFER and EUROFER ODS are similar to CEA ODS with small grains and added alloying elements, acting as hardening mechanisms. Both EUROFER alloys contain tungsten, a carbide former, and EUROFER ODS also has the yttrium content creating a dispersion of yttria nanoclusters.

In EUROFER, during implantation, the helium will collect at the lowest energy sites, which in this case will be the grain boundaries. As the majority of the helium collects in the high grain boundary density, there is very little left in the matrix to cause hardening. In CEA ODS and EUROFER ODS the nanoclusters are very closely spaced therefore helium only has to diffuse a short distance before it is attracted to and trapped by a nanocluster.

Helium causes hardening through various mechanisms. When bubbles coalesce into voids, these voids are above the dislocation interaction limit and therefore disrupt dislocation motion. Similarly, sufficient helium collected around an yttria nanocluster can also grow large enough to act as a dislocation movement limiter.

Finally, helium collecting at grain boundaries can act as a pin, reducing the possibility of grain boundary sliding.

When helium implantation is combined with self-ion iron implantation, the hardening effect appears to be lessened (Section 16.3). The reason for this is the higher damage/dpa caused by the self-ions creating a significant number of lattice point defects which act as low energy helium traps. The point defects work in a similar way to the distribution of nanoparticles in the ODS materials; a wide dispersion of point defects means a fine distribution of tiny bubbles. By way of comparison, single beam implantation causes a lower density of larger bubbles and, thereby reducing the retardation of dislocation motion and resultant hardening.

As EUROFER showed very similar results to CEA ODS and EUROFER ODS, rather than the significantly different Fe-14wt%Cr, it can be concluded that it is the small grained, particle-containing microstructure that has the most influence on how helium is handled in these materials. Specifically, the dispersion of yttria particles in the ODS materials does not have a significantly better influence on the detrimental helium effects compared to the carbide distribution of EUROFER.

Table 35 – Yield stress (GPa) and ± data range
U= unimplanted, 75= 75appm He, 2000= 2000appm He,
He+Fe= 2000appm He+ 4.5dpa Fe, I= implanted condition
Value range is experimental range, Difference range is max. value range of I and U.

		Values			Difference (I-U)			
		Nanohardness	Micropillar	Microcantilever	Nanohardness	Micropillar	Microcantilever	Average Difference**
Fe-14wt%Cr	U	0.95 (±0.03)	0.57 (±0.15)	1.18 (+2.06, -1.14)	-	-	-	-
	2000	1.81 (±0.02)	-	-	0.86 (±0.03)	-	-	0.86
	He+Fe	1.10 (±0.03)	0.62 (±0.08)	-	0.15 (±0.03)	0.05 (±0.15)	-	0.10
CEA ODS	U	1.84 (±0.03)	0.76 (±0.15)	3.24 (+0.51, -0.70)	-	-	-	-
	75	1.85 (±0.07)	-	3.30 (+1.91, -1.62)	0.01 (±0.07)	-	0.06 (+1.91, -1.62)	0.03
	2000	2.24 (±0.10)	-	2.34 (+3.00, -1.40)	0.40 (±0.10)	-	-0.90 (+3.00, -1.40)	-0.25
	He+Fe	1.92 (±0.07)	0.77 (±0.10)	-	0.08 (±0.07)	0.01 (±0.15)	-	0.04
EUROFER	U	1.31 (±0.08)	1.40 (±0.20)	2.44 (+1.32, -2.18)	-	-	-	-
	75	1.24 (±0.05)	-	2.47 (+0.80, -0.65)	-0.07 (±0.08)	-	0.03 (+1.32, -2.18)	-0.02
	2000	1.66 (±0.07)	-	2.68 (+0.98, -0.83)	0.35 (±0.08)	-	0.24 (+1.32, -2.18)	0.30
	He+Fe	1.44 (±0.10)	1.39 (±0.23)	-	0.13 (±0.10)	-0.01 (±0.23)	-	0.06
EUROFER ODS	U	1.75 (±0.08)	0.54 (±0.19)	2.78 (+0.86, -0.84)	-	-	-	-
	75	1.73 (±0.10)	-	3.48 (+1.62, -0.79)	-0.02 (±0.10)	-	0.70 (+1.62, -0.79)	0.34
	2000	2.20 (±0.05)	-	4.00 (+0.85, -1.16)	0.45 (±0.08)	-	1.22 (+0.85, -1.16)	0.84
	He+Fe	1.98 (±0.07)	0.53 (±0.42)	-	0.23 (±0.08)	-0.01 (±0.42)	-	0.11
Average Range		±4%	±26% *(±19%)	+60%, -46%				

*Excluding high range EUROFER ODS He+Fe
**No range is given for 'Average Difference' as the nanoindentation and micropillar results would be massively skewed by the wide and variable microcantilever ranges.

.

Table 36 - Average change in yield stress (GPa) unimplanted to implanted across all experiment

a) includes all data.

a)	75	2000	He+Fe
Mean	0.12	0.43	0.08

b) does not include anomalous CEA ODS 2000appm He microcantilever or EUROFER ODS 75appm He microcantilever results.

b)	75	2000	He+Fe
Mean	0.00	0.60	0.08

H= nanohardness, P= micropillar, C= microcantilever

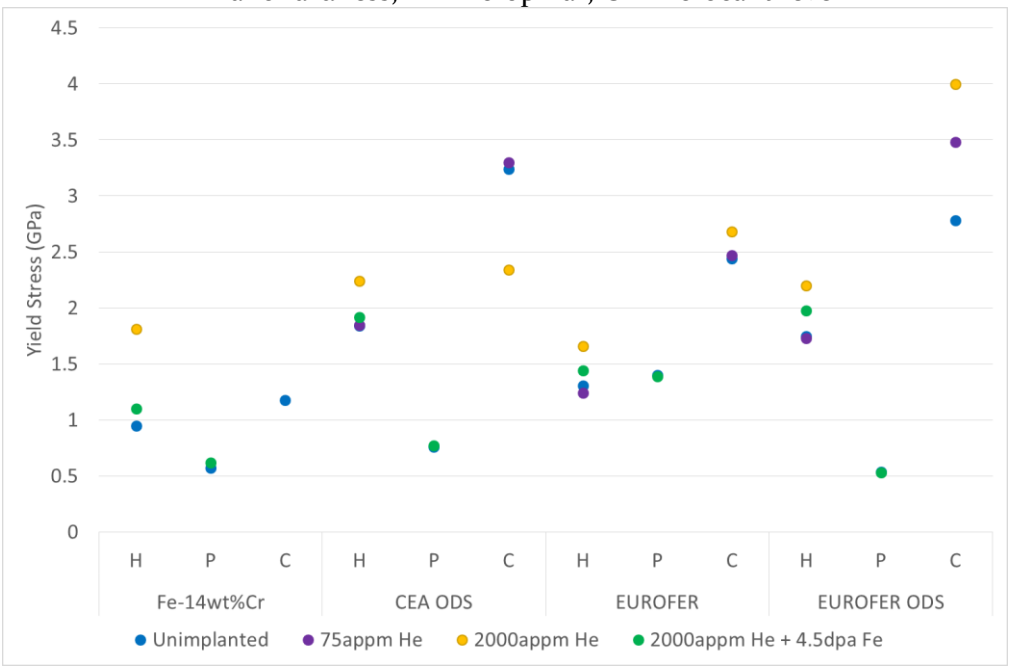

Figure 189 - Yield stress (GPa) measured for each implantation condition and experimental method.

Figure 190 - Difference in yield stress (GPa) for each implantation condition and experimental method.
Difference = Implanted – Unimplanted
The anomalous CEA ODS 2000appm He microcantilever result (-0.90) has been omitted.

As deep ion implantation is not possible, micro/macrohardness tests are unsuitable for investigating implanted materials. Nanoindentation was the ideal method for testing the conditions investigated in this thesis.

Although nanoindentation is subject to the Indentation Size Effect (ISE), this is well understood and documented [134][151]; extrapolation of nanoindentation data can therefore be used to apply nanoscale results to macroscale problems. Figure 69 shows a good example of continuous data across the nano and microhardness scales.

Although hardness values of implanted materials are limited in depth (and therefore subject to ISE), comparison with unimplanted material hardness at equivalent depths provides a good indication of hardening due to implantation (Figure 71). Use of Vickers hardness to extend the range tested was useful for assessing the depths over which the Indentation Size Effect must be considered.

The micropillar compression experiments were designed to investigate the deformation modes of the different materials and how they were affected by implantation. Previous work [165][164] showed implantation changing slip plane movement as a result of increasing dislocation density. At low density (~$10^{14}m^{-3}$), single dislocation sources activate and exhaust themselves as nucleating dislocation segments run out of the pillar. Before the next dislocation source can nucleate, sufficient stress must build up to activate the source. This results in widely spaced single slip planes running across each pillar. Under implantation, as dislocation density increases, the greater number of sources allow more slip planes to activate without significant increase in stress between dislocation movements. This results in a greater number of more closely spaced slip planes. These effects were noted in this work in Fe-14wt%Cr. The other materials have much higher natural dislocation density (~10^{15}-$10^{16}m^{-3}$) and smaller grain sizes, increasing the probability of micropillars containing one or more

grain boundaries. The interaction of dislocations with each other, with grain boundaries and with oxide/carbide particles means each active dislocation will only move a short distance before it meets an obstacle and the slip of another dislocation is more favourable, resulting in pillar barrelling.

Quantitatively, micropillars are subject to a size effect [166] and therefore yield stresses are not directly comparable to macroscale results. Micropillar data are, however, comparable with data from other small scale testing methods (Figure 188). The EUROFER results are inconsistent in relation to the other materials (twice the expected yield stress) but consistent within the EUROFER results across implantation conditions.

Overall, micropillar compression testing provided good insight into how microstructure affects deformation, specifically that a more complicated microstructure (smaller grain size, precipitates, high dislocation density) leads to complex slip on multiple planes (cf. simple microstructure – single slip on widely spaced planes). The quantitative results, however, e.g. the EUROFER yield stress discrepancy, show good trends within materials, but are unreliable for comparison between materials.

Microcantilever testing was initially to be used in this project to investigate grain boundary fracture. However, the limited strain rates possible in the nanoindenter meant fracture investigation in these relatively ductile materials was not possible. Since all cantilevers bent rather than fractured, the investigation moved onto looking at yield and elastic moduli. Very few of the cantilevers showed a distinct yield point, and therefore stress at 2% strain had to be used as an indicator of strength. This led to overestimation of yield compared with the other micromechanical methods.

Measuring elastic modulus using microcantilevers is regarded as limited in use, as the recorded stress and strain values rely on highly accurate measurements of cantilever dimensions and the assumption that simple beam theory is completely

applicable. Without fully automated systems of cutting and measuring cantilevers, there will be inherent errors in recorded cantilever dimensions. Wide moduli ranges were observed (Figure 136). These are therefore not uncommon [175][177], and it must be accepted that while average moduli tend to fit macroscale results, the ranges observed will be large.

TEM was used in this investigation to see where the implanted gases come to rest within the microstructures. It was possible to identify bubbles in the 2000appm He and Ne implanted Fe-14w%Cr samples. However, no bubbles were seen in the other materials or implantation conditions; if present, they were below the limit of the TEM resolution achievable. TEM combined with EDX for chemical mapping would have provided useful evidence of gas distribution after implantation, but the difficulties in detecting helium and neon meant that the EDX experiments were less effective than intended.

The micropillars, microcantilevers and TEM foils were all produced with FIB milling. Currently FIB is the only technique suitable for producing micromechanical testing specimens in implanted materials. General microstructural TEM foils can be electropolished from bulk material, but when specific cross-sectional areas are required (e.g. through indentations), FIB needs to be used for the locational accuracy. The use of FIB, however, brings up the issue of the potential damage caused by the gallium ions. This damage can cause marked changes in measured mechanical properties between the same materials produced by FIB and by non-FIB routes [198]. For this project, the production of micromechanical specimens was identical for implanted and unimplanted samples. Therefore all samples will be affected to the same degree by the gallium damage. How the gallium interacts with the iron ion-irradiation damage is unclear, but will be limited to the surface 30nm. The marked differences in behaviour between implanted and unimplanted specimens (particularly Fe-14wt%Cr pillars) show

that the deep iron ion damage rather than shallow gallium ion damage is the controlling defect population. Therefore the use of FIB machining can be justified as a suitable technique for this scale of work.

Ion implantation was used in this work as a simulation of the lattice damage and transmutation/implantation of gases to which materials would be subject in a fusion or GenIV fission reactor. Its use is limited, as it fails to match the dose rates, isotope transmutation and gas production of neutron irradiation [28]. It does, however, provide a radiation-free method of producing damage in materials for experimental testing. It has been shown that ion implantation can provide a reasonable simulation of neutron irradiation microstructural damage [47]. The resultant hardening should be equivalent between neutron and ion irradiation if the damage levels/dpa are the same in both methods. The path is unimportant if the final product (measured in terms of damage type and concentration) is the same. Production of samples to specific implantation levels is relatively simple to organise and quick to undertake. The combination of these reasons makes it an effective technique for short timescale projects such as this thesis.

Each of the experimental techniques used in this project provided valuable information about different aspects of the influence of helium implantation on the mechanical and microstructural properties of a range of iron-chromium based alloys.

34 Summary

Ion implantation, as a simulation of the damage sustained by structural materials in the extreme temperature and irradiation environment inside fusion and fission fast breeder reactors, is a useful method for radiation-free, experimental testing of materials. The thin surface damaged layers produced by ion implantation necessitate the use of micromechanical testing techniques, but it has been shown that these can be used to provide useful information on the mechanical properties and deformation mechanisms of materials, and their changes with varying levels of ion implantation.

CEA ODS, EUROFER and EUROFER ODS all showed significantly higher hardness and yield stress values than Fe-14wt%Cr in their unimplanted states. The same three materials also showed superior radiation resistance in terms of helium management. There is a demonstrated lack of an effect of helium implantation on the mechanical properties and bubble-life feature formation in EUROFER. The fact that this is similar to the CEA ODS and EUROFER ODS results, rather than the significantly different Fe-14wt%Cr, allows the conclusion to be formed that it is the small grained, particle-containing microstructure that has the most influence on how helium is handled in these materials. Specifically, the dispersion of yttria particles in the ODS materials does not have a significantly better influence on the detrimental helium effects compared to the carbide distribution of EUROFER.

When considering implanted RAFM alloys, it can be concluded that a small grained, particle-containing microstructure, whether the particles are carbides or dispersed oxides, produces the best radiation resistance in terms of helium control.

Chapter 8
Further Work

This study provided an overview of how various mechanical properties are affected by ion implantation in a range of ODS and non-ODS iron-chromium alloy variants. Areas of this project could be extended to provide more mechanical property data, to investigate why the different materials behave in specific ways and how this information could be used for future alloy development.

This chapter discusses the various areas of interest, followed by a proposal of work that could directly follow this thesis.

35 Neutron vs. Ion

If these materials are to be used for nuclear applications, the next extension to this project would be to investigate how well ion implantation simulates neutron irradiation, and therefore how applicable the conclusions drawn from the ion implantation experiments are (cf. neutron irradiation discussed in Chapter 1, Section 3.1.)

The simplest method for comparing ions and neutrons would be to perform identical micromechanical tests on materials neutron irradiated to the same damage levels as the ion implantations. However, performing neutron irradiation is not as simple as ion implantation; material samples must be held in a reactor for a significant length of time (damage rate is ~20dpa/year) and once the required damage level is reached, samples must cool to safe levels of radiation before investigation in a hot cell. There are several neutron irradiation experiments currently in progress or cooling e.g. BOR-60 (currently undergoing a six year irradiation schedule) and the UCSB Advanced

Test Reactor (where samples are now cooling) – samples from these are ready for experimentation.

36 Size Effects

As discussed in Chapter 1, Section 5.3, micromechanical testing presents the issue of size effects. Hardie [175] investigated size effects in micromechanics of ion implanted iron chromium alloys. ODS materials however, have significant microstructural differences compared with the Fe-Cr alloys Hardie investigated (precipitates and small grain size), therefore size effects may be different.

In this project, size effects present in hardness testing were investigated using a combination of nanoindentation and microhardness testing (Chapter 3). These showed no obvious difference in the size effects in ODS and non-ODS materials, but confirmed that the size/depth of indentation affects measured hardness, and for an accurate bulk hardness, test size should be >10μm. It is not possible, however, to investigate these depths in implanted materials due to restrictions on implantation energies.

Mechanical property size effects in unirradiated samples are relatively easy to investigate. Microcantilevers can be FIB cut in a wide range of sizes – the limiting factors at the nanoscale are FIB cutting accuracy and increased significance of FIB gallium damage; the lower size limit is >0.5μm width/depth. Larger scales are limited by sample preparation time – the larger the cantilever, the more material has to be removed. Faster milling can be achieved by increasing milling current, but above ~5nA the Ga^+ beam shape and size is insufficiently confined for anything but rough shape milling. With unlimited FIB time, any size cantilever could be made, but experimentally ~100μm is the sensible maximum cantilever length.

Macroscale 3-point bend testing of the same materials could be performed on small beams. The standard Oxford Nuclear Materials size is 1x1x10mm – smaller than this

and dimensional accuracy becomes an issue for cutting and polishing. However, this does present a five orders of magnitude increase on the largest FIB cut size.

Further work on extrapolation, design of experiments in the size gap and increase of size towards reactor components would be useful in determining the relevance of the micromechanical tests.

Size effects in implanted materials are limited by the experimentally possible damage depth. Ion implantation is limited to a few microns depth; therefore the size of microcantilevers must be of the same order of magnitude. Possible solutions for greater damage depth include proton irradiation (6MeV ≈ 200μm depth), or neutron irradiation (>5mm), thereby allowing larger scale testing, but also requiring hot cell facilities.

37 Atom Probe Tomography and Transmission Electron Microscopy

APT and TEM enables characterisation of irradiation effects on both structure and chemistry of the nano-scale oxide particles in ODS alloys [96]. With irradiation-induced cluster particle size and number density, APT can provide compositional data for even the smallest solute clusters. Work continues in this area with potential to investigate different material compositions, implantation conditions (self-ion/helium/combined) and neutron irradiated materials as they become available.

38 Material Compositions

Four materials were used in this project: ODS and non-ODS, Fe-14wt%Cr and EUROFER. This investigated the addition of ODS precipitates, but did not allow direct comparison of the ODS materials which have different compositions and processing routes. To maximise the benefits of ODS alloys, composition should be investigated, e.g. a range of alloys with identical processing conditions and variations of weight% in

the alloying elements. Cr, Y and Ti would be obvious elements to investigate in a basic ODS alloy. Subjecting this whole range to identical ion irradiations and the range of mechanical tests in this project would help determine the elements improving mechanical properties and irradiation response. Current experiments in the Oxford Nuclear Materials group are investigating the oxide particle composition, replacing the yttrium content of ODS alloys with hafnium.

39 Processing Route

Another way of changing the microstructure (and therefore mechanical properties) is to change the components of the processing route – powder production, powder milling and powder pressing. The initial powder can be produced from elemental or pre-alloyed powders (via gas or liquid atomisation) and combined in one of various mills (e.g. planetary ball mill or attritor mill). The milling speed and time have significant effects on how yttrium combines into the powder with milling time. Finally, the microstructure can be affected by powder compaction. HIP and direct powder extrusion are the most common methods, but hot pressing and spark plasma sintering are being investigated. Producing sets of materials of identical composition, each processed with different milling conditions would provide important insights into ODS processing design.

Processing scale-up also needs consideration. For experimental work, small scale powder processing and hot isostatic pressing are suitable. If, however, ODS materials are to be used in nuclear reactors, large quantities of materials need to be manufactured. ODS materials cannot be melt processed (due to the oxide particles), so any processing route must produce near-final-shape parts, potentially in very large sections.

40 ODS Particle Size and Density

Changing processing conditions results in changed size and density of oxide particles. Increasing HIP temperature decreases particle density and correspondingly increases the size of the dispersed oxide particles. Helium implanted samples prepared for TEM imaging reveal that bubble and particle densities in ODS alloys are strongly correlated. A direct association is apparent between the helium bubbles and the oxide particles; the gas accumulation process appears to be controllable via the particle dispersion by varying the consolidation temperature of the ODS alloys.

Further experiments with a range of alloys should be completed to determine whether the trend may be material composition specific. Further investigation should follow to see how particle density affects the response to implantation damage as well as the implanted helium.

41 Irradiation with Argon

The series of experiments that used implanted neon were designed for mapping the distribution of gas in the material after implantation. Neon was used as an analogue for helium. A noble gas was required because they have similar atomic structures and are mostly inert. Neon is the closest in size to helium and should, therefore, produce the most similar damage structure. TEM imaging revealed bubble-like structures, however, EDX scans of the neon implanted samples identified no neon. Due to the neon peak overlapping slightly with the iron peak, it cannot be certain whether the neon diffused out or was not properly detected. One method of determining this would be to go one atomic shell larger and implant with argon. Argon has a significantly larger size than the original helium, so it would not be as useful as a direct analogue, but could provide insight to gas distribution within microstructures.

42 Specific Proposed Further Work

With further time and resources the most obvious extension to the work in this thesis would be to continue with the same range of materials and experimental methods with an increased range of irradiation conditions.

With the current helium range of unimplanted, 75appm and 2000appm, any observation of trends with changes in He appm is limited. The microcantilever results, for example, appeared to show trends of increasing yield stress with helium content, with only three implantations, however, this could simply be scatter in the results. Increasing the range to include e.g. 500, 1000 and 1500appm He would give further insight into the change in mechanical properties with helium concentration. The intermediate levels would also be useful in TEM investigation to determine the concentration of gas required for bubble-like features to form in the lattice, and this could be combined with hardness testing to investigate any correlation between bubble formation and hardness increase.

The concentration range could also be extended at the higher end to include e.g. 3000 and 4000appm He. At 2000appm He, various microstructural features in CEA ODS, EUROFER and EUROFER ODS suppress bubble formation. In combination with TEM, higher helium contents could be used to establish a helium saturation concentration in the precipitate containing materials, where bubble-like features will form despite their designed irradiation resistant microstructure.

43 Future of ODS Materials

For ODS materials to be a serious contender for future nuclear reactors, significant work must be performed to provide a complete set of mechanical property responses to irradiation damage. The materials will need to fit a wide range of mechanical and safety parameters before commercial use. The large number of variables (composition, processing, damage levels etc.) means much experimental work must be completed in different areas, leading into modelling and extrapolation to fill a whole property matrix. Investigation on the nano- and microscale is significantly important, as understanding microstructural responses is key to the development of commercial scale structural uses of ODS steels.

References

[1] T. Pratchett, *The Science of Discworld*. Ebury Press, 2002.

[2] D. J. C. MacKay, *Sustainable Energy - Without the hot air*. UIT Cambridge Ltd, 2009.

[3] H. Bolt, V. Barabash, W. Krauss, J. Linke, R. Neu, S. Suzuki, and N. Yoshida, "Materials for the plasma-facing components of fusion reactors," *J. Nucl. Mater.*, vol. 329–333, pp. 66–73, Aug. 2004.

[4] R. Stoller, "Advanced Computational Materials Science: Application to Fusion and Generation IV Fission Reactors (Workshop Report)," Jul. 2004.

[5] "World Nuclear." [Online]. Available: www.world-nuclear.org/info/info8.html. [Accessed: 15-Sep-2011].

[6] "European Nuclear Society." [Online]. Available: http://www.euronuclear.org/info/encyclopedia/n/nuclear-fission.htm. [Accessed: 03-Oct-2014].

[7] M. R. Gilbert, S. L. Dudarev, S. Zheng, L. W. Packer, and J.-C. Sublet, "Transmutation, gas production, and helium embrittlement in materials under neutron irradiation .," 2011.

[8] R. A. Gross, *Fusion Energy*. Wiley, 1984.

[9] "JET." [Online]. Available: wwww.jet.efda.org/wp-content/uploads/JET-main-features.pdf. [Accessed: 15-Sep-2011].

[10] "JET." [Online]. Available: www.jet.efda.org/fusion-basics/conditions-for-a-fusion-reactor. [Accessed: 14-Jan-2010].

[11] "ITER." [Online]. Available: www.iter.org.

[12] D. Hambling, “Star power: Small fusion start-ups aim for break-even,” *New Sci.*, no. 2825, pp. 36–39, 2011.

[13] “ITER.” [Online]. Available: www.iter.org/proj/iterandbeyond. [Accessed: 13-Nov-2013].

[14] “EURATOM.” [Online]. Available: ec.europa.eu/research/energy/euratom/index_en.cfm?pg=fusion&section=iter-future. [Accessed: 13-Nov-2013].

[15] “EFDA Fusion Electricity - A roadmap to the realisation of fusion energy,” 2012.

[16] D. Stork and T. Todd, “DEMO and the technical feasibility of fusion reactors,” 2011.

[17] “IPP.” [Online]. Available: www.ipp.mpg.de/ippcms/eng/pr/fusion21/zuendung/index.html. [Accessed: 08-Feb-2010].

[18] “Gen IV.” [Online]. Available: www.gen-4.org/index.html. [Accessed: 26-Aug-2011].

[19] “GIF and Generation IV,” 2007.

[20] “A technology roadmap for Generation IV nuclear energy systems - US DOE Nuclear Energy Research Advisory Committee, Generation IV International Forum.”

[21] “Gen-IV International Forum.” [Online]. Available: https://www.gen-4.org/gif/jcms/c_9353/systems. [Accessed: 03-Oct-2014].

[22] G. S. Was, *Fundamentals of Radiation Materials Science*. Springer, 2007.

[23] D. J. Bacon and Y. N. Osetsky, “Dislocation-Obstacle Interactions at Atomic Level in Irradiated Metals,” *Math. Mech. Solids*, vol. 14, no. 1–2, pp. 270–283, Jan. 2009.

[24] G. R. Odette, M. J. Alinger, and B. D. Wirth, “Recent Developments in Irradiation-Resistant Steels,” *Annu. Rev. Mater. Res.*, vol. 38, no. 1, pp. 471–503, Aug. 2008.

[25] H.-C. Schneider, B. Dafferner, and J. Aktaa, “Embrittlement behaviour of low-activation alloys with reduced boron content after neutron irradiation,” *J. Nucl. Mater.*, vol. 321, pp. 135–140, Sep. 2003.

[26] C. Heintze, F. Bergner, and M. Hernández-Mayoral, “Ion-irradiation-induced damage in Fe–Cr alloys characterized by nanoindentation,” *J. Nucl. Mater.*, vol. 417, pp. 980–983, Oct. 2011.

[27] N. Akasaka, S. Yamashita, T. Yoshitake, S. Ukai, and A. Kimura, “Microstructural changes of neutron irradiated ODS ferritic and martensitic steels,” *J. Nucl. Mater.*, vol. 329–333, pp. 1053–1056, Aug. 2004.

[28] S. Rogozkin, A. Aleev, A. Nikitin, A. Zaluzhnyi, P. Vladimirov, A. Möslang, and R. Lindau, “Atom probe characterization of nano - scaled features in irradiated Eurofer and ODS Eurofer steel,” 2009, p. EC IAEA Topical Meeting on: Development of new str.

[29] D. Kramer, H. R. Brager, C. G. Rhodes, and A. G. Pard, “Helium embrittlement in type 304 stainless steel,” *J. Nucl. Mater.*, vol. 25, pp. 121–131, 1968.

[30] W. Jäger, R. Manzke, H. Trinkaus, G. Creclius, R. Zeller, J. Fink, and H. L. Bay, “Density and pressure of helium in small bubbles in metals,” *J. Nucl. Mater.*, vol. 111–112, pp. 674–680, 1982.

[31] I. Kim, J. D. Hunn, N. Hashimoto, D. L. Larson, P. J. Maziasz, K. Miyahara, and E. H. Lee, “Defect and void evolution in oxide dispersion strengthened ferritic steels under 3.2 MeV Fe+ ion irradiation with simultaneous helium injection,” *J. Nucl. Mater.*, vol. 280, pp. 264–274, 2000.

[32] L. K. Mansur and E. H. Lee, “Theoretical basis for unified analysis of experimental data and design of swelling-resistant alloys,” *J. Nucl. Mater.*,

vol. 179–181, pp. 105–110, Mar. 1991.

[33] L. L. Hsiung, M. J. Fluss, S. J. Tumey, B. W. Choi, Y. Serruys, F. Willaime, and A. Kimura, "Formation mechanism and the role of nanoparticles in Fe-Cr ODS steels developed for radiation tolerance," *Phys. Rev. B*, vol. 82, p. 184103, Nov. 2010.

[34] T. Yamamoto, "TEM Observation of Dual Ion Beam Irradiated F82H mod.3 and MA957," *Fusion React. Mater. Progr.*, vol. 49, 2010.

[35] D. S. Gelles, "On quantification of helium embrittlement in ferritic/martensitic steels," *J. Nucl. Mater.*, vol. 287, pp. 838–840, 2000.

[36] T. Yamamoto, G. R. Odette, H. Kishimoto, J.-W. Rensman, and P. Miao, "On the effects of irradiation and helium on the yield stress changes and hardening and non-hardening embrittlement of ~8Cr tempered martensitic steels: Compilation and analysis of existing data," *J. Nucl. Mater.*, vol. 356, pp. 27–49, Sep. 2006.

[37] "ORNL." [Online]. Available: www.ornl.gov/sci/rrd/pages/hfir.html. [Accessed: 30-Aug-2011].

[38] P. Hosemann, Y. Dai, E. Stergar, A. T. Nelson, and S. A. Maloy, "Small-Scale Testing of In-Core Fast Reactor Materials," *J. Nucl. Sci. Technol.*, vol. 48, no. 4, pp. 575–579, 2011.

[39] M. A. Pouchon, J. Chen, and W. Hoffelner, "Microcharacterization of damage in materials for advance nuclear fusion plants," *Adv. Mater. Res.*, vol. 59, pp. 269–274, 2009.

[40] A. Kohyama, A. Hishinuma, Y. Kohno, K. Shiba, and A. Sagara, "The development of ferritic steels for DEMO blanket," *Fusion Eng. Des.*, vol. 41, pp. 1–6, Sep. 1998.

[41] "IFMIF." [Online]. Available: www.ifmif.org. [Accessed: 29-Nov-2013].

[42] "ITER." [Online]. Available: www.iter.org/newsline/272/1630. [Accessed: 29-Nov-2013].

[43] I. L. Singer, “Surface analysis, ion implantation and tribological processes affecting steels,” *Appl. Surf. Sci.*, vol. 18, pp. 28–62, 1984.

[44] C. Heintze, F. Bergner, R. Koegler, and R. Lindau, “The Influence of Helium and ODS on the Irradiation-Induced Hardening of Eurofer97 at 300°C,” *Adv. Sci. Technol.*, vol. 73, pp. 124–129, Oct. 2010.

[45] V. Levy, D. Gilbon, and C. Rivera, “Influence of helium on swelling in steels,” *Eff. Radiat. Mater. 12th Int. Symp.*, vol. 870, pp. 317–329, 1985.

[46] H. Kishimoto, K. Yutani, R. Kasada, and A. Kimura, “Helium cavity formation research on oxide dispersed strengthening (ODS) ferritic steels utilizing dual-ion irradiation facility,” *Fusion Eng. Des.*, vol. 81, pp. 1045–1049, Feb. 2006.

[47] C. Abromeit, “Aspects of simulation of neutron damage by ion irradiation,” *J. Nucl. Mater.*, vol. 216, pp. 78–96, Oct. 1994.

[48] S. M. Myers, P. M. Richards, W. R. Wampler, and F. Besenbacher, “Ion-beam studies of hydrogen-metal interactions,” *J. Nucl. Mater.*, vol. 165, pp. 9–64, Apr. 1989.

[49] L. Malerba, “Multi-scale modelling of irradiaion effects in nuclear power plant materials,” in *Understanding and Mitigating Ageing in Nuclear Power Plants*, 2010, pp. 456–543.

[50] C. Deo, C. Tomé, R. Lebensohn, and S. Maloy, “Modeling and simulation of irradiation hardening in structural ferritic steels for advanced nuclear reactors,” *J. Nucl. Mater.*, vol. 377, pp. 136–140, Jun. 2008.

[51] L. Gámez, E. Martínez, J. M. Perlado, P. Cepas, M. J. Caturla, M. Victoria, J. Marian, C. Arévalo, M. Hernández, and D. Gómez, “Kinetic Monte Carlo modelling of neutron irradiation damage in iron,” *Fusion Eng. Des.*, vol. 82, pp. 2666–2670, Oct. 2007.

[52] M. J. Norgett, M. T. Robinson, and I. M. Torrens, “A proposed method of calculating displacement dose rates,” *Nucl. Eng. Des.*, vol. 33, pp. 50–54, 1975.

[53] R. E. Stoller, M. B. Toloczko, G. S. Was, A. G. Certain, S. Dwaraknath, and F. A. Garner, "On the use of SRIM for computing radiation damage exposure," *Nucl. Instruments Methods Phys. Res. Sect. B*, vol. 310, pp. 75–80, 2013.

[54] I. Charit and K. L. Murty, "Structural materials issues for the next generation fission reactors," *J. Mater.*, vol. 62, no. 9, pp. 67–74, 2010.

[55] A. W. Kleyn, "Magnetic Confinement: fusion in ITER - beams and surfaces," 2006.

[56] E. E. Bloom, R. W. Conn, J. W. Davis, R. E. Gold, R. Little, K. R. Schultz, D. L. Smith, and F. W. Wiffen, "Low activation materials for fusion applications," *J. Nucl. Mater.*, vol. 122–123, pp. 17–26, 1984.

[57] "Stanford." [Online]. Available: gcep.stanford.edu/pdfs/qa4ScQIicx-kve2pX9D7Yg/baluc_fusion_05_06.pdf. [Accessed: 20-Sep-2011].

[58] K Seidel, "Experimental investigation of radioactivity induced in the fusion power plant structural materials EUROFER and in other steels by D/T reactions," *ICFRM-10*, 2001.

[59] B. van der Schaaf, F. Tavassoli, C. Fazio, E. Rigal, E. Diegele, R. Lindau, and G. LeMarois, "The development of EUROFER reduced activation steel," *Fusion Eng. Des.*, vol. 69, pp. 197–203, Sep. 2003.

[60] R. L. Klueh, E. T. Cheng, M. L. Grossbeck, and E. E. Bloom, "Impurity effects on reduced-activation ferritic steels developed for fusion applications," *J. Nucl. Mater.*, vol. 280, pp. 353–359, 2000.

[61] A.-A. F. Tavassoli, A. Alamo, L. Bedel, L. Forest, J.-M. Gentzbittel, J.-W. Rensman, E. Diegele, R. Lindau, M. Schirra, R. Schmitt, H. . Schneider, C. Petersen, A.-M. Lancha, P. Fernandez, G. Filacchioni, M. F. Maday, K. Mergia, N. Boukos, P. Spätig, E. Alves, and E. Lucon, "Materials design data for reduced activation martensitic steel type EUROFER," *J. Nucl. Mater.*, vol. 329–333, pp. 257–262, Aug. 2004.

[62] M. Victoria, S. Dudarev, J. L. Boutard, E. Diegele, R. Lässer, A. Almazouzi, M. J. Caturla, C. C. Fu, J. Källne, L. Malerba, K. Nordlund, M. Perlado, M. Rieth, M. Samaras, R. Schaeublin, B. N. Singh, and F. Willaime,

"Modelling irradiation effects in fusion materials," *Fusion Eng. Des.*, vol. 82, pp. 2413–2421, Oct. 2007.

[63] E. E. Bloom, "The challenge of developing structural materials for fusion power systems," *J. Nucl. Mater.*, vol. 263, pp. 7–17, 1998.

[64] M. Rieth, M. Schirra, A. Falkenstein, P. Graf, S. Heger, H. Kempe, R. Lindau, and H. Zimmermann, "EUROFER 97 - Tensile, Charpy, Creep and Structural Tests," 2003.

[65] L. Schäfer, "Tensile and impact behavior of the reduced-activation steels OPTIFER and F82H mod," *J. Nucl. Mater.*, vol. 287, pp. 707–710, 2000.

[66] B. S. J. Kang, K. Ogawa, L. Ma, M. A. Alvin, N. Wu, and G. Smith, "Materials and components development for advance turbine systems - ODS alloy development," 2010.

[67] M. A. Harper, "Improved ODS alloy for heat exchanger tubing," in *Department of Energy*, 2002, pp. 1–13.

[68] D. K. Mukhopadhyay, F. H. Froes, and D. S. Gelles, "Development of oxide dispersion strengthened ferritic steels for fusion," *J. Nucl. Mater.*, vol. 258–263, pp. 1209–1215, 1998.

[69] M. . Alinger, G. . Odette, and D. . Hoelzer, "The development and stability of Y–Ti–O nanoclusters in mechanically alloyed Fe–Cr based ferritic alloys," *J. Nucl. Mater.*, vol. 329–333, pp. 382–386, Aug. 2004.

[70] S. Oh, J. Lee, C. Jang, and A. Kimura, "Irradiation hardening and embrittlement in high-Cr oxide dispersion strengthened steels," *J. Nucl. Mater.*, vol. 386–388, pp. 503–506, 2009.

[71] S. Kavithaa, R. Subramanian, and P. C. Angelo, "Yttria dispersed 9Cr martensitic steel synthesized by mechanical alloying - hot isostatic pressing," *Trans. Indian Inst. Met.*, vol. 63, no. 1, pp. 67–74, 2010.

[72] C. Suryanarayana, E. Ivanov, and V. . Boldyrev, "The science and technology of mechanical alloying," *Mater. Sci. Eng. A*, vol. 304–306, pp. 151–158, May 2001.

[73] C. C. Koch, "Materials synthesis by mechanical alloying," *Annu. Rev. Mater. Sci.*, no. 6, 1989.

[74] P. S. Gilman and J. S. Benjamin, "Mechanical Alloying," *Annu. Rev. Mater. Sci.*, vol. 13, pp. 279–300, 1983.

[75] M. K. Miller, K. F. Russell, and D. T. Hoelzer, "Characterization of precipitates in MA/ODS ferritic alloys," *J. Nucl. Mater.*, vol. 351, pp. 261–268, Jun. 2006.

[76] M. K. Miller, E. A. Kenik, K. F. Russell, L. Heatherly, D. T. Hoelzer, and P. J. Maziasz, "Atom probe tomography of nanoscale particles in ODS ferritic alloys," *Mater. Sci. Eng. A*, vol. 353, pp. 140–145, 2003.

[77] M. K. Miller, D. T. Hoelzer, E. A. Kenik, and K. F. Russell, "Stability of ferritic MA/ODS alloys at high temperatures," *Intermetallics*, vol. 13, no. 3–4, pp. 387–392, Mar. 2005.

[78] S. Ukai, T. Nishida, H. Okada, T. Okuda, M. Fujiwara, and K. Asabe, "Development of Oxide Dispersion Strengthened Ferritic Steels for FBR Core Application, (I)," *J. Nucl. Sci. Technol.*, vol. 34, no. 3, pp. 256–263, Mar. 1997.

[79] M. Ratti, D. Leuvrey, M. H. Mathon, and Y. de Carlan, "Influence of titanium on nano-cluster (Y, Ti, O) stability in ODS ferritic materials," *J. Nucl. Mater.*, vol. 386–388, pp. 540–543, Apr. 2009.

[80] Z. Oksiuta and N. Baluc, "Role of Cr and Ti Contents on the Microstructure and Mechanical Properties of ODS Ferritic Steels," *Adv. Mater. Res.*, vol. 59, pp. 308–312, 2009.

[81] M. K. Miller, C. L. Fu, M. Krcmar, D. T. Hoelzer, and C. T. Liu, "Vacancies as a constitutive element for the design of nanocluster-strengthened ferritic steels," *Front. Mater. Sci. China*, vol. 3, no. 1, pp. 9–14, Nov. 2008.

[82] S. Ohtsuka, S. Ukai, M. Fujiwara, T. Kaito, and T. Narita, "Nano-structure control in ODS martensitic steels by means of selecting titanium and oxygen contents," *J. Phys. Chem. Solids*, vol. 66, pp. 571–575, Feb. 2005.

[83] P. Hosemann, E. Stergar, L. Peng, Y. Dai, S. A. Maloy, M. A. Pouchon, K.

Shiba, D. Hamaguchi, and H. Leitner, “Macro and microscale mechanical testing and local electrode atom probe measurements of STIP irradiated F82H, Fe–8Cr ODS and Fe–8Cr–2W ODS,” *J. Nucl. Mater.*, vol. 417, pp. 274–278, Oct. 2011.

[84] J. Benjamin, “Mechanical alloying – a perspective,” *Met. Powder Rep.*, vol. 45, no. 2, pp. 122–127, 1990.

[85] P. D. Sketchley, P. L. Threadgill, and I. G. Wright, “Rotary friction welding of an Fe3Al based ODS alloy,” *Mater. Sci. Eng. A*, vol. 329–331, pp. 756–762, 2002.

[86] B. K. Kad, “Optimization of Oxide Dispersion Strengthened Fe3Al Alloy Tubes: Application Specific Development for the Power Generation Industry.”

[87] G. R. Odette and D. T. Hoelzer, “Irradiation-tolerant nanostructured ferritic alloys: Transforming helium from a liability to an asset,” *J. Mater.*, pp. 84–92.

[88] E. A. Marquis, “Core/shell structures of oxygen-rich nanofeatures in oxide-dispersion strengthened Fe–Cr alloys,” *Appl. Phys. Lett.*, vol. 93, p. 181904, 2008.

[89] L. Hsiung, M. Fluss, S. Tumey, J. Kuntz, B. El-Dasher, M. Wall, B. Choi, A. Kimura, F. Willaime, and Y. Serruys, “HRTEM study of oxide nanoparticles in K3-ODS ferritic steel developed for radiation tolerance,” *J. Nucl. Mater.*, vol. 409, pp. 72–79, Feb. 2011.

[90] N. J. Cunningham, Y. Wu, E. Haney, and G. R. Odette, “Characterization of the Composition and Structure of Y-Ti-O Rich Precipitates in Nanostructured Ferritic Alloy MA957 by Transmission Electron Microscopy and Atom Probe Tomography,” pp. 22–27, 2009.

[91] C. A. Williams, E. A. Marquis, A. Cerezo, and G. D. W. Smith, “Nanoscale characterisation of ODS–Eurofer 97 steel: An atom-probe tomography study,” *J. Nucl. Mater.*, vol. 400, pp. 37–45, May 2010.

[92] C. A. Williams, J. M. Hyde, G. D. W. Smith, and E. A. Marquis, “Effects of heavy-ion irradiation on solute segregation to dislocations in oxide-dispersion-strengthened Eurofer 97 steel,” *J. Nucl. Mater.*, vol. 412, pp. 100–105, May 2011.

[93] C.-L. Chen, A. Richter, R. Kögler, and G. Talut, "Dual beam irradiation of nanostructured FeCrAl oxide dispersion strengthened steel," *J. Nucl. Mater.*, vol. 412, pp. 350–358, 2011.

[94] D. Sakuma, S. Yamashita, K. Oka, S. Ohnuki, L. . Rehn, and E. Wakai, "Y2O3 nano-particle formation in ODS ferritic steels by Y and O dual ion-implantation," *J. Nucl. Mater.*, vol. 329–333, pp. 392–396, Aug. 2004.

[95] O. Kalokhtina, B. Radiguet, Y. de Carlan, and P. Pareige, "Study of Nano-cluster Formation in Fe-18Cr ODS Ferritic Steel by Atom Probe Tomography," in *MRS Spring*, 2010.

[96] A. J. London, S. Lozano-Perez, S. Santra, S. Amirthapandian, B. K. Panigrahi, C. S. Sundar, and C. R. M. Grovenor, "Comparison of atom probe tomography and transmission electron microscopy analysis of oxide dispersion strengthened steels," *J. Phys. Conf. Ser.*, vol. 522, Jun. 2014.

[97] S. Ukai and M. Fujiwara, "Perspective of ODS alloys application in nuclear environments," *J. Nucl. Mater.*, vol. 307–311, pp. 749–757, Dec. 2002.

[98] R. Lindau, A. Möslang, M. Schirra, P. Schlossmacher, and M. Klimenkov, "Mechanical and microstructural properties of a hipped RAFM ODS-steel," *J. Nucl. Mater.*, vol. 307–311, pp. 769–772, Dec. 2002.

[99] M. A. Auger, T. Leguey, A. Muñoz, M. A. Monge, V. de Castro, P. Fernández, G. Garcés, and R. Pareja, "Microstructure and mechanical properties of ultrafine-grained Fe–14Cr and ODS Fe–14Cr model alloys," *J. Nucl. Mater.*, vol. 417, pp. 213–216, Oct. 2011.

[100] M. Klimenkov, "Quantitative measurement of argon inside of nano-sized bubbles in ODS steels," *J. Nucl. Mater.*, vol. 411, pp. 160–162, Apr. 2011.

[101] A. D. Brailsford and L. K. Mansur, "The effect of precipitate-matrix interface sinks on the growth of voids in the matrix," *J. Nucl. Mater.*, vol. 103–104, pp. 1403–1408, 1981.

[102] C Burrows, "ODS processing effects on bubble density (DPhil Thesis),"

University of Oxford, 2015.

[103] K. Yutani, H. Kishimoto, R. Kasada, and A. Kimura, “Evaluation of helium effects on swelling behavior of oxide dispersion strengthened ferritic steels under ion irradiation,” *J. Nucl. Mater.*, vol. 367–370, pp. 423–427, 2007.

[104] G. Bonny, D. Terentyev, and L. Malerba, “Identification and characterization of Cr-rich precipitates in FeCr alloys: An atomistic study,” *Comput. Mater. Sci.*, vol. 42, pp. 107–112, Mar. 2008.

[105] A. Hasegawa, M. Ejiri, S. Nogami, M. Ishiga, R. Kasada, A. Kimura, K. Abe, and S. Jitsukawa, “Effects of helium on ductile-brittle transition behavior of reduced-activation ferritic steels after high-concentration helium implantation at high temperature,” *J. Nucl. Mater.*, vol. 386–388, pp. 241–244, Apr. 2009.

[106] R. J. Kurtz, “Status of RAFM steel development,” in *ICFRM-13*, 2007.

[107] M. J. Gorley, “Powder processing of oxide dispersion strengthened alloys for nuclear applications (DPhil Thesis),” University of Oxford, 2014.

[108] S. J. Zinkle, “Advanced materials for fusion technology,” *Fusion Eng. Des.*, vol. 74, pp. 31–40, 2005.

[109] “Microindentation Hardness Testing.”

[110] J. B. Pethica, R. Hutchings, and W. C. Oliver, “Hardness measurement at penetration depths as small as 20 nm,” *Philos. Mag. A*, vol. 48, no. 4, pp. 593–606, 2013.

[111] “Nanoindentation.” [Online]. Available: www.nanoindentation.cornell.edu/machine/nanoindentation-machine.htm. [Accessed: 04-Jun-2010].

[112] N. Gane, “The Direct Measurement of the Strength of Metals on a Sub-Micrometre Scale,” *Proc. R. Soc. Lond. A. Math. Phys. Sci.*, vol. 317, no. 1530, pp. 367–391, 1970.

[113] H. Nili, K. Kalantar-zadeh, M. Bhaskaran, and S. Sriram, "In situ nanoindentation: Probing nanoscale multifunctionality," *Prog. Mater. Sci.*, vol. 58, pp. 1–29, Jan. 2013.

[114] C. A. Schuh, "Nanoindentation studies of materials," *Mater. Today*, vol. 9, no. 5, pp. 32–40, 2006.

[115] J. D. Nowak, K. A. Rzepiejewska-Malyska, R. C. Major, O. L. Warren, and J. Michler, "In-situ nanoindentation in the SEM," *Mater. Today*, vol. 12, pp. 44–45, 2010.

[116] J. R. Greer, J. Y. Kim, and M. J. Burek, "The in-situ mechanical testing of nanoscale single-crystalline nanopillars," *J. Mater.*, vol. 61, no. 12, pp. 19–25, 2009.

[117] E. A. Stach, T. Freeman, A. M. Minor, D. K. Owen, J. Cumings, M. A. Wall, T. Chraska, R. Hull, J. W. Morris, A. Zettl, and U. Dahmen, "Development of a Nanoindenter for In Situ Transmission Electron Microscopy," *Microsc. Microanal.*, vol. 7, pp. 507–517, 2001.

[118] C. E. Carlton and P. J. Ferreira, "In situ TEM nanoindentation of nanoparticles.," *Micron*, vol. 43, pp. 1134–1139, Nov. 2012.

[119] A. C. Fischer-Cripps, "Nanoindentation," in *Mechanical Engineering Series 1*, New York, NY: Springer New York, 2011, pp. 21–38.

[120] W. C. Oliver and G. M. Pharr, "An improved technique for determining hardness and elastic modulus using load and displacement sensing indentation experiments," *J. Mater. Res.*, vol. 7, no. 6, pp. 1564–1583, 1992.

[121] T. P. Weihs, S. Hong, J. C. Bravman, and W. D. Nix, "Mechanical deflection of cantilever microbeams : A new technique for testing the mechanical properties of thin films," *J. Mater. Res.*, vol. 3, no. 5, pp. 931–942, 1988.

[122] A. T. Jennings and J. R. Greer, "Tensile deformation of electroplated copper nanopillars," *Philos. Mag.*, vol. 91, no. 7–9, pp. 1108–1120, Mar. 2011.

[123] J. McCarthy, Z. Pei, M. Becker, and D. Atteridge, “FIB micromachined submicron thickness cantilevers for the study of thin film properties,” *Thin Solid Films*, vol. 358, pp. 146–151, 2000.

[124] J. S. K. Gibson, “Tungsten For Fusion Power Applications (Masters Thesis),” University of Oxford, 2011.

[125] D. E. J. Armstrong, M. E. Rogers, and S. G. Roberts, “Micromechanical testing of stress corrosion cracking of individual grain boundaries,” *Scr. Mater.*, vol. 61, pp. 741–743, Oct. 2009.

[126] D. E. J. Armstrong, “Measuring Elastic , Plastic and Fracture Properties using Micro-Cantilever Testing (DPhil Thesis),” University of Oxford, 2009.

[127] Y. Yang, J. C. Ye, J. Lu, F. X. Liu, and P. K. Liaw, “Effects of specimen geometry and base material on the mechanical behavior of focused-ion-beam-fabricated metallic-glass micropillars,” *Acta Mater.*, vol. 57, pp. 1613–1623, Mar. 2009.

[128] R. M. Langford, P. M. Nellen, J. Gierak, and Y. Fu, “Focused Ion Beam Micro- and Nanoengineering,” *MRS Bull.*, vol. 32, no. May, pp. 417–423, 2007.

[129] M. D. Uchic and D. M. Dimiduk, “A methodology to investigate size scale effects in crystalline plasticity using uniaxial compression testing,” *Mater. Sci. Eng. A*, vol. 400–401, pp. 268–278, Jul. 2005.

[130] J. Reuteler, “Introduction to FIB-SEM: Basic Physics and Applications.” [Online]. Available: http://www.nonmet.mat.ethz.ch/Infrastructure/FIB/FIB-SEM_Introduction_JR.pdf. [Accessed: 10-Oct-2015].

[131] J. R. Greer, W. C. Oliver, and W. D. Nix, “Size dependence of mechanical properties of gold at the micron scale in the absence of strain gradients,” *Acta Mater.*, vol. 53, pp. 1821–1830, Apr. 2005.

[132] J. Greer and W. Nix, "Nanoscale gold pillars strengthened through dislocation starvation," *Phys. Rev. B*, vol. 73, no. 24, p. 245410, Jun. 2006.

[133] K. W. McElhaney, J. J. Vlassak, and W. D. Nix, "Determination of indenter tip geometry and indentation contact area for depth-sensing indentation experiments," *J. Mater. Res.*, vol. 13, no. 5, pp. 1300–1306, Jan. 2011.

[134] W. D. Nix and H. Gao, "Indentation size effects in crystalline materials: a law for strain gradient plasticity," *J. Mech. Phys. Solids*, vol. 46, no. 3, pp. 411–425, 1998.

[135] J. Gong and A. J. Wilkinson, "Anisotropy in the plastic flow properties of single-crystal α titanium determined from micro-cantilever beams," *Acta Mater.*, vol. 57, pp. 5693–5705, Nov. 2009.

[136] S. H. Chen and B. Feng, "Size effect in micro-scale cantilever beam bending," *Acta Mech.*, vol. 219, pp. 291–307, Feb. 2011.

[137] C. Motz, D. Weygand, J. Senger, and P. Gumbsch, "Micro-bending tests: A comparison between three-dimensional discrete dislocation dynamics simulations and experiments," *Acta Mater.*, vol. 56, pp. 1942–1955, May 2008.

[138] N. A. Fleck, G. M. Muller, M. F. Ashby, and J. W. Hutchinson, "Strain gradient plasticity: theory and experiment," *Acta Mater.*, vol. 42, no. 2, pp. 475–487, 1994.

[139] T. A. Parthasarathy, S. I. Rao, D. M. Dimiduk, M. D. Uchic, and D. R. Trinkle, "Contribution to size effect of yield strength from the stochastics of dislocation source lengths in finite samples," *Scr. Mater.*, vol. 56, pp. 313–316, Feb. 2007.

[140] D. M. Dimiduk, M. D. Uchic, and T. A. Parthasarathy, "Size-affected single-slip behavior of pure nickel microcrystals," *Acta Mater.*, vol. 53, pp. 4065–4077, Sep. 2005.

[141] R. Lindau, A. Möslang, M. Rieth, M. Klimiankou, E. Materna-Morris, A. Alamo, A.-A. F. Tavassoli, C. Cayron, A.-M. Lancha, P. Fernandez, N. Baluc, R. Schäublin, E. Diegele, G. Filacchioni, J. W. Rensman, B. v. d.

Schaaf, E. Lucon, and W. Dietz, “Present development status of EUROFER and ODS-EUROFER for application in blanket concepts,” *Fusion Eng. Des.*, vol. 75–79, pp. 989–996, Nov. 2005.

[142] “Surrey Ion Beam Centre.” [Online]. Available: http://www.surrey.ac.uk/ati/ibc/index.htm.

[143] B. Cui, “Ion implantation Presentation,” in *University of Waterloo*.

[144] M. B. Lewis, “Diffusion of ion implanted helium in vanadium and niobium,” *J. Nucl. Mater.*, vol. 152, pp. 114–122, 1988.

[145] S. J. Zinkle, A. Möslang, T. Muroga, and H. Tanigawa, “Multimodal options for materials research to advance the basis for fusion energy in the ITER era,” *Nucl. Fusion*, vol. 53, no. 10, p. 104024, 2013.

[146] T. Yamamoto, G. R. Odette, P. Miao, D. T. Hoelzer, J. Bentley, N. Hashimoto, H. Tanigawa, and R. J. Kurtz, “The transport and fate of helium in nanostructured ferritic alloys at fusion relevant He/dpa ratios and dpa rates,” *J. Nucl. Mater.*, vol. 367–370, pp. 399–410, Aug. 2007.

[147] N. Marochov and P. J. Goodhew, “A comparison of the growth of helium and neon bubbles in nickel,” *J. Nucl. Mater.*, vol. 158, pp. 81–86, Aug. 1988.

[148] “Jannus, CEA.” [Online]. Available: http://jannus.in2p3.fr/.

[149] MTS, *MTS Nanoindenter XP Manual*. 2002.

[150] M. R. Begley and J. W. Hutchinson, “The mechanics of size-dependent indentation,” *J. Mech. Phys. Solids*, vol. 46, no. 10, pp. 2049–2068, 1998.

[151] G. M. Pharr, E. G. Herbert, and Y. Gao, “The Indentation Size Effect: A Critical Examination of Experimental Observations and Mechanistic Interpretations,” *Annu. Rev. Mater. Res.*, vol. 40, no. 1, pp. 271–292, Jun. 2010.

[152] R. K. Abu Al-Rub and G. Z. Voyiadjis, “Analytical and experimental determination of the material intrinsic length scale of strain gradient

plasticity theory from micro- and nano-indentation experiments," *Int. J. Plast.*, vol. 20, pp. 1139–1182, Jun. 2004.

[153] R. K. Abu Al-Rub and G. Z. Voyiadjis, "A physically based gradient plasticity theory," *Int. J. Plast.*, vol. 22, pp. 654–684, Apr. 2006.

[154] D. Tabor, "The Hardness of Solids," *IOP Sci.*, pp. 145–179.

[155] P. Zhang, S. X. Li, and Z. F. Zhang, "General relationship between strength and hardness," *Mater. Sci. Eng. A*, vol. 529, pp. 62–73, Nov. 2011.

[156] *Table for Vickers Hardness Number*. Matsuzawa Seiki Co. Ltd.

[157] E. O. Hall, "III Discussion of Results," in *The Deformation and Ageing of Mild Steel*, 1951.

[158] N. J. Petch, "The clevage strength of polycrystals," *J . Iron Steel Inst.*, no. 173, pp. 25–28, 1953.

[159] A. Kimura, "Mechanism of radiation damage evolution in 9Cr-ODS martensitic steels," *Japan Sci. Technol. Agency*, vol. 35, no. 41, p. 59, 2004.

[160] S. . Bull, "Modelling the hardness response of bulk materials, single and multilayer coatings," *Thin Solid Films*, vol. 398–399, pp. 291–298, Nov. 2001.

[161] S. . Bull, E. . Berasetegui, and T. . Page, "Modelling of the indentation response of coatings and surface treatments," *Wear*, vol. 256, pp. 857–866, May 2004.

[162] S. J. Bull, "Nanoindentation of coatings," *J. Phys. D. Appl. Phys.*, vol. 38, pp. R393–R413, Dec. 2005.

[163] J. E. Bradby, J. S. Williams, and M. V. Swain, "Pop-in events induced by spherical indentation in compound semiconductors," *J. Mater. Res.*, vol. 19, no. 1, pp. 380–386, 2004.

[164] E. M. Grieveson, D. E. J. Armstrong, S. Xu, and S. G. Roberts,

"Compression of self-ion implanted iron micropillars," *J. Nucl. Mater.*, vol. 430, pp. 119–124, Nov. 2012.

[165] E. M. Grieveson, "Micromechanical Testing of Fusion Reactor Materials (Masters Thesis)," University of Oxford, 2010.

[166] C. P. Frick, B. G. Clark, S. Orso, A. S. Schneider, and E. Arzt, "Size effect on strength and strain hardening of small-scale [111] nickel compression pillars," *Mater. Sci. Eng. A*, vol. 489, pp. 319–329, 2008.

[167] G. F. Vander Voort, *Metallographic Principles and Practice*. New York: ASM International, 1999.

[168] B. Kondori and A. Benzerga, "Discrete Dislocation Simulations of Taper Effects in Micropillar Compression," in *2013 TMS Annual Meeting & Exhibition*, 2013.

[169] H. Fei, A. Abraham, N. Chawla, and H. Jiang, "Evaluation of Micro-Pillar Compression Tests for Accurate Determination of Elastic-Plastic Constitutive Relations," *J. Appl. Mech.*, vol. 79, 2012.

[170] H. Zhang, B. E. Schuster, Q. Wei, and K. T. Ramesh, "The design of accurate micro-compression experiments," *Scr. Mater.*, vol. 54, pp. 181–186, Jan. 2006.

[171] H. Bei, S. Shim, M. K. Miller, G. M. Pharr, and E. P. George, "Effects of focused ion beam milling on the nanomechanical behavior of a molybdenum-alloy single crystal," *Appl. Phys. Lett.*, vol. 91, no. 11, p. 111915, 2007.

[172] R. A. Renzetti, H. R. Z. Sandim, R. E. Bolmaro, P. a. Suzuki, and A. Möslang, "X-ray evaluation of dislocation density in ODS-Eurofer steel," *Mater. Sci. Eng. A*, vol. 534, pp. 142–146, 2012.

[173] M. A. Tschopp and D. L. McDowell, "Grain boundary dislocation sources in nanocrystalline copper," *Scr. Mater.*, vol. 58, pp. 299–302, Feb. 2008.

[174] C. J. Healy and G. J. Ackland, "MD Simulations of Compression of

Nanoscale Iron Pillars," *MRS Proc.*, vol. 1369, 2011.

[175] C. D. Hardie, "Micro-Mechanics of Irradiated Fe-Cr Alloys for Fusion Reactors (DPhil Thesis)," 2013.

[176] F. Halliday, "Micromechanical Testing of Fusion Reactor Materials (Masters Thesis)," University of Oxford, 2008.

[177] J. S. K. Gibson, "Mechanical Behaviour of Irradiated Tungsten for Fusion Power (DPhil Thesis)," University of Oxford, 2015.

[178] G. B. Viswanathan, E. Lee, D. M. Maher, S. Banerjee, and H. L. Fraser, "Direct observations of dislocation substructures formed by nano-indentation of the α-phase in an α/β titanium alloy," *Mater. Sci. Eng. A*, vol. 400–401, pp. 463–466, Jul. 2005.

[179] J. T. M. Hosson, W. A. Soer, A. M. Minor, Z. Shan, E. A. Stach, S. A. Syed Asif, and O. L. Warren, "In situ TEM nanoindentation and dislocation-grain boundary interactions: a tribute to David Brandon," *J. Mater. Sci.*, vol. 41, pp. 7704–7719, Nov. 2006.

[180] M. Mata, O. Casals, and J. Alcalá, "The plastic zone size in indentation experiments: The analogy with the expansion of a spherical cavity," *Int. J. Solids Struct.*, vol. 43, pp. 5994–6013, Oct. 2006.

[181] D. B. Williams and C. B. Carter, *Transmission Electron Microscopy*, Second. Springer, 2009.

[182] S. Fréchard, M. Walls, M. Kociak, J. P. Chevalier, J. Henry, and D. Gorse, "Study by EELS of helium bubbles in a martensitic steel," *J. Nucl. Mater.*, vol. 393, pp. 102–107, Aug. 2009.

[183] B. Yao, D. J. Edwards, R. J. Kurtz, G. R. Odette, and T. Yamamoto, "Multiscale Simulation of Transmission Electron Microscopy Imaging of Helium Bubbles in Iron," *Fusion React. Mater. Progr.*, vol. 51, pp. 85–89, 2011.

[184] M. R. Louthan, "Tritium Decay, Irradiation and Hydrogen/Helium Effects on Type 316L Austenitic Stainless Steel," *U.S. Dep. Energy*, 2001.

[185] S. G. Roberts, "Oxford University Microplasticity of Materials Course,"

2007.

[186] M. Eddahbi, M. A. Monge, T. Leguey, P. Fernández, and R. Pareja, "Texture and mechanical properties of EUROFER 97 steel processed by ECAP," *Mater. Sci. Eng. A*, vol. 528, pp. 5927–5934, Jul. 2011.

[187] J. J. Huet, L. Coheur, L. DeWilde, J. Gedpot, W. Hendrix, and W. Vandermeulen, "Fabrication and mechanical properties of ODS ferritic alloys canning tubes for fast reactor fuel pins," in *TMS/AIME topical conderence on ferritic alloys for use in nuclear energy technologies*, 1984, pp. 329–334.

[188] "Detection Limits," *XPS International*. .

[189] V. A. Borodin and P. V. Vladimirov, "Diffusion coefficients and thermal stability of small helium-vacancy clusters in iron," *J. Nucl. Mater.*, vol. 362, pp. 161–166, 2007.

[190] "Total Materia." [Online]. Available: http://www.keytometals.com/page.aspx?ID=CheckArticle&site=kts&NM=164. [Accessed: 16-Dec-2014].

[191] W. Smith and J. Hashemi, *Foundations of Materials Science and Engineering*, 4th ed. McGraw-Hill, 2006.

[192] M. V Nathal and L. J. Ebert, "The Influence of Cobalt, Tantalum, and Tungsten on the Elevated Temperature Mechanical Properties of Single Crystal Nickel-Base Superalloys," *Metall. Trans. A*, vol. 16A, no. October, pp. 1863–1870, 1985.

[193] T. Narita, S. Ukai, S. Ohtsuka, and M. Inoue, "Effect of tungsten addition on microstructure and high temperature strength of 9CrODS ferritic steel," *J. Nucl. Mater.*, vol. 417, no. 1–3, pp. 158–161, Oct. 2011.

[194] G. Welsch, R. Ioyer, and E. W. Collings, *Materials Properties Handbook: Titanium alloys*. ASM International, 1993.

[195] "www.steeluniversity.org." [Online]. Available:

http://www.steeluniversity.org/content/html/eng/default.asp?catid=172&pageid=2081271822. [Accessed: 20-Jun-2014].

[196] G. E. Totten, L. Xie, and K. Funatani, *Handbook of Mechanical Alloy Design*. CRC Press, 2003.

[197] D. Preininger, "Effect of particle morphology and microstructure on strength, work-hardening and ductility behaviour of ODS-(7–13)Cr steels," *J. Nucl. Mater.*, vol. 329–333, pp. 362–368, Aug. 2004.

[198] S. Xu, Z. Yao, and M. L. Jenkins, "TEM characterisation of heavy-ion irradiation damage in FeCr alloys," *J. Nucl. Mater.*, vol. 386–388, pp. 161–164, Apr. 2009.

[199] T. Pratchett, *Interesting Times*. Victor Gollancz, 1994.

Appendices

Appendix A – CalTech SEMentor Videos

All the SEMentor videos are available on the enclosed CD. The tables below indicate the notable features of each video with times in seconds.

Fe-14wt%Cr

Unimplanted 1	Contact: 0.08 Massive collapse: 1.47 Test end: 2.00 Top not flat therefore bending. Slip in line of sight (top 2.5µm).
Unimplanted 2	Contact: 0.08 Massive collapse: 0.44 Test end: 0.57 Slip below line of sight (top 2.5µm).
Unimplanted 3	Contact: 0.08 Massive collapse: 0.43 Test end: 1.08 Not full contact on top Slip below line of sight (top 2µm).

Implanted 1	Contact: 0.08 Slip starts: 0.54 Test end: 1.54 Slight bowing at top before slip. Slip in line of sight (top 2µm).
Implanted 2	Contact: 0.08 1st Slip starts: 0.28 2nd Slip starts: 0.56 Test end: 1.54 Not flat topped. Slip in line of sight (top 1.5µm).
Implanted 3	Contact: 0.08 Slip starts: 0.32 Test end: 0.41 Fairly fast slip. Slip in line of sight (top 2µm).

CEA ODS

Unimplanted 1	No Video
Unimplanted 2	Contact: ~0.08 Test end: 2.01 Slow gradual barrelling of top ~2µm
Unimplanted 3 *(no data)*	Contact: 0.08 Test end: 1.51 Slow gradual barrelling of top ~2µm
Unimplanted 4	Contact: 0.08 Test end: 2.00 Slow gradual barrelling of top ~2µm Possible small slip 1.20 Slip visible in top section – possibly due to curving of pillar during testing.
Unimplanted 5	Contact: 0.08 Test end: 1.53 Slow gradual bowing of top ~2µm, slight bending.

Implanted 1	Contact: 0.08 Test end: 1.55 Not flat topped. Slight barrelling of whole length. Elastic recovery with tip retract.
Implanted 2	Contact: 0.08 Slip starts: 1.05 Massive slip: 1.22 Test end: 1.25 Slight barrelling of whole length. Tip of pillar sheared off and stuck to diamond punch.
Implanted 3	Contact: 0.08 Slip starts: 1.18 Massive slip: 1.34 Test end: 1.39 Not fully flat. Slight barrelling of whole length. Tip of pillar sheared off.
Implanted 4	Contact: 0.08 Test end: 1.52 Slight barrelling of whole length.
Implanted 5	Contact: 0.08 Test end: 1.49 Slight barrelling of whole length. Slight bending of pillar.

Appendix B – Microcantilever Load-Displacement Graphs

Microcantilever Load-Displacement Results

The nanoindentation software outputs load-displacement data to Excel for further analysis. All graphs in this section are formatted to the same scale for ease of comparison, with the exception of CEA ODS where there are two graphs for each condition – one showing the full range of data and one cropped to the scale of all the other graphs.

Load-Displacement

The nanoindenter was set to displace each cantilever by 2000nm, and it measures that displacement from the point it calculates the tip has touched the surface of the material. The loads required to deform these cantilevers, however, are sufficiently small that the surface find calculation does not always work effectively. These graphs were drawn from the raw data and the surface position manually determined where required. This means that the actual displacement in the test varies from 1000nm to >2000nm.

The following section shows the load-displacement graphs of each of the four materials – Fe-14wt%Cr, CEA ODS, EUROFER and EUROFER ODS – in each of three implantation conditions – unimplanted, 75appm He and 2000appm He (except for 75appm He in Fe-14wt%Cr where no sample was produced).

Fe-14wt%Cr

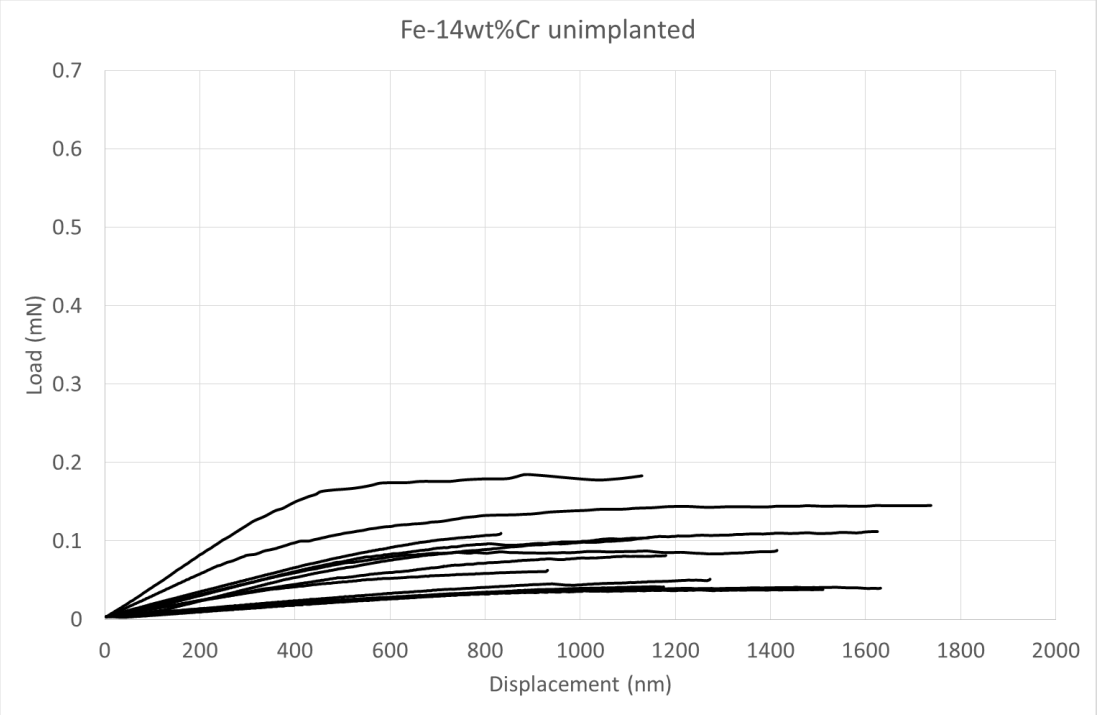

Figure 191 – Load vs. Displacement – Fe-14wt%Cr unimplanted

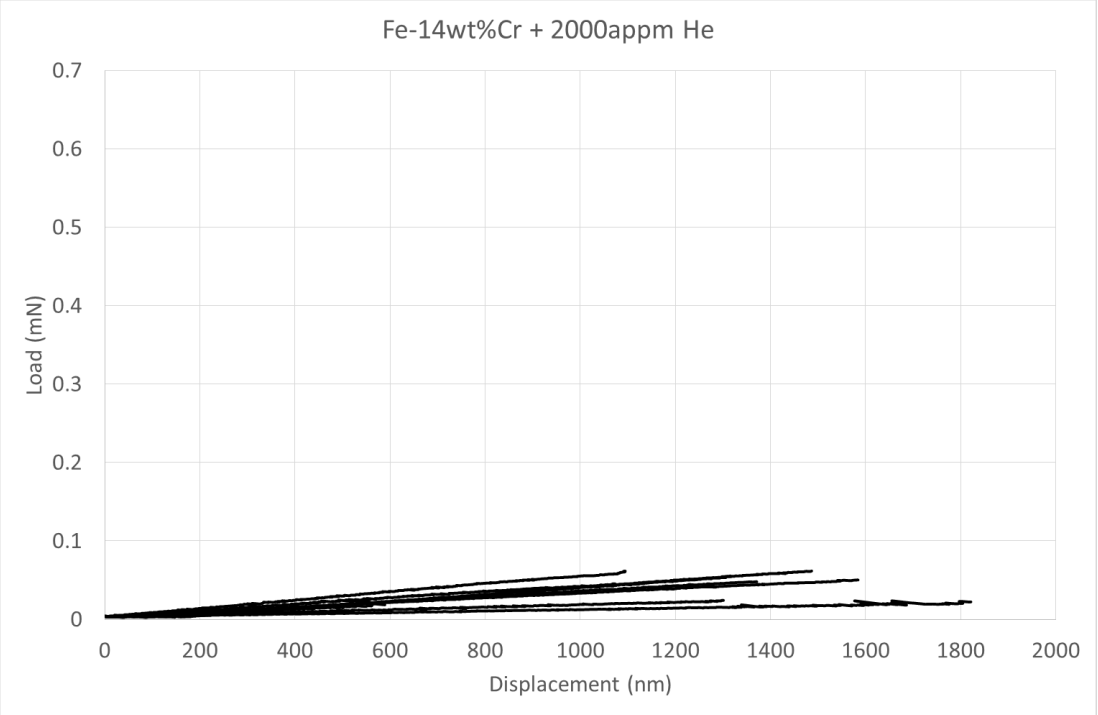

Figure 192 – Load vs. Displacement – Fe-14wt%Cr 2000appm He

CEA ODS

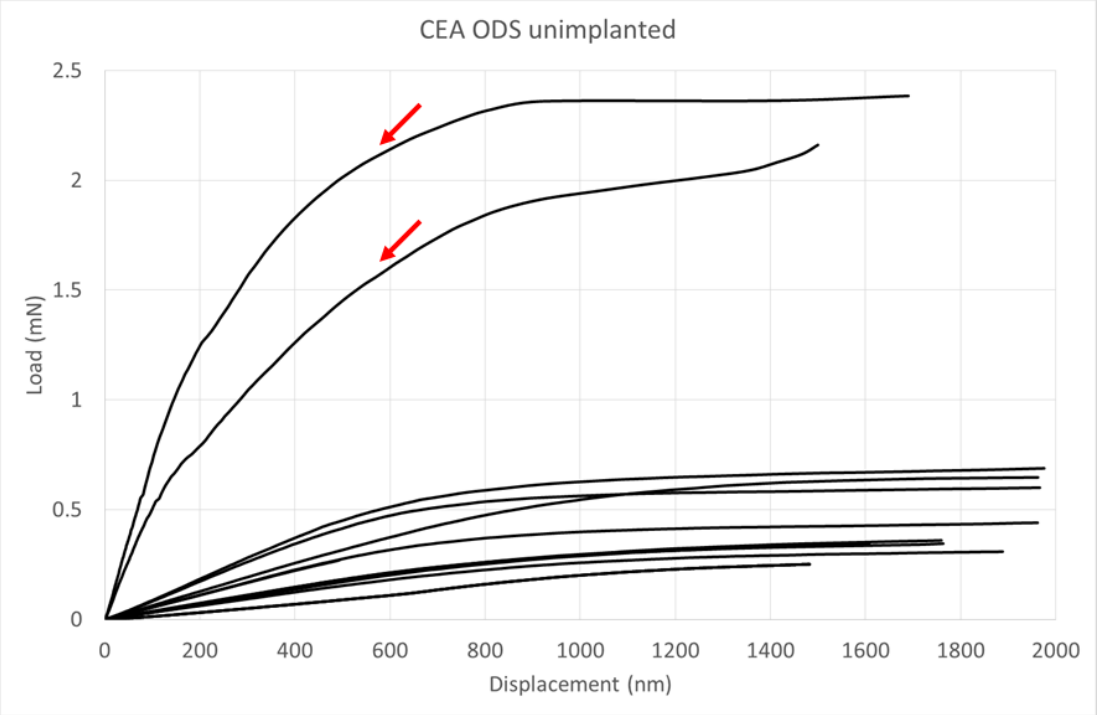

Figure 193 – Load vs. Displacement – CEA ODS unimplanted, full range
Red arrows indicate results with a load greater than 0.7mN at a displacement of 1000nm.

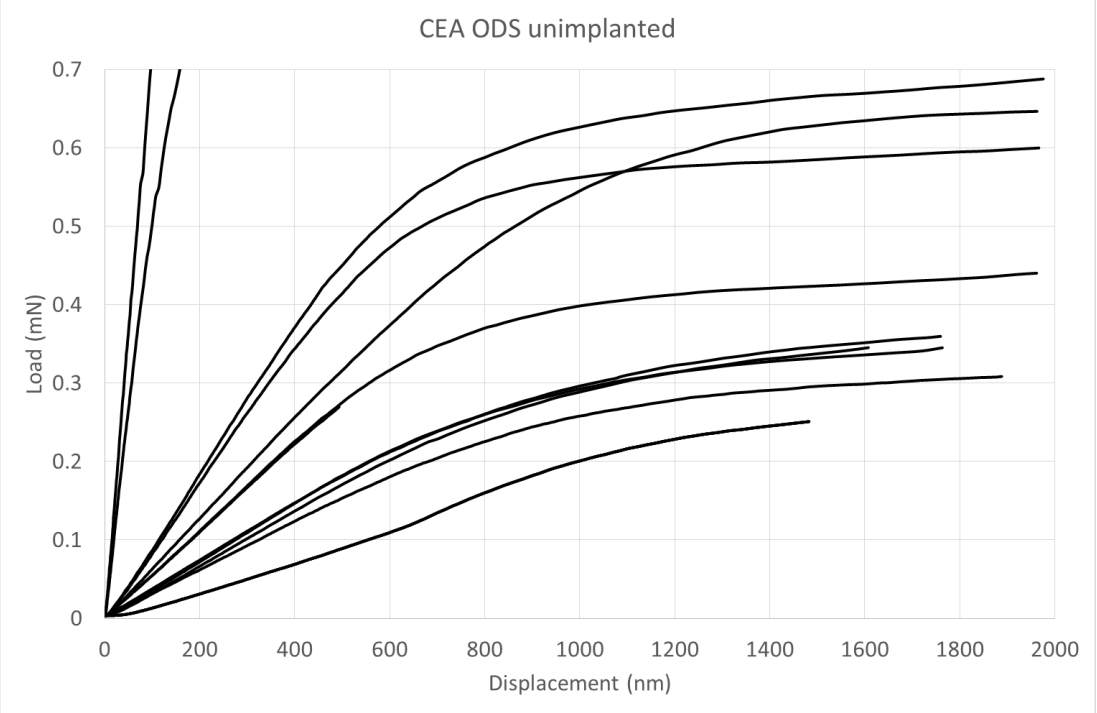

Figure 194 – Load vs. Displacement – CEA ODS unimplanted, reduced range

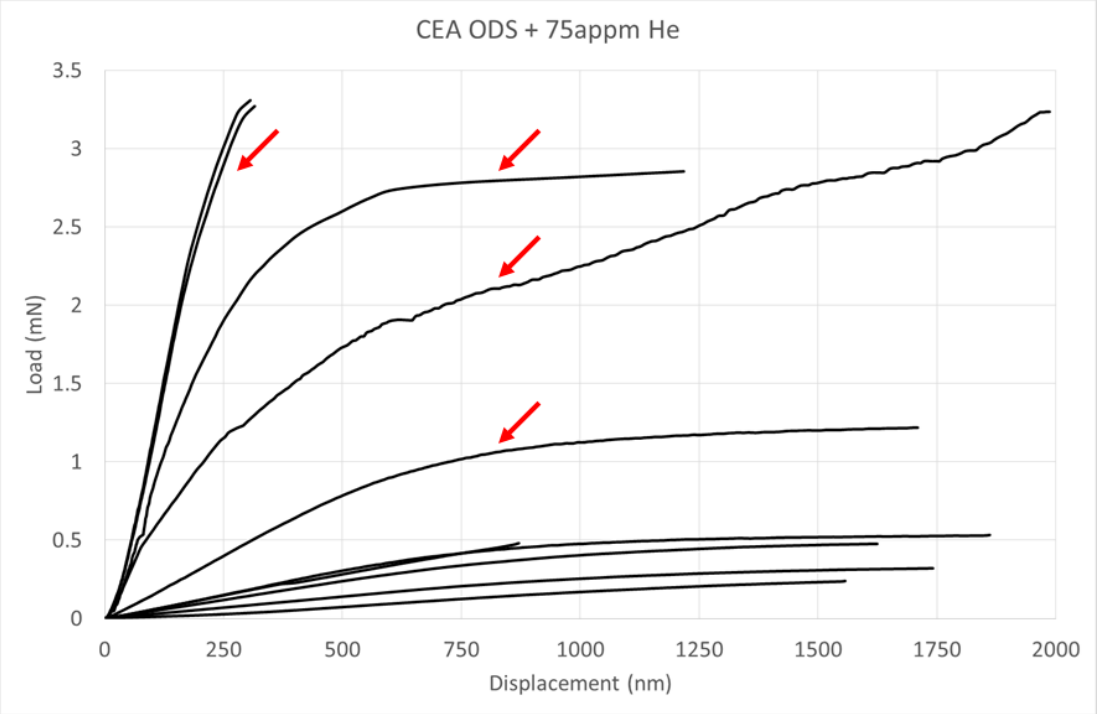

Figure 195 – Load vs. Displacement – CEA ODS 75appm He, full range
Red arrows indicate results with a load greater than 0.7mN at a displacement of 1000nm.

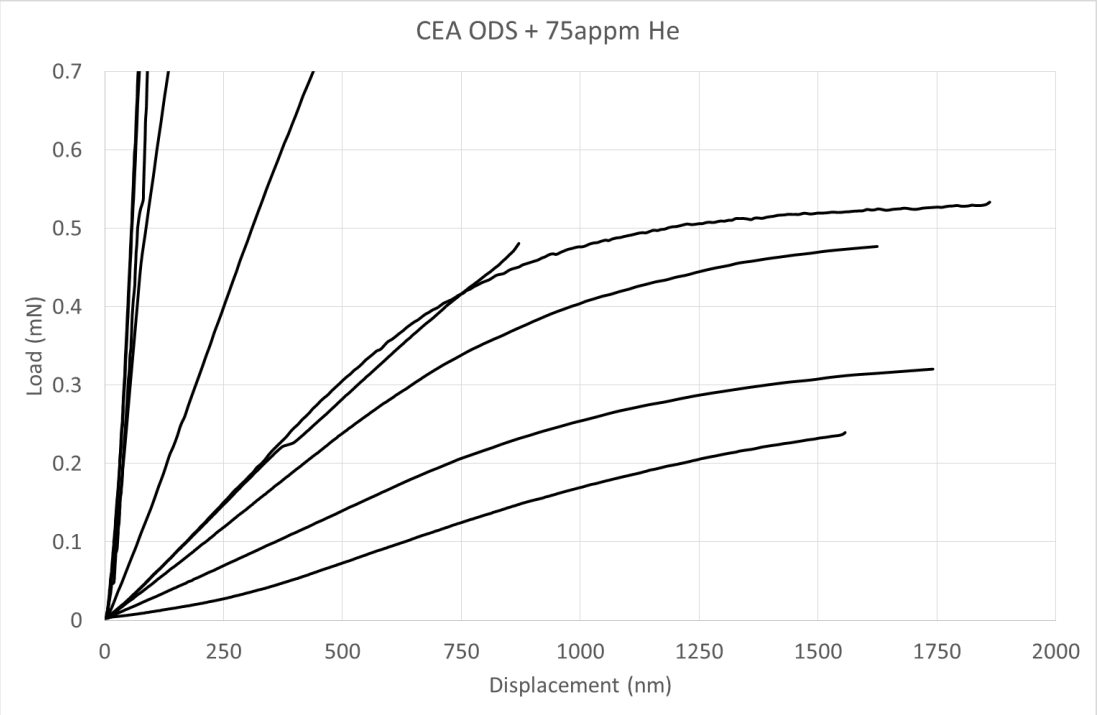

Figure 196 – Load vs. Displacement – CEA ODS 75appm He, reduced range

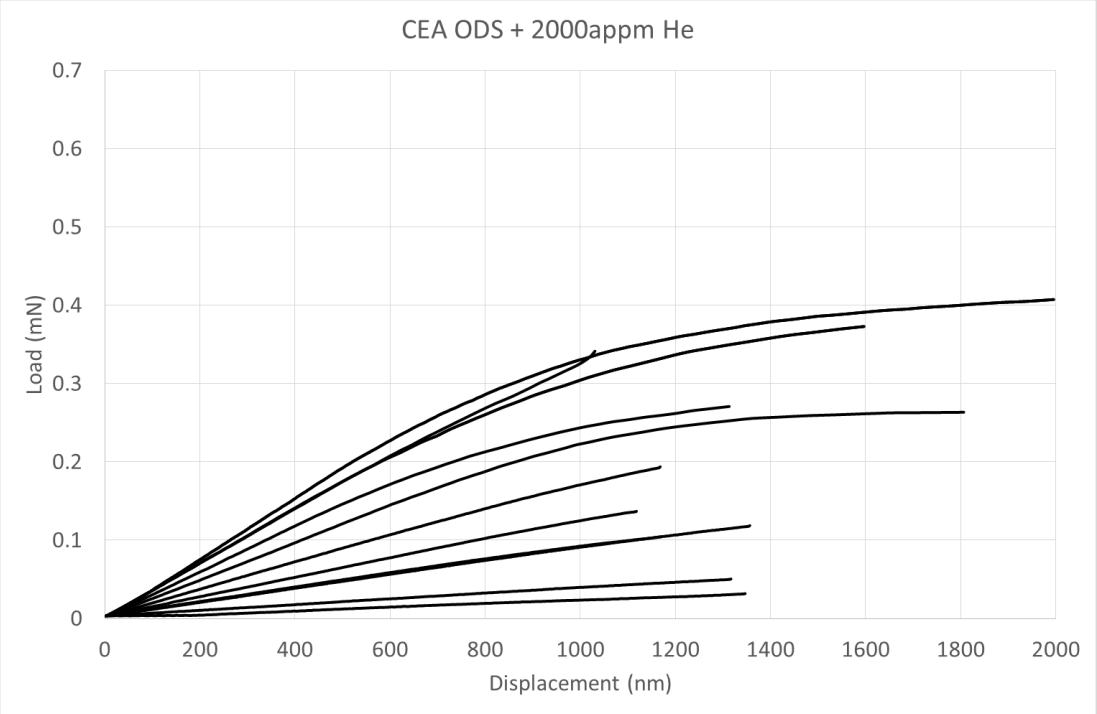

Figure 197 – Load vs. Displacement – CEA ODS 2000appm He

EUROFER

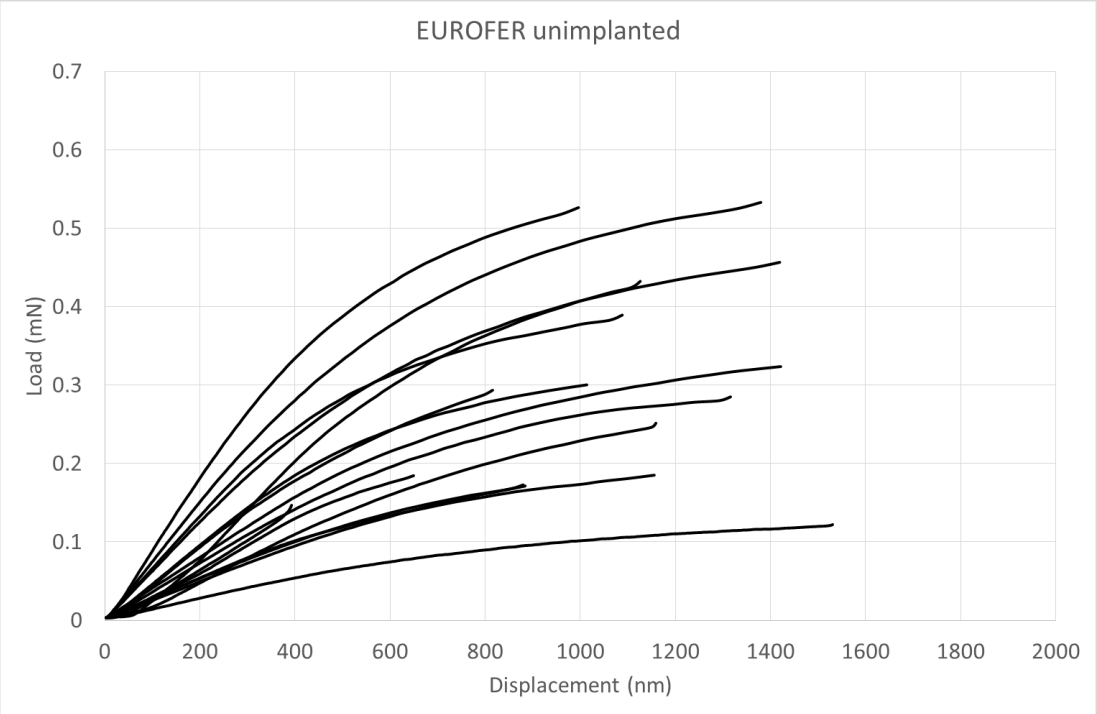

Figure 198 – Load vs. Displacement – EUROFER unimplanted

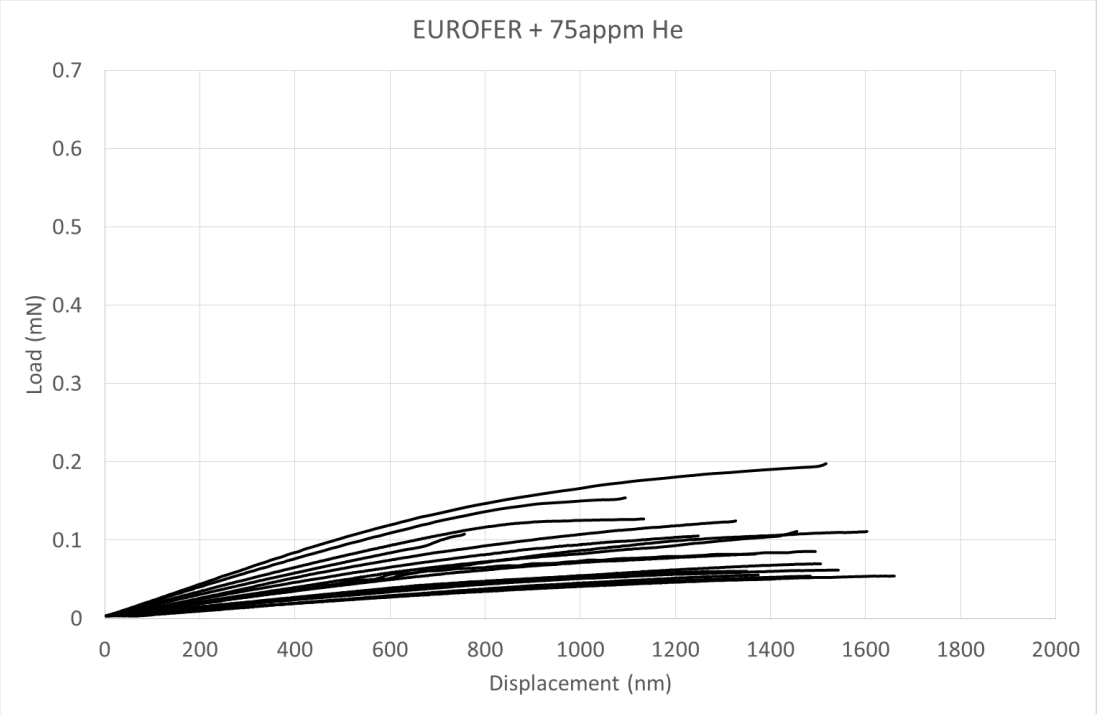

Figure 199 – Load vs. Displacement – EUROFER 75appm He

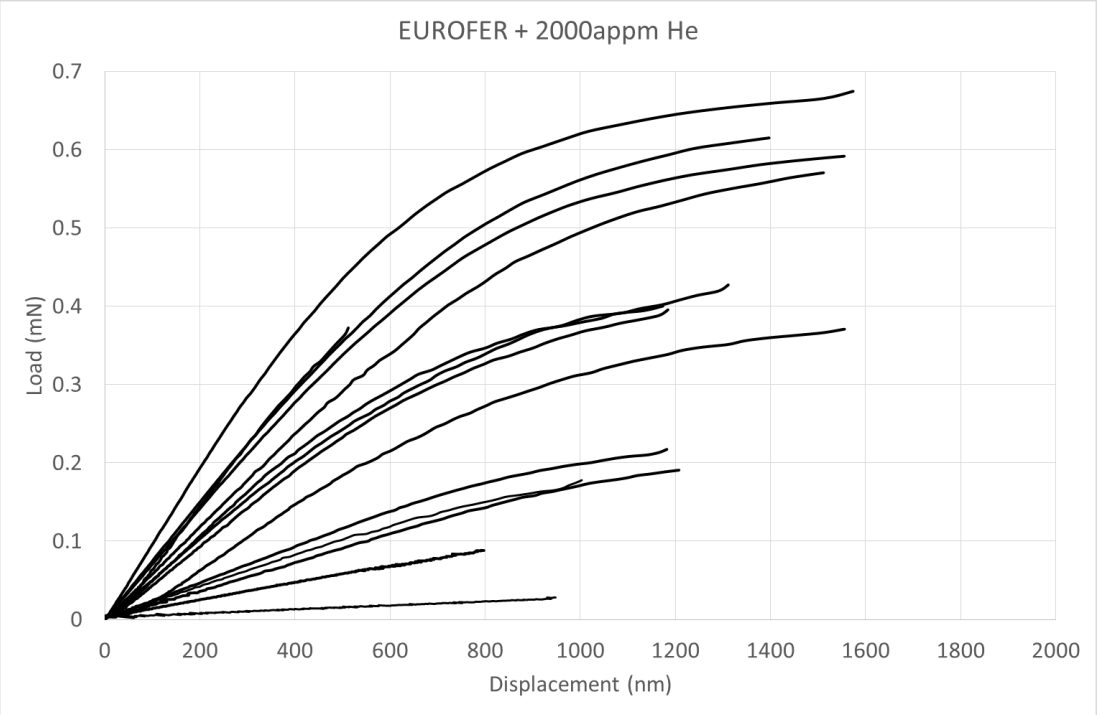

Figure 200 – Load vs. Displacement – EUROFER 2000appm He

EUROFER ODS

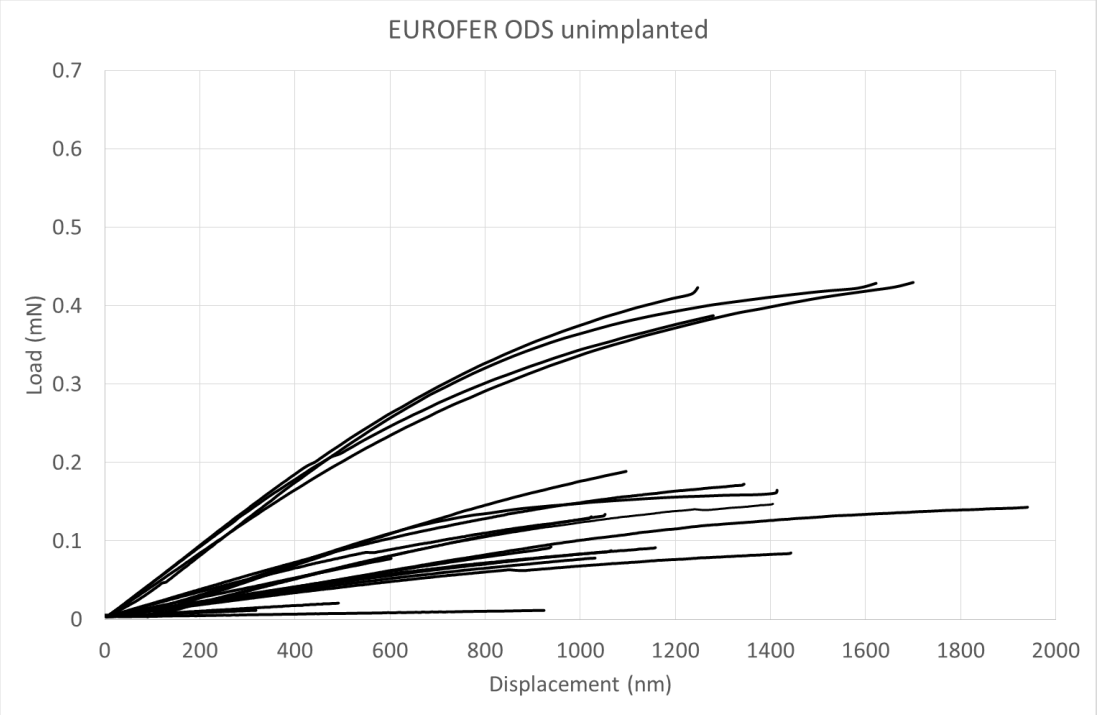

Figure 201 – Load vs. Displacement – EUROFER ODS unimplanted

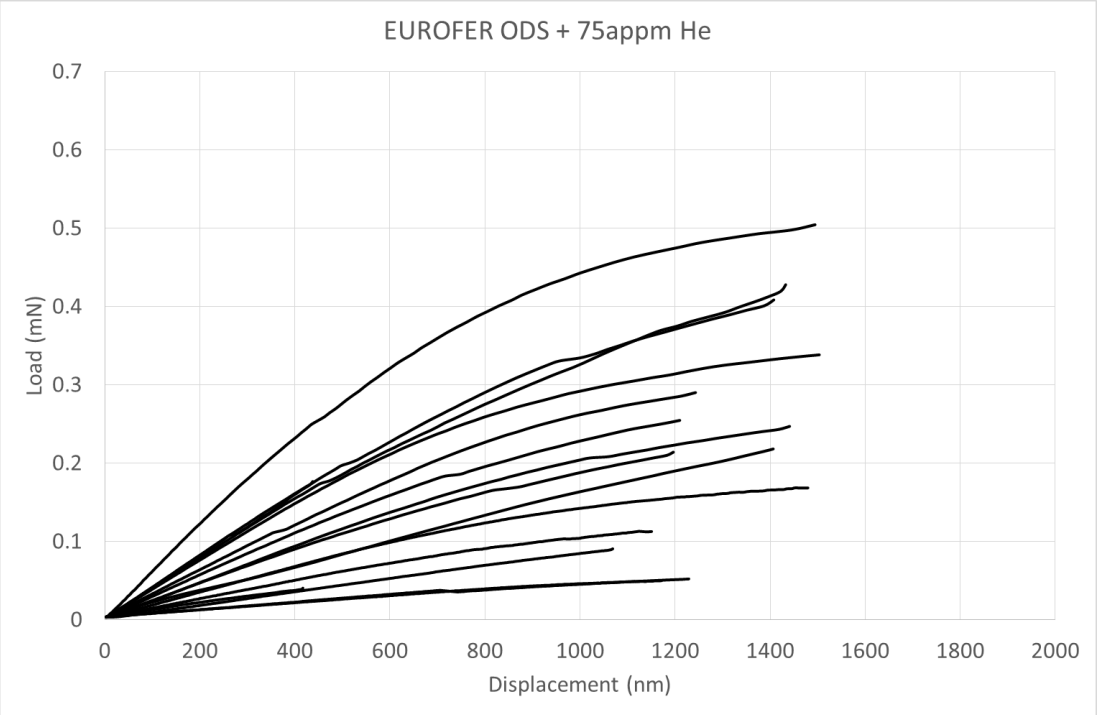

Figure 202 – Load vs. Displacement – EUROFER ODS 75appm He

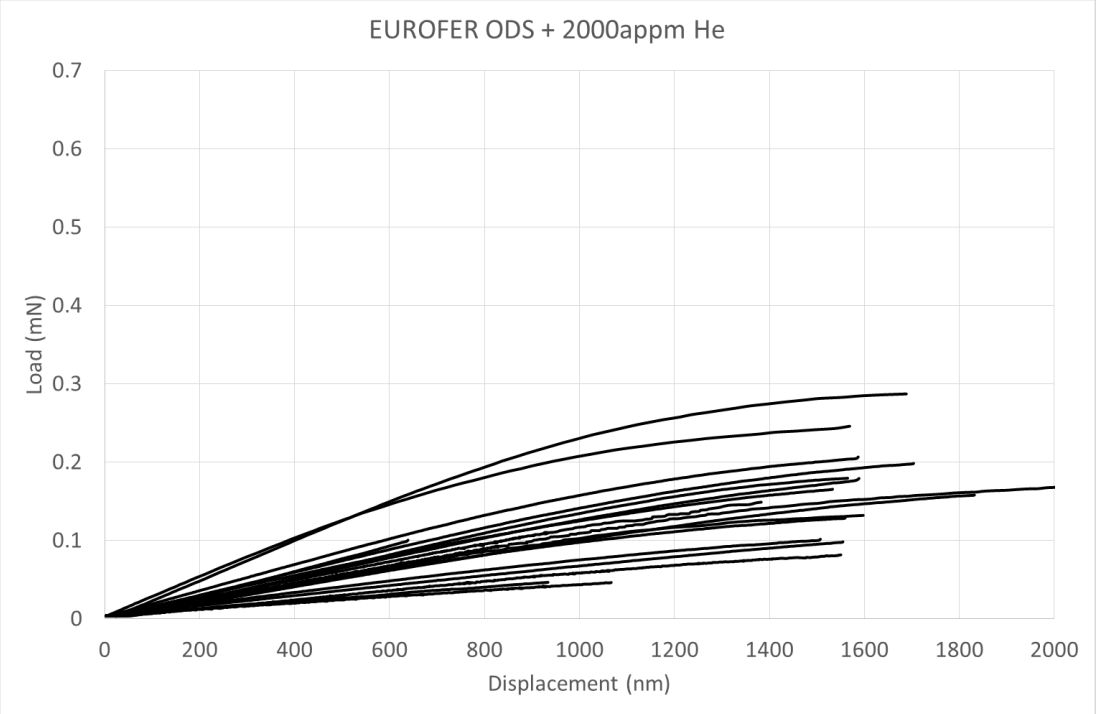

Figure 203 – Load vs. Displacement – EUROFER ODS 2000appm He

Appendix C – Calculation of Helium Densities

Known information

Atomic radius of iron: 126pm = 1.26×10^{-10}m

Oxide particle density: 2.5-6.7x10^{23} particles/m^3, ave. 4.6x10^{23} m^{-3} [102]

Oxide particle size: 1.0-1.6nm diameter, ave. 1.3x10^{-12}m [102]

Volume of BCC unit cell:

$$v = e^3 \qquad \text{where} \qquad e = \frac{4r}{\sqrt{3}}$$

$$e = \frac{4 * 1.26 * 10^{-10}}{\sqrt{3}}$$

$$e = 2.91 * 10^{-10}$$

$$v = e^3 = 2.46 * 10^{-29}\ m^3$$

Unit cells per m^3:

$$\frac{1}{2.46 * 10^{-29}} = 4.07 * 10^{28}$$

BCC has two atoms be unit cell, therefore atoms per m^3:

$$2 * 4.07 * 10^{28} = 8.13 * 10^{28}$$

$$8.13 * 10^{28} = 8.13 * 10^{22} Million$$

Helium atoms per m^3:

$$2000appm * 8.13 * 10^{22} Million\ atoms = 1.6 * 10^{26} He\ atoms/m^3$$

Helium atoms per nm^3:

$$\frac{He\ per\ m^3}{nm^3 per\ m^3} = \frac{1.6 * 10^{26}}{1 * 10^{27}} = 0.16\ He\ atoms/nm^3$$

Helium atoms per particle:

$$\frac{He\ per\ m^3}{particles\ per\ m^3} = \frac{1.6 * 10^{26}}{4.6 * 10^{23}} = 353\ He\ atoms/\text{particle}$$

Surface area of oxide particle:

$$A = 4\pi r^2 = 4 * \pi * (0.65 * 10^{-9})^2 = 5.3 * 10^{18} m^2$$

Particle surface area per m^3:

$$4.6 * 10^{23} * 5.3 * 10^{-18} = 2.44 * 10^6\ m^2/m^3$$

Helium per surface area:

$$\frac{1.6 * 10^{26}}{2.44 * 10^6} = 6.6 * 10^{19} particles/m^2 = 66\ particles/nm^2$$

"++?????++ Out of Cheese Error. Redo From Start."
— Sir Terry Pratchett, Interesting Times [199]